THE INFLUENCE OF MORPHOLOGY ON EXCITONS IN SINGLE CONJUGATED MOLECULES

by

Alexander Thiessen

A dissertation submitted to the faculty of
The University of Utah
in partial fulfillment of the requirements for the degree of

Doctor of Philosophy

in

Physics

Department of Physics and Astronomy

The University of Utah

December 2014

The University of Utah Graduate School

STATEMENT OF DISSERTATION APPROVAL

The dissertation of **Alexander Thiessen**

has been approved by the following supervisory committee members:

John M. Lupton	, Chair	**06/12/2014** Date Approved
Christoph Boehme	, Member	**06/12/2014** Date Approved
Mikhail E. Raikh	, Member	**06/12/2014** Date Approved
Inese I. Ivans	, Member	**06/30/2014** Date Approved
Michael D. Morse	, Member	**06/12/2014** Date Approved

and by **Carleton DeTar**, Chair/Dean of

the Department/College/School of **Physics and Astronomy**

and by David B. Kieda, Dean of The Graduate School.

ABSTRACT

The electronic properties of π-conjugated molecules are strongly related to their molecular shape and morphology of assembly in three-dimensional space. Understanding the various structure-property relationships is relevant to the applications of these materials in optoelectronic devices such as organic light-emitting diodes, field effect transistors and photovoltaic cells. The fact that conjugated systems interact with visible light opens these materials to a plethora of noninvasive spectroscopic investigation techniques.

In this work, electronic properties of different π-conjugated systems are studied spectroscopically on the ensemble and the single molecule levels. Single molecule spectroscopy is advantageous in that it allows the investigation of the individual nuclear building blocks that contribute to the properties of the ensemble. Additionally, transient photoluminescence spectroscopy methods can provide useful insight into the temporal evolution of the emissive states. In combination with these methods, novel π-conjugated model molecules are used to probe processes related to exciton dynamics. For the first time, the spatial localization of excited states is probed experimentally in a molecule with a circular chromophoric structure. In addition, a set of model molecules with different geometries is employed to study exciton relaxation in π-conjugated systems. The molecular morphology is utilized to distinguish between processes such as nuclear reorganization and torsional relaxation. Furthermore, single molecule spectroscopy is used to study the electronic structure of individual polymer chains in the photovoltaic cell material poly-(3-hexylthiophene). Optical spectra of this polymer are known to change with the morphology of the bulk film. Single molecule studies reveal that individual polymer chains exhibit similar behavior and indicate that spectral diversity is an intrinsic property of single P3HT molecules.

The main results of this work are the following: (1) Excitations in a molecule with rigid circular geometry are shown to localize randomly between different parts of the

molecule and show no correlation with the orientation of the excitation light polarization. (2) Model systems can be used to differentiate between different dynamics of exciton relaxation and, furthermore, processes such as torsional relaxation can be inhibited by a rigid molecular structure. (3) The electronic structure of single P3HT molecules is strongly dependent on polymer chain conformation and can be influenced by the surrounding host polymer.

Is the termite aware of the extent of its work?

To what drives us.

And to the journey.

CONTENTS

LIST OF FIGURES

ACKNOWLEDGMENTS

This work would not have been possible without the help and support of a number of people whom I would like to express my deepest gratitude:

- **Prof. John M. Lupton** for accepting me in his group at the University of Utah and being constantly inspiring and enthusiastic about scientific research; for being a great thinker and supporter of new ideas; for the continuous challenge and guidance that he provided to me; for sustaining the subtle balance between creativity and productivity and, thus, a very enjoyable atmosphere in his group.

- **Prof. Michael H. Bartl, Prof. Christoph Boehme, Prof. Inese I. Ivans, Prof. Michael D. Morse, and Prof. Mikhail E. Raikh** for taking interest in my work and serving on my Supervisory Committee. In particular, I acknowledge **Prof. Christoph Boehme** and **Prof. Mikhail E. Raikh** for the support during my graduate school years. I am deeply indebted to **Prof. Mikhail E. Raikh** for his extraordinary lectures inspiring a greater sense of scientific intuition.

- **Dr. Nicholas J. Borys** with whom I shared my office with for over four years. Nick provided invaluable guidance beyond my initial graduate school time. I will always value our – sometimes heated – scientific discussions on experimental and theoretical topics.

- **Dr. Kipp J. van Schooten**, **Dr. Sebastian Bange**, and **Dr. Eyal Shafran** for valuable scientific discussions on work-related subjects and beyond.

- **Prof. Sigurd Höger**, **Dr. A. Vikas Aggarwal**, **Dr. Stefan-S. Jester**, and **Alissa Idelson** from the University of Bonn for providing novel π-conjugated materials, including their characterization, and for various discussions related to chemistry and physics as part of a very fruitful and enjoyable collaboration.

- **Prof. David A. Vanden Bout**, **Dr. Takuji Adachi**, and **Dr. Jan Vogelsang** for inviting me to the University of Austin and uncovering the subtleties of single π-conjugated polymers chains together.

- **Douglas Baird**, **Sebastian Bange**, **Nick Borys**, **Debangshu Chaudhuri**, **Philippe Klemm**, **Dongbo Li**, **Sue Liu**, **Kipp van Schooten**, **Eyal Shafran**, and **Manfred Walter** for making the Nanoscale Optoelectronics Group in Utah a great and fun place to work.

- **Dr. Jan Vogelsang**, **Florian Steiner**, **Dominik Würsch**, **Ines Caspers**, and **Tobias Haug** from the University of Regensburg for their help with the equipment at the University of Regensburg and the joint scientific effort.

- **Kathy Blair**, **Matt DeLong**, **Heidi Frank**, **Jackie Hadley**, **Vicki Nielsen**, **Harold Simpson**, **Kathrine Skollingsberg**, **Jolene Snyder**, **Wayne Wingert**, **Deana Young** and **Shawn Merrill** for their help with administration and facilities and several other favors.

- **Dr. Philipp A. Rahe** for putting up with me as a roommate and for all valuable discussions and projects on a scientific and nonscientific level.

- **Dr. Andrew Smith** for supplying the greatest dry-aged steaks on earth, including other culinary delicatessen.

- **Nick**, **Kipp**, and **Andy** for proof-reading this work.

Finally, I would like to thank my parents, **Emilia Bender** and **Peter Thiessen**, and my sister, **Hedwig Thiessen**, for being exceptional individuals, forming an integral part of my life who continuously believe in me and support me, despite being thousands of miles away.

CHAPTER 1

INTRODUCTION

The beauty of π-conjugated molecules lies in the fact that they interact with visible light. Nature has been taking advantage of this feature since the beginning of photosynthesis – a sophisticated and resourceful process of energy harvesting. Although mankind has been using organic dyes for centuries, it is only in the last few decades that π-conjugated molecules – closely related to those dyes – gained rigorous popularity in the scientific community. Beyond the potential for practical application [1–3], study of basic optoelectronic processes is crucial for the understanding of the physical principles in these materials.

A π-conjugated polymer chain is made of a collection of repetitive monomer units that are linked chemically. In the ideal case, the electrons in the π-orbitals are delocalized over the extent of the chain. However, conformational variations can introduce structural defects due to kinks and twists in the polymer backbone causing interruptions in the π-system. Similar interruptions occur from chemical defects that are introduced during material synthesis or by reactions with other chemical species post synthesis. A schematic π-conjugated chain is shown in Figure 1.1.

Uninterrupted π-segments are called chromophores and contain electrons that are capable of responding to the electric field of photons. Upon absorption of light, the electron is promoted to a higher energy level and relaxes to a coulombically bound electron-hole pair (exciton). The relaxation process dissipates heat and causes self-trapping (localization) of the exciton [4, 5]. The extent of the exciton can be smaller than the size of the chromophore and naturally raises the question of where on the segment the exciton will localize. After the exciton is formed, it can migrate to adjacent chromophores that are located on the same or on another polymer chain. Energy migration requires coupling between the chain segments [6, 7]. Furthermore, the coupling can

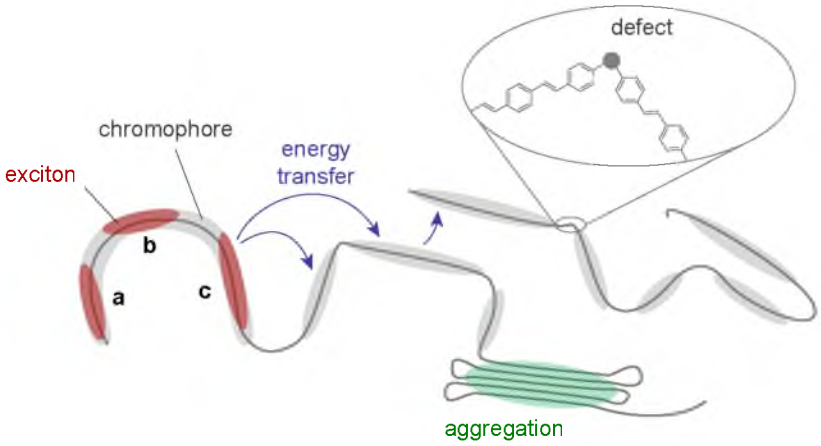

Figure 1.1. Schematic view of π-conjugated polymer chains. Absorption of light by a chromophore (gray) creates an excited state which randomly localizes to an exciton (red) somewhere on the chain (**a**, **b** or **c**). After localization, the exciton can undergo energy transfer to adjacent chromophores. Aggregation of chains modifies the electronic structure of the system.

be strong enough to cause electronic level splitting [8, 9] giving rise to energy shifts in emission and absorption spectra. All of the processes described here strongly depend on the electronic structure that is governed by the shape of the molecule.

There are different ways to influence the shape and structure (morphology) of molecules. One approach is to design model molecules with well defined chemical structures. Another possibility is to control molecular conformation with external parameters such as the immediate environment. In this work, both approaches were employed and the results were studied spectroscopically on the single molecule level. The main advantages of this technique are its noninvasive nature and its ability to resolve contributions from single entities that constitute the ensemble [10–12].

The practical relevance of determining where an exciton localizes might not be immediately obvious. Not only does it help to understand the mechanism of localization, the overall process of exciton localization is important for the dynamics of exciton migration. However, interpretation of experimental studies on exciton localization are inherently tedious without precise knowledge of the molecular structure. We eliminate this factor of uncertainty by using a well defined, structurally rigid spoked-wheel macrocycle molecule where the π-conjugation on the perimeter is decoupled from the structural centerpiece. The localization dynamics in our model system are studied with single

molecule polarization spectroscopy techniques which provide spatial information on the absorbing and emitting units (Chapter 3). Our results show that localization in these systems is indeed dynamic and nondeterministic – the exciton localizes randomly on different parts of the ring.

Torsional relaxation following the excitation event is in some cases known to introduce severe structural changes to the molecular geometry. A famous example is the photoisomerization of retinal constituting a crucial biological mechanism in human vision [13, 14]. However, structural relaxation results in a loss of excitation energy and is ultimately undesirable in terms of light harvesting processes. In this work, the extent of structural relaxation and the associated energy loss in model systems with different geometries that are based on the same building blocks is studied (Chapter 4). A combination of transient and single molecule spectroscopy techniques supported by Monte Carlo simulations provide a comprehensive picture in which the extent of structural relaxation is dominated by molecular shape, size and internal degrees of freedom.

In addition to careful selection of chemical building blocks, electronic structure of a material can be modified solely by its morphology. This feature is appealing as it allows adjustment of optical spectra to fit desired functionality. In naturally occurring light harvesting complexes precise arrangement of chromophore units creates coupling and aids the absorption of solar radiation [15]. It may seem serendipitous that one of the most popular π-conjugated polymers that is employed for photovoltaic studies [16] also exhibits a strong susceptibility of its optical properties to morphological changes [17, 18]. While this material, poly(3-hexylthiophene), has been extensively studied in bulk, single molecule studies are sparse [19–23]. Investigations performed in this work show that chromophoric diversity is largely influenced by morphological variations on the single molecule level (Chapter 5), and not by bulk packing.

The following part of Chapter 1 is intended to provide a brief introduction to the concepts relevant for the processes described above. Timescales of excited state dynamics and interactions between chromophores are discussed. Chapter 2 introduces the studied material systems and the principles of the experimental and computational methods used in this work and also includes a detailed description of their practical implementation. The following chapters contain detailed discussions of the experimen-

tal results. Chapters 3 and 4 study structural influences on exciton localization as well as structural relaxation in custom-made π-conjugated model systems. In Chapter 5, the morphology of single polymer chains is modified with external parameters and the effects on exciton dynamics are investigated.

1.1 Interactions of π-Conjugated Chromophores with Light

Before emerging into more detailed discussions of exciton formation and localization in Sections 1.1.2 and 1.1.3, a broader overview on possible events after absorption of light is given and the structure of optical spectra in π-conjugated systems is discussed (Section 1.1.1).

When π-conjugated systems interact with light, a photon is absorbed and excites an electron to a higher energy state. The groundstate generally consists of paired electrons. Depending on the electron spin configuration that can be antiparallel or parallel, these states have a singlet (S_n) or triplet (T_n) multiplicity, respectively; here n is the principal quantum number. Due to the exchange interaction, triplet states are always lower in energy than singlet states of the same quantum number $n > 0$. Following selection rules, optical transitions between different spin manifolds are not allowed. Accordingly, electrons from a singlet ground state are more likely to be promoted to a higher excited state of the same spin symmetry ($S_0 \rightarrow S_n$). Because electrons respond very quickly to the electric field of a photon, the absorption process is very fast and occurs on timescales of $\sim 10^{-15}$ s [24]. A schematic overview of possible transitions between different states is shown in a Jablonski diagram in Figure 1.2.

Each of the electronic states accommodates numerous vibrational levels with smaller energy spacing. Optical transitions into higher vibrational levels of the singlet states are possible and are explained with the help of the Franck-Condon principle in the following chapter. Electrons excited to these high lying vibrational states can relax under the assistance of phonons within $10^{-12} - 10^{-10}$ s to the vibrational ground state of the excited state. In addition, electrons can cross over to a lower electronic state. This internal conversion (IC) is highly dependent on electron-phonon coupling and occurs within $10^{-11} - 10^{-9}$ s. Both of these processes are hard to access experimentally and computationally but are crucial for the understanding of excited state dynamics including

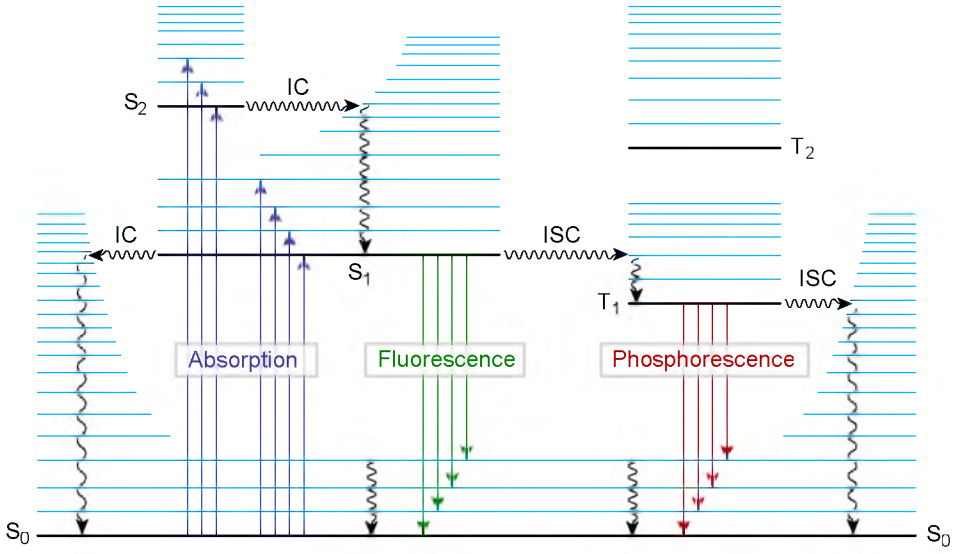

Figure 1.2. A Jablonski diagram shows the possible transitions between electronic (black) and vibrational (light blue) states of a molecule. Radiative and nonradiative transitions are depicted by straight and wavy lines, respectively. The notations are: internal conversion IC, intersystem crossing ISC, singlet ground state S_0, singlet excited state S_n, and triplet excited state T_n.

exciton formation, relaxation and the emerging consequences for transport [25–29]. A more dedicated discussion of this subject is found in Sections 1.1.2 and 1.1.3.

In the 1950s, long before ultrafast spectroscopic techniques and modern computational methods, Michael Kasha established, what he called, "a most useful spectroscopic criterion," stating: "The emitting electronic level of a given multiplicity is the lowest excited level of that multiplicity." [30]. His conclusion, based on purely empirical results, became known as Kasha's rule and is a tribute to the remarkable efficiency of the phonon-assisted energy relaxation. However, rare exceptions to Kasha's rule are found e.g., in azulene and other molecules [31]. Nonetheless, emission is usually observed from the S_1 or T_1 state and is termed fluorescence or phosphorescence, respectively. The latter requires intersystem crossing (ISC) between the spin manifolds and becomes weakly allowed due to spin-orbit coupling. In organic materials made of elements with low atomic numbers, spin-orbit coupling is relatively inefficient and the decay times of fluorescence ($\sim 10^{-9}$ s) and phosphorescence ($10^{-6} - 1$ s) are remarkably different. In fact, for the purpose of single molecule spectroscopy on organic molecules, the triplet

state is considered a "dark" state, owing to the low phosphorescence quantum yield.

1.1.1 The Franck-Condon Principle

Because coupling between electrons and nuclei in π-conjugated systems is relatively strong [25], vibronic signatures are generally observed in optical spectra and are manifested in more or less distinct transition lines. The probability for such transitions can be described following the Franck-Condon principle. Important assumptions of the principle are the Born-Oppenheimer approximation, and low temperature. The former allows to decouple electron motion from (vibrational) motion of the nuclei, owing to the roughly four orders of magnitude difference in masses of electrons and nuclei. From the low temperature assumption follows that higher vibrational states are not populated. Thus, excitation occurs exclusively from the vibrational ground level of the electronic ground state. This assumption is valid for most π-conjugated systems where the most dominant vibrational mode (C=C double bond stretching) is at energies of 1600 cm^{-1}, which is much higher than the thermal energy (kT) at room temperature, which is only $\sim$ 200 cm^{-1}. Because the position of the nuclei, expressed in a generalized configuration coordinate q, is assumed not to change during excitation, dipole-allowed optical transitions are called "vertical" or "Franck-Condon" transitions (Figure 1.3).

According to the Born-Oppenheimer approximation, the total wavefunction[1] can be factorized in an electronic ϕ_n and vibrational part $\chi_n(v_n)$. The latter is the harmonic oscillator function[2] with vibrational quantum number v. The transition probability $P_{v_0=0,v_1}$ from the ground state $\chi_0(v_0 = 0)$ to a vibrational level v_1 of the excited state S_1 is given by [32]

$$P_{v_0=0,v_1} \propto \left|\langle\phi_0|\mathbf{M}|\phi_1\rangle\right|^2 \cdot \underbrace{\left|\langle\chi_0(v_0=0)\,|\,\chi_1(v_1)\rangle\right|^2}_{\text{Franck-Condon factor}}, \tag{1.1}$$

where $\mathbf{M} = e\mathbf{r}$ is the electric dipole moment vector summing over all electrons in the system. The first term in Equation (1.1) is the squared electronic dipole matrix element

[1] Rotational vibrations are ignored here due to their small overall contribution. The spin wavefunction is neglected for simplicity.

[2] The harmonic oscillator functions of the ground and excited state are defined with respect to different zero-positions of the generalized configuration coordinate q which arise due to geometric relaxation of the molecule in the excited state.

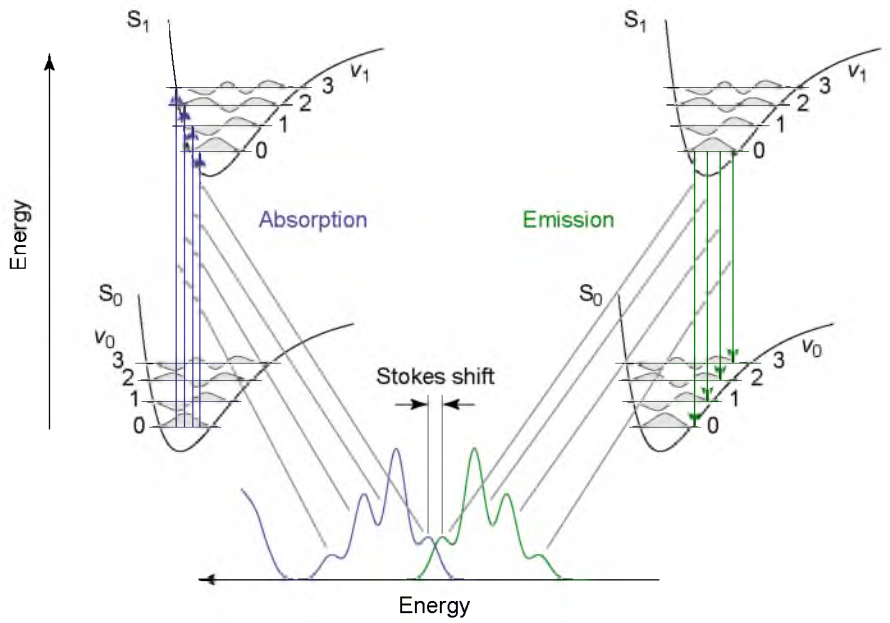

Figure 1.3. Optical transitions according to the Franck-Condon principle.

quantifying the electronic transition intensity. The second term is the Franck-Condon factor that distributes this intensity between different vibrational satellites of the progression.

After excited state relaxation, following Kasha's rule, emission occurs from the vibrational ground state $v_1 = 0$ to any of the vibrational levels of the ground electronic state, creating mirror symmetry between the absorption and emission spectra (Figure 1.3). In cases of energy loss due to exciton relaxation or energy transfer, the zero-phonon lines of the absorption and emission spectra are separated in energy, this separation is referred to as the Stokes shift. The energy separation is minimized in molecular systems with a rigid structure such as perylenes or the π-conjugated polymer ladder-type poly(paraphenylene) [33].

Being the squared overlap integral of displaced harmonic oscillator functions, the Franck-Condon factor can be related to the Huang-Rhys parameter S [32],

$$\left|\langle \chi_1(v_1 = 0) \,|\, \chi_0(v_0)\rangle\right|^2 = \frac{e^{-S} S^{v_0}}{v_0!} \,, \tag{1.2}$$

which itself is related to the shift Δq of the equilibrium positions following excitation

$$S = \frac{M\omega}{2\hbar}(\Delta q)^2 \,. \tag{1.3}$$

Here M is the reduced mass and ω the angular frequency of the harmonic oscillator. The Huang-Rhys parameter quantifies the strength of electron-phonon coupling and can be inferred from the integrated emission intensities $I_{\nu_1 \to \nu_0}$ [33]

$$\frac{I_{0\to 0}}{\sum_{\nu_0=0}^{\infty} I_{0\to \nu_0}} = e^{-S} \ . \tag{1.4}$$

From Equation (1.2) it becomes obvious that the 0–0 transition is followed by vibronic replicas, called a vibronic progression, which adhere to Poissonian statistics. The influence of coupling on the relative emission intensity is demonstrated in Figure 1.4.

The intensity ratio of the vibronic lines is thus a powerful tool in the estimation of electron-phonon coupling. For example, dipole forbidden transitions in H-Aggregates[3] can borrow oscillator strength through phonon coupling and become weakly allowed (Section 1.2.1). Consequently, characterization of vibronics shines light on the underlying emission mechanism and helps understand the excitonic character at hand, as will be discussed in Chapter 5.

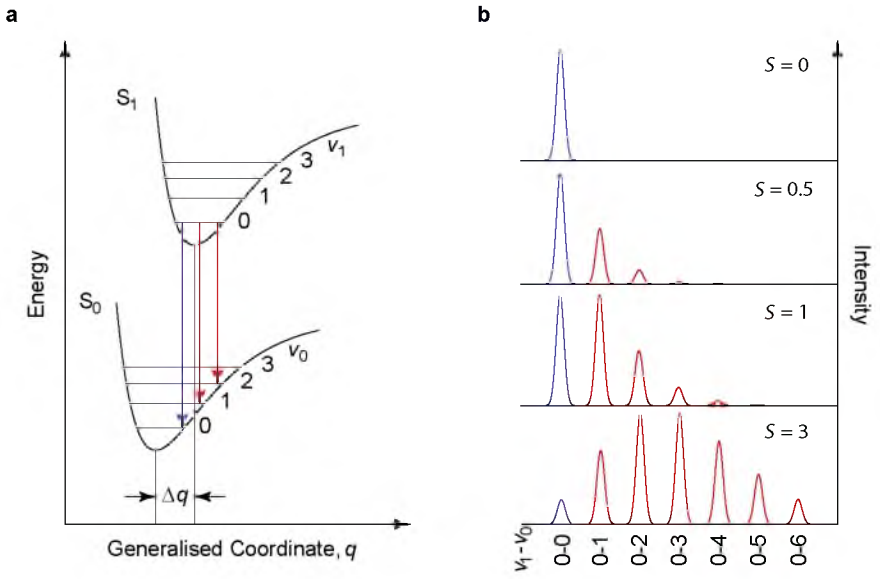

Figure 1.4. Vibronic progression. **a**, The minima of the ground and excited state potential curves are shifted by the difference in equilibrium position Δq. **b**, Franck-Condon intensity distribution for different Huang-Rhys parameters $S \propto (\Delta q)^2$. Labels on the x-axis denote the transition from state ν_1 to ν_0.

[3] An H-aggregate results from a cofacial alignment of monomers, whose lowest transition dipole moments cancel out.

1.1.2 Exciton Localization Through Nuclear Reorganization

Following the absorption of a photon, a molecule undergoes different dynamic processes until it finally relaxes to the ground vibrational level of the first excited electronic state. In principle, the electronic and nuclear degrees of freedom of a molecule consisting of n electrons and N nuclei can be fully described by the many body Hamiltonian

$$\hat{\mathbf{H}} = \underbrace{-\sum_{i=1}^{n} \frac{1}{2}\nabla_i^2}_{\hat{\mathbf{T}}_\mathrm{e}} \underbrace{-\sum_{I=1}^{N} \frac{1}{2M_I}\nabla_I^2}_{\hat{\mathbf{T}}_\mathrm{N}} + \underbrace{\sum_{i\neq j}^{n} \frac{1}{|\mathbf{r}_i - \mathbf{r}_j|}}_{\hat{\mathbf{V}}_\mathrm{ee}} + \underbrace{\sum_{I\neq J}^{N} \frac{Z_I Z_J}{|\mathbf{R}_I - \mathbf{R}_J|}}_{\hat{\mathbf{V}}_\mathrm{NN}} \underbrace{-\sum_{i,I}^{n,N} \frac{Z_I}{|\mathbf{r}_i - \mathbf{R}_I|}}_{\hat{\mathbf{V}}_\mathrm{eN}}, \tag{1.5}$$

where M_I are the nuclear masses, Z_I the atomic numbers and $\mathbf{r}$ and $\mathbf{R}$ the coordinates of electrons and nuclei, respectively. The terms in Equation (1.5) are the electron $\hat{\mathbf{T}}_\mathrm{e}$ and nuclear $\hat{\mathbf{T}}_\mathrm{N}$ kinetic energy, and $\hat{\mathbf{V}}_\mathrm{ee}$, $\hat{\mathbf{V}}_\mathrm{NN}$ and $\hat{\mathbf{V}}_\mathrm{eN}$ are the electron-electron repulsion, nuclear-nuclear repulsion and electron-nuclear attraction. In the Born-Oppenheimer approximation the contribution of the nuclear kinetic energy term $\hat{\mathbf{T}}_\mathrm{N}$ to the total energy of the system is considered negligible and allows for the separation of electron and nuclear motion. This assumption is part of the necessary simplifications to solve the many-body problem.

Part of the Born-Oppenheimer approximation is the adiabatic approximation where the off-diagonal nuclear kinetic energy coupling terms (i.e., the nonadiabatic coupling) are neglected, and the electronic states are assumed to be well separated in energy. As a result, electrons are restricted to the adiabatic potential energy surface without transitioning between different electronic states. However, when electronic states are close enough to cross, nonadiabatic coupling becomes significant, and the Born-Oppenheimer approximation breaks down [29, 34]. Nonadiabatic processes allow transitions between electronic state potential surfaces and are crucial for the description of, e.g., internal conversion, photoisomerization and photochemical reactions [34].

The motion of both nuclei and in particular of electrons is very fast. Accordingly, experimental observations are inherently difficult but are becoming accessible with the emergence of ultrafast techniques. The following picture of excited state dynamics is based off recent literature reports on theoretical modeling and experimental results.

Immediately after the absorption of a photon, the excited state is delocalized over the extent of the chromophore. Coupling to phonon modes leads to a rapid vibrational

relaxation and successive contraction of the excited state wavefunction [25, 26]. This phonon induced excited state localization is caused by nuclear geometry distortion and is referred to as exciton[4] "self-trapping": the nuclei rearrange to screen the electron-hole entity. The spatial extent of the exciton is primarily governed by the coulombic interaction within the electron-hole pair, which is quite significant due to the low dielectric constant of organic materials.

Exciton localization is very fast and occurs typically within 10 – 100 fs [26, 27, 35]. Nuclear reorganization usually results in altered atomic bond distances and sometimes causes planarization of the molecule in the excited state [25, 29], which can be observed as a change in the transition dipole moment orientation after excitation [26]. In some cases the relaxation involves torsional changes in the molecular geometry, as will be discussed in the following chapter.

1.1.3 Exciton (De)localization Through Torsional Relaxation

The phonon mediated exciton trapping that was discussed in the previous chapter is a very fast process. Its timescale of tens of fs corresponds to just a few C-C vibration cycles [35]. The relatively quick response of the nuclei leads to rapid localization. Further structural reorganization can occur through torsional motion of the molecule that causes excited state *de*localization and lowers its energy [26, 29]. Owing to the larger mass involved in this twist motion, torsional relaxation is much slower (on the timescale of ~ 100 ps) and thus distinguishable from the initial, phonon-assisted relaxation [26, 36]. However, very fast (<0.1 ps) torsional relaxation as a result of excitation to higher electronic states ($n > 1$) has also been reported [28].

Photoisomerization, shown in Figure 1.5, is a famous example of a photoinduced conformational change in molecules such as stilbene and rhodopsin. The latter is a compound that is found in the retina of the human eye and is essential for the mechanism of vision. After excitation, phonon-assisted coupling allows nonadiabatic crossing from the excited state of rhodopsin to the electronic ground state potential surface within ~ 200 fs [13, 14]. Following this rapid transfer the molecule relaxes to batho-

[4] An "exciton" is a quasiparticle and originates from Frenkel's description of excitation-packets capable of moving in a lattice of atoms (Yakov Il'ich Frenkel was born in Rostov-on-Don, Russia, where the author of this thesis spent his childhood summers).

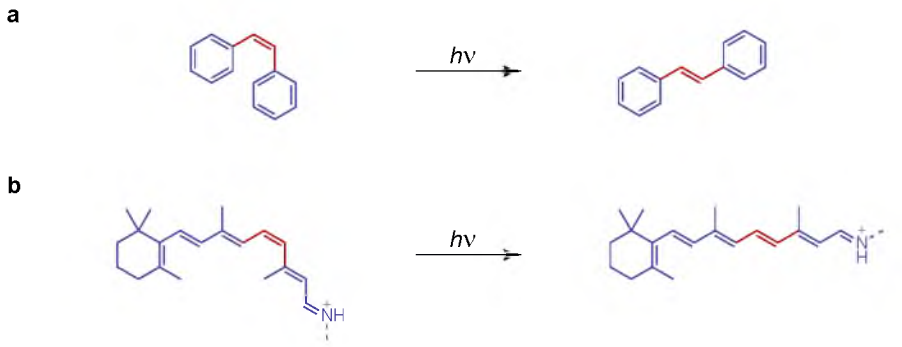

Figure 1.5. Photoinduced torsional relaxation. Absorption of a light quantum ($h\nu$) leads to photoisomerization from *cis*-stilbene to *trans*-stilbene (**a**). Photoisomerization of retinal, bound to the protein rhodopsin (**b**), constitutes a crucial step in the human vision mechanism.

rhodopsin within ~ 1 ps [14] making this process one of the fastest conformational changes in nature.

While nature's obvious objective for the vision process is to exploit the conformational change, it should be noted that excitation energy in photoisomerization is lost to heat. In contrast, for the purpose of light harvesting, it is desirable to avoid energy losses due to structural relaxation. Further, fluctuations in torsional angles can introduce interruptions in the π-conjugation adding complexity to the dynamics of exciton relaxation and are considered to be important for energy transfer on short time scales [37]. The extent of structural relaxation is inherently highly dependent on the molecular structure and makes exploration of model systems an important task as will be discussed in Chapter 4.

1.2 Interaction of Excitons with the Environment

The discussion in this section is focused on excitonic interactions in different regimes of electromagnetic coupling. While Section 1.2.1 considers strongly interacting aggregated molecules, Section 1.2.2 is focused on energy transfer between chromophores in (very) weakly coupled systems. Both scenarios require careful consideration when dealing with bulk materials or folded chains of single polymer molecules containing multiple chromophores.

1.2.1 Excitons in Aggregated Molecules

The interaction of two molecules in the ground state can be either attractive or repulsive and ultimately decides over the existence of the electronic ground state of the dimer. The discussion in this section focuses solely on dimers with an attractive ground-state potential.

In general, the ground-state energy of two interacting molecules can be approximated [5] as [8]

$$E_g = E_1 + E_2 + \langle \psi_1 \psi_2 \,|\, V_{12} \,|\, \psi_1 \psi_2 \rangle \ , \tag{1.6}$$

where $E_{1(2)}$ is the ground-state energy of the individual molecule 1 (or 2) with wavefunction $\psi_{1(2)}$ and V_{12} the intermolecular interaction energy. If the two molecules are identical, the ground state energies are equal ($E_1 = E_2$) and the aggregate is referred to as a physical dimer[6]. The last term in Equation (1.6) is the coulombic binding energy W and must be negative for the dimer to be stable (Figure 1.6a).

In the lowest excited state of a dimer, either molecule 1 or molecule 2 is in the excited state and the total wavefunction is a linear combination of $\psi_1^* \psi_2$ and $\psi_1 \psi_2^*$. Here, the asterisk denotes the excited state. In a dimer (identical monomers), the energies of the individual molecular excited states are equal ($E_1^* = E_2^*$), and the degeneracy of the dimer excited state energy is lifted (Davydov splitting) according to

$$E_\pm = E_1^* + E_2 + W' \pm \beta \ , \tag{1.7}$$

where $\beta = \langle \psi_1^* \psi_2 \,|\, V_{12} \,|\, \psi_1 \psi_2^* \rangle$ is the resonance interaction energy (the exchange interaction) that splits the two energy states, and $W' = \langle \psi_1^* \psi_2 \,|\, V_{12} \,|\, \psi_1^* \psi_2 \rangle$ is the coulombic interaction energy of the charge distribution between the states ψ_1^* and ψ_2 (or ψ_1 and ψ_2^*).

Optical transitions to the states E_+ and E_- are governed by the relative orientation of the monomers in the dimer and can be written as

$$\mathbf{M}_\pm = \frac{1}{\sqrt{2}} (\mathbf{M}_1 \pm \mathbf{M}_2) \ , \tag{1.8}$$

---

[5] For simplicity, vibrational and spin states as well as configuration interactions are neglected.

[6] This definition is as opposed to a chemical dimer, where two monomers are connected by at least one new chemical bond (Chapter 4 and Chapter 3)

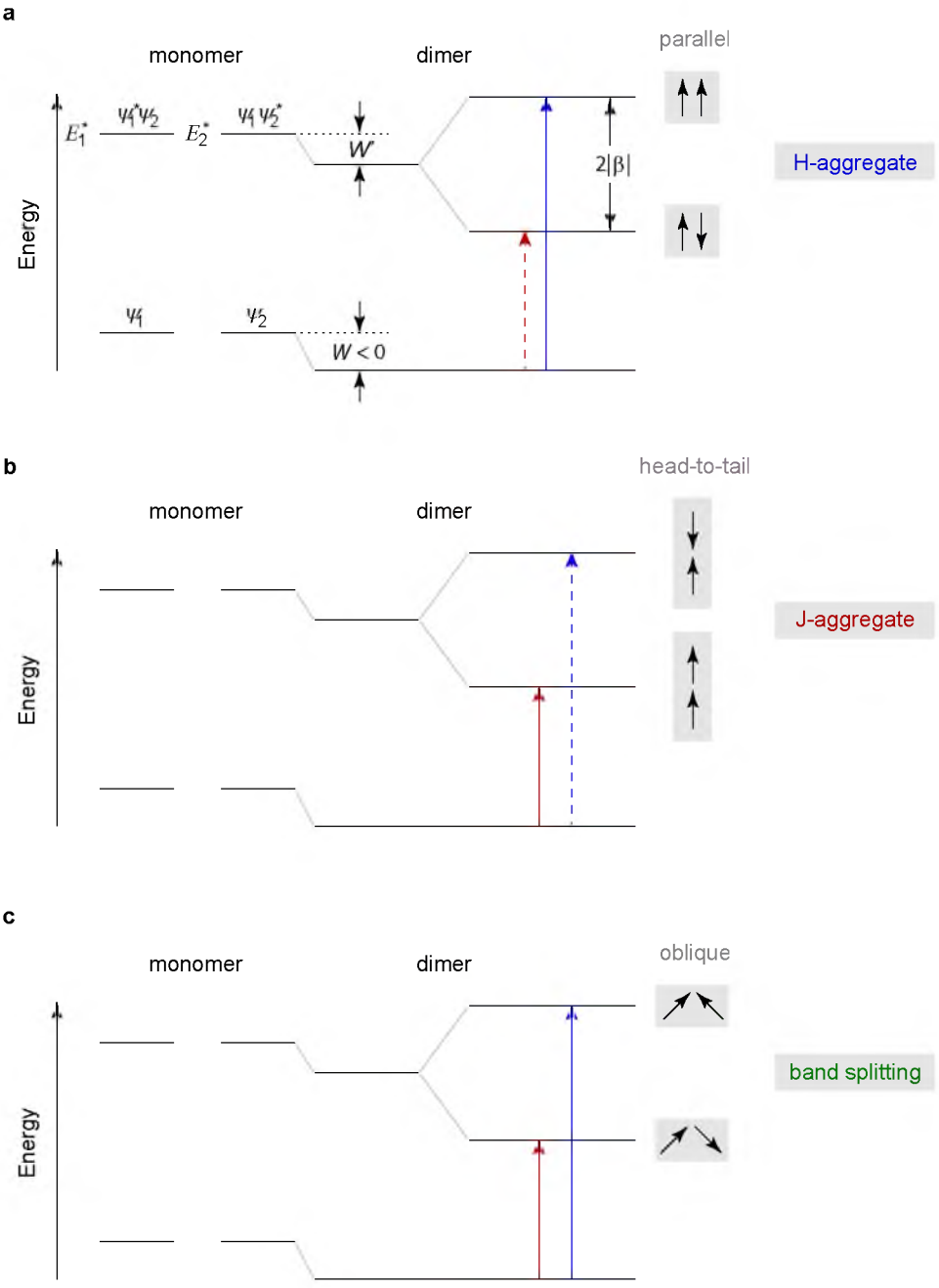

Figure 1.6. Exciton band splitting in molecular dimers. **a**, The Coulomb interaction energies W and W' shift the ground and excited state energy of the dimer, respectively. The excited state energy is split due to the resonance interaction energy β. The relative orientation of monomer transition dipoles (gray boxes) can be parallel (**a**), head-to-tail (**b**) or oblique (**c**) as observed in H-aggregates, J-aggregates and systems with split bands, respectively. Straight and dashed lines indicate dipole-allowed and dipole-forbidden transitions, respectively.

where $\mathbf{M}_1$ and $\mathbf{M}_2$ are the transition dipole moment vectors of monomer 1 and monomer 2, respectively. Possible vector configurations are shown in Figure 1.6 (gray boxes). When either $\mathbf{M}_+$ or $\mathbf{M}_-$ is zero, the optical transition becomes dipole-forbidden as indicated by dashed lines. As a result, the absorption spectra are shifted either to higher (blue) or lower (red) energies. These two cases are referred to as H-aggregate (Figure 1.6a) or J-aggregate formation [7] (Figure 1.6b).

An interesting case arises when the angle between the monomer transition moments is nonzero (or 180°) (Figure 1.6c). In this case, $\mathbf{M}_+$ and $\mathbf{M}_-$ are both allowed but orthogonal to each other. As a result, both transitions can be observed in absorption as was elegantly demonstrated in a bridged naphthyl dimer by Scholes *et al.* [38].

J-aggregates appear in form of a pronounced intensity band at lower energies in absorption as well as emission [9, 39], with increased oscillator strength compared to the monomers. At the same time the 0-0 to 0-1 peak ratio is higher than in the monomer spectrum as a result of decreased phonon coupling [40]. Examples of J-aggregation are also found in nature; for example, in light harvesting complexes present in plants. In these complexes precise arrangement of porphyrins increases coupling, giving rise to a new absorption band, which facilitates harvesting of solar radiation [15].

While it is easy to identify H-aggregates as an emerging high energy absorption band, e.g., by increasing the solution concentration, emission from ideal H-aggregates is practically not observed: the competition between radiative decay from the high-energy split band and internal conversion effectively diminishes the fluorescence quantum yield. However, emission from the low energy level in H-aggregates is observed in real systems and most likely arises from imperfect dipole alignment [41]. In other cases, H-aggregate emission is thought to become weakly allowed due to coupling to the ground vibrational states [17, 40, 42] – a model that was developed to explain specific spectral features, where emission intensity of the second vibronic peak (0-1) dominates over the zero phonon peak (0-0). Despite the validity of the proposed model, characterization of the emission features, as described in Section 1.1.1, is crucial for the identification of the spectral species, known to arise in well ordered bulk phasees [18, 43].

---

[7] J-aggregates are named after Edwin E. **J**elly (one of the first observers), whereas H-aggregates are named after the observed **h**ypsochromic spectral shift following aggregate formation.

1.2.2 Energy Transfer Between Chromophores

A molecule, excited to a higher electronic state (a donor D), can transfer its energy to another molecule (the acceptor A). Generally, this process is referred to as excitation energy transfer (EET) and can occur via different mechanisms.

When an excited molecule emits a photon that is absorbed by another molecule, energy is transferred radiatively. The process of photon reabsorption is sometimes called a "cascade" or "trivial energy transfer process" and requires an overlap between the donor's emission and acceptor's absorption spectrum. It becomes important at distances longer than ~ 100 Å [8], but is generally rather inefficient. At shorter distances, however, there are nonradiative energy transfer processes, of which two will be discussed here: Förster type [44] and Dexter type [45] energy transfer.

The Förster type resonance transfer, also referred to as Förster resonance energy transfer (FRET) involves the Coulomb interaction of two weakly coupled transition dipole moments of a donor $\boldsymbol{\mu}_D$ and an acceptor $\boldsymbol{\mu}_A$ molecule given by

$$V_{DA} = \frac{\boldsymbol{\mu}_D \cdot \boldsymbol{\mu}_A - 3(\boldsymbol{\mu}_A \cdot \hat{\mathbf{r}})(\boldsymbol{\mu}_D \cdot \hat{\mathbf{r}})}{r^3} \ , \tag{1.9}$$

where r, the distance between donor and acceptor, is assumed to be much larger than the size of the dipoles. The interaction can also be written as

$$V_{DA} = \frac{|\boldsymbol{\mu}_D||\boldsymbol{\mu}_A|}{r^3}\kappa \ . \tag{1.10}$$

Here, $\kappa = \cos\theta_{AD} - 3\cos\theta_A \cos\theta_D$ is an orientation factor, θ_{AD} is the angle between the dipoles, and θ_A and θ_D are the angles between the dipoles and the vector $\hat{\mathbf{r}}$, respectively. Using Fermi's Golden rule [8], the transition rate k_{DA} between donor and acceptor can be expressed as

$$k_{DA} = \frac{2\pi}{\hbar^2}|V_{DA}|^2 J_{DA} \ , \tag{1.11}$$

where $J_{DA} = \int_0^\infty I_D(\lambda)\epsilon_A(\lambda)\lambda^4 \mathrm{d}\lambda$ is the integral overlap over the wavelength λ of the normalized emission spectrum of the donor $I_D(\lambda)$ and the absorption spectrum of the acceptor $\epsilon_A(\lambda)$. The transfer rate can be written in terms of a critical transfer distance R_0, at which the energy transfer rate k_{DA} and the spontaneous decay rate of the donor k_D are equal. In other words, the probability of energy transfer is 50 % for

$$k_{DA} = \frac{1}{\tau_D}\left(\frac{R_0}{r}\right)^6 \ , \tag{1.12}$$

with the fluorescence lifetime $\tau_D = 1/k_D$ of the donor given in the absence of an acceptor. The critical distance R_0 is also referred to as the Förster radius and is typically on the order of tens of Å [24].

From Equation (1.10) and Equation (1.11), the relation $k_{DA} \propto \kappa^2$ becomes apparent. The squared orientation factor can have values of $0 \leq \kappa^2 \leq 4$ and imposes important consequences on the orientation of the interacting sites in a polymer as illustrated in Figure 1.7a. Energy transport can occur only if donor and acceptor transition dipoles are not perpendicular, and is most efficient when they are colinear.

In addition to chromophore orientation, temperature plays a key role in the FRET mechanism. Optical spectra become thermally broadened at higher temperatures due to coupling to vibrations, as shown in Figure 1.7b. As a consequence, the spectral overlap J_{DA} is highly temperature dependent and FRET can be strongly inhibited at low temperatures.

Dexter type energy transfer is based on intermolecular orbital overlap between the donor and acceptor molecules. Accordingly, the energy transfer rate k'_{DA} depends exponentially on the distance r between donor and acceptor [24]

$$k'_{DA} \propto J'_{DA} e^{-r} \ , \tag{1.13}$$

where $J'_{DA} = \int_0^\infty I_D(\lambda)\epsilon_A(\lambda)\lambda^4 \mathrm{d}\lambda$ is the spectral integral overlap. The exponent in Equation (1.13) limits the efficiency of Dexter type energy transfer to distances below ~ 1Å.

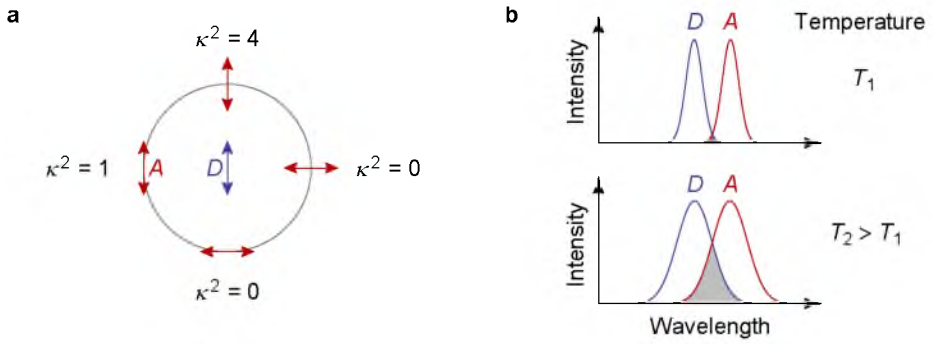

Figure 1.7. Key features of the Förster energy transfer. **a**, The orientation between donor D and acceptor A transition dipole results in different values of the orientation factor κ^2. **b**, Thermal broadening increases the spectral overlap between the donor emission and acceptor absorption.

One problem with this simple depiction of FRET is that chromophores on single polymer chains and in particular in bulk samples are packed very closely and the point-dipole approximation breaks down. This realization has led to the development of modified energy transfer models [46, 47]. Most of these models, however, consider the excitons to be static. In particular, energy transfer within ~ 100 ps after excitation is convoluted with diverse exciton dynamics, such as nuclear and torsional relaxation, as discussed in Sections 1.1.2 and 1.1.3. Recent attempts to model energy transport in chromophores, which respond dynamically to the flow of excitation energy, show promising results [37] but remain to be confirmed by experiment.

1.3 References

[1] R. D. Miller and E. A. Chandross, Chem. Rev. **110**, 1 (2010).

[2] S. R. Forrest and M. E. Thompson, Chem. Rev. **107**, 923 (2007).

[3] J.-L. Brédas and J. R. Durrant, Acc. Chem. Res. **42**, 1689 (2009).

[4] C. Wu, S. V. Malinin, S. Tretiak, and V. Y. Chernyak, Nat Phys **2**, 631 (2006).

[5] O. R. Tozer and W. Barford, J. Phys. Chem. A **116**, 10310 (2012).

[6] E. Collini and G. D. Scholes, Science **323**, 369 (2009).

[7] J. A. Leegwater, J. Phys. Chem. **100**, 14403 (1996).

[8] M. Pope and C. E. Swenberg, *Electronic Processes in Organic Crystals and Polymers*, Oxford University Press Inc., New York, Oxford, 2 edition, 1999.

[9] F. Würthner, T. E. Kaiser, and C. R. Saha-Möller, Angew. Chem. Int. Ed. **50**, 3376 (2011).

[10] E. Barkai, Y. Jung, and R. Silbey, Annu. Rev. Phys. Chem. **55**, 457 (2004).

[11] P. F. Barbara, A. J. Gesquiere, S.-J. Park, and Y. J. Lee, Acc. Chem. Res. **38**, 602 (2005).

[12] J. M. Lupton, Adv. Mater. **22**, 1689 (2010).

[13] R. Schoenlein, L. Peteanu, R. Mathies, and C. Shank, Science **254**, 412 (1991).

[14] P. Kukura, D. W. McCamant, S. Yoon, D. B. Wandschneider, and R. A. Mathies, Science **310**, 1006 (2005).

[15] G. D. Scholes and G. Rumbles, Nat Mater **5**, 683 (2006).

[16] M. T. Dang, L. Hirsch, and G. Wantz, Adv. Mater. **23**, 3597 (2011).

[17] J. Clark, C. Silva, R. H. Friend, and F. C. Spano, Phys. Rev. Lett. **98**, 206406 (2007).

[18] A. Moulé and K. Meerholz, Adv. Mater. **20**, 240 (2008).

[19] T. Sugimoto, Y. Ebihara, K. Ogino, and M. Vacha, ChemPhysChem **8**, 1623 (2007).

[20] T. Sugimoto, S. Habuchi, K. Ogino, and M. Vacha, J. Phys. Chem. B **113**, 12220 (2009).

[21] T. Adachi et al., J. Phys. Chem. C **114**, 20896 (2010).

[22] T. Adachi et al., J. Phys. Chem. Lett. **2**, 1400 (2011).

[23] T. Adachi et al., J. Phys. Chem. B **116**, 9866 (2012).

[24] B. Valeur, *Molecular Fluorescence: Principles and Applications*, Wiley-VCH, Weinheim, 2002.

[25] S. Tretiak, A. Saxena, R. L. Martin, and A. R. Bishop, Phys. Rev. Lett. **89**, 097402 (2002).

[26] M.-H. Chang, M. Hoffmann, H. L. Anderson, and L. M. Herz, J. Am. Chem. Soc. **130**, 10171 (2008).

[27] T. E. Dykstra et al., J. Phys. Chem. B **113**, 656 (2009).

[28] J. Clark, T. Nelson, S. Tretiak, G. Cirmi, and G. Lanzani, Nat Phys **8**, 225 (2012).

[29] T. Nelson, S. Fernandez-Alberti, A. E. Roitberg, and S. Tretiak, Acc. Chem. Res. **47**, 1155 (2014).

[30] M. Kasha, Discuss. Faraday Soc. **9**, 14 (1950).

[31] D. Chaudhuri et al., Angew. Chem. Int. Ed. **52**, 13449 (2013).

[32] H. Yersin, editor, *Highly Efficient OLEDs with Phosphorescent Materials*, Wiley-VCH Verlag GmbH & Co. KGaA, 2008.

[33] H. Bässler and B. Schweitzer, Acc. Chem. Res. **32**, 173 (1999).

[34] L. González, D. Escudero, and L. Serrano-Andrés, ChemPhysChem **13**, 28 (2012).

[35] W. Barford, J. Phys. Chem. A **117**, 2665 (2013).

[36] S. I. Hintschich, F. B. Dias, and A. P. Monkman, Phys. Rev. B **74**, 045210 (2006).

[37] T. R. Nelson, *Nonadiabatic Excited State Molecular Dynamics: Perspectives for a Robust Future*, PhD thesis, University of Rochester, 2013.

[38] G. D. Scholes, K. P. Ghiggino, A. M. Oliver, and M. N. Paddon-Row, J. Am. Chem. Soc. **115**, 4345 (1993).

[39] D. M. Eisele, J. Knoester, S. Kirstein, J. P. Rabe, and D. A. Vanden Bout, Nat Nano **4**, 658 (2009).

[40] F. C. Spano, Acc. Chem. Res. **43**, 429 (2010).

[41] D. Chaudhuri et al., Nano Lett. **11**, 488 (2011).

[42] F. C. Spano, J. Chem. Phys. **122**, 234701 (2005).

[43] P. J. Brown et al., Phys. Rev. B **67**, 064203 (2003).

[44] T. Förster, Ann. Phys. (Berlin) **437**, 55 (1948).

[45] D. L. Dexter, J. Chem. Phys. **21**, 836 (1953).

[46] G. D. Scholes, Annu. Rev. Phys. Chem. **54**, 57 (2003).

[47] E. Hennebicq et al., J. Am. Chem. Soc. **127**, 4744 (2005).

CHAPTER 2

MATERIALS AND METHODS

The choice of materials to study and the methods that are used to study them is a question of mutual compatibility. In consideration of these aspects, this chapter gives an introduction to the studied materials and sample preparation techniques, which is followed by an introduction to the spectroscopic methods employed in this work.

2.1 Materials

The plethora of structural variety in organic materials complicates experimental implementation and interpretation of scientific results. A glimpse of this variety will be given in the case of the photovoltaic cell material poly(3-hexylthiophene) in the first part of this chapter. Subsequently, π-conjugated model systems and polymer matrix materials for single molecule experiments will be introduced.

As mentioned in the introduction of Chapter 1, π-conjugated polymers are generally very disordered (Figure 1.1). One of the reasons for this disorder is due to the unsaturated alkyl side chains attached to the polymer backbone in order to make the long chains that are soluble in organic solvents. High solubility enables processing of these materials from solution at low cost, which is one of the requirements of the material in order to compete with the well established production techniques of electronics based on inorganic materials. Despite the presence of alkyl chains as backbone substituents, there is one particular π-conjugated polymer, poly(3-hexylthiophene) (P3HT)[1] that exhibits a strong tendency for self-organization[2]. The π-conjugation of the polymer's back-

[1] It should be noted that there are different varieties of P3HT. The alkyl side-chain can be attached to either side of the thiophene ring as a result of the polymerization process. Consequently, one refers to regio-regular or regio-random P3HT for regularly alternating and randomly alternating alkyl chain positions, respectively. The chains depicted in Figure 2.1c are the regio-regular material.

[2] The amount of crystallinity depends on the processing conditions and the degree of regio-regularity.

bone is comprised of polymerized thiophene units as shown in Figure 2.1a,b. Ordering of the chains in the bulk material, as depicted in Figure 2.1c, facilitates overlap of the π-orbitals (π-π-stacking) between adjacent chains and improves the polymer's ability to transport chargecarriers [1–3]. Furthermore, optical spectra of the well-ordered bulk phase are shifted to lower energies, which is attributed to H-aggregation in the literature [4, 5] as mentioned in Chapter 1. However, P3HT occurs also in a disordered or amorphous form, as is the case for the majority of conjugated polymers.

The morphology of a chain is defined by the shape as well as the conformation and chemical structure of the polymer. The building blocks of P3HT, for example, contain the pentagonal monomer unit thiophene. Depending on the relative orientation of the thiophene rings, two conformations are possible without interrupting the π-conjugation or inducing strain in the chemical bonds. The isomeric structures are shown in Fig-

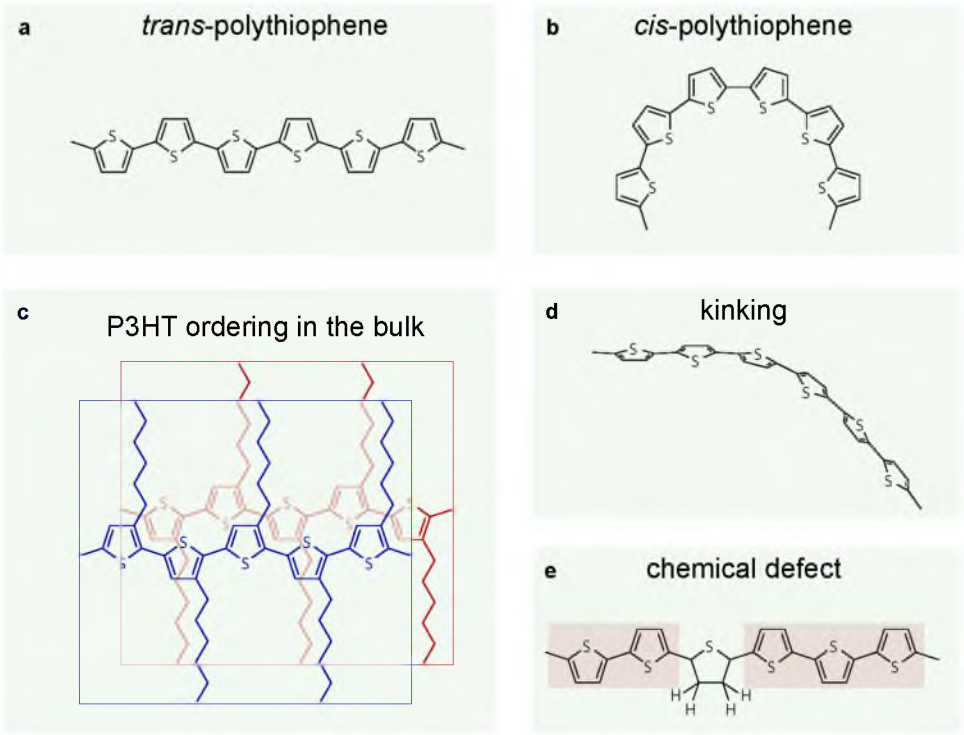

Figure 2.1. Conformations and ordering of polythiophenes. The relative orientation of thiophene rings allows two significantly different chain conformations with uninterrupted π-conjugation: all *trans*-polythiophene (**a**) and all *cis*-polythiophene (**b**). **c**, Chain ordering of poly(3-hexylthiophene) (P3HT) in the bulk. Adapted from [3]. Relatively strong chain deformations such as azimuthal kinking (**d**) do not necessarily interrupt the π-conjugation in contrast to chemical defects (**e**). Adapted from [6].

ure 2.1a and Figure 2.1b. Polythiophene is thus an important example of chain bending without interruption of conjugation. Computational studies show that even strong bending and kinking (Figure 2.1d) of polythiophene chains does not interrupt the π-conjugation [6] in contrast to chemical defects (Figure 2.1e). However, such an effect is not necessarily true for all π-conjugated polymers.

The structural richness of amorphous π-conjugated polymers can complicate or even impede a clear correlation between structure and photophysical properties. One method of circumventing the factor of structural uncertainty is to employ π-conjugated model systems of known structure. Model systems have successfully been used in the past to study aggregation [7] or energy transfer [8, 9] as well as photophysical properties of cyclic conjugated systems [10–13]. The latter are particularly intriguing because of their similarity to light-harvesting complexes [14, 15].

The model systems investigated in this work were synthesized[3] and kindly provided by the group of Sigurd Höger from the University of Bonn (*Rheinische Friedrich-Wilhelms-Universität Bonn*, Bonn, Germany). The goal was to create a model for π-conjugated polymers with a known structure, high structural rigidity, and a high photoluminescence quantum yield. More importantly, the system was intended to have a high degree of symmetry (a circular structure) in order to study the effect of exciton localization (Section 1.1.2).

The chemical structure of the model molecule is shown in Figure 2.2a. The spoked-wheel macrocycle molecule (closed ring) is based on a carbazole bridged phenylene-ethynylene-butadiynylene scaffold supported by six spokes emerging from a central hub manifold. The phenyl rings of the spokes, which are connected to the *N*-phenyl-carbazole of the rim, are rotated out of the ring plane and are thus not part of the π-conjugation of the rim (green).

In addition to the cyclic conjugated system, the rim of the closed ring was reproduced in a quasilinear fashion in form of the oligomers shown in Figure 2.2b. The monomer comprises a sixth of the full rim segment, whereas the length of the hexamer

[3] Particular gratitude goes to Vikas A. Aggarwal who did most of the synthesis work on the compounds investigated in this work.

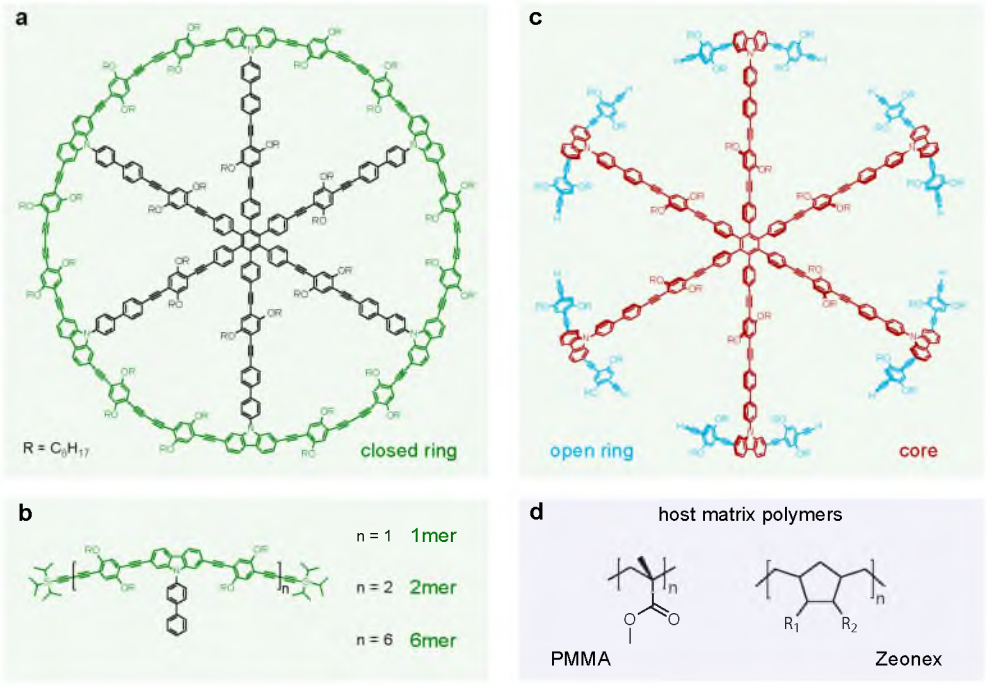

Figure 2.2. Chemical structures of π-conjugated model molecules and host matrix materials. **a**, Spoked-wheel macrocycle molecule with conjugation along the rim (green); **b**, monomer, dimer and hexamer model compounds; **c**, open ring (red and blue) and core (red only) molecules; **d**, matrix polymers poly(methyl methacrylate) (PMMA) and Zeonex with side groups R, which control solubility (adapted from [16]).

corresponds to the circumference of the full rim. All oligomers are terminated with triisopropylsilyl protecting groups to avoid polymerization.

To enable a more rigurous interpretation of the characterization and to better understand the chromophoric system of the conjugated macrocycle, two additional molecules were utilized: the open ring molecule and the core as shown in Figure 2.2c. The open ring molecule contains six spokes with a monomer unit attached to each tip (red and blue), whereas the spokes of the core molecule are terminated with carbazole units (red). As opposed to the strong coupling between chromophore units in the closed ring, the chromophores situated on the monomer units of the open ring are disconnected and only weakly coupled. Both the closed and the open ring have features that are found in naturally occurring light-harvesting complex systems: strong coupling in the closed ring and a multichromophoric assembly in the open ring [14, 15].

The model systems described here were used to investigate exciton localization, ex-

citon relaxation and energy transfer which were introduced in Chapter 1 and will be discussed in more detail in Chapters 3 and 4.

The last two materials that require consideration are the host matrix polymers. These materials are used in the single molecule spectroscopy to disperse the analyte[4] molecules at a well-defined concentration, providing a "natural" amorphous environment for the analytes. In this work the polymer materials poly(methyl-methacrylate) (PMMA) and the cyclo olefin polymer Zeonex were used. The chemical structures[5] are shown in Figure 2.2d.

Single molecule spectroscopy poses several requirements on the matrix materials. Of these requirements, the most important are: optical transparency, low fluorescence contamination signal and chemical inertness with the analyte. Two different matrices are used in this work as a method of controlling the the morphology of single P3HT chains, as will be discussed in Chapter 5.

2.2 Single Molecule Spectroscopy

Single molecule spectroscopy enables optical investigation of emission from individual molecules. The first optical detections of single molecules were reported in the 1970s [17], and the technique soon became a powerful and noninvasive tool to study biological macromolecules under physiological conditions [18]. Pioneering contributions to the single molecule spectroscopy on π-conjugated polymers can be attributed to the group of Paul Barbara [19–21].

Single molecule spectroscopy requires three basic ingredients: an excitation source, a properly prepared sample and an efficient detection system. The simple detection of photoluminescence from single molecules is relatively simple provided that the signal from the molecule exceeds the background signal and noise. This requirement poses some restrictions on the analyte and the setup.

A molecule with a large optical absorption cross-section and a high fluorescence quantum yield is a good start for obtaining sufficient signal from the emitter. Conse-

[4] A substance whose properties are subject to study.

[5] The full chemical structure of Zeonex is not public knowledge. The structure of Zeonex in Figure 2.2d is adapted from [16].

quently, π-conjugated molecules with a large chromophoric system are better candidates for single molecule spectroscopy than smaller molecules. The signal is ideally collected by an objective with a high numerical aperture and optical components with minimized losses from scattering and absorption. In order to minimize background signals from Raman or Rayleigh scattering or fluorescent contaminants in the sample, the excitation volume must be minimized. Confocal detection schemes are usually combined with avalanche photo-diodes (Section 2.4.2), whereas wide-field detection requires large imaging sensors such as a charge-coupled device (CCD, Section 2.4.1).

One of the challenges in single molecule spectroscopy is to ensure that emission in fact originates from individual molecules. A relatively simple and reliable method is to deposit the molecules by spin-coating in a concentration series (Section 2.5). Ideally, the density of well-separated diffraction-limited spots scales with the concentration of the solution. Additional confirmation can be provided from spectrally resolving the diffraction-limited fluorescence spots with an optical grating. A single emitter should show only one 0-0 transition peak. However, in the presence of multiple chromophores in a large polymer chain can result in multiple emission peaks [22], provided that the emission energy is not identical. Alternatively, the number of emitters can be estimated from photon statistics [23–25] and will be introduced in Section 2.2.2.

A detection scheme with a CCD camera that was used in this work is shown in Figure 2.3. A wide-field fluorescence image contains several well-separated bright spots. Some of the spots can be selected by closing the aperture slit (i.e., selecting a vertical stripe of the image) and blocking out the major part of the image. The selected spots can be resolved with an optical diffraction grating, resulting in a spectral image. Figure 2.3b shows two very narrow 0-0 intensity peaks recorded at 4 K with the corresponding vibronic progressions (0-1) at higher wavelengths. Performing the measurement at cryogenic temperatures offers several advantages [26]. The optical transition is not coupled to vibrational modes of the environment which drastically reduces the spectral line width [27] as can be seen in the inset of Figure 2.3b. Spectra recorded at low temperatures usually show well-resolved vibronic peaks and can be up to two orders of magnitude narrower than the room temperature ensemble spectra (inset in Figure 2.3b). In addition, low temperatures increase the photochemical stability allowing for detection

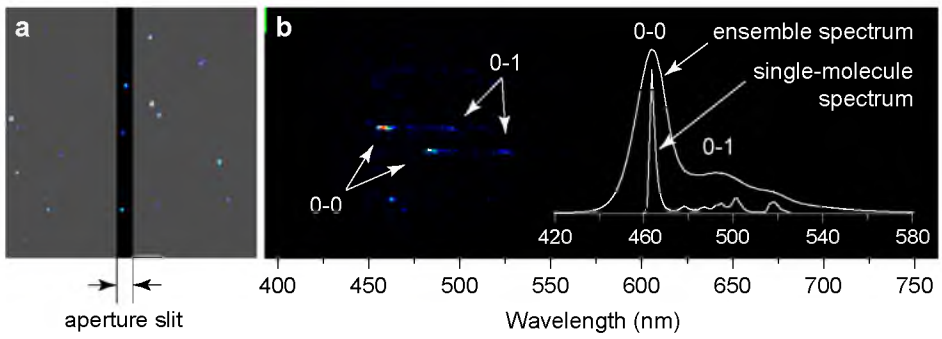

Figure 2.3. CCD-based detection scheme of single molecule spectroscopy. **a**, Optical wide-field microscope image with bright diffraction limited emission spots from single molecules. The size of the image is $\sim 40 \times 40\ \mu m^2$. **b**, Spectrally resolved microscope image with signal from four molecules at 4 K. The inset shows the inhomogeneously broadened ensemble emission spectrum from the analytes dissolved in toluene at room temperature and a narrow single molecule spectrum recorded at 4 K.

over long periods of time, and also reduces the amount of spectral diffusion [17, 28].

This brief introduction to single molecule spectroscopy outlines only a fraction of the possibilities of this versatile techniques. Broad reviews of contemporary single molecule techniques can be found in numerous publications [17, 18, 21, 26, 29, 30]. In this work, single molecule spectroscopy was used to study the nature of optical transitions in P3HT (Chapter 5) as well as to investigate the geometry of emitting and absorbing units of π-conjugated model systems (Chapters 3 and 4) by means of polarization spectroscopy in combination with time correlated photon measurements, which will both be briefly discussed in the following two sections.

2.2.1 Polarization-Resolved Spectroscopy

Polarization spectroscopy is a very powerful technique to address molecular morphology by probing the orientation of the absorbing and the emitting dipoles of single molecules [9, 20, 31]. The geometry of the absorbing units can be assessed by tracing out the excitation ellipse by rotation of the polarization of the excitation light as shown in Figure 2.4. The emission intensity $I(\alpha)$ is modulated as a function of rotation angle α according to

$$I(\alpha) \propto 1 + M\cos(2\alpha)\ , \tag{2.1}$$

where the modulation depth M is given by the minimum and the maximum values of

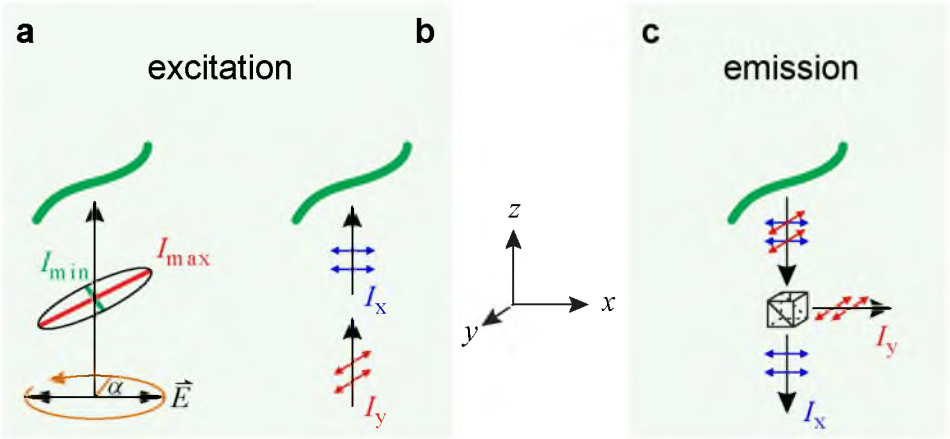

Figure 2.4. Polarization spectroscopy probes the orientation of the absorbing and emitting units. **a**, The excitation ellipse of a molecule (green) is traced by rotating the electric field of the excitation light around the angle α and detecting the emission intensity as a function of α. **b**, A molecule can be excited successively with light of perpendicular polarization I_x and I_y. **c**, The orientation of the emitting unit can be probed by splitting the emission into orthogonal polarization components with a polarizing beam splitter.

the intensity trace

$$M = \frac{I_{\max} - I_{\min}}{I_{\max} + I_{\min}} \,. \tag{2.2}$$

Modulation values can range between 0 and 1 indicating an isotropic or highly anisotropic absorbing system, respectively.

Alternatively, the orientation of the absorbing units can be quantified in terms of the linear dichroism D by exciting the molecule with successive light beams of orthogonal polarization (Figure 2.4b). The linear dichroism is given by

$$D = \frac{I_x - I_y}{I_x + I_y} \,. \tag{2.3}$$

Similarly, the orientation of the emitting units can be probed by splitting the emission intensity with a polarizing beam splitter and detecting the orthogonal polarization intensities with two detectors as shown in Figure 2.4c. In this case, one refers to linear dichroism in emission.

Dichroism values range from -1 to $+1$ and correspond to a difference in the dipole orientation angle of 90°. A value of $D = 0$, however, can either be a result of a dipole oriented at 45° with respect to the polarizing beam splitter (Figure 2.4c), or a fully isotropic emitter.

2.2.2 Photon Statistics

A two-level electronic system which is able to absorb and emit a photon can only be in the excited or the ground state. Accordingly, it can either emit or absorb one photon at a time. This signal can be split into two signal streams of equal intensity and by means of a beam splitter detected by two separated detectors recording the time difference as shown in Figure 2.5a. A single photon can only be detected at one or the other detector and therefore the probability of measuring two events with zero time difference between the detectors is zero. This anticorrelation between the two channels causes a characteristic dip (antibunching dip) in the detected intensity at zero time difference between the detectors [23, 25].

Modern time-correlated single-photon counting (TCSPC) instruments allow detection of photons in combination with a precise recording of the time of arrival. In a similar fashion to a conventional photon antibunching experiment, these data can be used to estimate the number of independent emitters under pulsed excitation [24, 32]. A schematic plot of the binning of the time between successive emission pulses is shown in Figure 2.5b. Noise in the measurement generally leads to a reduction of the dip. However, from the signal to noise ratio the threshold for a certain number of expected emitters can be calculated [24] allowing for an estimation of the number of present

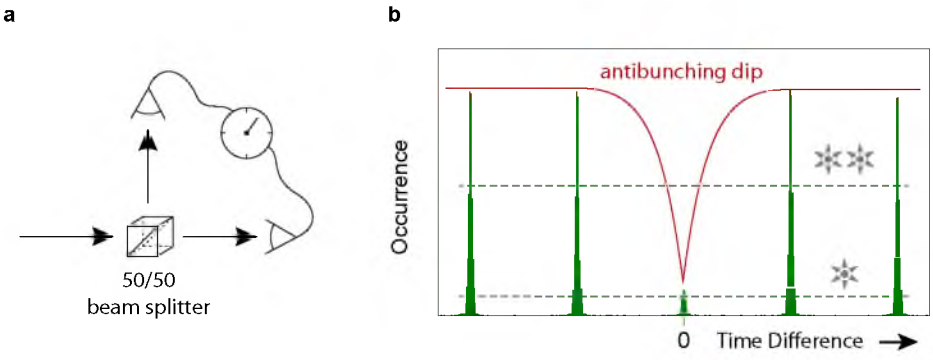

Figure 2.5. Photon arrival time statistics. **a**, Emission from the source is split with a 50/50 beam splitter and detected with two separate detectors that record the time of arrival. **b,** The photon arrival coincidence counts show a characteristic antibunching dip (red) at zero time difference in the presence of a single photon-source. Coincidence counts can also be plotted in bins (green). Antibunching dip threshold values (dashed lines) calculated from the signal to noise of the measurement for one and two emitters, respectively.

emitters. These thresholds are illustrated by dashed lines in Figure 2.5b.

2.3 Ensemble Spectroscopy

Optical absorption and emission spectra can provide important information about the electronic structure of material systems. However, sample preparation, data acquisition, and data analysis (including proper corrections) are often times mutually interrelated. Morphology in a bulk film and particle density in a solvent can strongly influence the electronic structure and thus optical spectra of a sample. In addition, particles with sizes close to the wavelength of the excitation laser act as Rayleigh scatterers, introducing baseline artifacts in absorption spectra. These are only a few examples of necessary considerations before planing an experiment.

2.3.1 Data Acquisition

Typically, solution concentration and film thickness for absorption measurements were adjusted to be below optical density of 0.05. The spectra were acquired with an absorption spectrograph[6]. As a reference, an identical sample without the analyte dispersed in the matrix was used. This procedure ensures adequate baseline correction even in the presence of Rayleigh scattering.

Most interactions between chromophores can easily be avoided in highly dilute analyte solutions. Due to this reason solutions for photoluminescence measurements were prepared with optical densities one or two orders of magnitude below unity.

2.3.2 Data Correction

All optical data acquired in the process of this work were background subtracted using reference samples or other methods. Spectra of single molecules were corrected by subtracting signal from the adjacent area of the substrate that did not contain single molecule signal. In addition, wavelength dependent detector sensitivity and other artifacts introduced by optical components (grating and long-pass filters) needed to be accounted for. This was done by measuring a white-light calibration spectrum[7] with

[6] *Olis (On-Line Instrument Systems Inc.)*, Bogart, GA, USA; model *Cary-17*.

[7] *Avantes USA*, Broomfield, CO, USA; model *AvaLight-HAL-CAL*.

all optical elements between source and detector. Calibration data provided by the manufacturer were used to calculate a sensitivity correction function.

2.3.3 Time Resolved Spectroscopy

Following optical excitation, excited states can undergo a number of different processes within their lifetime as discussed in Chapter 1. Migration dynamics between sites within the intermolecular and intramolecular energy landscape can provide compelling information on the underlying system. Unfortunately, this information is "smeared out" during time-averaging, which is intrinsic to steady-state measurements. In the past, several advanced methods have been developed that allow access to such dynamics on different time scales [33, 34].

A particularly powerful tool is a so-called streak camera, which is based on an image intensifier. One advantage of this instrument is that it provides temporal resolution in combination with spectral information. The operating principle of a streak camera is shown in Figure 2.6. The center piece is a streaking unit that sweeps electrons in an oscillating electric field, thus spreading optical signals of different time origin in the vertical direction of the detector plane. Connected before the streaking unit is a grating monochromator that spectrally disperses the signal wavelength components. This combination produces a two-dimensional intensity map ("streak image") resolved in wavelength and time.

The streak camera[8] and a grating monochromator[9] used in this work, is capable of achieving a temporal resolution of approximately 4 ps. The signal detection window of approximately 6 ns was limited by the repetition rate of the excitation laser and the photoluminescence lifetime of the sample. Integration times varied between ms to several min and were optimized to sample brightness. All streak images were corrected for background signal, streaking curvature[10], and detection sensitivity.

---

[8] *Hamamatsu Corporation,* Bridgewater, NJ USA; model *C5680.*

[9] *Bruker Optics, Inc.*, Billerica, MA USA; model *250IS SureSpectrum* imaging spectrograph, 250 mm focal length with a ruled grating, 50 G/mm with 600 nm blaze wavelength.

[10] Instruction Manual for the *Hamamatsu Corporation C5690 Streak Camera.*

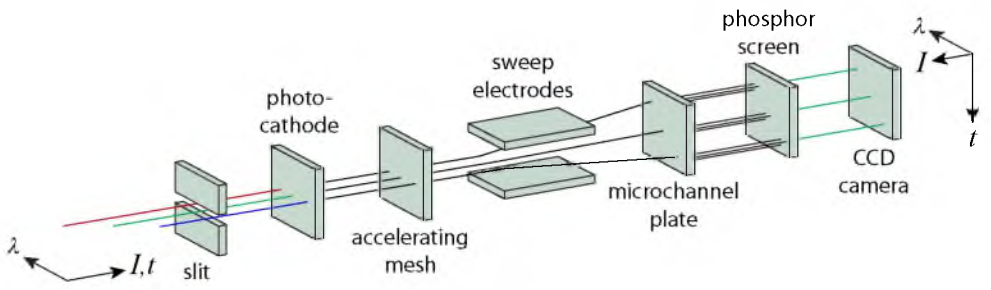

Figure 2.6. Streaking unit of a streak camera. Spectrally dispersed light from a monochromator with different intensities and time components passes a horizontal slit. Photons eject electrons at the photocathode and are accelerated towards two sweeping electrodes. The oscillating electric field deflects electrons in vertical direction, effectively separating photons emitted at different times. A microchannel plate (optionally) multiplies the electrons before they reach a phosphor screen and cause emission of light. The photons are detected by a charged coupled device (CCD) camera.

2.3.4 Time Resolved Fluorescence Anisotropy

For linear excitations, the interaction of chromophores and light is dipolar in nature. The polarization of a photon can be used to relate to the orientation of an absorbing unit, and consequently to the molecular geometry. In the case of polarized excitation light, as shown in Figure 2.7a, the fluorescence anisotropy [33] is defined as

$$r = \frac{I_{\parallel} - I_{\perp}}{I_{\parallel} + 2I_{\perp}} \ , \tag{2.4}$$

which is the ratio of the anisotropic and isotropic fluorescence parameters [35]. It is appropriate to note that in contrast to anisotropy, polarization, P[11], is defined as

$$P = \frac{I_{\parallel} - I_{\perp}}{I_{\parallel} + I_{\perp}} \ . \tag{2.5}$$

In both equations, $I_{\parallel}$ and $I_{\perp}$ are emission intensities with polarization components parallel and perpendicular to the excitation polarization. In order to select each component, linear polarizing filters can be used.

For a single fluorophore with colinear transitions[12], a maximal value of $r = 1$ can be obtained. However, in homogeneous solutions, a perfectly oriented excited state population cannot be achieved [33]. Instead, linearly polarized optical excitation of a

[11] Linear dichroism D, used in this work, is defined similarly but measured in a different configuration.

[12] Absorption and emission dipole are colinear.

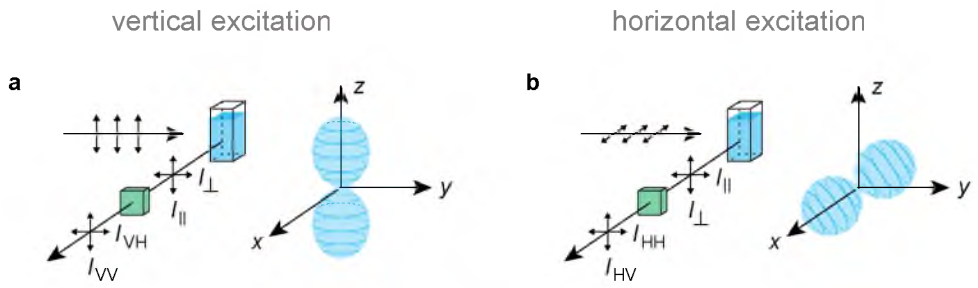

Figure 2.7. Fluorescence anisotropy measurement in L-format configuration. Different excited state distributions (blue lobes) result under vertical (**a**) and horizontal excitation (**b**) for a solution of isotropically distributed linear absorbers. Polarization components $I_\parallel$ and $I_\perp$ from the solution are slightly modified after passing through optical components such as a monochromator (green box). The detected intensity components are I_{VH} and I_{VV} for vertical extitation (**a**), and I_{HH} and $I_{HV}$for horizontal excitation (**b**), respectively. Adapted from [33].

solution with randomly oriented dipoles creates a distribution of excited states that resembles a "dumbbell" as shown in Figure 2.7. This distribution of excited states reduces the maximum anisotropy value from unity to $r = 0.4$. From Figure 2.7, it also becomes apparent that the setup geometry is crucial to observe a finite anisotropy. This particular configuration is known under the term, L-format.

Generally, optical components (grating, etc.) between the sample and the detector exhibit polarization dependent sensitivity. Anisotropy can be expressed in terms of detected intensities I_{VV} and I_{VH}, where the first subscript denotes excitation and the second detection polarization orientation [33];

$$r = \frac{I_{VV} - G I_{VH}}{I_{VV} + G I_{VH}} \,. \tag{2.6}$$

Here, $G = I_{HV}/I_{HH}$ is a correction factor which corrects for the polarization dependence of the optical components. This value can be measured experimentally from a system with isotropic emission such as a solution of randomly distributed emitters under horizontal excitation as shown in Figure 2.7b.

Although steady state anisotropy can provide important information about the relation of the absorbing and the emitting dipole, much more can be learned from time-resolved anisotropy measurements. In particular, this technique has been extensively used to study protein dynamics [36, 37], as well as processes in other material systems [38, 39]. In this work, time resolved fluorescence anisotropy is employed to gain insight

into intramolecular energy transfer, rotational diffusion, and excited-states reorganization of molecular geometry of various model systems.

2.4 Experimental Configurations

Parts of this work were only possible because of the extraordinary preexisting experimental conditions at the University of Utah and the strong collaborative spirit with the groups at the University of Regensburg (Regensburg, Germany) and the University of Bonn (*Rheinische Friedrich-Wilhelms-Universität Bonn*, Bonn, Germany).

The following two sections describe experimental configurations used for measurements at the University of Utah (low-temperature setup) and University of Regensburg (room-temperature setup). Only the Utah setup allows measurements at cryogenic temperatures, whereas room-temperature experiments can be carried out on both setups. In this regard the nomenclature was merely chosen for simple distinction.

2.4.1 Low-Temperature Setup

The experimental setup in Utah was originally designed and assembled by Manfred Walter and Nicholas Borys. The automation was developed with the help of home-written LabView codes, realized by Kipp van Schooten and Nicholas Borys. Additional detailed descriptions of the setup can be found in References [40, 41].

A schematic overview of the setup is given in Figure 2.8b. The centerpiece is formed by a pulsed Ti:sapphire laser[13] used as excitation source. The laser provides pulses of 140 fs duration at a rate of 80 MHz and is tunable over a wavelength range of 680 – 1080 nm. A second harmonic generation unit[14] was used to halve the wavelength to 340 – 540 nm.

The laser beam was passed through optical components (mirrors, waveplates, focusing lens) and directed onto the film sample at an incidence angle of ~ 60° through the quartz window of a liquid-helium cooled cryostat[15]. Emission from the sample

[13] *Coherent Inc.*, Santa Clara, CA, USA; model *Chameleon Ultra II.*

[14] *APE GmbH*, Berlin, Germany; model *fs-SHG for Chameleon with Autotracker.*

[15] *Janis Research Company Inc.*, Wilmington, MA, USA; model *ST-500*; temperature controller *model 331S.*

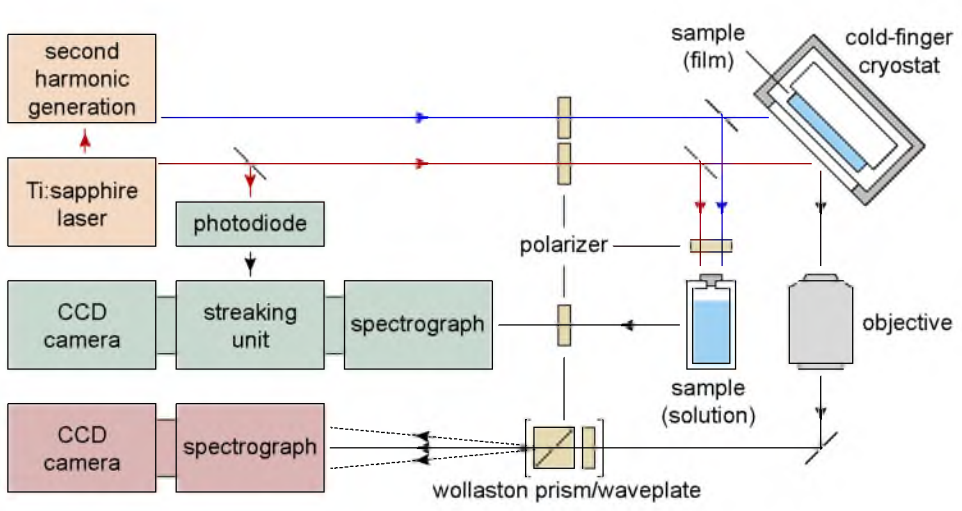

Figure 2.8. Schematic view of the low-temperature setup.

was detected with a long working-distance microscope-objective[16] at an angle of ~ 0°. Alternatively, the excitation beam was directed onto a quartz fluorescence cuvette for ensemble solution experiments. Photoluminescence signal from the solution was detected at an angle of 90° to the excitation beam, for reasons explained in Section 2.3.4.

Polarizers were used to change the linear polarization direction of excitation light between the horizontal and vertical state ($\lambda/2$-waveplate[17]) or to create circularly polarized light ($\lambda/4$-waveplate[18]). For anisotropy measurements, emission from the cuvette was passed through a polarizing filter[19]. A Wollaston prism[20] was used for simultaneous measurements of horizontal and vertical emission polarization in both imaging and in the spectrally resolved detection modes. The emission signals were passed through high quality long-pass interference filters[21] in order to block scattered laser light.

---

[16] *Olympus America Inc.*, Melville, NY, USA; model *SLCPlanFl*; magnification, 40; numerical aperture, 0.55; infinity corrected; corrective collar, 0 – 2.6 mm.

[17] *Newport Corporation*, Irvine, CA, USA; model *10RP52-1*, 400 – 700 nm.

[18] *Newport Corporation*, Irvine, CA, USA; model *10RP54-1*, 400 – 700 nm.

[19] *Newport Corporation*, Irvine, CA, USA; model *10LP-VIS-B*, 430 – 670 nm.

[20] *CVI Melles Griot*; model *WLST-5.0-CA-425-675*.

[21] *Chroma Technology Corporation*, Bellows Falls, VT USA; and *Omega Optical, Inc.*, Brattleboro, VT USA; and *Semrock, Inc.*; Rochester, NY USA.

For single particle measurements, emission was directed onto an imaging spectrograph in front of a CCD camera cooled to −30 °C. The spectrograph[22] allowed direct detection through a mirror (imaging mode) or an optical grating with a narrowed entrance slit (spectroscopy mode).

For time-resolved measurements, emission was directed to the entrance of an imaging spectrograph[23] in front of a streak camera[24], described in Section 2.3.3. The laser pulse was detected with a photo-diode and synchronized with the streak camera by a phase lock loop.

2.4.2 Room-Temperature Setup

The experimental setup at the University of Regensburg was designed and assembled by Jan Vogelsang, Thomas Stangl, Florian Steiner and Dominik Würsch. A schematic view of the setup is shown in Figure 2.9.

The center piece of the setup is an inverted microscope[25] with a high numerical aperture oil immersion objective [26]. A fiber-coupled diode[27] laser operating in quasi-continuous wave mode at of 405 nm was used as the excitation source. The polarization of the excitation light was rotated with an electro-optical modulator (EOM)[28] and an additional $\lambda/4$ waveplate. A dichroic mirror[29] was used to pass excitation light into the microscope and blocked from reaching the detector. The signal from the sample was detected in wide-field mode by an EMCCD camera[30] or by avalanche photo-diodes

---

[22] *Princeton Instruments / Acton,* Trenton NJ, USA; model *SpectraPro SP-2556 Imaging Spectrograph*; 500 nm focal length with a mirror or ruled grating ARC-1-015-500, 68 × 68 mm^2, 150 G/mm with 500 nm blaze wavelength or ARC-1-005-600, 68 × 68 mm^2, 50 G/mm with 600 nm blaze wavelength.

[23] *Bruker Optics, Inc.,* Billerica, MA USA; model *250IS SureSpectrum.*

[24] *Hamamatsu Corporation,* Bridgewater, NJ USA; model *C5680.*

[25] *Olympus Europa SE & CO. KG,* Hamburg, Germany; model *Olympus IX71.*

[26] *Olympus Europa SE & CO. KG,* Hamburg, Germany; model *UPLSAPO 60XO,* 1.35 NA.

[27] *PicoQuant GmbH,* Berlin, Germany; model *LDH-C-405.*

[28] *FastPulse Technology Inc.,* Saddle Brook, NJ, USA; model *3079-4PW.*

[29] *AHF analysentechnik AG,* Tübingen, Germany; model *RDC 405 nt.*

[30] *Andor Technology USA,* South Windsor, CT, USA; model *iXon3 897.*

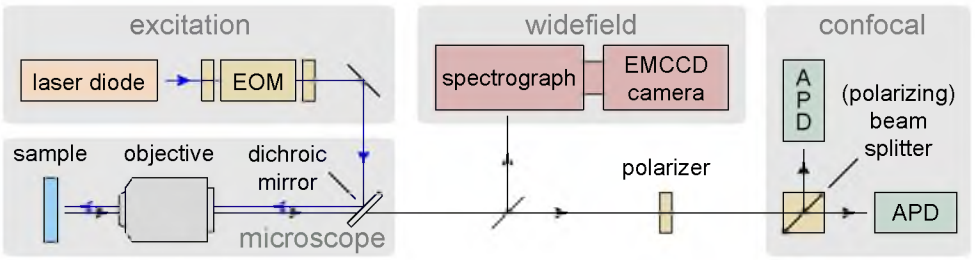

Figure 2.9. Schematic view of the room-temperature setup.

(APD)[31] in confocal mode. For linear dichroism measurements, the fluorescence was split by a polarizing beam splitter[32]. A Hanbury-Brown-Twiss geometry was employed for measurement of photon statistics with two APD detectors. The measurement starts when a photon is recorded by one detector and stops when the other detector registers the next photon.

2.5 Sample Preparation

Sample preparation is a crucial step for conducting single molecule spectroscopy experiments (Section 2.2). Two different types of samples qualifying for ensemble and single particle measurements were employed in this work. An overview is given in Figure 2.10.

In order to achieve desired deposition control of thin film samples the analyte needs to be dissolved in a suitable solvent. In this work, the organic solvents toluene or chloroform were used exclusively. Depending on the deposition procedure, film thickness can be varied from 10s of nm to the bulk scale. For example, a bulk film can be created through dropcasting, a method where a small volume of the solution is dropped on a substrate and is left to evaporate, leaving behind the neat substance in amorphous or crystalline form (Figure 2.10c). Molecular interaction can be avoided by depositing a submonolayer film (Figure 2.10e). A technique called spin-coating can produce homogeneous films by dropping the analyte solution on a rotating substrate. The film thickness is controlled by the sample rotation frequency as well as the initial solution

[31] *PicoQuant GmbH*, Berlin, Germany; model *τ-SPAD-20*.

[32] *Thorlabs Inc.*, Newton, NJ, USA; model *CM1-PBS251*.

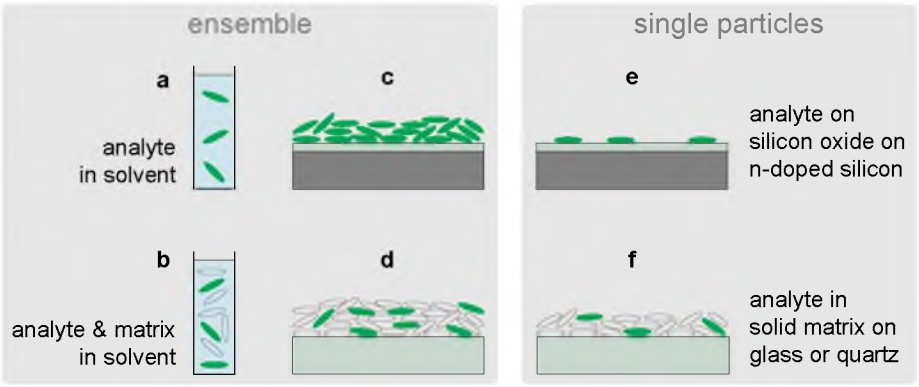

Figure 2.10. Samples for ensemble and single particle optical measurements. Dropcasting the solutions (**a**) and (**b**) yields a bulk (**c**) and analyte-in-matrix ensemble (**d**) film, respectively. Precise deposition control via spincoating produces samples with spatially separated analytes (**e**,**f**) from the same solution.

concentration.

An alternative approach to avoiding analyte-analyte interactions is to disperse the analyte in a solid polymer matrix (Figure 2.10d). In the interest of a spectroscopist, the matrix material needs to be chemically inert and optically transparent. While retaining matrix-analyte interactions, the amorphous surrounding can be a desired model for a native analyte environment and yet facilitate single particle studies. For this purpose, the film needs to be dilute and thin enough for the analyte to be well separated (Figure 2.10f).

In addition to the high purity requirements for the analyte, the matrix polymer constituting the larger fraction of the sample, as well as the substrate, need to be free of contaminants. The experiments performed at the low-temperature setup (University of Utah) and the room-temperature setup (University of Regensburg, Germany) involved slightly different, but well established, substrate cleaning procedures. In both cases, substrates were treated to remove organic and inorganic surface contamination, which can give rise to undesired photoluminescence signals from the substrate.

2.5.1 Substrate Cleaning Procedure for Low-Temperature Setup

Silicon[33], glass[34], and quartz[35] substrates were cleaned in glass beakers held by custom-made Teflon® holders following this protocol:

1. Sonicate in acetone for 10 min.
2. Sonicate in isopropanol for 10 min.
3. Rinse with ultrapure water.
4. Sonicate in ultrapure water for 10 min.
5. Rinse with ultrapure water.
6. Sonicate with ultrapure water for 10 min.
7. Dry with nitrogen (or argon) under a flow hood.

Silicon substrates were baked at 415 – 500 °C for 30 min in air immediately after the drying step. Glass and quartz substrates required backcoating with aluminum, as described below. Following aluminum coating, cleaning steps 1 – 7 were repeated with just 5 min runs and the substrates were baked at 415 – 500 °C for 30 min in air.

2.5.2 Substrate Cleaning Procedure for High-Temperature Setup

Borosilicate glass[36] substrates were cleaned in glass beakers held by custom-made Teflon® holders following these steps:

1. Soak in ultrapure water with 2 % Hellmanex[37] for at least 30 min.
2. Rinse with ultrapure water.

---

[33] *MicroFab, University of Utah*; n-doped silicon wavers with a 30 nm grown oxide layer.

[34] *Carolina Biological Supply*, Burlington, NC, USA; 0.2 mm thick coverslips.

[35] *Chemglass Life Sciences*, Vineland, NJ, USA; 0.25 mm thick coverslips.

[36] *Carolina Biological Supply*, Burlington, NC, USA; 0.2 mm thick coverslips.

[37] *Hellma Analytics*, Müllheim, Germany, supplied by VWR, USA.

3. Dry with nitrogen.

4. Ozone clean (oxygen atmosphere and UV light)[38] for 15 min.

2.5.3 Aluminum Backcoating

Aluminum coating on the back of the substrate acts as a mirror and prevents contamination fluorescence from laser excitation of anything behind the substrate to leak through it. After the cleaning steps 1 – 7, substrates were transferred in a vacuum deposition chamber[39], held by a custom made substrate holder, and a 100 nm thick layer of aluminum was evaporated at a rate of 0.5 – 5 Å/s. Deposition was carried out at base pressures of $10^{-5} - 10^{-6}$ mbar.

2.5.4 Solution Preparation and Film Deposition

All substances were kept and handled in a glovebox under inert nitrogen atmosphere. Solutions were prepared by dissolving substances in toluene[40] or chloroform[41]. Heating toluene solutions to 75 °C for 30 min was found to further solvation. This initial solution was diluted for ensemble measurements in a cuvette[42], or for single particle measurements on a substrate. For well separated emission spots in single molecule samples, the particle density was adjusted in a concentration series. Typically, concentrations in the range of $10^{-12} - 10^{-13}$ mol/L were used.

While single particle samples of P3HT[43] were spin-coated at 5000 rpm without a matrix on bare silicon oxide, samples of the ring molecules and oligomers were spin-coated dynamically[44] on quartz or glass substrates at 2000 rpm from toluene solutions

---

[38] *Novascan Technologies, Inc.*, Ames, IA, USA; PSD Pro Series UV.

[39] *M. Braun Inc.*, Stratham, NJ, USA, custom configuration.

[40] *EMD Chemicals*, USA; grade OmniSolv.

[41] *EMD Chemicals*, USA; grade OmniSolv.

[42] *Starna Cells Inc.*, Atascadero, CA, USA; Model Spectrosil 10 mm.

[43] *EMD Chemicals*, USA; poly(3-hexylthiophene); regio-regularity, 95.7 %; weight average molecular weight, 65.2 kDa; polydispersity index, 2.2; used as received.

[44] The solution is dropped on the rotating substrate after final angular velocity is reached.

containing 1 % and 6 % of PMMA[45], resulting in 20 nm or 200 nm thick matrix layers, respectively.

Dropcast ensemble films of P3HT in PMMA or Zeonex[46] matrix were made from toluene solutions with 10 g/L matrix and $10^{-10} - 10^{-11}$ mol/L P3HT concentration. The solutions were dropped on aluminum backcoated quartz substrates at 75 °C and left to dry in the glovebox.

Film samples were exposed to ambient atmosphere for a short time during transfer to the spectroscopy setups. Samples in the low-temperature setup were attached vertically to the cold-finger cryostat with silver paste[47] acting as an adhesive with good thermal conduction and kept under vacuum (10^{-7} mbar) during the measurement. Samples for the room-temperature setup were mounted horizontally onto the microscope in a custom-made gas flow-cell sample holder. During the course of the measurement, samples were optionally exposed to a constant inert gas flow (nitrogen) or ambient (air) atmosphere.

2.6 References

[1] H. Sirringhaus et al., Nature **401**, 685 (1999).

[2] J.-F. Chang et al., Chem. Mater. **16**, 4772 (2004).

[3] R. Colle, G. Grosso, A. Ronzani, and C. M. Zicovich-Wilson, Phys. Status Solidi B **248**, 1360 (2011).

[4] F. C. Spano, J. Chem. Phys. **122**, 234701 (2005).

[5] J. Clark, C. Silva, R. H. Friend, and F. C. Spano, Phys. Rev. Lett. **98**, 206406 (2007).

[6] W. J. D. Beenken and T. Pullerits, J. Phys. Chem. B **108**, 6164 (2004).

[7] J. Brazard, R. J. Ono, C. W. Bielawski, P. F. Barbara, and D. A. Vanden Bout, J. Phys. Chem. B **117**, 4170 (2013).

[8] K. Becker et al., J. Am. Chem. Soc. **128**, 680 (2006).

[9] T. Stangl et al., J. Am. Chem. Soc. **135**, 78 (2013).

---

[45] *Sigma-Aldrich*, USA; poly(methyl methacrylate); weight average molecular weight, 96.7 kDa; number average molecular weight, 47.7 kDa.

[46] *Zeon Europe GmbH*, Düsseldorf, Germany; Zeonex 480 granulate.

[47] *Conrad Electronic SE*, Hirschau, Germany; *Silberleitlack*; article number 530042.

[10] K. Becker, M. Fritzsche, S. Hoger, and J. M. Lupton, J. Phys. Chem. B **112**, 4849 (2008).

[11] J. K. Sprafke et al., J. Am. Chem. Soc. **133**, 17262 (2011).

[12] E. Mena-Osteritz, F. Zhang, G. Götz, P. Reineker, and P. Bäuerle, Beilstein J. Nanotechnol. **2**, 720 (2011).

[13] O. Varnavski, P. Bäuerle, and T. Goodson III, Opt. Lett. **32**, 3083 (2007).

[14] G. D. Scholes and G. Rumbles, Nat. Mater. **5**, 683 (2006).

[15] G. D. Scholes, G. R. Fleming, A. Olaya-Castro, and R. van Grondelle, Nat. Chem. **3**, 763 (2011).

[16] F. A. Feist, G. Tommaseo, and T. Basché, J. Phys. Chem. C **113**, 11484 (2009).

[17] T. Basché, Single Mol. **2**, 237 (2001).

[18] S. Weiss, Science **283**, 1676 (1999).

[19] D. A. Vanden Bout et al., Science **277**, 1074 (1997).

[20] D. Hu et al., Nature **405**, 1030 (2000).

[21] P. F. Barbara, A. J. Gesquiere, S.-J. Park, and Y. J. Lee, Acc. Chem. Res. **38**, 602 (2005).

[22] F. Schindler et al., Angew. Chem. Int. Ed. **44**, 1520 (2005).

[23] T. Basché, W. E. Moerner, M. Orrit, and H. Talon, Phys. Rev. Lett. **69**, 1516 (1992).

[24] K. D. Weston et al., Anal. Chem. **74**, 5342 (2002).

[25] T. Basché, S. Kummer, and C. Bräuchle, Excitation and emission spectroscopy and quantum optical measurements, in *Single-Molecule Optical Detection, Imaging and Spectroscopy*, pages 31–67, VCH Verlagsgesellschaft mbH, 2007.

[26] J. M. Lupton, Adv. Mater. **22**, 1689 (2010).

[27] F. A. Feist, G. Tommaseo, and T. Basché, Phys. Rev. Lett. **98**, 208301 (2007).

[28] Y. Berlin, A. Burin, J. Friedrich, and J. Köhler, Phys. Life Rev. **4**, 64 (2007).

[29] W. E. Moerner and M. Orrit, Science **283**, 1670 (1999).

[30] E. Barkai, Y. Jung, and R. Silbey, Annu. Rev. Phys. Chem. **55**, 457 (2004).

[31] K. Becker et al., J. Phys. Chem. B **112**, 4859 (2008).

[32] P. Tinnefeld et al., J. Am. Chem. Soc. **124**, 14310 (2002).

[33] J. R. Lakowicz, *Principles of Fluorescence Spectroscopy*, Kluwer Academic/Plenum, New York, 3rd edition, 2006.

[34] J. R. Lakowicz, P. A. Koen, H. Szmacinski, I. Gryczynski, and J. Kuśba, J. Fluoresc. **4**, 117 (1994).

[35] J. R. Lakowicz and C. D. Geddes, *Topics in Fluorescence Spectroscopy*, volume 5, Springer, 2002.

[36] G. Weber, Biochem. J. **51**, 145 (1952).

[37] G. Weber, Biochem. J. **51**, 155 (1952).

[38] T. Goodson, Annu. Rev. Phys. Chem. **56**, 581 (2005), PMID: 15796712.

[39] C. Geddes, J. Fluoresc. **12**, 343 (2002).

[40] M. J. Walter, *Light-Harvesting in Single Conjugated Polymer Chains and Semiconductor Nanocrystals*, PhD thesis, University of Utah, 2009.

[41] N. J. Borys, *Optical Structure-Property Relations in Metal and Semicoductor Nanoparticles*, PhD thesis, University of Utah, 2011.

CHAPTER 3

FLUCTUATING EXCITON LOCALIZATION IN GIANT π-CONJUGATED SPOKED-WHEEL MACROCYCLES

Before immersing into studies of morphology related phenomena in more disordered conjugated polymers, the more primal question with regards to exciton formation is addressed: Where in a chromophore does the exciton localize? A novel π-conjugated model molecule was synthesized specifically to address this question. The ideal model molecule to answer this question has to fulfill certain requirements. For instance, the molecular structure needs to be known to a high degree of certainty. Consequently, the molecule must be rigid enough to withstand processing conditions. In addition, the chromophoric system must be designed to fit experimental conditions. To accomplish these requirements, a circular and structurally persistent π-conjugated macrocycle molecule was created. In this chapter, single molecule polarization experiments reveal that exciton localization fluctuates randomly between different parts of the molecule perimeter. The process is attributed to phonon-assisted spontaneous symmetry breaking.

This chapter is reprinted from a paper published in September 2013 in the journal *Nature Chemistry* in volume 5 on pages 964-970. The paper was highlighted in the *News and Views* section of *Nature Chemistry* in volume 5 on pages 903-904. The manuscript was coauthored with Jan Vogelsang, Sigurd Höger and John M. Lupton, as well as A. Vikas Aggarwal, Alissa Idelson and Daniel Kalle (who synthesized the model systems and characterized the molecules analytically), Dominik Würsch, Thomas Stangl and Florian Steiner (who performed parts of the experiments) and Stefan-S. Jester (who performed scanning tunneling microscopy measurements). Subheadings for the text are inserted here for structural clarity and are not part of the published manuscript.

3.1 Abstract

Conjugated polymers offer potential for many diverse applications, but we still lack a fundamental microscopic understanding of their electronic structure. Elementary photoexcitations (excitons) span only a few nanometres of a molecule, which itself can extend over microns, and how their behaviour is affected by molecular dimensions is not immediately obvious. For example, where is the exciton formed within a conjugated segment and is it always situated on the same repeat units? Here, we introduce structurally rigid molecular spoked wheels, 6 nm in diameter, as a model of extended π conjugation. Single-molecule fluorescence reveals random exciton localization, which leads to temporally varying emission polarization. Initially, this random localization arises after every photon absorption event because of temperature-independent spontaneous symmetry breaking. These fast fluctuations are slowed to millisecond timescales after prolonged illumination. Intramolecular heterogeneity is revealed in cryogenic spectroscopy by jumps in transition energy, but emission polarization can also switch without a spectral jump occurring, which implies long-range homogeneity in the local dielectric environment.

3.2 Introduction

Cyclic structures of various levels of symmetry are ubiquitous in nature, from benzene and pyrrole to members of the porphyrin family, such as haem or chlorophylls, to photosynthetic antenna complexes [1], and structural rigidity is crucial to these molecules on different length scales. However, synthetic compounds that derive macroscopic functions by mimicking elementary aspects of electron or energy transfer in organic semiconductors tend to be linear in structure [2]. Although such materials, most notably π-conjugated polymers, possess a range of desirable functional characteristics, to formulate a comprehensive microscopic picture of how individual covalently bound monomer units arrange in space to form discrete π-conjugated segments remains challenging [3–6]. Conjugation and shape of the molecule are fundamentally interlinked [5]. On the one hand, spectroscopic techniques can, in principle, unveil information on electronic structure. On the other hand, physical shape, which can exhibit a level of diversity reminiscent of conformational degrees of freedom in proteins, is much harder

to assess.

A conjugated polymer consists of a chain of repeating monomer units. π electrons delocalize between the monomers, but may become localized on longer scales because of the formation of chemical or structural defects [7]. An individual segment of the polymer that supports the π orbital is referred to as a chromophore and the elementary excitation on a chromophore is an exciton (a tightly bound electron-hole pair). The optical properties of polymers, such as spectral shape (width of energy bands and strength of vibronic coupling), are accounted for by excitonic coupling models in which intrachromophoric interactions between monomers are described in the framework of J aggregates, and interactions between chromophores are ascribed to either J (inline) or H aggregation (cofacial) [8]. The exciton itself is of the order of 2 nm in size, which can be much smaller than the actual conjugated segment [7]. Depending on the magnitude of structural relaxation in the excited state, the exciton may be free to move within the chromophore, and thereby increase transition intensity because the number of electrons involved in the transition increases [8], but it may also become localized [7]. Proximal chromophores can couple to each other, which leads to further spreading of excitation energy in the macromolecule [9, 10].

Fluorescence spectroscopy is often used to infer information on electronic structure, coupling mechanisms and conformation, but without definitive knowledge of molecular conformation to begin with, the parameters remain intractable. In particular, it is not self-evident that an exciton should always form on precisely the same monomer units of a chromophore. Also, structural relaxation in the excited state breaks molecular symmetry and leads to exciton self-trapping [11, 12] (the spatial localization of excitation energy caused by the nuclear rearrangement of the molecule after a redistribution in charge density). Does this process always follow the same pathway? To examine this question, we designed a giant molecular spokedwheel structure with a conjugated shape-persistent macrocyclic rim as a model of chromophore formation and interchromophoric coupling [13]. Using single-molecule techniques, we uncovered two distinct localization mechanisms: spontaneous symmetry breaking (with the exciton localizing randomly to different parts of the ring after every photoexcitation event) and slower photoinduced symmetry breaking, which leads to fluctuating exciton localization on the

millisecond timescale.

3.3 Results and Discussion

3.3.1 Ring Design

The design of conjugated macrocyclic structures requires careful consideration of rigidity to prevent scissions in the π system caused by deformation of the overall ring as a result of the limited persistence length of rigid-rod building blocks [14]. We employed a phenylene-ethynylene-butadiynylene-based scaffold [15], which offers an optimum in rigidity combined with desirable optical properties in the visible spectrum, to template carbazole units. Previously studied carbazole-based compounds had electronic transitions in the ultraviolet spectrum [16–18], which makes them poorly suited to single-molecule investigations, and porphyrin-based macrocycles of comparable rigidity to our rings showed very low fluorescence yields [19–25] with optical transitions in the near-infrared region. Other intriguing cyclic structures were not conjugated fully [26, 27]. Figure 3.1 illustrates the design approach. Six *N*-phenylcarbazole units are linked to each other by phenylene-ethynylene-butadiynylene moieties and form the nominally conjugated rim (green) of the spoked wheel 1, where the spokes are not part of the rim conjugation. The ring is synthesized by Buchwald-Hartwig coupling of the rim segments 2 (green) and spoke modules 3 (red), selective removal of the cyanopropyldimethylsilyl protecting group from 4 [28] and coupling of the resulting acetylene to the hub 6 in a sixfold Sonogashira reaction. Subsequent deprotection of 7 leads to the spoked-wheel precursor 8, which is cyclized in a palladium-catalysed reaction under pseudo high-dilution conditions and purified by recycling gel permeation chromatography (GPC) to give 1 in 54% yield. The purity is confirmed by mass spectrometry, NMR spectroscopy and GPC (Supplementary Section S2 in Appendix A). We compared ring 1 to model oligomers 9-11. The structural rigidity is visualized in the scanning tunnelling micrographs (STM) in Figure 3.2 (for details see Supplementary Section S4 in Appendix A). Although interactions with the hexagonal graphite substrate lattice and dense packing of the molecules induce slight distortions in the ring geometry, no apparent ruptures in the wheel structures are seen, which indicates that effective tunnelling arises from conjugation in the rim.

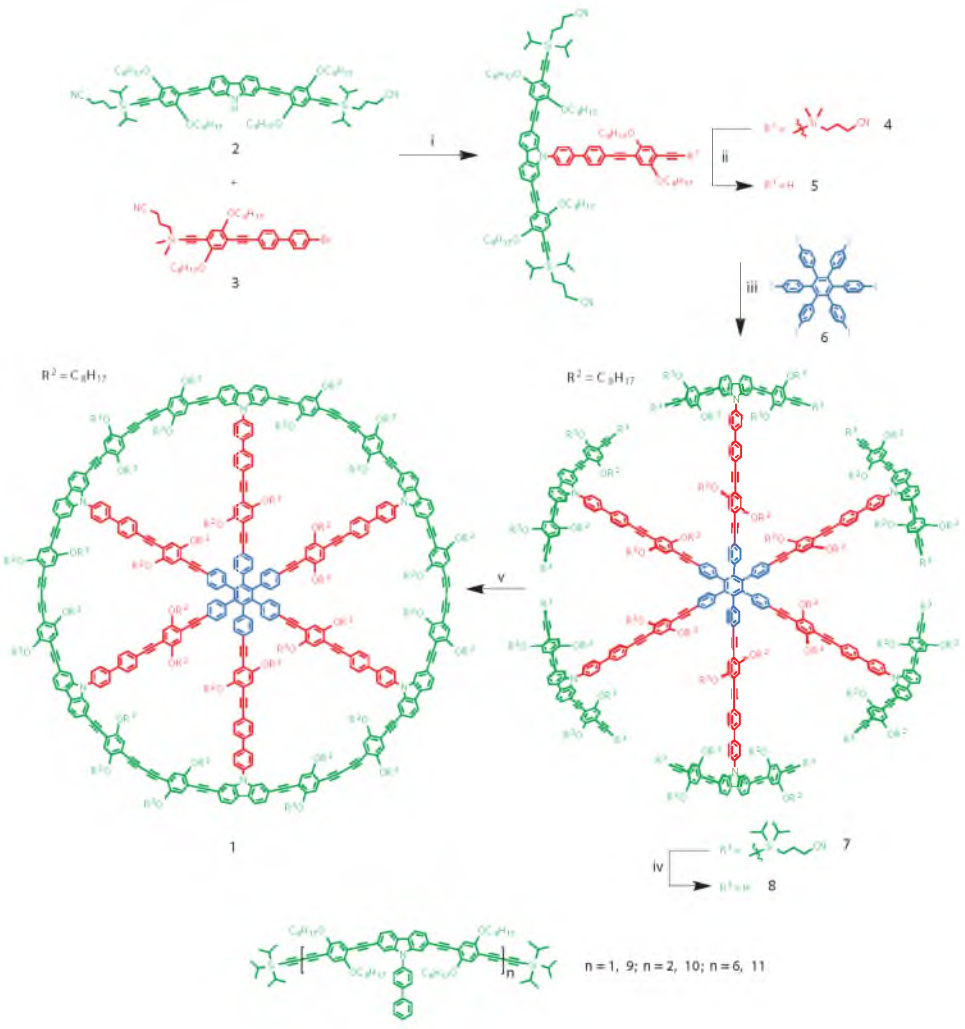

Figure 3.1. Structure and synthesis of the spokes and ring 1, and of the noncyclic analogues 9-11. **i**, 2-Di-*tert*-butylphosphino-2',4',6'-triisopropylbiphenyl, tris(dibenzylideneacetone)dipalladium(0)(Pd_2dba_3), NaO^tBu, toluene, 80 °C, 1 h, 66%; **ii**, K_2CO_3 , THF, methanol, room temperature (r.t.), 1 h, 95%; **iii**, Pd_2dba_3, P^tBu_3, CuI, piperidine, 120 °C, 16 min microwave irradiation, 74%; **iv**, tetra-*n*-butylammonium fluoride, THF, r.t., 3 h, 74%; **v**, $Pd(PPh_3)_2Cl_2$, CuI, I_2, air, THF, NH^iPr_2, 50 °C, 60 h, 54%.

Figure 3.2. Fluctuations in exciton localization caused by spontaneous symmetry breaking. **a**, Excitation with arbitrarily polarized light leads to exciton formation. Excitons relax to segments of length comparable to the dimer length. Owing to bond-length changes in the excited state, the local potential in the proximity of the exciton is modified. Such exciton localization occurs anywhere on the ring. Linear dichroism can be measured in either excitation (by switching laser polarization, left) or emission (by passing fluorescence through a polarizing beam splitter, right). **b**, Linear dichroism histograms in excitation and emission for 1,597 dimer (2mer), 1,273 hexamer (6mer) and 730 ring molecules. Black bars indicate instrument response for fluorescent beads. STM images are shown with the graphite substrate axes indicated in white. **c**, Temporal photon correlation (pulsed excitation). Fluorescence passes through a beam splitter and is recorded with two photodiodes. At delay $\tau = 0$ ns between the detectors, photon coincidence approaches zero; photon antibunching implies the activity of precisely one chromophore. Dashed lines show calculated thresholds for one (lower) and two emitters (upper). The experiment was carried out at a 20 MHz repetition rate, which gave 50 ns spacing on the τ axis. **d**, Cross-correlation $g^2_{\mathrm{cross}}(\tau)$ between two detector channels of orthogonal polarization shows no discernible timescale for polarization fluctuations, which implies that initially ring emission appears unpolarized.

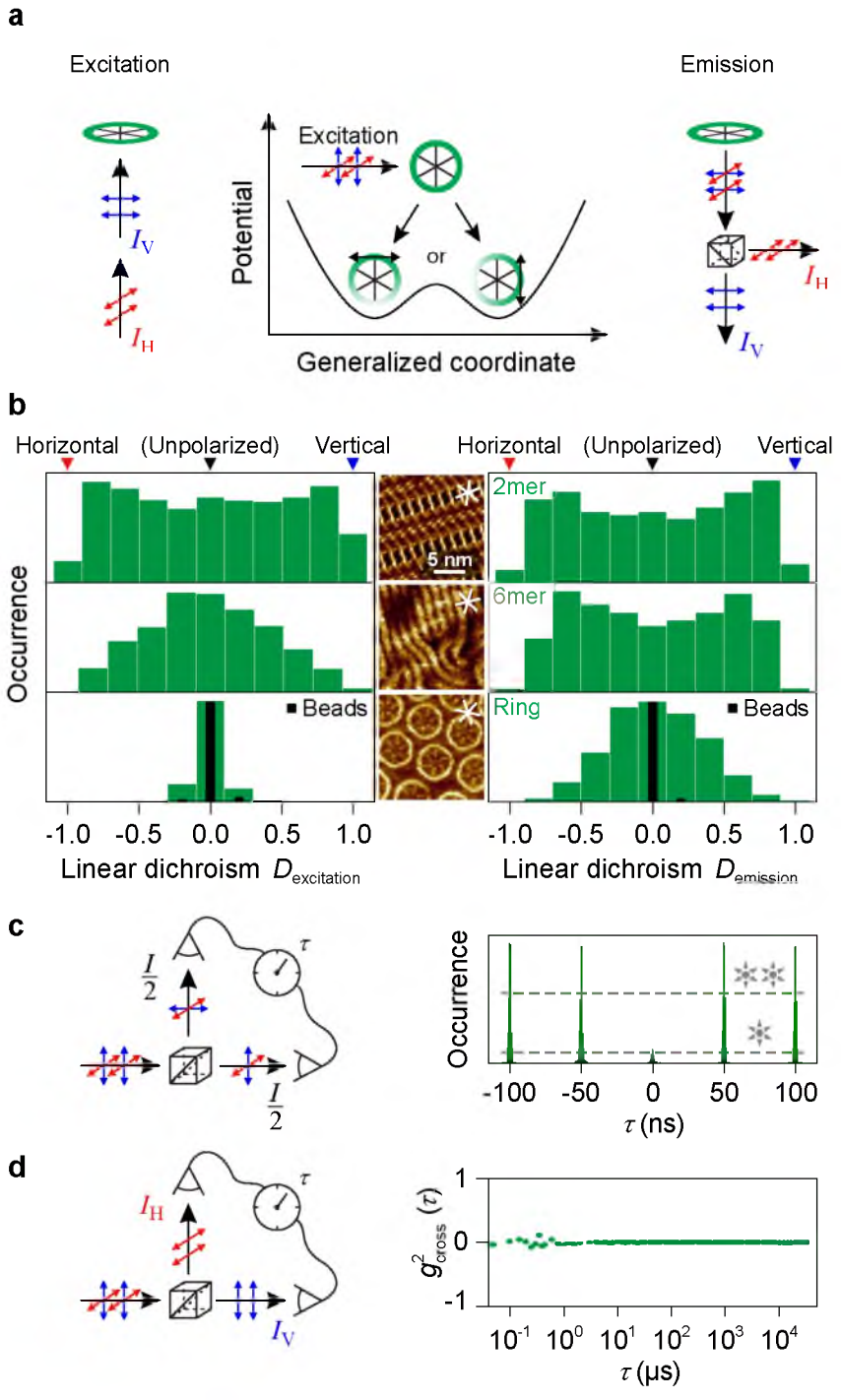
a
Excitation
Emission
Excitation
Potential
or
Generalized coordinate
I_V
I_H
I_H
I_V
b
Horizontal
(Unpolarized)
Vertical
Horizontal
(Unpolarized)
Vertical
Occurrence
2mer
6mer
Beads
Ring
Beads
5 nm
-1.0 -0.5 0.0 0.5 1.0
-1.0 -0.5 0.0 0.5 1.0
Linear dichroism $D_{excitation}$
Linear dichroism $D_{emission}$
c
$\frac{I}{2}$
τ
$\frac{I}{2}$
Occurrence
-100 -50 0 50 100
τ (ns)
d
I_H
τ
I_V
$g^2_{cross}(\tau)$
1
0
-1
10^{-1} 10^0 10^1 10^2 10^3 10^4
τ (μs)

It is not immediately obvious whether conjugation extends along the entire rim and whether the ring should be emissive at all. In molecules of six-fold symmetry, the S_0–S_1 transition is suppressed, as, for example, in benzene. Some larger macrocycles also show inhibited fundamental transitions [29–33]. However, slight interactions with the environment can break molecular symmetry and so make the transition allowed. A notable example is the B850 band in the light-harvesting system LH-II; on the basis of dipole selection rules, thermally activated emission from the B850 band would be expected because the lowest-lying state is dipole forbidden [34]. However, thermally activated emission is not observed experimentally [34].

1 is, indeed, highly emissive, with a quantum yield of $71 \pm 5\%$ and a short radiative lifetime of 840 ± 60 ps. The results of room-temperature absorption and emission spectroscopy (Supplementary Section S5 in Appendix A) of the ring and model linear compounds in solution are summarized in Table 3.1. The oligomers exhibit a bathochromic shift in emission and absorption with increasing size from the monomer to the dimer, which implies improved electronic delocalization [35]. Little difference is seen between dimer and hexamer, which illustrates that delocalization does not extend significantly beyond two monomers. Comparable porphyrin-based conjugated ring structures [21] fluoresce in the near-infrared region with a quantum yield of 0.12%, nearly three orders of magnitude lower than found here.

3.3.2 Room-Temperature Single-Molecule Spectroscopy

What is the microscopic nature of absorption and emission in 1? Which part of the ring absorbs light, and where is light emitted? Figure 3.2a sketches the problem. In excitation, ring symmetry should be preserved because incident light of any polarization can be absorbed. Yet emission should arise from the formation of a linear transition dipole, situated anywhere on the annulus. Slight structural relaxation in the excited state or perturbation of the structure by the environment will break symmetry [34, 36–38] and generate distinct local potential minima [11] into which the exciton relaxes randomly. These microscopic characteristics of the π system are best resolved by single-molecule techniques that overcome random averaging effects between molecules.

Table 3.1. Absorption, PL, PL quantum yield (PLQY) and PL lifetimes measured in toluene or chloroform solutions at r.t.

	Absorption maximum (nm)	Molar absorptivity ($cm^{-1}M^{-1}$) (at λ_{max} (nm))*	Absorption edge (nm)	PL maximum (nm)	PL lifetime (ns)	PLQY (%)	Radiative lifetime (ns)
Monomer 9	413	61,200(417)	431	431	0.97 ± 0.01	84 ± 5	1.15 ± 0.07
Dimer 10	422	200,000(425)	459	459	0.58 ± 0.01	69 ± 5	0.84 ± 0.06
Hexamer 11	426	500,000(430)	460	460	0.47 ± 0.01	66 ± 5	0.71 ± 0.06
Ring 1	443	420,000(444)	462	462	0.60 ± 0.01	71 ± 5	0.84 ± 0.06

* At the maximum of the lowest energy absorption band in chloroform solution.

Single molecules were diluted in Zeonex or poly(methylmethacrylate) (PMMA) matrices at picomolar concentrations and imaged at room temperature and 4 K in two separate fluorescence microscopes. We first addressed the nature of the absorbing transition dipole by determining the distribution of excitation polarization anisotropy values from molecule to molecule. Polarization anisotropy was quantified in terms of linear dichroism. We recorded photoluminescence (PL) intensity under alternating horizontally (H) and vertically (V) polarized excitation. Linear dichroism is defined by the ratio of emission intensities I under the two excitation polarizations, $D_{\mathrm{excitation}}$ (D_{ex}) = $(I_{\mathrm{V}} - I_{\mathrm{H}})/(I_{\mathrm{V}} + I_{\mathrm{H}})$ (refs [4, 39]). A linear dipole oriented randomly in a plane will yield a distribution that peaks at ±1 (ref. [40]). A value of $D_{\mathrm{ex}} = 0$ will originate either from unpolarized absorption, or from a dipole oriented at 45° with respect to both excitation planes. As molecule and dipole orientation are distributed randomly, the statistics of D_{ex} provide information on whether molecular absorption is polarized or unpolarized. Figure 3.2b shows histograms of linear dichroism in excitation for the dimer, hexamer and ring. Following Table 3.1, the dimer constitutes the effective exciton size in the hexamer and ring.

As expected, the dimer displays an almost linearly polarized absorption, the distribution matching a simple statistical simulation for a linear dipole [40]. Deviations from a perfect linear dipole arise because the dimer is slightly bent, as seen in the STM image. As length increases, the conjugated system becomes more distorted, which lowers the measured D_{ex} values and narrows the distribution. For 1, D_{ex} approaches zero–effectively, the molecules are unpolarized absorbers. To assess the experimental resolution, a histogram of 200 fluorescent beads (perfect unpolarized multichromophoric absorbers and emitters) of comparable spectral properties and photon count rates is superimposed (black bars, Figure 3.2b). Identical results were obtained in wide-field microscopy, which implies that the confocal laser excitation is free of polarization-distortion artefacts despite the high numerical aperture (NA) objective used [41] (see Supplementary Section S9 in Appendix A) for discussion).

Comparison of the rings to LHII is also interesting: despite similar dimensions and symmetry, isotropic absorption was not seen in experiments that involved single complexes [36–38]. Other synthetic ring structures have been studied only by ensemble

fluorescence depolarization [15, 21], which reveals ultrafast loss in polarization memory that is compatible with our single-molecule results.

At the excitation wavelength used (405 nm), the spokes of the wheel account for ~ 20% of the overall absorption, because spoke and rim absorption overlap spectrally (Supplementary Section S5 in Appendix A). It is only possible to discriminate spokes and rim in emission, as the spectra are shifted by 43 nm. Exciton generation must lead to symmetry breaking in the excited state because of changes in bond-length alternation and structural relaxation [11]. We can image this symmetry breaking directly through the polarization anisotropy in emission, which was again measured by the linear dichroism. Fluorescence was excited with alternating horizontal and vertical polarized light, and the emission was split into two orthogonally polarized components from which D_{emission} (D_{em}) was computed, as illustrated on the right side of Figure 3.2a (see Supplementary Section S1.2 in Appendix A for details). D_{ex} and D_{em} could therefore be calculated for the same molecule, which makes the D_{ex} and D_{em} histograms directly comparable. Identical results were found for excitation with circularly polarized light. Only the first 100 ms of illumination are considered for reasons discussed below. For the dimer, the D_{em} distribution is virtually identical to that in excitation because the molecule is too small for additional localization to arise in the excited state. For the hexamer, the effect of exciton localization to a unit comparable to the dimer is clearly visible – the D_{em} distribution resembles that of the dimer. More dipole orientations are available for excitation than for emission of the hexamer, which makes the D_{ex} histogram narrower than that for D_{em}. The situation is very different for 1. Although the photophysics is comparable to that of the dimer, the D_{em} histogram is much narrower than that of the dimer, which implies that single molecules appear to emit primarily unpolarized light. Unpolarized reference beads show identical histograms of D_{ex} and D_{em} (black bars, Figure 3.2b). However, for 1 the D_{em} distribution is not as narrow as that of D_{ex}. This broadening of the D_{em} histogram implies the possibility that excited-state localization occurred on some single rings during the experiment. In contrast, if localization took place on all molecules within 100 ms of illumination and always occurred deterministically, that is at the same position, the D_{em} histogram would match that of the dimer.

The dynamic nature of exciton-phonon coupling can give rise to localization fluc-

tuations and thus unpolarized PL, but so would simultaneous emission from multiple chromophores. To exclude this possibility, we studied the statistics of single photons emitted by the rings. Figure 3.2c shows the photon correlation, measured by splitting the emission into two equal paths and recording photon arrival times, as illustrated in the sketch on the left, averaged over 100 single molecules. The dashed horizontal lines indicate the anticipated correlation thresholds based on photon count rates and background signal for one and two photons (lower and upper, respectively). Only one photon is emitted at a time, which leads to the pronounced photon antibunching dip at zero delay between the two detectors. However, the polarization of this photon is not predetermined. Figure 3.2d shows the temporal cross-correlation of two orthogonally polarized detectors averaged over 95 molecules (first 100 ms of illumination). The correlation is flat – there is no characteristic timescale for polarization fluctuations. These results imply that single photons are emitted one at a time, and originate from different randomly varying segments on the ring, which leads to arbitrary fluctuations in emission polarization. Molecular symmetry is broken spontaneously, and a different localization occurs after each photoexcitation event.

The situation becomes very different on longer timescales. Under prolonged illumination, photomodification of the molecule may occur, for example, through the generation of a radical species [10]. This photomodification will lead to a quasistatic breaking of molecular symmetry, sketched in Figure 3.3a. Changes in photomodification with time can induce fluctuations in excited-state localization. This effect is resolved clearly in the temporal evolution of linear dichroism. Figure 3.3b exemplifies a molecule for which linear dichroism is measured simultaneously in excitation and emission (further examples are given in Supplementary Section S6 in Appendix A). The total fluorescence intensity shows discrete single-step blinking and an approximate halving of count rate after 12 s of illumination. The corresponding D_{ex} is zero for the first 10 s, and subsequently rises as the overall emission intensity decreases, presumably because part of the ring is photobleached [10]. D_{em} sets out at zero, drifting to a value of 0.4, and subsequently shows strong discrete jumps between positive and negative values. After continued illumination, fluctuations in localization occur, which lead to jumps in transition dipole orientation. The temporal evolution of linear dichroism caused by

Figure 3.3. Photoinduced fluctuations in exciton localization apparent in the temporal dynamics of single-ring luminescence. **a**, Photomodification of the ring can distort the excited-state potential quasistatically, which leads to a preferred polarization in emission. Changes in photomodification result in switching of emission polarization. **b**, PL intensity, excitation and emission anisotropy of a single-ring molecule. At short times into the measurement, the emission polarization appears isotropic. The excitation anisotropy remains zero as the emission anisotropy initially increases from zero and subsequently exhibits random jumps, which correspond to changes in emissive dipole orientation. **c**, Evolution of the linear dichroism histogram in excitation and emission with time for 644 single ring molecules. The excitation remains isotropic, whereas the emission becomes anisotropic with time because of photoinduced localization in the excited state.

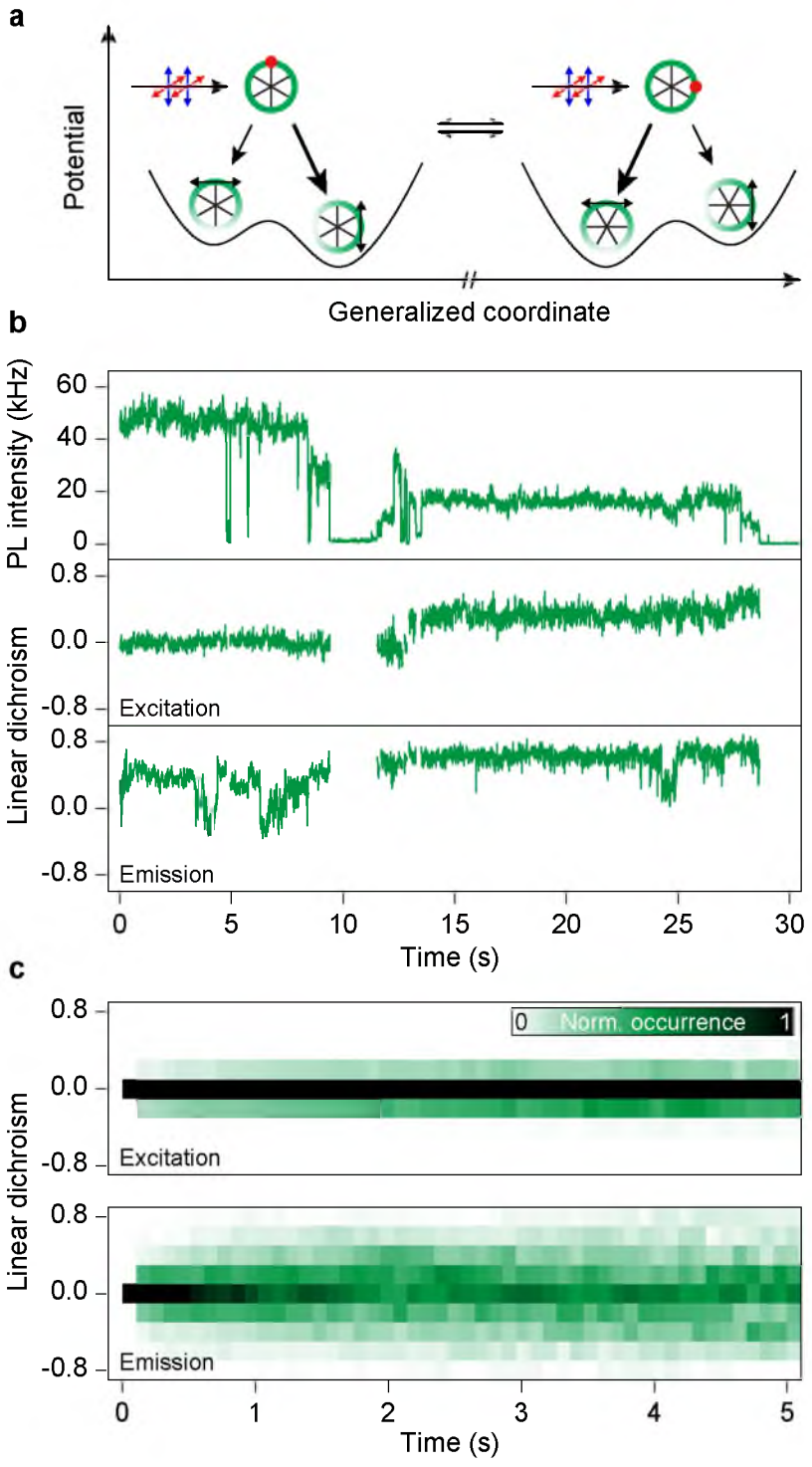
a
Potential
Generalized coordinate
b
PL intensity (kHz)
60
40
20
0
Linear dichroism
0.8
0.0
-0.8
Excitation
Emission
0
5
10
15
20
25
30
Time (s)
c
0 Norm. occurrence 1
Excitation
Emission
0
1
2
3
4
5
Time (s)

photomodification can be visualized by plotting the D_{em} histogram as a function of time (Figure 3.3c). We selected molecules that exhibit $|D_{\mathrm{em}}| < 0.1$ within the first 100 ms of illumination and did not drop by more than 30% in intensity over 5 s. This initial D_{em} value can correspond to unpolarized PL or emission from a dipole at ~ 45°orientation with respect to the two detectors. Out of 2,000 single molecules, 32% fell within this narrow range. For a random distribution of dipoles, one would expect [40] only 6% of all molecules to be oriented at ~ 45°, which implies that the low D_{em} values arise primarily from unpolarized emission. The histogram clearly broadens over time. No such broadening is observed for dimers (not shown). We did not find evidence that this broadening is reversible under interruption of the illumination (Supplementary Information in Appendix A). No broadening is seen in the corresponding D_{ex} histogram, which implies that the ring remains, to a first approximation, an isotropic absorber under continued illumination.

At the onset of photoexcitation, that is within the first ~ 100 ms, single-ring fluorescence can appear unpolarized because the emission jumps between equally weighted chromophores on the ring after every absorption event. With time, random photoinduced localization occurs, which leads to nonzero D_{em} values, which can then switch or drift randomly over ms to s. Although such ms fluctuations in linear dichroism have been observed previously in multichromophoric macromolecules [40, 42, 43], their structural or electronic origin remains unclear. The rings demonstrate that these fluctuations are a secondary effect and only arise as a consequence of illumination. Initially, the symmetry of the molecule is preserved, so that random spontaneous symmetry breaking in the excited state can be observed. Consequently, spontaneous symmetry breaking is also virtually independent of temperature as it constitutes a purely intramolecular effect with no coupling to the heat bath. At 4 K, ~ 20% of rings showed ($|D_{\mathrm{em}}| < 0.1$) under the initial illumination, which is comparable to the room-temperature measurement (Supplementary Section S8 in Appendix A).

3.3.3 Cryogenic Single-Molecule Spectroscopy

Although they do not affect spontaneous symmetry breaking, cryogenic temperatures do offer the advantage of overcoming thermal broadening to reveal the energetic

heterogeneity of different chromophores within one ring molecule. In conjugated polymers, single chromophore spectra with linewidths orders of magnitude narrower than the ensemble have been identified [44, 45]. Analogously, we can resolve typical [45] single-chromophore transitions in single rings at 4 K, as described in Figure 3.4a (black line). The spectrum consists of a strong, asymmetric peak at 465 nm, followed by a series of similar but weaker vibronics. Whereas the single molecule exhibits a linewidth, < 2 nm, the ensemble solution spectrum in Figure 3.2a (green line) spans > 20 nm. The histogram of 0-0 transitions of 117 different single molecules (grey bars) closely matches the 0-0 electronic transition in the ensemble (green line), which implies that the ensemble is made up of distinct single-molecule transitions that differ because of varying interactions with the environment. Chromophores can therefore be distinguished by their transition energy [46].

Generally, emission switching between chromophores in a single conjugated polymer chain is accompanied not only by a change in dipole orientation, but also by a modification of transition energy [46]. This situation can also be observed in 1, for which we resolved linear dichroism spectrally by splitting emission into orthogonal polarization components. To study the fluctuations in exciton localization and their impact on the chromophore energy, we focused on molecules that show polarized emission after prolonged illumination (see the Supplementary Information in Appendix A for further discussion). Figure 3.4b gives an example of a fluorescence spectral trace that resolves the two polarization components (coloured red and blue). At 4 K, fluctuations in linear dichroism are slower than at room temperature. Weak spectral jitter, characteristic of single-chromophore transitions [45], is visible in the trace. After a blinking event (in which the molecule turned dark) at 120 s into the measurement, the emission polarization jumps, as does the transition wavelength. This situation corresponds to dipole rotation by approximately 45°because only one polarization channel is active before the event, but both are equally strong afterwards, as seen in the integrated emission intensity (lower part of Figure 3.4b). The case is very different for the molecule shown in Figure 3.4c. Discrete reversible switching in dipole orientation occurs without discernible spectral change, which leads to an anticorrelation of horizontal and vertical components. Spectrally, it appears that only one chromophore is emitting, even though

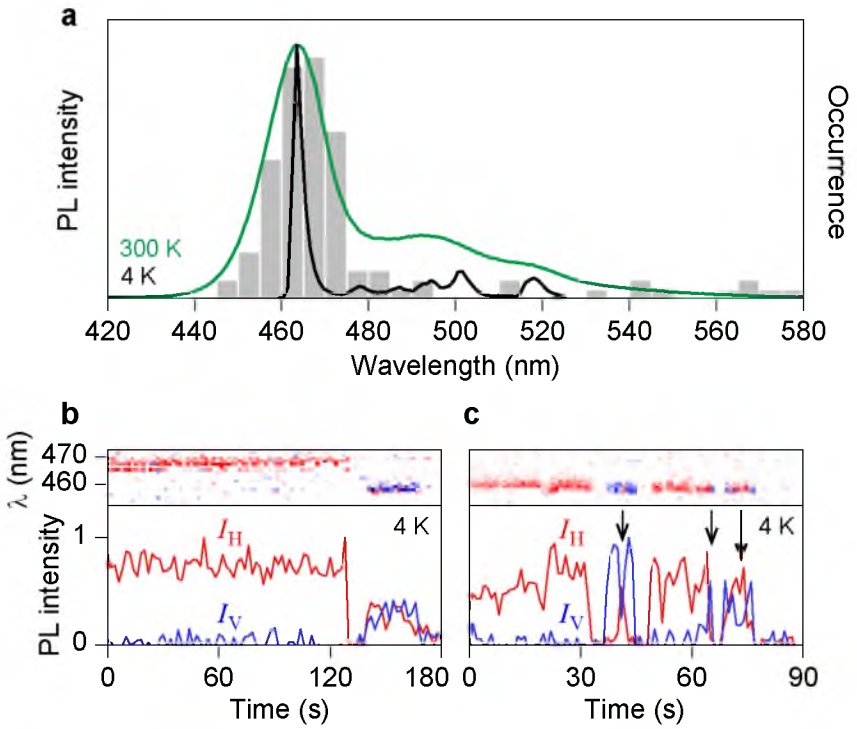

Figure 3.4. Low-temperature PL spectroscopy of single rings showing switching in transition energy and polarization. **a**, A typical single-molecule PL spectrum at 4 K (black line) exhibits a dominant zero-phonon line and discrete vibronic side bands, and an inhomogeneously broadened ensemble solution spectrum at 300 K (green line). The distribution of zero-phonon transition wavelengths for 117 single rings is superimposed. **b**,**c**, Fluorescence spectral trace and intensity as a function of time resolved for horizontally (red) and vertically (blue) polarized PL. Jumps in polarization, for example, at 120 s, generally coincide with a change in emission wavelength because a different chromophore emits on the ring (**b**). Reversible switching of the polarization can also occur without any change in emission energy (**c**), which implies that the energy of different chromophores on the ring remains controlled by the same dielectric environment. Arrows mark the anticorrelation in reversible switching between polarization planes.

the emissive part of the ring rotates by ~ 90°. This observation suggests that the π system experiences a homogeneous environment on length scales that exceed the size of the dimer, the emissive unit in the ring. Even though the exciton localizes to different parts of the molecule, in some situations the same effective dielectric environment is probed so that the transition energy remains unchanged. This phenomenon could potentially arise from longrange electronic correlations existing in the bath [47]. Such effects are, however, quite rare: out of 89 single molecules at 4 K, seven showed jumps in polarization without a spectral shift, and four showed a shift.

3.4 Conclusion

In conclusion, we have demonstrated that exciton localization in π-conjugated macromolecules is a fundamentally nondeterministic process that arises randomly on different monomer units. The phenomenon is important to microscopic modelling of energy transfer pathways in organic electronic devices, and may contribute to the origin of intramolecular interchromophoric electronic coherences reported in conjugated polymers [2]; chromophores, the polarizable species, are not necessarily static entities.

3.5 Methods

The synthetic methods and characterization of the materials are described in Supplementary Information (Appendix A). Single-molecule emission was studied at room temperature in air or under cryogenic conditions in vacuo. For room-temperature measurements, the analyte molecules were embedded in a PMMA (M_n = 46 kDa, Sigma Aldrich) host matrix. The following steps were conducted. (1) Borosilicate glass coverslips were cleaned in a 2% Hellmanex III (Hellma Analytics) solution, followed by rinsing with MilliQ water. (2) The glass coverslips were transferred into an ultraviolet-ozone cleaner (PSD Pro Series UV, Novascan) to bleach the glass coverslips from residual contaminant fluorescent molecules. (3) The analyte was diluted in toluene to single-molecule concentration (~ 10^{-12} M) and mixed with a 1% w/w PMMA/toluene solution. (4) The analyte-PMMA-toluene solution was spin coated dynamically (Laurell, WS-400-6NPP-Lite set at 2,000 r.p.m.) onto the glass coverslips, which led to a film thickness of about 50 nm with an average analyte density of 40 individual molecules in a range of 50 × 50 mm^2. (5) Single-molecule emission was studied under ambient conditions. It was

found that under the latter conditions, and under exposure to dry nitrogen at room temperature, the single-molecule emission was reduced substantially. This is most probably because of the build-up of triplet excitons, which can be quenched by molecular oxygen.

Fluorescence transients, including the linear dichroism in excitation and emission, of single ring molecules were recorded in a confocal fluorescence microscope. An inverted microscope (IX71, Olympus) with a high numerical aperture objective (NA = 1.49, APON 60XOTIRF, Olympus) was used. The excitation source was a fibre-coupled diode laser (LDH-C-405, PicoQuant) with a wavelength of 405 nm in a quasicontinuous wave mode (pulsed excitation, 20 MHz repetition rate). The excitation light was passed through a clean-up filter (HC Laser Clean-up MaxDiode 405/10, AHF Analysentechnik) and a Glan-Thompson polarizer to provide linearly polarized excitation light. The polarization of the excitation light was switched by an electro-optical modulator (3079-4PW, Fast-Pulse Technology Inc.) and an additional $\lambda/4$ waveplate between horizontal and vertical polarization every 500 µs, as described elsewhere [48]. The laser beam was expanded and collimated via a lens system and coupled into the oil-immersion objective through the back port of the microscope and a dichroic mirror (RDC 405 nt, AHF Analysentechnik). A diffraction-limited spot was generated with an excitation power of 50 nW to ensure that all measurements were performed in the linear excitation regime, far below single-molecule saturation intensity. The fluorescence signal was either split by a polarizing beam splitter (CM1-PBS251, Thorlabs) into two orthogonal polarizing detection channels or by a 50/50 beam splitter into two equivalent detection channels. Avalanche photodiodes from PicoQuant (τ-SPAD-20) were used as detectors and the signal was recorded with a time-correlated singlephoton counting module from PicoQuant (HydraHarp 400). For low-temperature measurements, the ring molecules were dispersed in an optically inert polymer matrix (Zeonex 480, Zeon Corporation) at concentrations of $\sim 10^{-6}$ gl^{-1} and spin coated on quartz substrates in a glove box under a nitrogen atmosphere to yield film thicknesses of 20 nm. The samples were mounted on the cold finger of a He cryostat (ST-500, Janis Research Company Inc.) and kept under a vacuum of $\sim 10^{-7}$ mbar during the measurement at 4 K. Fluorescence was detected with a long working-distance microscope objective (7.7 mm, NA 0.55, Olympus America Inc.) that projects the emission onto the entrance slit of a 50 cm spectrograph (ARC-1-015-500,

Princeton Instruments) with a CCD camera (CoolSnap:HQ2, Princeton Instruments).

Full details of the experimental methods are given in the Supplementary Information (Appendix A).

3.6 Acknowledgements

The authors are indebted to the Volkswagen Foundation for providing collaborative funding. A.V.A. and A.T. acknowledge financial support by the Fonds der Chemischen Industrie. J.M.L. is a David & Lucile Packard Foundation fellow and is grateful for a European Research Council Starting Grant (MolMesON, #305020).

3.7 Author Contributions

A.V.A., A.I., D.K. and S.H. designed and synthesized the compounds. A.T., D.W., T.S., F.S., J.V. and J. M. L. conceived, designed and performed the spectroscopy experiments and analysed the data. S-S.J. and S.H. performed and interpreted the STM experiments. A.T., J.V., S.H. and J.M.L. wrote the manuscript.

3.8 References

[1] G. D. Scholes, G. R. Fleming, A. Olaya-Castro, and R. van Grondelle, Nat. Chem. **3**, 763 (2011).

[2] I. Hwang and G. D. Scholes, Chem. Mater. **23**, 610 (2010).

[3] J. M. Lupton, ChemPhysChem **13**, 901 (2012).

[4] D. Hu et al., Nature **405**, 1030 (2000).

[5] B. J. Schwartz, Nat. Mater. **7**, 427 (2008).

[6] B. J. Schwartz, Annu. Rev. Phys. Chem. **54**, 141 (2003).

[7] H. Bässler and B. Schweitzer, Acc. Chem. Res. **32**, 173 (1999).

[8] R. Tempelaar, A. Stradomska, J. Knoester, and F. C. Spano, J. Phys. Chem. B **117**, 457 (2013).

[9] M. Lippitz, Phys. Rev. Lett. **92**, 103001 (2004).

[10] J. Hernando, Phys. Rev. Lett. **93**, 236404 (2004).

[11] S. Tretiak, A. Saxena, R. L. Martin, and A. R. Bishop, Phys. Rev. Lett. **89**, 097402 (2002).

[12] A. Ruseckas et al., Phys. Rev. B **72**, 115214 (2005).

[13] D. Mössinger, J. Hornung, S. Lei, S. De Feyter, and S. Höger, Angew. Chem. Int. Ed. **46**, 6802 (2007).

[14] M. Mayor and C. Didschies, Angew. Chem. Int. Ed. **42**, 3176 (2003).

[15] D. Mössinger et al., J. Am. Chem. Soc. **132**, 1410 (2010).

[16] S. H. Jung, Angew. Chem. Int. Ed. **45**, 4685 (2006).

[17] S. C. Simon, B. Schmaltz, A. Rouhanipour, H. J. Räder, and K. Müllen, Adv. Mater. **21**, 83 (2009).

[18] L. Arnold, H. Norouzi-Arasi, M. Wagner, V. Enkelmann, and K. Müllen, Chem. Commun. **47**, 970 (2011).

[19] H. S. Cho, J. Am. Chem. Soc. **125**, 5849 (2003).

[20] T. Hori, Chem. Eur. J. **12**, 1319 (2006).

[21] J. K. Sprafke et al., J. Am. Chem. Soc. **133**, 17262 (2011).

[22] M. C. O'Sullivan et al., Nature **469**, 72 (2011).

[23] J. Yang, M. C. Yoon, H. Yoo, P. Kim, and D. Kim, Chem. Soc. Rev. **41**, 4808 (2012).

[24] M. Hoffmann et al., Angew. Chem. Int. Ed. **47**, 4993 (2008).

[25] M. Iyoda, J. Yamakawa, and M. J. Rahman, Angew. Chem. Int. Ed. **50**, 10522 (2011).

[26] T. Kawase and H. Kurata, Chem. Rev. **106**, 5250 (2006).

[27] T. Kawase, Angew. Chem. Int. Ed. **46**, 1086 (2007).

[28] S. Höger and K. Bonrad, J. Org. Chem. **65**, 2243 (2000).

[29] M. Bednarz, P. Reineker, E. Mena-Osteritz, and P. Bäuerle, J. Lumin. **110**, 225 (2004).

[30] A. Bhaskar, J. Phys. Chem. B **111**, 946 (2007).

[31] E. Mena-Osteritz, F. Zhang, G. Götz, P. Reineker, and P. Bäuerle, Beilstein J. Nanotechnol. **2**, 720 (2011).

[32] O. Varnavski, P. Bäuerle, and T. Goodson III, Opt. Lett. **32**, 3083 (2007).

[33] F. Zhang, G. Götz, H. D. F. Winkler, C. A. Schalley, and P. Bäuerle, Angew. Chem. Int. Ed. **48**, 6632 (2009).

[34] R. Kunz, J. Phys. Chem. B **116**, 11017 (2012).

[35] S. Tretiak and S. Mukamel, Chem. Rev. **102**, 3171 (2002).

[36] S. Tubasum, R. J. Cogdell, I. G. Scheblykin, and T. o. Pullerits, J. Phys. Chem. B **115**, 4963 (2011).

[37] S. Tubasum, D. Thomsson, R. Cogdell, I. Scheblykin, and T. Pullerits, Photosynth. Res. **111**, 41 (2012).

[38] M. A. Bopp, A. Sytnik, T. D. Howard, R. J. Cogdell, and R. M. Hochstrasser, Proc. Natl Acad. Sci. USA **96**, 11271 (1999).

[39] O. Mirzov et al., Small **5**, 1877 (2009).

[40] T. Stangl et al., J. Am. Chem. Soc. **135**, 78 (2013).

[41] D. Thomasson, G. Sforazzini, H. L. Anderson, and I. G. Scheblykin, Nanoscale **5**, 3070 (2013).

[42] M. Forster, D. Thomsson, P. R. Hania, and I. G. Scheblykin, Phys. Chem. Chem. Phys. **9**, 761 (2007).

[43] C. Flors, J. Phys. Chem. C **111**, 4861 (2007).

[44] F. A. Feist, G. Tommaseo, and T. Basché, Phys. Rev. Lett. **98**, 208301 (2007).

[45] F. Schindler, J. M. Lupton, J. Feldmann, and U. Scherf, PNAS **101**, 14695 (2004).

[46] J. G. Müller, M. Anni, U. Scherf, J. M. Lupton, and J. Feldmann, Phys. Rev. B **70**, 035205 (2004).

[47] S. L. Wu, F. Liu, Y. Shen, J. S. Cao, and R. J. Silbey, New J. Phys. **12**, 105012 (2010).

[48] D. A. Higgins, D. A. Vanden Bout, J. Kerimo, and P. F. Barbara, J. Phys. Chem. **100**, 13794 (1996).

CHAPTER 4

EXCITON LOCALIZATION IN EXTENDED π-ELECTRON SYSTEMS: COMPARISON OF LINEAR AND CYCLIC STRUCTURES

Exciton dynamics are an integral part of the photophysical processes in π-conjugated materials. During relaxation of the excited state, part of the energy is converted into nuclear motion and lost to the heat bath. Understanding these processes can contribute to the development of more efficient optoelectronic devices, such as organic light emitting devices and photovoltaic cells. Furthermore, photo-activated structural reorganization is in some cases a necessity. An example of this is the torsional relaxation of protein-bound retinal in the human eye, which enables vision. The timescales of nuclear rearrangement and molecular reorganization following formation of the excited state are, however, difficult to access experimentally. This chapter demonstrates that π-conjugated model systems can be used to study phenomena related to exciton dynamics. The combination of transient ensemble spectroscopy and subensemble techniques allows separation between the effects of nuclear rearrangement and molecular restructuring upon transitioning between the ground and excited state.

This chapter is based on a manuscript that is in preparation for submission and was coauthored with Jan Vogelsang, Sigurd Höger and John M. Lupton, as well as Dominik Würsch (who performed parts of the single molecule spectroscopy experiments) and Stefan-S. Jester (who performed scanning tunneling microscopy measurements). Subheadings for the text are inserted here for structural clarity and are not part of the published manuscript.

4.1 Abstract

We employ six π-conjugated model systems of different molecular shape to investigate the extent of exciton self-trapping and torsional motion following optical excitation. Our studies combine steady state and transient fluorescence spectroscopy in ensemble with polarization spectroscopy on single molecules supported by Monte Carlo simulations. One of our model systems (dimer) experiences a significant spectral red shift within ~ 100 ps that is attributed to a torsional relaxation. This relaxation mechanism is inhibited in the structurally rigid macrocycle molecule. However, both systems show a high degree of exciton localization but with very different consequences: While in the macrocycle the exciton randomly localizes on different parts of the ring, in the dimer, localization leads to a well defined exciton resembling emission characteristics of a perfectly linear dipole. Monte Carlo simulations help us to quantify the degree of structural difference between the emitting and absorbing units in terms of disorder parameters. Our results show that model systems can be utilized to separate between different exciton dynamics and provide insight into mechanisms such as self-trapping and torsional relaxation.

4.2 Introduction

Understanding the photophysics of conjugated polymers is crucial to their technological application in organic light-emitting diodes and photovoltaic cells [1–3]. Excited state dynamics are inherent to both applications and ultimately determine the efficiency of these devices. Photoexcitation promotes an electron to a higher electronic state. The modified electron density is quickly followed by the nuclei initiating phonon modes. Due to strong electron-phonon coupling the excited state relaxes through the vibrational states manifold and becomes trapped by the rearranged nuclei in form of an exciton [4]. In addition, molecular reorganization, such as torsional motion, can further (de)localize the excited state [5]. While nuclear reorganization occurs on timescales of < 100 fs, torsional relaxation is generally two to three orders of magnitude slower [6, 7]. Both mechanisms constitute a loss of excitation energy and are ideally avoided in functional devices [8]. On the intermediate timescale, the excited state can undergo energy transfer of coherent nature or in terms of a Förster based hopping mechanism [9–11].

In principle, it should be possible to distinguish between these three processes with the right choice of model systems and experimental methods of investigation. Here, we study the extent of structural relaxation upon excitation and interrelated energy loss in π-conjugated model systems of similar building blocks composed in a variety of different geometries, shown in Figure 4.1.

The interplay between structural rigidity and electronic structure in such large macromolecules is evidently complex and not always intuitive. A large conjugated circular structure would not be expected to fluoresce from the S_1 state since this transition is dipole forbidden. Such a suppression of fluorescence has indeed been observed in porphyrin-based macrocycles, and in oligothiophene structures [12–14]. In contrast, our

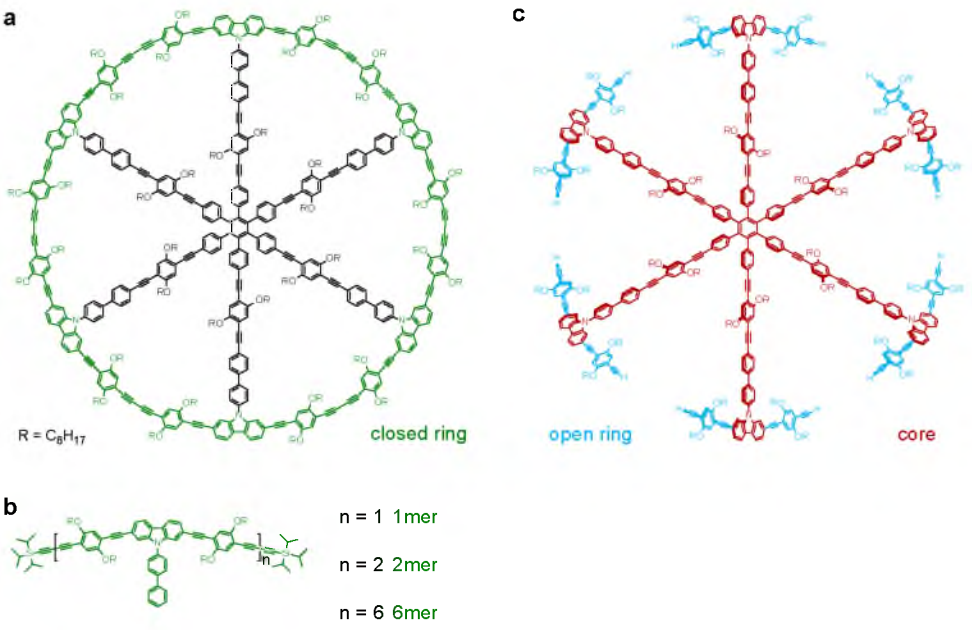

Figure 4.1. Chemical structures of the model systems to differentiate between excitonic localization processes in extended π-conjugated macromolecules. **a**. The closed ring model system is based on a carbazole bridged phenylene-ethynylene-butadiynylene scaffold (ring rim, green) stabilized by six spokes which emerge from a central hub (black). The phenyl groups in the spokes connecting to the carbazole units are rotated out of the ring plane leaving the rim π-conjugation disconnected from the structural centerpiece. **b**, Oligomers constitute the linear model system of the ring's rim. While the monomer corresponds to one-sixth of the rim, the hexamer covers the full length of the rim. All oligomers are terminated with triisopropylsilyl end groups. **c**. The open ring carries monomer units attached to the spokes (red and blue), whereas the core (red) has only a carbazole unit at the end of each spoke. Individual spoke segments are allowed to rotate around the internal axis.

carbazole ring structures do show strong fluorescence from the S_1 level, which we have previously attributed to spontaneous symmetry breaking in the excited state which localizes the molecular exciton on a rim segment, enabling fluorescence [15]. An estimate of the magnitude and nature of structural relaxation can be derived from the Stokes shift between absorption and emission, and in particular from the transient fluorescence spectrum. Further insight into the influence of molecular structure on the emitting and absorbing units can be provided by leaving the ensemble behind and transitioning to the single molecule level [16], where intermolecular energy transfer is inhibited. In addition, single molecule polarization techniques can probe absorbing and emitting units of individual molecules and provide additional information on the amount of exciton localization [17, 18]. Careful selection of methods and model materials allows us to discern between different exciton relaxation mechanisms induced by electron-phonon coupling, torsional relaxation and Förster-type energy transfer.

4.3 Results and Discussion

4.3.1 Model Systems and Room-Temperature Steady State Ensemble Spectroscopy

Our model systems are based on a carbazole bridged phenylene-ethynylene-butadiynylene scaffold [15, 19] assembled into effectively one-dimensional (oligomers), two-dimensional (closed ring, core) and three-dimensional (open ring) geometries. The chemical structures are shown in Figure 4.1. The design of the macrocycle molecule (closed ring) was chosen primarily to provide shape persistency to the π-conjugation of the closed ring's rim, Figure 4.1a. Six spokes emerging from a central hub manifold are connected to the *N*-phenyl-carbazole bridged phenylene-ethynylene-butadiynylene elements. Because the phenyl groups of the spokes adjacent to the N-carbazole units are rotated out of the molecule plane, π-conjugation of the rim is effectively disconnected from the center moiety. In addition, the perimeter of the closed ring is translated into a linear configuration in the three different oligomer structures shown in Figure 4.1b. The smallest unit (monomer) comprises one-sixth of the closed ring's rim with the *N*-phenyl-carbazole unit at its center. The longest unit (hexamer) is equal to the full perimeter of the closed ring. All oligomers are terminated with triisopropylsilyl end groups. The open ring molecule, shown in Figure 4.1c, is based on the closed ring

with the rim dissected at six points between the spokes. Each spoke carries a monomer building block with the full structure resembling six anchors attached to a common centerpiece. The arrangement becomes particularly interesting because each anchor is anticipated to rotate around the shank axis, thus, limiting the anchor's crown to a plane perpendicular to the spokes plane. Finally, we also considered the model system of the structural centerpiece (core). The core carries only the carbazole unit (red) and not the (blue) phenylene-ethynylene building block of the monomer.

Room-temperature absorption and emission spectroscopy of the compounds in toluene solution is summarized in Figure 4.2. The emission spectra of the oligomers show a bathochromic shift from the monomer to the dimer suggestive of improved electronic delocalization. However, there is almost no spectral shift between the dimer and the hexamer, illustrating that excitonic coherence [20] does not extend significantly beyond two monomers. At the same time, the dimer exhibits the strongest Stokes shift ($\sim$ 40 nm) of all oligomers. The substantial blue-shift of $\sim$ 20 nm of the open ring emission compared to the monomer is attributed to the absence of silanylene groups in the open ring. The exact values of absorption and emission peak positions are summarized in Table 4.1. Interestingly, the spectra of the spokes and the open ring structure are remarkably similar. We will show below that the emission in the open ring structure indeed originates from the carbazole anchor crowns and not from the spokes.

4.3.2 Time-Resolved Fluorescence Spectra and Fluorescence Depolarization

While the absorption peak of the carbazole compounds experiences a continuous red-shift in the series monomer-dimer-hexamer-ring (Figure 4.2), the emission peak energy only changes between monomer and dimer and then remains constant for the larger structures. The dimer shows a substantial Stokes shift between absorption and emission, indicating a high degree of structural relaxation. Insight into the relaxation processes can be provided by time-resolved fluorescence spectroscopy as presented in Figure 4.3. The dimer experiences a strong transient emission peak red-shift following photoexcitation, readily visible in the streak camera images (white arrow in panel a). The relative peak energy $\Delta E(t) = E(t) - E_{t=0}$ is plotted in Figure 4.3b. It is not immediately obvious why the strongest energy shift occurs in the dimer, totaling over 40 meV, whereas

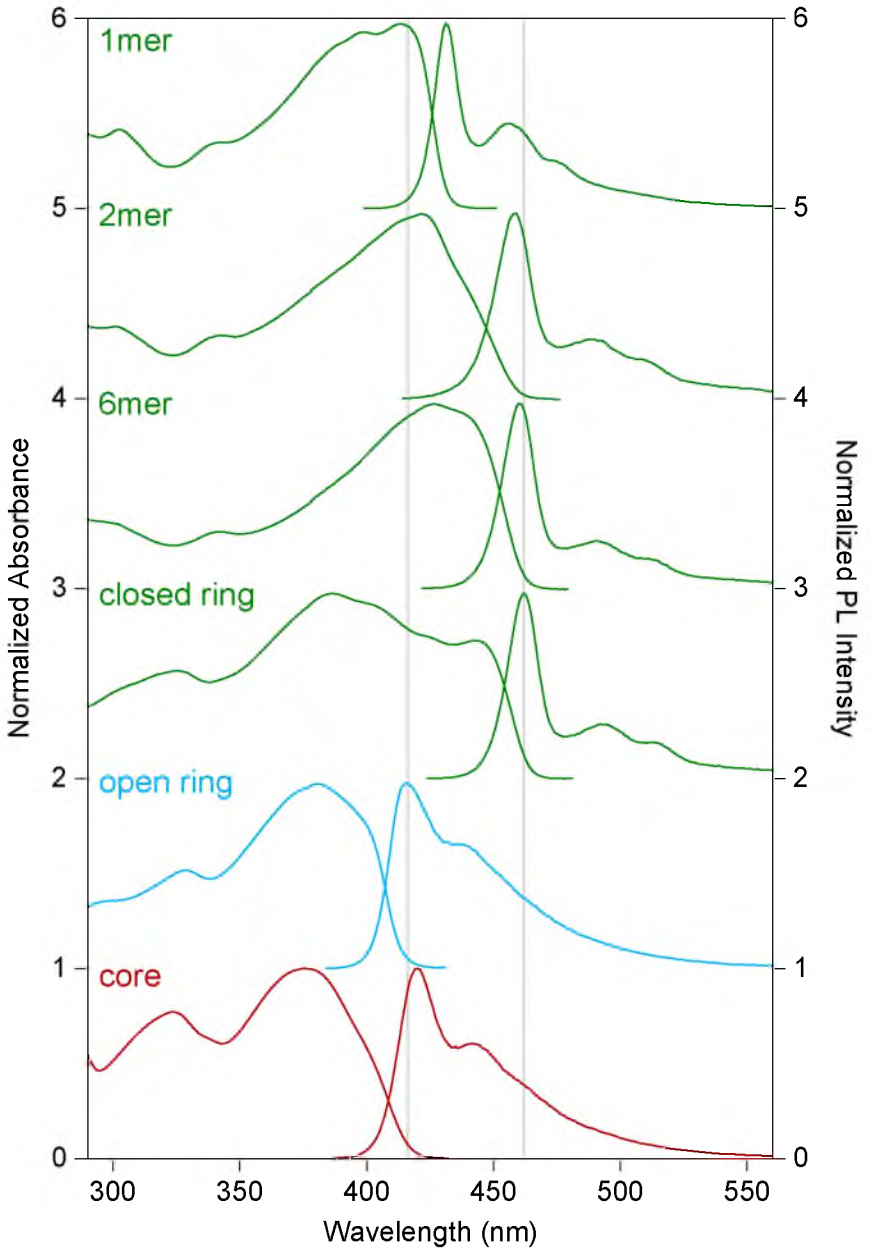

Figure 4.2. Steady state optical spectra of the model systems. The increase of the size of the chromophoric system causes a progressive red shift of the low energy absorption peak from monomer to dimer over hexamer to closed ring. In contrast, the red shift of the emission saturates with chain length for the dimer, suggesting that the emissive units in the hexamer and closed ring structures are effectively of the size as the emissive unit in the dimer. The open-ring emission peak is slightly blue shifted compared to the monomer due to the lack of silanylene end groups in the open ring. Although absorption and emission of the spokes unit and the open ring structure appear identical, emission in the open ring occurs from the crown (the monomer unit) and not from the spokes. Gray lines are added for visual aid.

Table 4.1. Absorption, PL, PL quantum yield (PLQY), PL lifetimes, and initial anisotropy $r_{t=0}$ measured in toluene solutions at room temperature.

	Absorption maximum (nm)	PL maximum (nm)	PL lifetime (ns)	PLQY (%)	Radiative lifetime (ns)
1mer	413	431	0.86	84	1.02 ± 0.06
2mer	422	459	0.58	69	0.84 ± 0.06
6mer	426	460	0.47	66	0.71 ± 0.06
closed ring	443	462	0.60	71	0.85 ± 0.06
open ring	381	414	0.94	62	1.52 ± 0.12
core	376	419	1.03	–	–
error	±2	±2	±0.01	±5	

the transient Stokes shift of the monomer or ring amounts to no more than 4 meV. Naively, one might anticipate the hexamer to exhibit a more pronounced energy shift, owing to the larger and more disordered molecular structure as well as the possibility of on-chain energy transfer. It is likely that the red shift is associated with torsional motion between monomer units that cannot occur in the monomer and is strongly slowed down in the hexamer due to the increased molecular size. Similarly slow structural relaxation on the timescale of > 100 ps has been reported for trifluorene [6], conjugated porphyrin oligomers [5] and PF2/6 [7] previously, although torsional relaxation is usually found to be somewhat faster in π-conjugated oligomers [21–23].

Although the steady state PL peak energy is virtually the same for the dimer, hexamer and the closed ring, further conjugation increases the pool of electrons contributing to the exciton wavefunction. This raises the emission oscillator strength [20] and hence lowers the radiative lifetime τ (Table 4.1) from $\tau_{1\text{mer}} = 1.02$ ns over $\tau_{2\text{mer}} = 0.84$ ns to $\tau_{6\text{mer}} = 0.71$ ns. The open ring approximately reflects the lifetime of the monomer with $\tau_{\text{open}} = 1.52$ ns , whereas the lifetime of the closed ring $\tau_{\text{closed}} = 0.85$ ns is almost identical to that of the dimer.

It is particularly interesting to look at the dynamics of the orientation of the emitting transition dipole of the model systems in order to identify ongoing processes occurring immediately after photoexcitation, in particular, interchromophoric coupling and intramolecular energy transfer. Figure 4.3c provides an overview of the temporal fluorescence anisotropy decay of the compounds in solution. An isotropic distribution

Figure 4.3. Time-resolved ensemble PL spectra and fluorescence anisotropy transients in solution. **a**, Streak camera images of the monomer, dimer, hexamer and closed ring molecules obtained in dilute toluene solution, at room temperature, plotting the PL intensity versus wavelength and time. The dimer shows a pronounced blue shift of the photoluminescence maximum (white arrow), which is caused by structural relaxation. This amount of relaxation is not observed in the hexamer nor in the ring structure. **b**, Temporal shift of the emission peak plotted as the relative energy change $\Delta E(t) = E(t) - E_{t=0}$. The dimer shows the largest energy loss during the first 200 ps suggesting a high degree of relaxation. **c**, The fluorescence anisotropy r, defined and measured as shown in the inset, quantifies the polarization memory in the excited state. The initial values of r depend on intramolecular depolarization that occurs on the fs-timescale and is linked to the geometry of the system. Within the measured time range, the anisotropy decay is governed by rotational diffusion of the molecules in solution which is practically inhibited for the larger systems. A fast depolarization component due to rotation of the crown units in the open ring structure is visible during the first 200 ps.

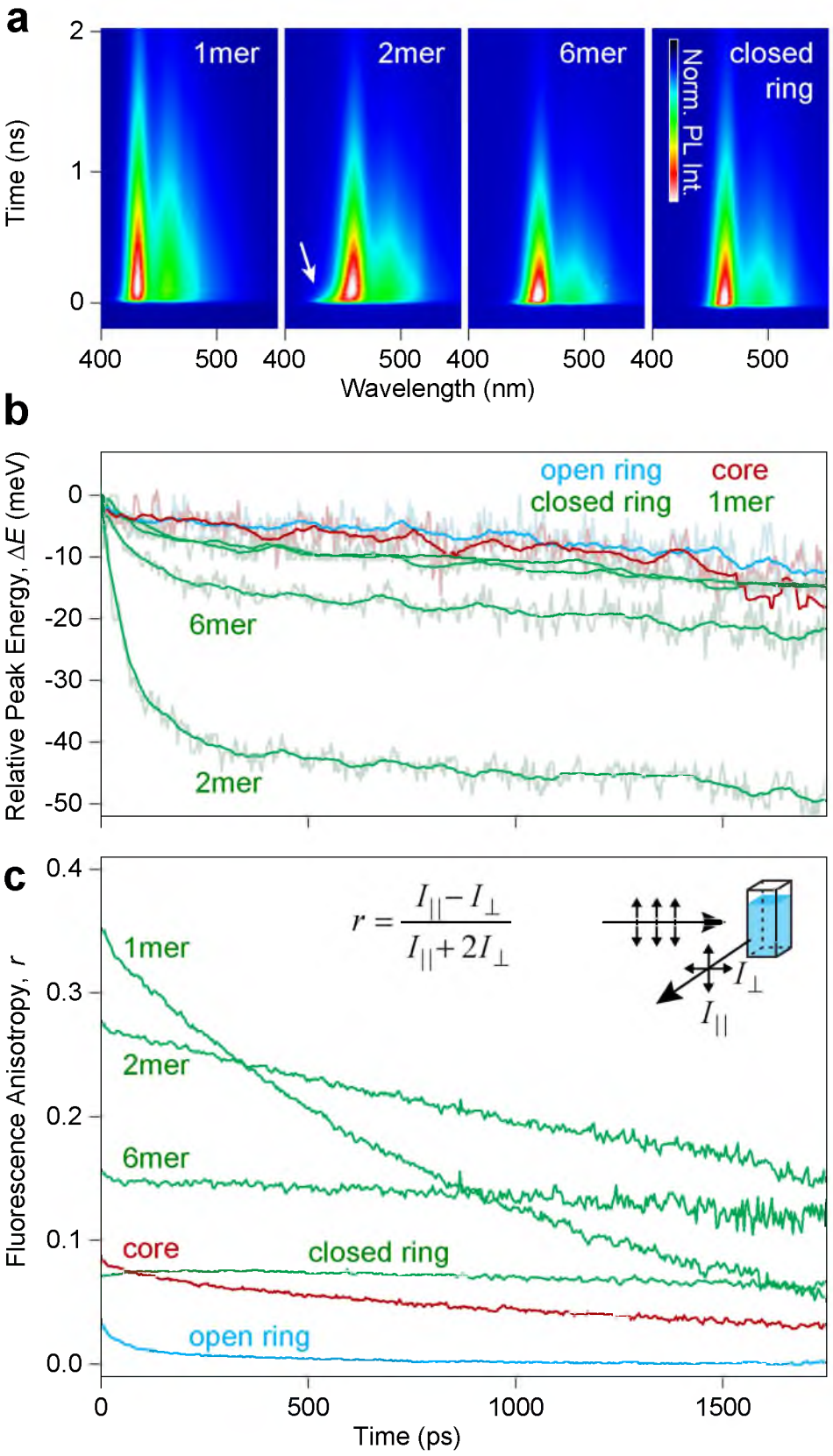
a
1mer
2mer
6mer
closed ring
Norm. PL Int.
Time (ns)
Wavelength (nm)
b
open ring
core
closed ring
1mer
6mer
2mer
Relative Peak Energy, ΔE (meV)
c
$r = \frac{I_{||} - I_{\perp}}{I_{||} + 2I_{\perp}}$
$I_{\perp}$
$I_{||}$
1mer
2mer
6mer
core
closed ring
open ring
Fluorescence Anisotropy, r
Time (ps)

of linear dipoles is expected to show an anisotropy $r = (I_{\parallel} - I_{\perp})/(I_{\parallel} + 2I_{\perp})$ of $r = 0.4$ [24]. Here, $I_{\parallel}$ and $I_{\perp}$ indicate vertical and horizontal polarization of the luminescence intensity under vertically-polarized laser excitation. The maximum value of 0.4 can only be reached if the absorption and emission dipoles are colinear. When this is not the case, the anisotropy deviates according to [25]

$$r = \frac{3\cos^2\beta - 1}{5}\ , \tag{4.1}$$

where β is the angle between the absorption and emission transition moments. The monomer shows an initial anisotropy value of $r_{t=0} = 0.35$ in Figure 4.3c. The subsequent decrease of r with time arises due to rotational diffusion of the molecules in the solvent. As chain length increases to the dimer and hexamer, a smaller initial r is determined due to greater bending of the molecular object, followed by a slower subsequent decay with time due to the larger radius of gyration. The closed ring displays no discernible dynamics in anisotropy around $r = 0.1$. Such a value is expected for ultrafast depolarization of fluorescence in a plane [14, 26], implying delocalization of excitation energy on a timescale < 2 ps. A similar behavior is observed for the spokes (red curve). However, for this compound an additional decay below $r = 0.1$ is observed, which likely originates from the smaller effective radius of gyration in solution and the reduced structural rigidity compared to the ring. The open ring structure, in contrast, exhibits complete fluorescence depolarization to $r \sim 0$ within 200 ps. This complete depolarization implies rotational displacement of the chromophores out of the molecular plane, adding a further degree of freedom for fluorescence depolarization by energy transfer.

Both transient PL spectra as well as time resolved polarization anisotropy reveal substantial differences between the different model systems which are masked when simply comparing ensemble PL spectra. The initial anisotropy values measured provide crucial information on the polarization memory following structural relaxation, intrachain energy transfer and exciton self-trapping occurring on the fs to ps time scale [10, 11, 27] However, much more can be learned by directly studying the absorbing and the emitting units of individual molecules which are inherently interrelated with the molecular shape.

4.3.3 Single Molecule Polarization Spectroscopy

Ensemble averaging effects can be overcome by studying morphology related characteristics of π-systems on the single molecule level [16, 28]. Dispersing the model systems in poly(methyl-methacrylate) at pM concentrations provides an amorphous environment in an inert polymer matrix and sufficient intermolecular spacing so that single molecules can be examined optically. The molecular concentration in the ~ 50 nm thick matrix film was adjusted to yield well separated, diffraction limited emission spots. We employ excitation polarization modulation and emission polarization spectroscopy to study characteristics of the absorbing and emitting units, respectively. As sketched in Figure 4.4a, the absorption ellipse of a single molecule can be traced by modulating its fluorescence intensity I with excitation polarization following

$$I(\alpha) \propto 1 + M\cos(2\alpha) \ , \tag{4.2}$$

where α is the angle of excitation polarization and M the modulation depth. Intensity modulation traces of individual molecules give a value of $0 \leq M \leq 1$ with $M = 1$ signifying a linear dipole and $M = 0$ an unpolarized absorber [29, 30]. These values are plotted in a histogram for the different compounds in Figure 4.4b-g, with the number of single molecules measured stated in each panel. As expected, the monomer exhibits near-perfect linearly-polarized absorption ($M \rightarrow 1$). As the chain length increases, the chromophores become more bent, lowering M (Figure 4.4b-d). The spokes exhibit a very broad histogram, with both high and low anisotropy values present. For both the closed ring and the open ring, the modulation approaches zero. Nonzero values in the histogram may conceivably arise due to slight out-of-plane orientation of the molecules and the finite signal-to-background ratio in the single-molecule measurement. However, none of the closed ring molecules show high M values as would be expected for rings lying perpendicular to the sample plane [31]. We therefore propose that out-of-plane orientations of the closed rings do not arise due to shear forces acting on the ring molecules during spin coating nor from an effective phase separation between these large molecules and the host matrix. In contrast, the emissive units in the open ring are flexible compared to the closed ring. Rotation of the chromophores of the open ring out of the molecular plane, as discussed in Figure 4.3c, will introduce anisotropy yet at the same time lower intensity since the transition dipoles point out of plane, decreasing

Figure 4.4. Geometries of absorbing and emitting units probed on the single-molecule level. **a**, Sketch of the excitation polarization ellipse of individual molecules, which is probed by rotating the polarization plane of the excitation light and recording the PL modulation depth M (left). The orientation of the emitting dipoles is determined by splitting the single-molecule PL into two orthogonal polarization channels and characterized by the linear dichroism D (right). **b-g**, Histograms of excitation polarization anisotropy for the different model systems. A clear trend towards lower M values is apparent when going from the monomer, a linearly polarized absorber, to the fully conjugated ring, which acts as an almost perfect isotropic molecular absorber. **f**, Splitting the M distribution of the open-ring structures into two equally large subsets of bright and dark molecules reveals the cause for the broadening of the histogram to higher M values. Molecules with anchor crowns rotated out of the molecule plane appear as more anisotropic, having higher modulation depths, but also couple radiation less effectively to the far field, appearing dimmer. **h-m**, Following the increasingly isotropic shape of the molecules from monomer to closed ring, a peak of linear dichroism around a value of 0 emerges in the single-molecule histograms. Whereas perfectly isotropic systems always result in $D = 0$, the histogram of an ideal linear dipole (black circles) peaks at $D \pm 1$. Only the dimer approaches this case (**i**). The number of molecules in a histogram is given in each panel.

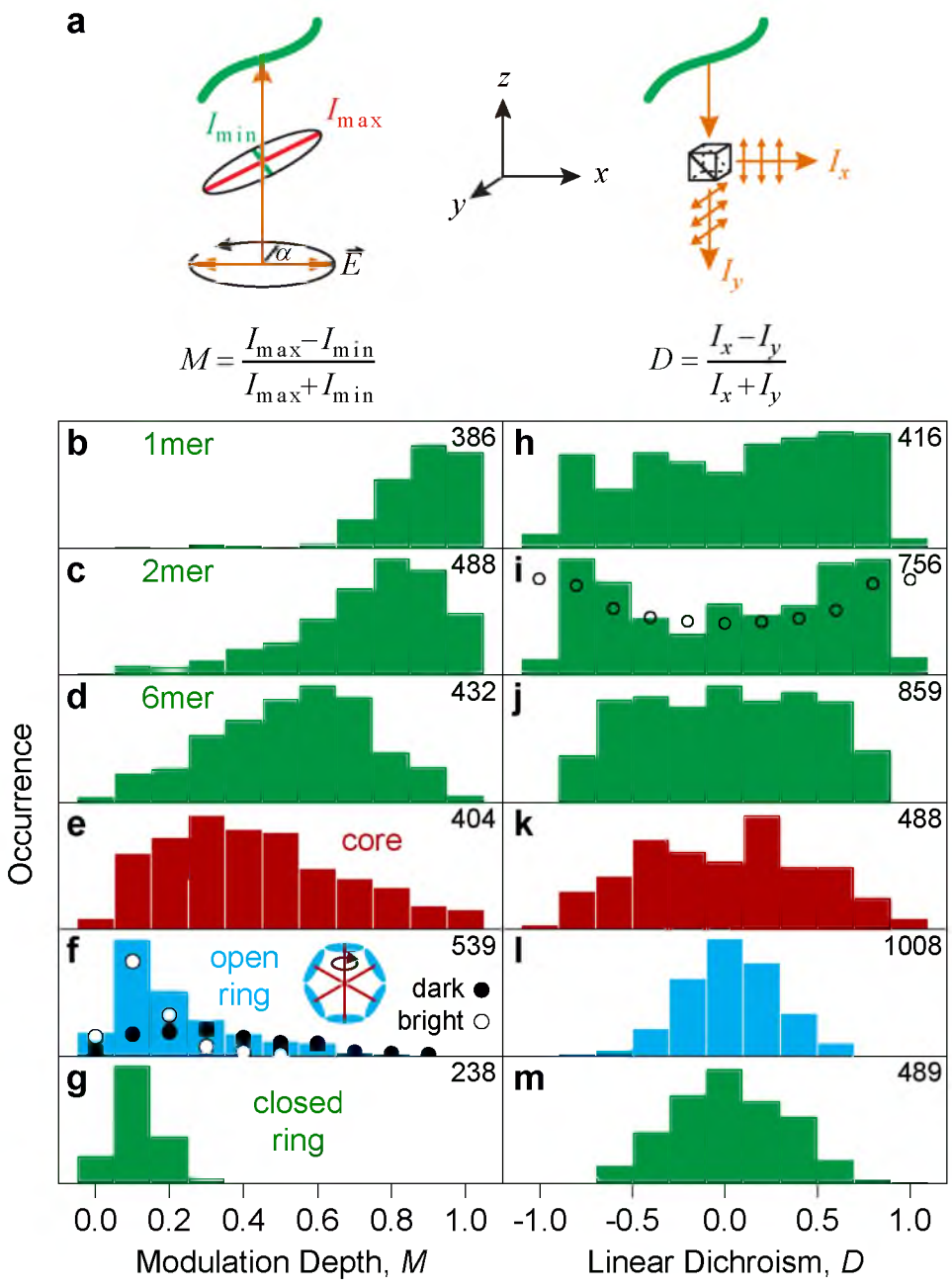
a
I_{min}
I_{max}
α
$\vec{E}$
z
x
y
I_x
I_y
$M = \frac{I_{max} - I_{min}}{I_{max} + I_{min}}$
$D = \frac{I_x - I_y}{I_x + I_y}$
b 1mer 386
c 2mer 488
d 6mer 432
e core 404
f open ring 539
dark
bright
g closed ring 238
h 416
i 756
j 859
k 488
l 1008
m 489
Occurrence
0.0 0.2 0.4 0.6 0.8 1.0
Modulation Depth, M
-1.0 -0.5 0.0 0.5 1.0
Linear Dichroism, D

the effective absorption cross-section. To test this hypothesis, panel f) superimposes the distributions for the brightest (white) and darkest (black) 50% of the open ring molecules on top of the average histogram. Indeed, the brighter the molecules, the more the M values tend to zero. This observation implies that it is indeed the rim unit in the open ring which is absorbing and not the spokes, since the spokes themselves cannot rotate out of the molecular plane. It is interesting to compare the open ring and the spokes directly since, in their unperturbed state, they have virtually the same D_{6h} symmetry. The scatter to high anisotropy for the spokes structure compared to the open ring must therefore be a result of reduced structural rigidity leading to the formation of less isotropic molecular objects.

The intramolecular morphology of the model systems is clearly reflected in the absorption modulation depth histograms. A narrow distribution with high M values is observed for the ordered, virtually straight monomer; a broad histogram is seen for the disordered hexamer; and a narrow distribution tending to $M \rightarrow 0$ is found both for the isotropic open ring and closed ring structures. A similar trend is observed for the emitting units classified by measuring the linear dichroism D under circularly polarized excitation. As depicted in Figure 4.4a, here, the PL is separated into two orthogonal polarization components by a polarizing beam splitter. Depending on the relative orientation between emitter and detectors, and the overall degree of linearity in dipole emission, the linear dichroism can assume values ranging from -1 to $+1$. A histogram of randomly distributed ideal dipoles would peak at values of $D = \pm 1$ with a pronounced dip around $D = 0$ [32]. This ideal distribution, arrived at by a simple Monte-Carlo simulation, is superimposed in the histogram in Figure 4.4i as open circles. In contrast, in an isotropic system with no preferential emission polarization, linear dichroism will always be zero. Given the signal to noise level in the experiment, the monomer and dimer D distributions in Figure 4.4h,i are fairly close to expectation for a single linear transition dipole. D in the hexamer (panel j) begins to deviate from linearity, with the histogram flattening and anisotropy peaking at $D = 0$. Likewise, the spokes structure, which constitutes a multichromophoric emitter, is only weakly polarized (panel k). Interestingly, the PL anisotropy for the closed rings (panel m) is virtually identical to that for the open rings. This loss of anisotropy in emission compared to the spokes must

again result from an increased rigidity of the open ring compared to the spokes alone. In contrast, the open ring structure (panel l), which is almost identical to the spokes, shows a much narrower distribution of D values centered around zero, implying unpolarized emission. The deviation of D values from zero in the perfectly isotropic closed ring structure has been shown to originate from spontaneous or photoinduced symmetry breaking, leading to a certain degree of localization of the emissive exciton. We have shown previously that individual closed ring molecules act as single photon sources and, yet, no correlation between excitation and emission polarization is observed [15]. The closed-ring exciton localizes dynamically and nondeterministically to the size of the dimer exciton, resulting in entirely random emission polarization from anywhere on the perimeter. Similar behavior was recently reported in naturally occurring photosynthetic complexes [33]. This feature is the result of the rigid molecular structure of the closed ring; the lack of structural integrity in the spokes and the hexamer broadens the D histograms significantly, in agreement with the observations made for the measurements of polarization anisotropy in excitation (M).

It is interesting to note that despite the fact that the monomer structure is less bent than the dimer, it is not the monomer but rather the dimer that approaches the case of an ideal dipole, with the D histogram peaking at ± 1. In particular, comparison of the corresponding M and D histograms appears to suggest a discrepancy between the geometry of the absorbing and the emitting units of the molecule. If absorption and emission were to occur from the same molecular unit, the histograms would have to be identical, which they are not (Figures 4.4b,c,h,i). While in absorption the monomer behaves more like an ideal dipole, showing overall higher anisotropy values and a smaller scatter (Figure 4.4b) than the dimer (Figure 4.4c), in emission, the situation is reversed: panel i more closely resembles the ideal case (open circles in Figure 4.4i than does panel h. In order to assess the level of structural change upon excitation, we carried out a simple Monte Carlo simulation of the M and D histograms for the monomer and dimer.

4.3.4 Simulation of Modulation Depth and Linear Dichroism Histograms

Measurement of polarization excitation anisotropy directly probes the shape of the absorbing chromophores and is strongly tied to the molecular shape carrying the con-

jugated system. In contrast, the emissive species may be prone to structural localization effects (exciton self-trapping) [4] or energy transfer [10]. We model the effect of excited-state relaxation in model molecules as outlined in Figure 4.5a. A monomer unit is discretized numerically and defined as being made up of ten equally long, linear dipole segments. Two of such units represent a dimer molecule, and are allowed to have a random dihedral angle θ between them. This assumption is based on the fact that a series of multiple triple bonds effectively flattens the angle-dependent rotation barrier allowing for virtually any orientation [34, 35]. Variation of the molecular shape is introduced by a bending angle θ_1 within the monomer unit, defined as the angle between the first and the last discretized element of one unit. For simplicity we assume continuous bending of the segments belonging to one repeat unit[1]. Disorder is introduced into the simulation through a normal distribution of bending angles $\theta_1 \sim \mathcal{N}\left(\mu_{1\text{mer}}, \sigma^2_{1\text{mer}}\right)$ leaving only two variable parameters in the simulation: the mean bending angle μ and the standard deviation σ. The dimer has two independent bending angles θ_1 and θ_2 for each of the two repeat units but both are restricted by the same normal distribution $\{\theta_1, \theta_2\} \sim \mathcal{N}\left(\mu_{2\text{mer}}, \sigma^2_{2\text{mer}}\right)$. Finally, each simulation set contains 20,000 molecules randomly oriented in three-dimensions and interacting with the electromagnetic field polarized in the sample plane. The best fit parameters are identified by minimizing a least-squares test of simulation results performed in steps of $\{\Delta\mu, \Delta\sigma\} = 0.5°$.

For clarity, the results of the simulations are plotted in Figure 4.5 as circles on top of the experimental histograms from Figure 4.4, using identical binning sizes. Our simple model reproduces the modulation depth histograms remarkably well (Figures 4.5b,c). In general, increasing the bending angle shifts the peak of the histogram to lower M values equally for monomer and dimer (not shown). However, for identical monomer and dimer bending angels, in the dimer, an increase in low anisotropy values and decrease around $M = 1$ occurs due to the higher molecular complexity and the resulting structural disorder. This complexity comes from the presence of two monomer units in the dimer instead of one and the random dihedral angle φ between them. Fits to the monomer

[1] Efforts to implement the exact structure comprised of two linear segments with a 24° bending angle introduced by the carbazole did not reproduce the experimental M histograms of monomer and dimer sufficiently.

Figure 4.5. Monte Carlo simulations of the excitation and emission anisotropy histograms of monomer and dimer, showing the effect of exciton localization in the excited state. **a**, A monomer unit is arbitrarily broken down into ten equally long linear dipole segments with an overall bending angle θ_1 between the first and the last segment. The dimer consists of two such units with independent individual bending angles θ_1 and θ_2, and a random dihedral angle φ between the two units. Assuming a normal distribution of bending angles $\theta \sim \mathcal{N}(\mu, \sigma^2)$ with mean angle μ and standard deviation σ leaves only two free simulation parameters, which are adjusted to fit the experimental distributions. **b,c**, Comparison of experimental data (bars) and simulation results (filled circles). The simulated distributions arise from 20,000 randomly chosen monomer and dimer conformations. The best agreement between experiment and simulation was achieved with a similar mean bending angle for monomer (53°) and dimer (57°) but with significantly different standard deviations. The inset shows three representative dimer conformations from the simulation. **d**, STM image of the hexamer on a graphite substrate showing that the extended molecules can undergo significant bending and distortion, despite the attractive interaction to the crystalline substrate. **e,f**, Linear dichroism experimental data (bars) and simulation results (filled circles). The same simulated data set as in excitation anisotropy (panels b,c) is considered. The experimental D histogram of the dimer is not well reproduced by the geometries extracted from the fit to excitation anisotropy (panel c), suggesting that the emissive region of the dimer is less bent than the absorbing unit. A simulation for an ideal linear dipole is shown for comparison (open circles). **g**, Assuming exciton localization on the less distorted unit of the two monomers making up the dimer, the measured distribution can be reproduced by the simulation (red filled circles). An example of such a localization process is illustrated in the inset on a molecular conformation employed in the simulation. Here, the emissive exciton is localized to the less distorted unit of the dimer, marked in red.

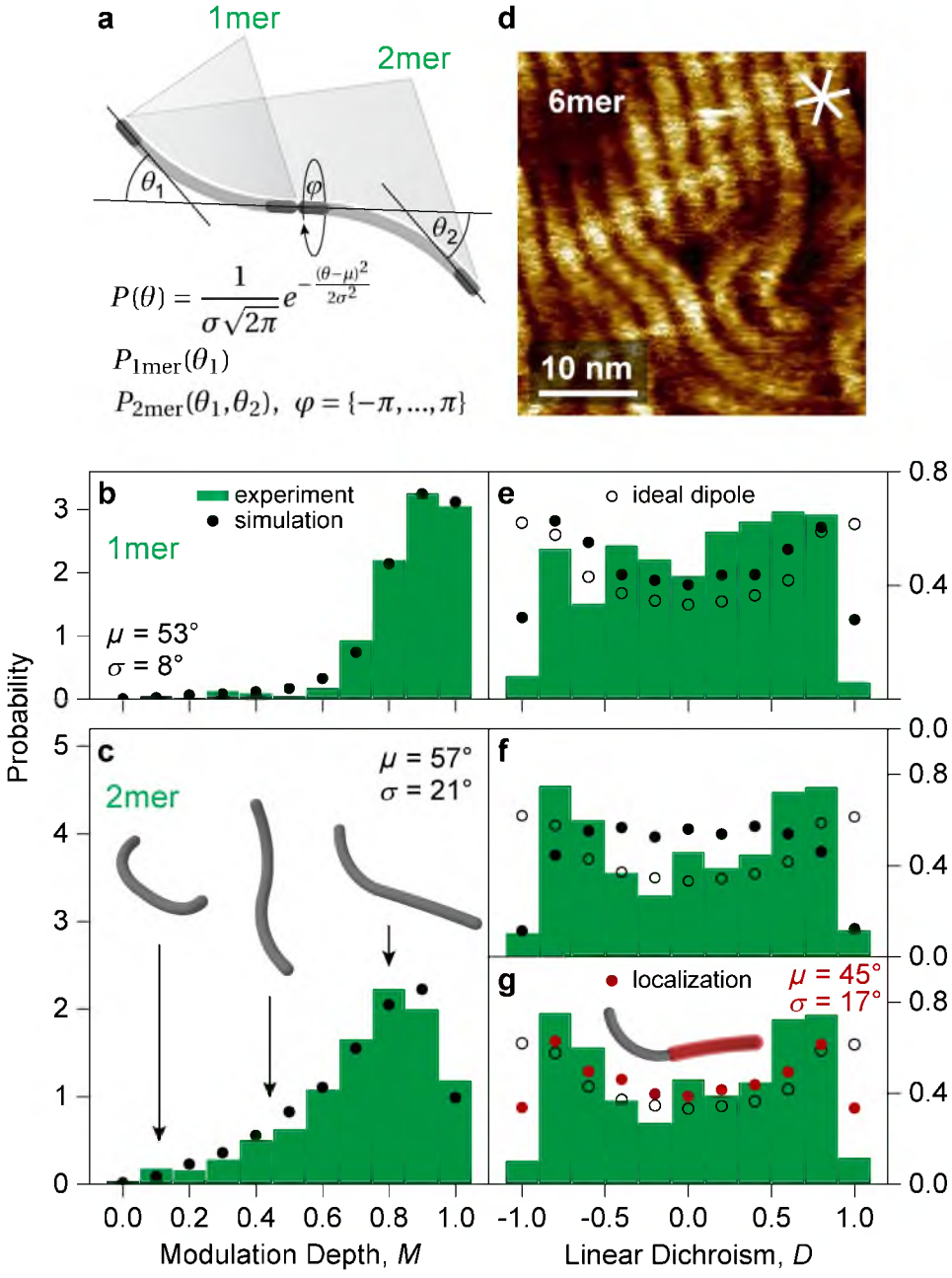
a
1mer
2mer
θ_1
φ
θ_2
$P(\theta) = \frac{1}{\sigma\sqrt{2\pi}} e^{-\frac{(\theta-\mu)^2}{2\sigma^2}}$
$P_{1mer}(\theta_1)$
$P_{2mer}(\theta_1, \theta_2),\ \varphi = \{-\pi, ..., \pi\}$
d
6mer
10 nm
b
experiment
simulation
1mer
μ = 53°
σ = 8°
e
ideal dipole
c
2mer
μ = 57°
σ = 21°
f
g
localization
μ = 45°
σ = 17°
Probability
Modulation Depth, M
Linear Dichroism, D

and dimer distributions yield very similar mean bending angle $\mu_{1\text{mer}} = 53°$ and $\mu_{2\text{mer}} = 57°$, respectively, as would be expected for identical building blocks. However, the full width of the dimer histogram was best reproduced with larger standard deviation of the bending angles for the dimer compared to the monomer ($\sigma_{2\text{mer}} = 21°$ vs. $\sigma_{1\text{mer}} = 8°$), indicating a more disordered system.

Three representative dimer conformations, incorporated in the simulated distributions, are sketched in Figure 4.5c. While these dimers appear to be strongly disformed, we note that similarly bent shapes are actually observed in scanning tunneling microscopy of the hexamer, shown in Figure 4.5d. This image was acquired on highly-oriented pyrolytic graphite substrate. Smaller molecules such as the dimer have a strong tendency for crystallization during the self-assembly on the substrate, so that such structural disorder cannot be observed for shorter chains. However, we opine that it is plausible that the dimer also experiences such bending similar to that seen in the hexamer when embedded in an amorphous polymer matrix as used in the single-molecule experiments.

Using the same sets of molecules we can compute the linear dichroism in emission, D, from the simulations, as shown in Figure 4.5e,f for the monomer and dimer, respectively. Without making any assumptions about localization, i.e., assuming that the emitting region of the molecule is identical to the absorbing region, we note that the measured D distribution of the monomer is much better reproduced by the simulation than the histogram of the dimer, even though the fits of the simulations to the M (absorption) values are of comparable quality. This deviation of the simulation of D values from measurement for the dimer provides evidence for a pronounced difference in the geometry of absorbing and emitting units. For comparison, the distribution of an ideal dipole is plotted (panel f, open circles), revealing a significant deviation from the situation of an ideal emitter in the case of the monomer.

We can estimate the effect of excited-state localization by assuming that the emissive unit is confined to the least-deformed region of a dimer molecule, as sketched in red in Figure 4.5g. This simple restriction drastically changes the shape of the simulated D histogram (red dots) calculated from the same set of simulated molecular conformations used in panels c) and f). The mean bending angle of the localization region ($\mu_{\text{loc}} = 45°$,

σ_{loc} = 17°) is substantially smaller than $\mu_{1\mathrm{mer}}$ and the shape of the histogram is very close to the case of an ideal dipole (open circles in Figure 4.4i). Our analysis follows simple geometrical arguments without taking into account nuclear relaxation in the molecular structure in the excited state [4]. Without considering such structural changes following excitation, our representation of localization is likely to underestimate the magnitude of spatial localization, but, nevertheless, offers a quantifiable estimate in terms of disorder parameters μ and σ. The result of the simulation reveals that before excitation, monomer units in the dimer are bent to a higher degree than in the monomer, while after excitation and consecutive structural reorganization they are bent less that in the monomer. However, the fact that we do not observe any change in ensemble polarization anisotropy (Figure 4.3c) on a timescale comparable to that of the dynamic red shift (Figure 4.3b) suggests that the structural relaxation in the excited state does not significantly contribute to a change of emission dipole orientation. Excited-state localization which gives rise to the marked difference between the single-molecule absorption and emission anisotropy histograms must therefore occur on sub-picosecond timescales [4].

4.4 Conclusions

We have investigated the extent of torsional motion and exciton self-trapping in π-conjugated model systems of different molecular shape. Steady state emission spectra from solutions of the dimer, hexamer and the closed ring indicate that the extent of the emissive unit is the same in all three systems. However, the emission peak of the dimer experiences a significant spectral red shift of $\sim$ 40 meV within $\sim$ 100 ps after excitation, which we attribute to torsional relaxation. This relaxation pathway is inhibited in the structurally rigid ring, while we speculate that torsional relaxation in the hexamer is heavily slowed down due to its large size. Single molecule polarization spectroscopy in excitation and emission helps us to estimate the degree of exciton self-trapping in our model systems. While the closed ring behaves almost like an isotropic emitter, because the exciton localizes dynamically on different parts of the ring [15], localization in the dimer leads to an emissive unit behaving almost as an ideal linear dipole. Monte Carlo simulations of excitation and absorption anisotropy histograms for the monomer and

the dimer suggest that in the dimer chromophores are more bent (μ_{2mer} = 57°) and disordered (σ_{2mer} = 21°) than in the monomer (μ_{1mer} = 53°, σ_{1mer} = 8°). However, after exciton localization the emissive unit in the dimer is less bent (μ_{loc} = 45°, σ_{loc} = 17°) than in the monomer, where exciton delocalization is limited by the smaller molecule size. Our custom made π-conjugated model systems allow us to differentiate between self-trapping due to nuclear reorganization and torsional relaxation involving motion of larger parts of the molecule. The comparison of ensemble and subensemble spectroscopy techniques in combination with model systems make potential candidates for investigations of polymer photophysics.

4.5 Methods

4.5.1 Synthesis of Model Materials

The synthesis and characterization of the oligomers, macrocycle and macrocycle precursor compounds is described elsewhere [15]. The spokes model system (red structure in Figure 4.1c was synthesized analogously to the macrocycle precursor molecule with the difference that instead of macrocycle rim segments, carbazole units were attached to the spokes in a Hartwig-Buchwald reaction [15].

4.5.2 Sample Preparation

All materials were stored and handled in an inert (nitrogen) atmosphere glovebox. Ensemble solutions were prepared by dissolving the model compounds in toluene (EMD Chemicals, OmniSolv) at concentrations of $\sim 10^{6} - 10^{7}$ mol/L. Single-molecule samples were prepared by dispersing the analytes in poly(methyl-methacrylate) (PMMA, M_w = 97 kDa, M_n = 46 kDa, PDI 2.1 from Sigma Aldrich Co.) on glass cover slips. The substrates were cleaned in a Hellmanex III (Hellma Analytics) MilliQ water solution (volume fraction 0.02), rinsed with MilliQ water and transferred in an UV-ozone cleaner (Novascan, PSD Pro Series UV) to oxidize residual organic contaminants. The analyte and PMMA were dissolved in toluene at concentrations of $\sim 10^{-12}$ mol/L and 1 g/L, respectively. The solution was dynamically spin-coated onto the glass cover slips at 2000 rpm resulting in film thicknesses of about 50 nm and an average analyte density of 40 molecules in an area of $50 \times 50\ \mu m^2$. Single-molecule samples were mounted on a microscope and measured under ambient conditions.

4.5.3 Wide-Field Polarized Excitation Fluorescence Microscopy

Wide-field fluorescence measurements were performed using an inverted microscope (Olympus IX71) with a 1.35 NA oil immersion objective (Olympus, UPLSAPO 60XO). A fiber-coupled diode laser (PicoQuant, LDH-C-405) operating in continuous wave mode at 405 nm was used as the excitation source. Laser fluorescence was removed from the excitation light by a narrow-pass filter (AHF analysis technology, HC Laser Clean-up MaxDiode 405/10) and a Glan-Thompson polarizer was used to provide linearly polarized excitation light. An electro-optical modulator (FastPulse Technology Inc., 3079-4PW) in combination with a $\lambda/4$ waveplate was used to rotate the polarization light [36]. Wide-field illumination over an area of $\sim 80 \times 80\ \mu m^2$ and an intensity of 100 mW/cm^2 on the sample was achieved by passing the laser beam through the back port of the microscope and a dichroic mirror (AHF analysis techniques RDC 405 nt) focused onto the back-focal plane of the objective. Sample emission was collected through the same objective and dichroic mirror, magnified 1.6× and detected with an EMCCD camera (Andor, iXon3 897). Scattered laser-light was removed with a fluorescence filter (AHF analysis techniques Edge Basic LP 405 long pass filter) prior to detection. Diffraction limited spots of single molecules covered $\sim 2 \times 2$ pixels at a resolution of $\sim$ 160 nm/pixel and an overall magnification of 96×.

Polarization modulation measurements were performed by rotating the excitation light in the x-y-plane by 180° at periods of 20 s. EMCCD images were recorded as a function of polarization angle. For the analysis, an area of $\sim 5 \times 5$ pixels for individual spots was integrated from which a local background of $\sim 13 \times 13$ pixels surrounding area was removed. Data analysis was performed using a home-written MATLAB code [37].

4.5.4 Linear Dichroism Measurements

Linear dichroism of single molecules was recorded with the same fluorescence microscope as described above for wide-field excitation and imaging, but a circularly polarized and collimated laser beam was coupled into the objective (Olympus, UPLSAPO 60XO). In order to find the analyte molecules, a fluorescence image of $\sim 20 \times 20\ \mu m^2$ (50 nm/pixel resolution) was recorded by stage scanning (Physik Instrumente, model P-527.3CL) at integration times of 2 ms/pixel. The excitation power of the diffraction limited spot was 50 nW at a wavelength of 405 nm. Spots with homogeneous fluorescence

intensity were manually selected and subsequently placed in the laser focus to record emission of single analyte molecules. The emission signal was split into two orthogonal polarization channels with a polarizing beam splitter (Thorlabs, CM1-PBS251). The signal was recorded with avalanche photodiodes (Picoquant, τ-SPAD-20) with a time-correlated single-photon counting module (Picoquant, HydraHarp 400). Automated experiment execution and data analysis was done with a home-written LabView program.

4.5.5 Time-Resolved Fluorescence Spectra and Transient Fluorescence Anisotropy

Time resolved measurements were performed using a Hamamatsu streak camera system comprising a spectrograph (Bruker 520IS, Bruker Corporation), a streaking unit (C5680, Hamamatsu Corporation) and an ORCA-ER CCD camera (C4742-95, Hamamatsu Corporation). The samples were excited using a frequency-doubled Ti:sapphire femtosecond laser system (HarmoniXX, APE GmbH and Chameleon Ultra II, Coherent Inc.), operating at 390 nm or 405 nm. Fluorescence anisotropy measurements were performed in an L-format configuration [25]. To account for the polarization-dependent instrument sensitivity an isotropic emission pattern was measured, generated with horizontally polarized excitation. All measurements were carried out on $\sim 10^{-6} - 10^{-7}$ mol/L solutions in 10 mm quartz cuvettes (Spectrosil Micro Fluorometer, Starna Cells Inc.). The maximal time resolution of the streak camera system was found to be 5.2 ps under excitation in the UV.

4.6 Acknowledgments

We are indebted to the Volkswagen Foundation for collaborative funding. AT acknowledges support from the University of Utah Graduate School.

4.7 References

[1] J. H. Burroughes et al., Nature **347**, 539 (1990).

[2] S. R. Forrest and M. E. Thompson, Chem. Rev. **107**, 923 (2007).

[3] J.-L. Brédas and J. R. Durrant, Acc. Chem. Res. **42**, 1689 (2009).

[4] S. Tretiak, A. Saxena, R. L. Martin, and A. R. Bishop, Phys. Rev. Lett. **89**, 097402 (2002).

[5] M.-H. Chang, M. Hoffmann, H. L. Anderson, and L. M. Herz, J. Am. Chem. Soc. **130**, 10171 (2008).

[6] S. I. Hintschich, F. B. Dias, and A. P. Monkman, Phys. Rev. B **74**, 045210 (2006).

[7] F. B. Dias et al., J. Chem. Phys **118**, 7119 (2003).

[8] D. Chaudhuri et al., Angew. Chem. Int. Ed. **52**, 13449 (2013).

[9] E. Collini and G. D. Scholes, Science **323**, 369 (2009).

[10] M. M.-L. Grage et al., J. Chem. Phys **118**, 7644 (2003).

[11] T. E. Dykstra et al., J. Phys. Chem. B **113**, 656 (2009).

[12] M. Hoffmann et al., Angew. Chem. Int. Ed. **47**, 4993 (2008).

[13] E. Mena-Osteritz, F. Zhang, G. Götz, P. Reineker, and P. Bäuerle, Beilstein J. Nanotechnol. **2**, 720 (2011).

[14] J. K. Sprafke et al., J. Am. Chem. Soc. **133**, 17262 (2011).

[15] A. V. Aggarwal et al., Nat. Chem. **5**, 964 (2013).

[16] J. M. Lupton, Adv. Mater. **22**, 1689 (2010).

[17] T. Adachi et al., J. Phys. Chem. B **116**, 9866 (2012).

[18] J. M. Lupton, ChemPhysChem **13**, 901 (2012).

[19] D. Mössinger et al., J. Am. Chem. Soc. **132**, 1410 (2010).

[20] S. Tretiak and S. Mukamel, Chem. Rev. **102**, 3171 (2002).

[21] R. E. Di Paolo et al., ChemPhysChem **8**, 2657 (2007).

[22] S. Westenhoff et al., Phys. Rev. Lett. **97**, 166804 (2006).

[23] P. Parkinson, C. Müiler, N. Stingelin, M. B. Johnston, and L. M. Herz, J. Phys. Chem. Lett. **1**, 2788 (2010).

[24] B. J. Schwartz, Annu. Rev. Phys. Chem. **54**, 141 (2003).

[25] J. R. Lakowicz, *Principles of Fluorescence Spectroscopy*, Kluwer Academic/Plenum, New York, 3rd edition, 2006.

[26] O. Varnavski, P. Bäuerle, and T. Goodson III, Opt. Lett. **32**, 3083 (2007).

[27] J. Clark, T. Nelson, S. Tretiak, G. Cirmi, and G. Lanzani, Nat. Phys. **8**, 225 (2012).

[28] A. Thiessen et al., PNAS **110**, E3550 (2013).

[29] D. Hu et al., Nature **405**, 1030 (2000).

[30] O. Mirzov et al., Small **5**, 1877 (2009).

[31] S. Tubasum, R. J. Cogdell, I. G. Scheblykin, and T. o. Pullerits, J. Phys. Chem. B **115**, 4963 (2011).

[32] T. Stangl et al., J. Am. Chem. Soc. **135**, 78 (2013).

[33] A. F. Fidler, V. P. Singh, P. D. Long, P. D. Dahlberg, and G. S. Engel, Nat. Commun. **5**, (2014).

[34] S. J. Greaves et al., J. Phys. Chem. A **110**, 2114 (2006).

[35] S. Toyota, Chem. Rev. **110**, 5398 (2010).

[36] D. A. Higgins, D. A. Vanden Bout, J. Kerimo, and P. F. Barbara, J. Phys. Chem. **100**, 13794 (1996).

[37] T. Adachi et al., J. Phys. Chem. C **114**, 20896 (2010).

CHAPTER 5

UNRAVELING THE CHROMOPHORIC DISORDER OF POLY(3-HEXYLTHIOPHENE)

Following studies on π-conjugated model systems with a known structure the focus is shifted to a disordered polymer material, poly(3-hexylthiophene) (P3HT), which is used extensively for photovoltaic applications. The polymer is well known to form well-ordered, crystalline regions in the bulk. In these regions, charge carrier mobility is higher than in the disordered material, which improves transport of charges in the photovoltaic device. In addition, the absorption spectrum of the bulk is extended to lower energies and aids in the collection of solar radiation. This observation poses the question of whether the modified electronic structure is intrinsic to the bulk or to the individual building blocks of the bulk, i.e., the single molecules. In this chapter, P3HT is investigated spectroscopically in the ensemble and on the single molecule level. Narrow optical transitions from individual polymer chains are identified over a wide spectral range. The emission energy from single molecules is shown to shift upon structural changes induced by the surrounding host matrix. This result suggests that the spectral breadth indeed originates from the structural disorder on the single molecule level.

This chapter is taken from a manuscript published online in 2013 in the *Journal Proceedings of the National Academy of Sciences of the United States of America* in volume 110 on pages E3550-6. The manuscript was coauthored by David Vanden Bout and John M. Lupton as well as Jan Vogelsang, Takuji Adachi and Florian Steiner who performed parts of the single molecule spectroscopy experiments. Subheadings for the text are inserted here for structural clarity and are not part of the published manuscript.

5.1 Significance

Ideal photovoltaic cells would be black, absorbing all of the sun's radiation, whereas nature's machinery for solar energy harvesting – photosynthesis – looks green. Organic semiconductor devices, based on molecular building blocks, lie conceptionally between the extremes of inorganic and photosynthetic light harvesting. How can organic solar cells appear almost black if they are based on molecular units? Using single-molecule spectroscopy, we identify the fundamental electronic building blocks of organic solar cells and reveal that discrete molecule-like transitions scatter over the entire visible spectrum. The fundamental molecular unit is narrowband, but disorder induces a continuum reminiscent of that characterizing highly ordered inorganic crystals.

5.2 Abstract

The spectral breadth of conjugated polymers gives these materials a clear advantage over other molecular compounds for organic photovoltaic applications and is a key factor in recent efficiencies topping 10%. However, why do excitonic transitions, which are inherently narrow, lead to absorption over such a broad range of wavelengths in the first place? Using single-molecule spectroscopy, we address this fundamental question in a model material, poly(3-hexylthiophene). Narrow zero-phonon lines from single chromophores are found to scatter over 200 nm, an unprecedented inhomogeneous broadening that maps the ensemble. The giant red shift between solution and bulk films arises from energy transfer to the lowest-energy chromophores in collapsed polymer chains that adopt a highly ordered morphology. We propose that the extreme energetic disorder of chromophores is structural in origin. This structural disorder on the single-chromophore level may actually enable the high degree of polymer chain ordering found in bulk films: both structural order and disorder are crucial to materials physics in devices.

5.3 Introduction

Despite half a century of research into organic photovoltaics [1], the promise of versatile paint-on solar-cell modules based on conjugated polymers has prompted a present flurry of activity in the field [2–5]. A particular appeal of such excitonic solar cells is that very little material is needed to efficiently absorb light. This is due to the fact that the os-

cillator strength of primary photoexcitations, electron-hole pairs with binding energies far exceeding kT, is focused in the excitonic transition. The obvious downside is that this concentration also means excitonic transitions are inherently narrow and usually offer only mediocre spectral overlap with the broad solar spectrum. How, then, can excitonic solar cells be designed with appropriate spectral breadth? Merely introducing energetic disorder in the underlying excitonic material should lead to low-energy traps, impeding charge harvesting.

Although the optical and electronic properties of conjugated polymers are not perfectly suited to photovoltaics, their absorption spectra are surprisingly broad despite the excitonic nature of the transitions. Moreover, the diversity in functional characteristics revealed by varying processing conditions has fueled the quest to formulate robust structure-property relationships between the electronic and optical properties and the underlying polymer structure [6–12]. Polythiophene derivatives have evolved into one of the chosen workhorse materials for solar-cell research [13, 14]. Early spectroscopic studies established extraordinary solvatochromic and thermochromic characteristics, which were attributed to large conformational changes in response to the immediate environment [15–17]. It is little surprise then that such diversity in device characteristics exists when using these materials [4]. Poly(3-hexylthiophene) (P3HT) (structure shown in Figure 5.1a) and related compounds were the first polymeric materials to exhibit signatures of two-dimensional electronic delocalization [18] due to a high level of interchain ordering most clearly visualized in X-ray diffractometry [19]. Despite this ordering, the optical absorption remains extremely broad, rendering the material favorable for photovoltaics. The striking dependence of P3HT ensemble optical properties on processing conditions has led to proposals that substantial dimerizing interchain interactions [20–23] could be involved. However, the signatures of excitonic dimerization, or H-aggregation, are not always straightforward to resolve conclusively [24]. H-aggregation should lead to a reduction in radiative rate [25]. Typically, upon aggregation of P3HT, a strong decrease in fluorescence quantum yield is observed, but this is accompanied by an increase in fluorescence rate [26] because nonradiative decay rates are also enhanced. It is not always trivial to distinguish an increase in nonradiative decay from deceleration of radiative decay, complicating a precise determination of transition oscillator strengths. For this

reason, most of the focus to date has been on interpreting spectral shape and vibronic coupling [23]. Although the origin of the magnitude of spectral shift between isolated and bulk-packed chains has been simply assigned to a "crystal shift" [23], a high degree of interchain ordering should also imply substantial planarization of the polymer with the associated increase in conjugation length [27] – which in turn decreases the strength of dipolar coupling that could lead to dimerization as the excited state becomes more delocalized [21].

Conclusively discriminating interchain from intrachain order is only possible by resorting to subensemble techniques such as single-molecule spectroscopy [28–35]. Here, we demonstrate the feasibility of reconciling fundamental spectroscopy of P3HT, shown in this study to be the most heterogeneous polymeric material studied to date on the single-chromophore level, with the excitonic single-chromophore picture [36–38] established for the most ordered polymers such as polyfluorenes [39] (PF), ladder-type poly(para-phenylenes) [40, 41] (LPPP), polydiacetylene [42, 43] (PDA), and poly(phenylene-ethynylene) [28] (PPE). On the level of single chromophores, P3HT behaves like other prominent materials, such as poly(phenylene-vinylenes) [41, 44] (PPVs), with the exception of exhibiting giant variability in transition wavelengths spanning almost 200 nm. The dominant photophysics of the ensemble – the striking red shift between solution and film photoluminescence (PL) – is controlled by energy transfer to low energy intrachain chromophores, in absence of the previously proposed "crystal shift" [23].

5.4 Results

5.4.1 Comparison of Ensemble and Single-Chromophore Spectroscopy

Nominally different conjugated polymer materials exhibit very similar spectral characteristics on the single-chromophore level [28]. Because long polymer chains can contain many chromophores [40], it is not always straightforward to ensure that a single chromophore is identified within the polymer. Comparison with oligomeric model compounds, use of narrow-band excitation, and cryogenic cooling of the sample have, however, enabled a reproducible framework for the identification of single chromophores [40]. We begin by comparing the ensemble PL spectra of P3HT in dilute toluene solution (10^{-4} mM) and in a drop-cast bulk film in Figure 5.1a.

Figure 5.1. Unraveling the spectral heterogeneity of P3HT using low-temperature single-molecule spectroscopy. **a**, Comparison of P3HT PL spectra in dilute toluene solution (green) and in a drop-cast bulk film (red) at room temperature. Six representative low-temperature (4 K) single-molecule spectra (gray), consisting of a zero-phonon line and a vibronic progression, are shown as examples, spanning the spectral region from dilute solution to bulk film. **b**, Normalized PL spectra of 115 single molecules, sorted by the peak energy of the 0-0 transition. The same 0-1 vibronic transition, shifted by 180 meV from the main peak, is seen for all spectra (lower). **c**, Correlation of 0-0 peak width with transition energy. The green circles represent averages over eight molecules, and the red line is a guide to the eye. **d**, The intensity of the vibronic peak does not depend on chromophore transition energy.

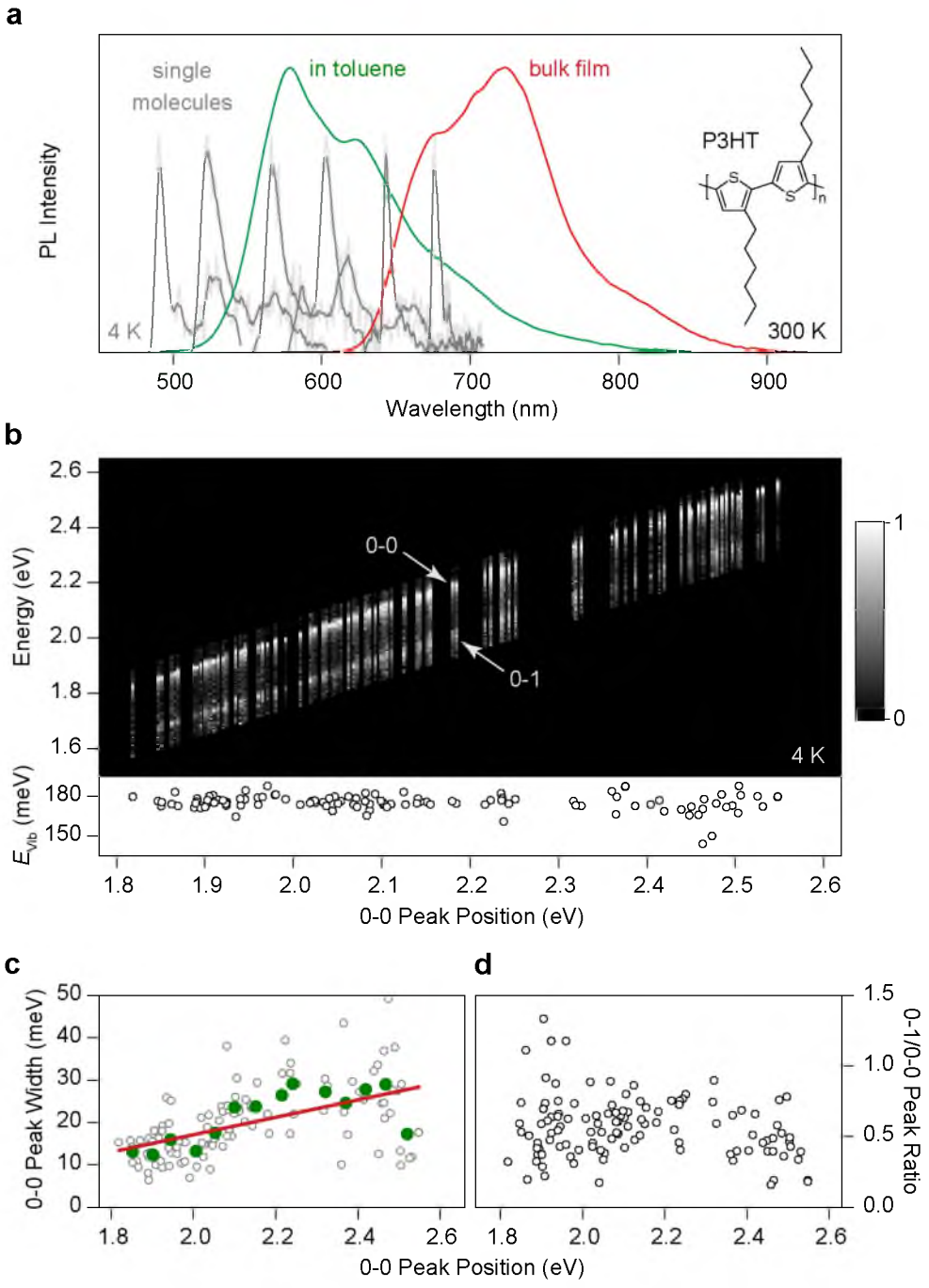
a
single molecules
in toluene
bulk film
P3HT
PL Intensity
4 K
300 K
500
600
700
800
900
Wavelength (nm)
b
Energy (eV)
0-0
0-1
4 K
1
0
E_{Vib} (meV)
180
150
1.8
1.9
2.0
2.1
2.2
2.3
2.4
2.5
2.6
0-0 Peak Position (eV)
c
0-0 Peak Width (meV)
d
0-1/0-0 Peak Ratio
0-0 Peak Position (eV)

Going from solution to the solid phase shifts the spectrum by over 100 nm (0.4 eV) to the red and modifies the spectral form. The bulk spectrum has been interpreted to show a shift of oscillator strength from the 0-0 to the 0-1 transition, assigned to H-aggregation [22], because bulk phase P3HT exhibits a high level of structural ordering in electron microscopy [5], scanning-probe microscopy [45], and other elastic scattering techniques [11, 46, 47]. The large spectral shift between solution and bulk has been assigned to the occurrence of a crystal shift in the H-aggregated chromophores embedded in an ordered environment of many other conjugated polymer chains [23]. Such a large spectral shift between solution and film is not observed in other common conjugated polymers. Six representative single-chromophore spectra, recorded at 4 K from isolated chains directly deposited from toluene onto a SiO_2 surface, are superimposed on the ensemble spectrum in gray. The single-chromophore spectra all have the same shape, a comparatively narrow asymmetric zero-phonon line with a low-energy acoustic phonon wing and a distinct vibronic band offset by 180 meV. The reduction of disorder broadening on the single-chromophore level facilitates determination of vibronic frequencies compared with the ensemble. The observed vibronics can be assigned to the ring C-C stretch (171 meV) and the symmetric C=C stretch modes (179 meV) [48]. The single-chromophore spectra, obtained under excitation at 458 nm, span a spectral range of 195 nm (0.8 eV). In the red-most spectrum, excitation and emission are separated by 0.9 eV, and yet the same universal [41], narrow single-chromophore spectral shape is observed.

To highlight the universality of chromophores, we plot 115 spectra in Figure 5.1b, sorted by 0-0 peak energy (see Section 5.9 for alternative forms of presenting the data). Including the vibronic progression, narrow spectral lines are found between 485 and 775 nm. The general spectral characteristics, in particular the energy of the dominant vibronic plotted beneath, remain unchanged regardless of peak energy. The distribution of peak positions is discussed in Section 5.9 and appears to be trimodal (see the discussion in Supporting Information text for possible origins of this distribution).

Interestingly, the 0-0 peak narrows slightly with decreasing energy, as plotted in Figure 5.1c. Such spectral narrowing is seen in PF [28] and PDA [49], where lower-energy transitions correspond to improved chain ordering (the formation of the β-phase in

PF). The opposite is seen in PPV [50], where chain bending induces a red shift and an increase in spectral jitter. Over the entire range of chromophore energies, the ratio between 0-0 and 0-1 PL peak intensities scatters substantially but does not vary systematically with transition energy (Figure 5.1d). Strong variations in the PL intensity of the vibronic progression between single chromophores have been reported previously, even in nominally rigid materials such as LPPP [51]. Such variations arise due to the slight distribution in ground-state molecular conformations, leading to differing structural relaxation energies and the resulting changes in the Franck-Condon progression, which become visible precisely because electronic and vibronic transitions are so narrow at low temperature. Examples of the interchromophoric scatter in 0-0/0-1 peak ratio are given in Section 5.9.

The single-chromophore PL spectra are identical in shape to that of different conjugated polymers [28] such as LPPP, PPV, PDA, PPE, and PF are discussed in Section 5.9, and exhibit the common blinking and spectral diffusion (spectral jitter). This similarity in spectral form strongly suggests that the narrow lines observed over such a broad spectral range arise from isolated chromophores [38]. Because narrow single-chromophore zero-phonon lines are observed as far to the red as 680 nm, we conclude that the high-energy side of the bulk spectrum (Figure 5.1a, red curve) is appropriately described by the presence of isolated rather than aggregated chromophores: the red shift of over 100 nm between solution and film can be mostly attributed to energy transfer from high-energy to low-energy chromophores. This conclusion, however, does not exclude the possibility of H-aggregate emission contributing to the red tail of the bulk PL spectrum. We stress that single-chromophore spectroscopy, by its very definition, probes only the emission from single chromophores; we cannot probe potential H-aggregate emission without resorting to well-defined dimer structures [52].

5.4.2 Difference in Polymer Chain Conformation Between Solution and Bulk Phase

Why do different chromophores dominate ensemble solution and bulk film spectra (Figure 5.1a)? The fundamental difference between the two cases is found in the underlying chain conformation, which can be controlled through the polarity of the immediate environment of the polymer [30]: a “good” solvent, or matrix, will lead to optimal

chain extension, driving the formation of well-solvated yet disordered spheres or globules. In contrast, a "poor" solvent promotes collapse of the polymer into toroidal or rod-like structures [29]. Solvent quality for nonpolar organic compounds like conjugated polymers generally decreases with increasing polarity of the solvent. This effect can be replicated in the solid state for single chains of P3HT by embedding them in different polymer matrices. Figure 5.2a compares dilute (10^{-4} mM, 100 times the concentration used in single-molecule experiments) solid solutions of P3HT in a virtually nonpolar Zeonex derivative (Zeonex 480) and in poly(methyl-methacrylate) (PMMA), which is more polar. The spectrum of P3HT embedded in Zeonex (green) closely resembles that of toluene solution, whereas the spectrum of P3HT embedded in PMMA (red) matches the peak and red tail of bulk P3HT. The mismatch in spectra at higher energy likely arises due to the presence of incompletely folded (i.e., blue-emitting) chains in PMMA. The effect of solvation is demonstrated influorescence micrographs of the films in Figure 5.2b. The P3HT/Zeonex film appears uniform in emission, whereas the P3HT/PMMA film shows discrete bright spots. Both images are displayed on the same intensity scale. In the P3HT/PMMA film, the background is darker than in P3HT/Zeonex, but the spots are much brighter. The formation of bright spots in PMMA suggests that multiple chains can aggregate together. In the following, we demonstrate that even single isolated chains in PMMA collapse into ordered structures.

Figure 5.3 reports measurements of the fluorescence modulation of single chains at room temperature under rotation of the polarization angle, θ, of the exciting laser within the sample plane. For a straight object, the overall transition dipole should lie along the axis of the π-orbitals, leading to a strong cosine-squared modulation of PL with laser polarization [29]. Such a modulation in intensity is sketched in Figure 5.3a. The depth of modulation, $M = (I_{\max} - I_{\min})/(I_{\max} + I_{\min})$, provides information on the degree of order regarding the transition dipoles of an individual chain. Examples of measurements are shown in Section 5.9. Figure 5.3b compares histograms for 738 single chains in Zeonex and 587 chains in PMMA. Whereas the PL excitation (i.e., absorption) of the molecules in Zeonex is mostly weakly polarized due to disorder, P3HT in PMMA [31] is predominantly ordered with M peaking around 0.8. Based on these M values, possible chain conformations are sketched at the top of Figure 5.4.

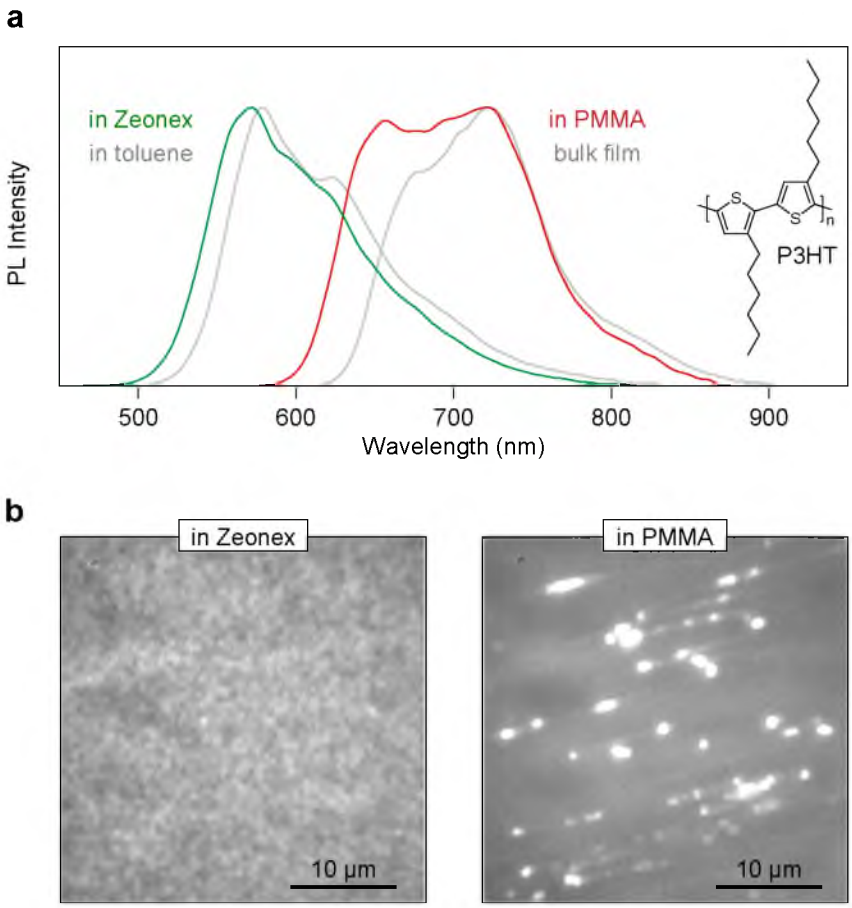

Figure 5.2. Replicating bulk and solution spectra in dilute matrix environments at room temperature. **a**, The ensemble spectrum of chains dispersed in the inert Zeonex matrix (green) closely matches that of isolated chains in toluene (gray). In contrast, PMMA leads to chain aggregation: the spectrum of P3HT diluted in PMMA at the same concentration as in Zeonex (red) resembles the bulk film emission (gray). In both cases, the concentration of P3HT is 100 times higher than in single-molecule experiments. **b**, The effect of matrix induced phase separation is visible in fluorescence micrographs of the spincoated films, plotted on the same intensity scale. In Zeonex, the film PL appears uniform, whereas in PMMA bright spots are seen corresponding to the formation of large multichain aggregates.

5.4.3 Chromophoric Emission at Room Temperature

Intrachain conformation should have a dramatic impact on single-chain photophysics: in the random-coil structure, the chromophores will couple only weakly to each other, effectively emitting independently. In the ordered structures, energy transfer should occur between chromophores because interchromophoric distances are reduced. Two distinct experiments in Figure 5.4 clearly demonstrate this interplay between conformation and photophysics. The insets in Figure 5.4a show two representative single-

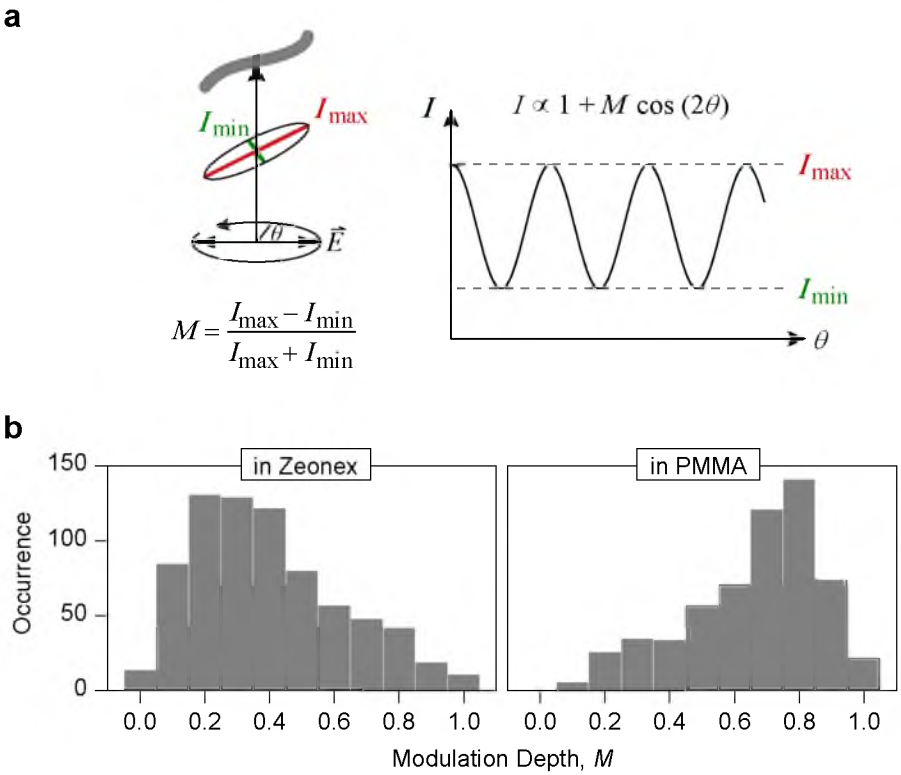

Figure 5.3. Shape dependence of single P3HT chains on matrix material at room temperature. **a**, The modulation of PL intensity under rotation of the plane of polarization of the exciting laser is recorded. The modulation depth M provides a measure of chain extension and order: chains that mix well with the matrix (i.e., are well solvated) form random-coil structures that absorb any polarization of light. Poorly solvated chains, however, collapse, leading to ordered anisotropic rod-like structures. **b**, Histogram of M values for single chains in Zeonex and PMMA. In Zeonex, isotropic structures are formed, whereas PMMA gives rise to highly anisotropic arrangements of the chains.

molecule spectra at room temperature, measured in Zeonex and PMMA, which closely resemble the ensemble (Figure 5.2a) for the solvated and collapsed structures, respectively. Figure 5.4a displays the PL intensity of a single chain as a function of time. The fluorescence beam is separated into two paths by a polarizing beam splitter and recorded with two separate photodiodes, allowing us to identify any change in orientation of the emissive transition dipole by quantifying the linear dichroism D as defined in the schematic. An ensemble of different dipole orientations will lead to $D \sim 0$, as will a single dipole coincidentally oriented at 45° with respect to both detectors. The example P3HT chain in Zeonex is approximately five times brighter than in PMMA, but exhibits strong fluctuations and a gradual overall decrease in intensity (bleaching). The emission

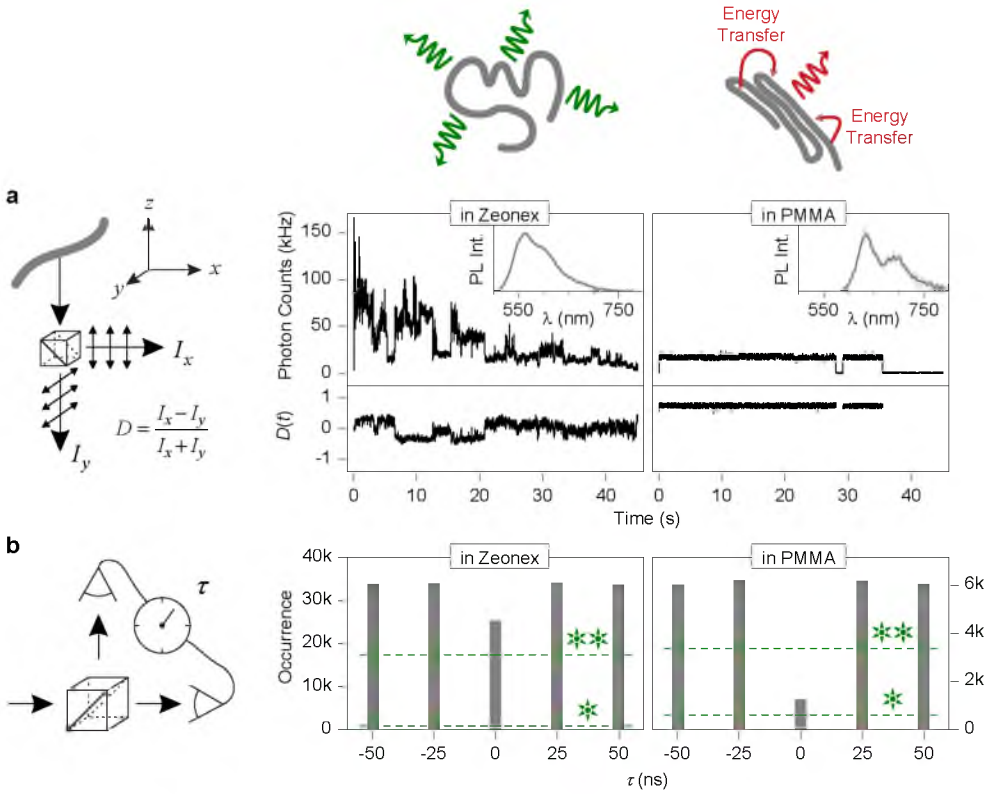

Figure 5.4. Excited-state properties of solvated (Zeonex) and collapsed (PMMA) single P3HT chains at room temperature. In solvated chains, the chromophores emit independently of each other (cartoon). In collapsed chains, energy transfer occurs to the lowest-energy chromophore. **a**, Fluorescence intensity and linear dichroism D, determined by splitting the emission into two orthogonal polarization components as illustrated in the image. In Zeonex, multistep blinking is observed. The emission is only weakly polarized ($D \sim 0$), exhibiting slight fluctuations as different chromophores switch on and off. In the PMMA collapsed-chain configuration, the fluorescence intensity is constant and shows single-step blinking. The emission is strongly polarized ($D \neq 0$) with no fluctuations. Representative single-chain PL spectra are shown in the inset. **b**, Photon statistics in emission, given by the cross-correlation of two photodetectors in the emission pathway. The molecules are excited by laser pulses (25-ns period), controlling photon arrival times τ. In Zeonex, multiple chromophores emit, leading to only a 20% dip in photodetector coincidence rates. In PMMA, a dip in coincidence rate by 80% is observed, because no more than one single photon is emitted for each laser pulse. Based on photon counts and background signal for the two cases, the maximum dip expected for a perfect single-photon or two-photon source is indicated by the dashed lines.

intensity does not drop completely to zero. In contrast, in PMMA, discrete blinking is observed. In Zeonex, the linear dichroism fluctuates around zero, exhibiting small jumps, which imply the involvement of multiple different chromophore emitters. In contrast, in the PMMA example, a high static D is found: either all dipoles are oriented along the same axis or only one single chromophore in the polymer is active at once. The first conclusion is inferred from the excitation polarization modulation in Figure 5.3b. Below, we demonstrate that indeed only one chromophore emits at a time from the single chain.

The number of multiple chromophores involved in the emission can be quantified by photon statistics obtained using a crosscorrelation between photodiodes detecting the fluorescence divided into two pathways with a (nonpolarizing) beam splitter (Figure 5.4b) [53–55]. Fluorescence is excited by a pulsed laser (488 nm) with a period of 25 ns. If only one photon is emitted by the molecule per laser pulse, it cannot be simultaneously picked up by both detectors. Therefore, for single emitters, the cross-correlation must drop to zero at zero delay τ between detector signals, a phenomenon known as photon antibunching. Because such cross-correlation analysis requires high photon counts, we average [53] over 80 and 30 single molecules for PMMA and Zeonex, respectively. In Zeonex, the cross-correlation signal at $\tau = 0$ is nearly identical to that at other delays, implying that, on average, multiple chromophores on the polymer emit at once and do not couple efficiently. In PMMA, the cross-correlation at $\tau = 0$ drops to 20% of coincidence photon counts compared with $\tau \neq 0$, implying predominant single-chromophore emission. Given the large number of chromophores on a chain, this phenomenon must result from energy transfer to the lowest-energy chromophore and concurrent singlet-singlet annihilation in the multichromophoric assembly [56].

5.5 Discussion

Cryogenic single-chain spectroscopy of P3HT reveals clear signatures of discrete intrachain chromophores. The diversity of spectral characteristics found in the ensemble when going from isolated to aggregated chains originates from these chromophores. Universal single-chromophore spectra, comparable in shape to those observed in many other materials, scatter over almost 200 nm, providing a measure of the level of inter-

chromophoric inhomogeneous broadening of ~ 0.8 eV, greatly exceeding prior estimates [23]. In comparison, the corresponding disorder extracted from identical experiments for LPPP is 0.03 and 0.2 eV for PPV [41]. Such a level of energetic disorder as found in P3HT is unprecedented in molecular emitters, and there is no immediately obvious explanation for this scatter based on conventional models of conjugation in P3HT [57].

Ensemble P3HT shows a large spectral shift upon going from dilute solution to the bulkfilm (Figure 5.1a). Because the transition between solution and film probes such a broad spectral range, intermediate states have been generated by means of solventvapor annealing to optimize both absorption and charge transport in solar cells [3, 8]. Despite this heterogeneity of ensemble P3HT, key elements of the bulk photophysics [22, 23] are consistent with the formation of discrete intrachain chromophores. We stress, however, that bulk spectral emission features extending beyond 700 nm may be associated with H-aggregation or charge-transfer phenomena [1], which would only arise in the bulk and cannot be probed readily by single-molecule techniques. Notable examples of spectral characteristics of bulk PL that we cannot probe here are the monotonic changes of spectral shape with temperature [23], and the evolution of the vibronic progression and temporal red shift in time-resolved PL [58]. These features can both be modeled with the H-aggregate picture [23].

The same universal spectral features are observed independent of energetic separation between excitation and emission. Ultrafast dissipation of excitation energy in P3HT has previously been concluded from photon-echo spectroscopy and was attributed to efficient coupling to vibrations [59]. However, the dissipation of 0.9 eV, the difference between excitation at 458 nm and emission at 680 nm, would require five quanta of the dominant vibration, which seems implausible. Because the emission intensity of all chromophores is comparable, we conclude that each chain most likely has very similar absorbing chromophores (presumably short conjugated units), which then populate the emissive chromophore by energy transfer. We note that when only one chromophore is present on a polymer chain, such as in β-phase PF, absorption and emission spectra exhibit the expected near-perfect mirror symmetry [39]. Even though multiple chromophores must exist on single P3HT chains, it is reasonable to assume that each single chromophore identified in Figure 5.1 by its emission also has a complementary spe-

cific mirror-symmetric absorbing feature [39]. The coexistence of short and long chromophores within a single polymer chain, distinguished by their transition energy and vibronic coupling strength, has been demonstrated previously in polyindenofluorene using single-chain light-harvesting action spectroscopy [60].

Intuitively, one may be inclined to speculate that the most extended chromophores are also the lowest-energy units. However, slight bending of the backbone, chain torsion, and changes in bond alternation can mask a strict correlation between conjugation length and lowering of the optical gap [50]. Semiempirical calculations have suggested that even substantial bending of the π-system in polythiophene need not necessarily disrupt conjugation [57]. Given the high degree of ordering of single-chain P3HT seen in polarization fluorescence modulation (Figure 5.3), it is tempting to surmise that, in these objects, the π-system is also the most extended [27]. However, the fact that the vibronic progression does not depend systematically on transition wavelength is crucial (Figure 5.1d). In PDA, for example, the most extended chains show a dramatic increase of 0-0 transition oscillator strength relative to the 0-1 peak at low temperature, because the extended π-system constitutes an effective linear J-aggregate [43]. It is conceivable that exciton self-trapping limits excitonic coherence and thus the transfer of oscillator strength to the purely electronic (0-0) transition. Such an effect has been suggested for β-phase PF [39], which also shows substantial vibronic coupling in near-perfectly extended chains under cryogenic conditions, in contrast to PDA. It is also conceivable that the broad energetic distribution of zero-phonon lines (Figure 5.1b) arises from an intrinsic Stark shift due to trapped charges [61]. However, in this case a correlation should exist between increased red shift and increased line width [62], which is not observed; the line width appears to decrease with decreasing transition energy.

The most red-emitting single chromophores (Figure 5.1) constitute the monomolecular precursor states for the red species in bulk P3HT films. Emission in the bulk occurs preferentially from these species, populated by energy transfer provided the polymer chain is sufficiently collapsed and ordered, as is the case in PMMA matrices or in the bulk. In this regard, P3HT behaves like many other conjugated polymers, such as poly[2-methoxy-5-(2'-ethylhexyloxy)-*p*-phenylene vinylene] (MEH-PPV) [63, 64], with the fundamental difference that interchromophoric energetic disorder is at least twice as large.

As more and more chains pack together, the quantum yield of fluorescence of the mesoscopic objects within the bulk film is reduced because the probability of exciton dissociation and charge formation increases with greater average exciton migration distances [24, 33]. Although we have identified isolated chromophores that emit at wavelengths of ~ 680 nm, a further red shift with respect to this purely chromophoric transition observed in bulk films may arise due to the previously described phenomenon of weak H-aggregation [22], due to a Stark effect resulting from the electric field emanating from local trapped charges [65], or from solid-state solvatochromic effects [1]. Finally, we note that it is both the conformation of the overall chain that changes with polarity (matrix) as well as the energetic distribution of chromophores that are responsible for such broad spectral variability. Nanoscale conformation therefore also affects ensemble absorption, enabling the tuning of absorption spectrum by solvent-vapor annealing [3, 8].

The most obvious origin of the energetic spread in universal single-chromophore spectra lies in structural variations between single chromophores. We conclude that single chromophores are both flexible and can adopt a wide range of subtly varying conformations: structural and energetic disorder dominates on the single-chromophore level. In contrast, in bulk films, an extraordinary high degree of order can be reached [19]. We propose that this unique feature of P3HT arises directly from the disorder on the single-chromophore level: as chains fold back on themselves or aggregate with other chains, there are always suitably shaped chromophores present so that a closely packed structure can be formed. It is conceivable that disorder on the single-chromophore level could actually breed order in the bulk.

P3HT constitutes one of the most heterogeneous material systems explored in the context of organic electronics, which, besides some of the impressive device characteristics [14], accounts for its continuing popularity in the field [13]. Nevertheless, conventional incremental materials development risks being impeded by lack of a robust understanding of primary photoexcitations in these systems. Is the primary photophysics of polythiophenes dominated by intermolecular interactions and H-aggregate species, or does the material actually adhere to the established concepts [36, 38, 41] of intrachain chromophores as derived from a wide range of compounds? Our single-molecule experiments tend to favor the latter notion, while leaving room for features of

H-aggregation or other bulk solvation effects in the red tail of the emission spectrum. In contrast to all polymeric materials studied previously, the energetic heterogeneity of chromophoric transitions spans almost 1 eV, i.e., much of the visible spectrum. Such a breadth of possible fundamental transition energies can only be accounted for by an extreme sensitivity of electronic structure to conformational variations, which explains the dramatic impact processing conditions have on bulk material properties [3, 8].

5.6 Methods

P3HT (regio-regularity, 95.7%; weight average molecular weight, 65.2 kDa; polydispersity index, 2.2) was purchased from EMD Chemicals and used as received. PMMA (weight average molecular weight = 96.7 kDa; number average molecular weight, 47.7 kDa) and Zeonex (Zeonex 480) were obtained from Sigma-Aldrich and Zeon Europe, respectively. Low-temperature single-molecule spectroscopy was carried out in a home-built fluorescence microscope as described previously [28]. The fluorescence was excited at 458 nm using a frequency-doubled Ti:sapphire femtosecond laser system (HarmoniXX, APE; and Chameleon Ultra II, Coherent). To minimize contamination of the weak fluorescence signal by background luminescence, single-chromophore spectra were recorded from samples deposited, without a polymer matrix, directly on top of SiO_2-covered Si wafers. The wafers were mounted in a liquid-helium cold-finger cryostat at 4 K under vacuum. Concentration series were performed to ensure that the single-molecule density varied as expected with solution concentration. Due to the low photon count rates, all experiments were carried out in spectral imaging mode [i.e., resolving the fluorescence spectrum [28]] rather than under direct two-dimensional imaging. This approach ensured that the observed fluorescence really did originate from single P3HT chains.

Room temperature fluorescence was recorded on a separate microscope setup based on an Olympus IX71. P3HT chains were embedded in a PMMA or Zeonex 480 host matrix according to a previously described procedure (65): (i) Borosilicate glass coverslips were cleaned in a 2% (vol/vol) Hellmanex III (Hellma Analytics) solution, followed by rinsing with MilliQ water. (ii) The glass coverslips were additionally bleached by a UV-ozone cleaner (Novascan; PSD Pro Series UV). (iii) The P3HT was diluted in toluene to single-molecule concentration ($\sim 10^{-12}$ to 10^{-13} M) and mixed with a 6% PMMA

or Zeonex 480/toluene solution. (iv) This solution was dynamically spin-coated in a nitrogen glove box at 2,000 rpm onto the glass coverslips, leading to a film thickness of $\sim 200-300$ nm with an average P3HT chain density of ~ 20 individual P3HT chains in a range of 50×50 μm^2. The sample was incorporated into a home-built gas flow cell and purged with nitrogen to prevent bleaching by oxygen. Excitation was carried out by a fiber-coupled diode laser (PicoQuant; LDH-D-C-485) at 485 nm under continuous-wave excitation for wide-field fluorescence microscopy or under pulsed excitation with a repetition rate of 40 MHz for confocal fluorescence microscopy and time-correlated single-photon counting. The excitation light was passed through a clean-up filter (AHF Analysentechnik; z485/10), expanded, and focused (or collimated) via a lens system onto the back focal plane of a 1.35 N.A. oil immersion objective (Olympus; UPLSAPO 60XO) through the back port of the microscope and a dichroic mirror (AHF Analysentechnik; z488RDC) for wide-field or confocal excitation. For wide-field microscopy, the fluorescence signal was imaged on an EMCCD camera (Andor; iXon 897) after an additional magnification of 1.6× and after passing a fluorescence filter (AHF Analysentechnik; RS488LP), whereas for confocal measurements, the fluorescence signal was split either by a polarizing beam splitter (Thorlabs; CM1-PBS251) into two orthogonal polarizing detection channels or by a 50/50 beam splitter and detected by two avalanche photodiodes (PicoQuant;τ-SPAD-20). The excitation intensities were set to ~ 1.5 and 150 W/cm^2 for wide-field and confocal excitation, respectively. The polarization rotation of the excitation beam, confocal detection, and photon statistics analysis were carried out as described previously [65]. For the antibunching measurements, we averaged the fluorescence traces of 80 single chains in PMMA and 30 single chains in Zeonex, respectively [53]. By considering the count rate, photodetector dark counts and the background intensity, we estimate the expected magnitude of the antibunching dip for a perfect single emitter as 10% and 2.5% for P3HT/PMMA and P3HT/Zeonex, respectively. These thresholds are indicated as dashed lines in Figure 5.4b.

5.7 Acknowledgment

We thank D. Lidzey and G. Khalil for helpful discussions. J.M.L. is indebted to The David and Lucile Packard Foundation for providing a fellowship. A.T. acknowledges the

Fonds der Chemischen Industrie for a Chemiefonds fellowship. D.V.B. acknowledges support from an Energy Frontier Research Center funded by the U.S. Department of Energy under Award Number DE-SC0001091. This work was partially funded by the European Research Council Starting Grant MolMesON (Grant 305020).

5.8 Author Contributions

J.V. and J.M.L. designed research; A.T., J.V., T.A., and F.S. performed research; J.V. and F.S. analyzed data; and A.T., J.V., T.A., D.V.B., and J.M.L. wrote the paper.

5.9 Supporting Information

5.9.1 Universal Single-Chromophore Transitions

Figure 5.5 plots the 115 single-chromophore spectra from Figure 5.1b in a waterfall representation (Figure 5.1a), and with all spectra normalized and shifted to a common origin (inset). The spectra are coded from red to blue, corresponding to low and high transition energy. Figure 5.5b-d show representative single-chromophore transitions from poly[2-methoxy-5-(2'-ethylhexyloxy)-*p*-phenylene vinylene] (MEH-PPV) [66], ladder-type poly(*para*-phenylene) [66], and β-phase polyfluorene [67], shifted along the x axis to the same origin. The transition characteristics of single chromophores in these very different materials are universal [66].

5.9.2 Histogram of Single-Chromophore Peak Positions

Figure 5.6 plots the histogram of peak positions of the 115 single-chromophore spectra reported in Figure 5.1b. Note that this histogram is in no way weighted by peak intensity, but simply reports peak occurrence. It is not possible to extrapolate this histogram to the ensemble spectrum of isolated polymer chains, or even to the bulk film, because the histogram is always weighted by the brightest, most stable chromophores. These units may or may not contribute to the majority of the emission in the ensemble. It is worth noting that the histogram appears to resemble a trimodal distribution. Other conjugated polymers such as polyfluorene [67] or MEH-PPV [68] exhibit bimodal distributions.

It is crucial to distinguish between chromophore conformation and overall chain conformation [69, 70]. The two may be interrelated but are revealed in different func-

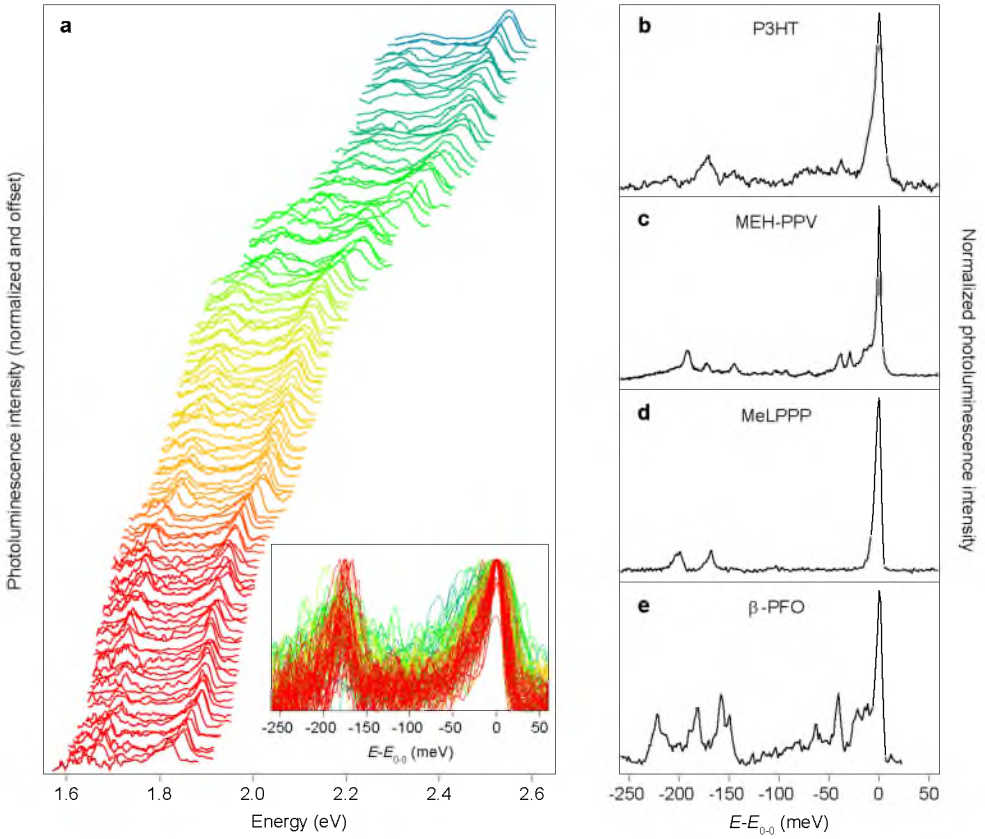

Figure 5.5. Universal shape of single-chromophore spectra of P3HT at 4 K. **a**, Waterfall plot of 115 single spectra, smoothed for clarity and sorted by transition energy. The inset shows the superposition of all spectra, shifted to a common origin. The spectra are color-coded from blue to red according to their transition energy. **b**-**e**, Representative single-chromophore spectra of P3HT, MEH-PPV, methyl-substituted ladder-type poly(para-phenylene) (MeLPPP), and β-phase poly (9,9-dioctylfluorene) (PFO). The spectral characteristics of these different materials are universal, displaying a dominant asymmetric zero-phonon line at the origin and a distinct vibronic progression that is determined by the chemical structure.

tions. Chromophore conformation controls spectral shape (vibronic coupling and spectral diffusion [71]) and transition energy, whereas chain shape controls the coupling between chromophores (e.g., by energy transfer) [68, 69]. In polyfluorene, a bimodal distribution of photoluminescence (PL) peak positions arises due to the fact that the chromophore (and often the entire chain) can exist in twisted or planarized conformation [67, 69]. Planarization, referred to as formation of the β-phase, leads to a spectral red shift in emission as well as a narrowing of the peak energy distribution. In MEHPPV, the peak distribution appears to be bimodal, too [68]. The bluer distribu-

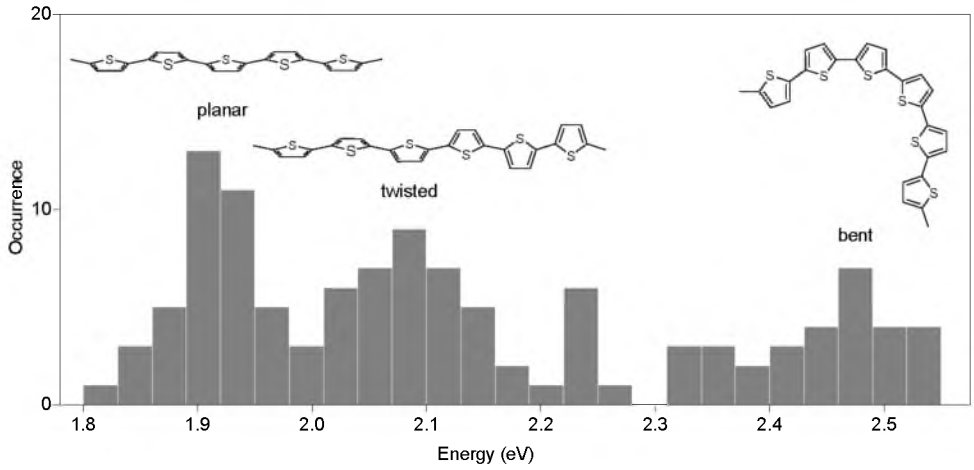

Figure 5.6. Histogram of the 0-0 emission peaks of the P3HT single-chromophore spectra shown in Figure 5.5. The histogram may be interpreted as being trimodal. In an analogy to other conjugated polymer materials, where distinct chromophore conformations have been identified, possible chromophore conformations of P3HT are sketched.

tion of peaks corresponds to stretched phenylenevinylene units, as can be resolved by polarization anisotropy measurements, whereas the red distribution arises due to bent chromophores [71]. Overall, there are therefore (at least) three distinct chain conformations that can impact the spectroscopy: bending, twisting, and planarization. At present, we do not have compelling evidence to correlate single-chain spectroscopy of poly(3-hexylthiophene) (P3HT) with chain conformation, other than observing that, at room temperature, the most extended units (i.e., the polymer chains with the highest M values) appear to correspond to the most red-shifted spectra (Figure 5.4a, inset). We tentatively propose that the three peaks in the histogram of peak positions correspond to the three conformational species illustrated in Figure 5.6: bending, as revealed in scanning tunneling microscopy measurements [72], resulting in high energy transitions; twisting at intermediate energies [71]; and planarization at low energies [67]. We stress that this tentative assignment remains entirely speculative at the present time.

5.9.3 Random Variations in Single-Chromophore Vibronic Intensity and Structural Relaxation

Figure 5.1d shows a substantial scatter in vibronic intensity of the single-chromophore PL spectra. This peak ratio is known to vary strongly between different single chromophores [73] due to slight changes in conformation and the resulting modifications in

structural relaxation energy. This variation is illustrated for P3HT in Figure 5.7a. Structural relaxation (the shift between ground and excited-state potential surfaces) controls the intensity of the vibronic sidebands in luminescence as sketched in Figure 5.7b. The strength of vibronic coupling is not constant from chromophore to chromophore, implying that microscopic models of excitonic coherence cannot necessarily be applied to describe the macroscopic spectrum with an averaged relaxation energy.

5.9.4 Dynamic Disorder in Single Chromophores

Dynamic disorder (i.e., the spectral jitter of single chromophores, also referred to as spectral diffusion) occurs in all single emitters, implying that the measured transition line width exceeds the homogeneous electronic line width. The effect can be particularly pronounced in conjugated polymers [66]: it has been shown that it can account for most of the conformation-dependent spectral broadening (> 0.1 eV) found in ensemble MEH-PPV [71]. Spectral diffusion is clearly seen in single P3HT chromophores, providing unambiguous evidence for the detection of single chromophores [66] and posing important limitations on the concept of the fundamental transition width of single chromophores in models of excitonic coupling. Figure 5.8a shows example fluorescence

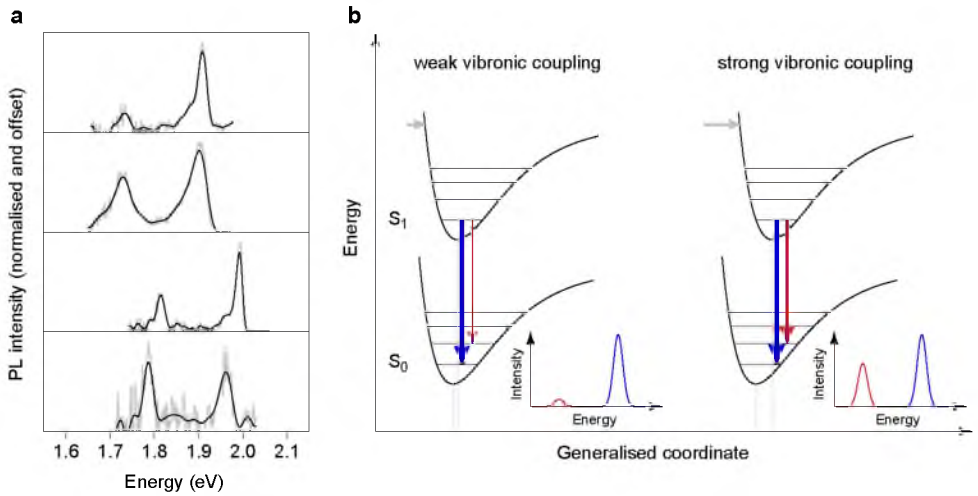

Figure 5.7. Variation of the intensity of the vibronic sideband in single-chromophore PL between different chromophores. **a**, Four spectra showing different ratios of 0-0 and 0-1 bands. The ratio varies randomly by a factor of 4. **b**, This variation can be rationalized by a simple Franck-Condon diagram in which the structural relaxation energy (gray arrow) differs between chromophores due to slight differences in ground-state conformation.

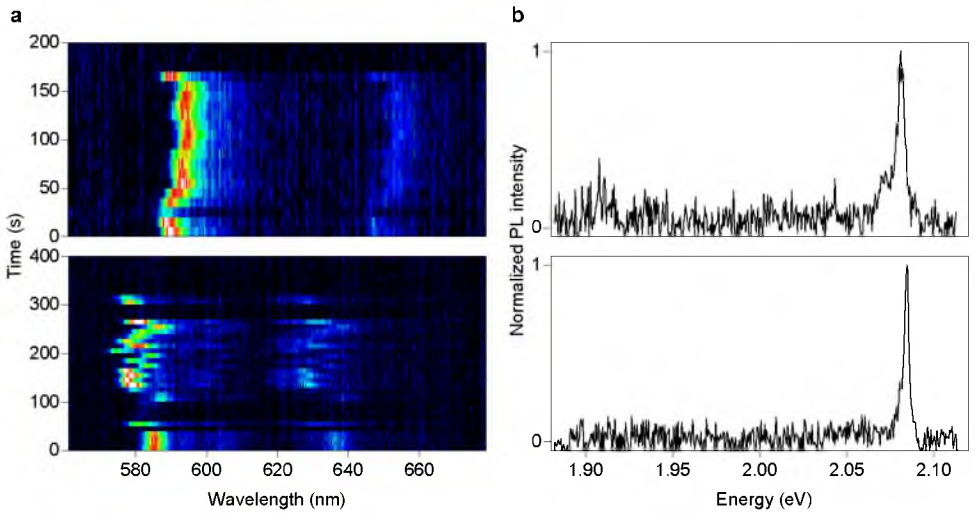

Figure 5.8. Influence of random spectral diffusion of single-chromophore emission on spectral line width in two representative chromophores. **a**, Temporal evolution of the emission. Each spectrum was integrated for 10 s. The spectra drift over 20 meV (upper) and 36 meV (lower). **b**, A single time slice from the traces. The upper panel exhibits a chromophore of spectral width 5 meV, and the lower panel, a narrower chromophore of width 3 meV.

traces of single P3HT chromophores as a function of time, exhibiting spectral meandering that will contribute to spectral broadening in the ensemble and bulk film. The implication of these observations is that the longer the single-molecule measurement lasts, the broader the spectrum becomes.

An understanding of spectral broadening mechanisms is crucial to developing models of interchromophoric interactions. Homogeneous line width controls both coherent coupling in aggregates [74] and incoherent FRET [75]. Both microscopic coupling mechanisms can strongly impact the ensemble emission spectrum. Single-molecule fluorescence spectroscopy typically provides an upper estimate of homogeneous line width because the transitions will be broadened artificially by spectral meandering during the measurement process. In MEH-PPV, for example, the homogeneous line width is so small (< 10 μeV) [76], that FRET relaxation pathways are frozen out at very low temperatures [70], leading to a blue shift in emission at low temperature. There is no obvious reason why the homogeneous line width of chromophores in P3HT should be much broader than those in MEH-PPV. Figure 5.8b provides two examples of single-chromophore spectra with transition line widths as narrow as 3 meV. Because spectral

diffusion occurs, broadening of this transition line is simply an artifact of the measurement: the faster the measurement, the narrower the transition. It is crucial to realize this phenomenon in theoretical descriptions that compute instantaneous couplings through an effective Hamiltonian.

5.9.5 Examples of Single-Molecule Fluorescence Polarization Measurements

The polymer chain conformation is assessed by performing fluorescence polarization modulation spectroscopy. A molecule with a single linear transition dipole will modulate its fluorescence as the plane of excitation polarization is rotated through an angle θ following a cosine-squared law. Deviations from a linear dipole result in a modification of fluorescence modulation following $I(\theta) \propto 1 + M\cos(2\theta)$, where θ is the angle of excitation polarization and M the modulation depth, a value of 1 signifying a linear dipole and 0 an unpolarized absorber. In this terminology, it is also equivalent to note that M is defined by the ratio of maximum to minimum emission intensities through $M = \frac{I_{max}-I_{min}}{I_{max}+I_{min}}$. To illustrate the data quality, Figure 5.9 plots three fluorescence intensity traces, along with fits, for single P3HT chains in PMMA and Zeonex, respectively.

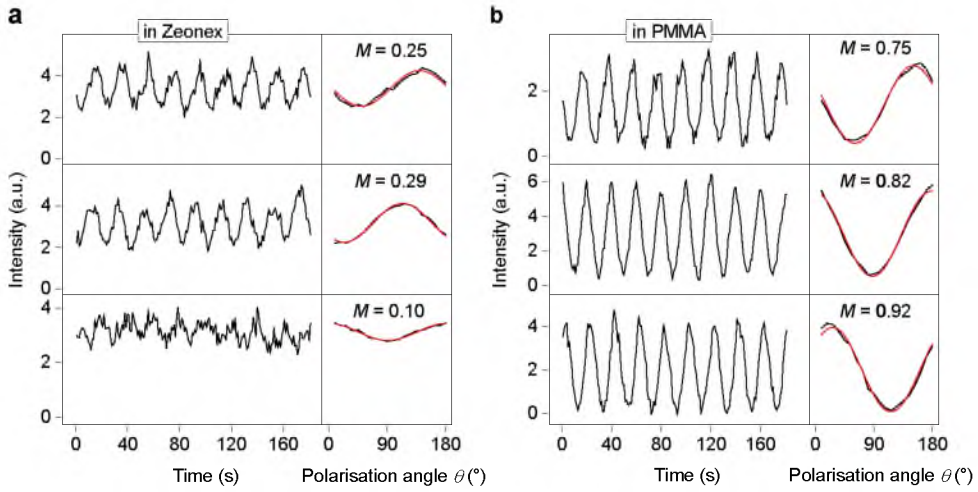

Figure 5.9. Example excitation polarization modulation traces of three single P3HT chains at room temperature (**a**) in Zeonex and (**b**) in PMMA. The averaged PL intensity is plotted as a function of polarization angle on the right-hand side of the panels (black line), with a cosine-square fit superimposed (red line).

5.10 References

[1] M. Pope and C. E. Swenberg, *Electronic Processes in Organic Crystals and Polymers*, Oxford University Press Inc., New York, Oxford, 2 edition, 1999.

[2] J. You et al., Nat. Commun. **4**, 1446 (2013).

[3] M. Campoy-Quiles et al., Nat. Mater. **7**, 158 (2008).

[4] Y. Kim et al., Nat. Mater. **5**, 197 (2006).

[5] X. N. Yang et al., Nano Lett. **5**, 579 (2005).

[6] M. D. Barnes and M. Baghar, J. Polym. Sci. Part B Polym. Phys. **50**, 1121 (2012).

[7] T. Erb et al., Adv. Funct. Mater. **15**, 1193 (2005).

[8] A. J. Moulé and K. Meerholz, Adv. Mater. **20**, 240 (2008).

[9] F. Padinger, R. S. Rittberger, and N. S. Sariciftci, Adv. Funct. Mater. **13**, 85 (2003).

[10] A. Zen et al., Macromolecules **39**, 2162 (2006).

[11] A. Salleo, R. J. Kline, D. M. DeLongchamp, and M. L. Chabinyc, Adv. Mater. **22**, 3812 (2010).

[12] I. McCulloch et al., Adv. Mater. **21**, 1091 (2009).

[13] M. T. Dang, L. Hirsch, and G. Wantz, Adv. Mater. **23**, 3597 (2011).

[14] G. Zhao, Y. He, and Y. Li, Adv. Mater. **22**, 4355 (2010).

[15] J. Roncali, Chem. Rev. **92**, 711 (1992).

[16] R. D. McCullough, Adv. Mater. **10**, 93.

[17] I. F. Perepichka, D. F. Perepichka, H. Meng, and F. Wudl, Adv. Mater. **17**, 2281 (2005).

[18] R. Osterbacka, C. P. An, X. M. Jiang, and Z. V. Vardeny, Science **287**, 839 (2000).

[19] H. Sirringhaus et al., Nature **401**, 685 (1999).

[20] E. T. Niles et al., J. Phys. Chem. Lett. **3**, 259 (2012).

[21] H. Yamagata, C. M. Pochas, and F. C. Spano, J. Phys. Chem. B **116**, 14494 (2012).

[22] J. Clark, C. Silva, R. H. Friend, and F. C. Spano, Phys. Rev. Lett. **98**, 206406 (2007).

[23] F. C. Spano, J. Clark, C. Silva, and R. H. Friend, J. Chem. Phys. **130**, 074904 (2009).

[24] A. Ruseckas et al., J. Photochem. Photobiol. A **144**, 3 (2001).

[25] D. Chaudhuri et al., Nano Lett. **11**, 488 (2011).

[26] S. Cook, A. Furube, and R. Katoh, Energy Environ. Sci. **1**, 294 (2008).

[27] F. Paquin et al., Phys. Rev. Lett. **106**, 197401 (2011).

[28] J. M. Lupton, Adv. Mater. **22**, 1689 (2010).

[29] D. H. Hu et al., Nature **405**, 1030 (2000).

[30] T. Huser, M. Yan, and L. J. Rothberg, PNAS **97**, 11187 (2000).

[31] T. Adachi et al., J. Phys. Chem. Lett. **2**, 1400 (2011).

[32] T. Adachi et al., J. Phys. Chem. B **116**, 9866 (2012).

[33] I. G. Scheblykin, A. Yartsev, T. Pullerits, V. Gulbinas, and V. Sundstroem, J. Phys. Chem. B **111**, 6303 (2007).

[34] T. Sugimoto, S. Habuchi, K. Ogino, and M. Vacha, J. Phys. Chem. B **113**, 12220 (2009).

[35] G. E. Khalil et al., J. Phys. Chem. B **115**, 12028 (2011).

[36] H. Bässler and B. Schweitzer, Acc. Chem. Res. **32**, 173 (1999).

[37] G. Rossi, R. R. Chance, and R. Silbey, J. Chem. Phys. **90**, 7594 (1989).

[38] M. L. Shand, R. R. Chance, M. Lepostollec, and M. Schott, Phys. Rev. B **25**, 4431 (1982).

[39] E. Da Como, N. J. Borys, P. Strohriegl, M. J. Walter, and J. M. Lupton, J. Am. Chem. Soc. **133**, 3690 (2011).

[40] F. Schindler et al., Angew. Chem. Int. Ed. **44**, 1520 (2005).

[41] F. Schindler, J. M. Lupton, J. Feldmann, and U. Scherf, PNAS **101**, 14695 (2004).

[42] T. Guillet et al., Phys. Rev. Lett. **87**, 087401 (2001).

[43] R. Lecuiller et al., Phys. Rev. B **66**, 125205 (2002).

[44] F. A. Feist and T. Basché, J. Phys. Chem. B **112**, 9700 (2008).

[45] E. Mena-Osteritz et al., Angew. Chem. Int. Ed. **39**, 2680 (2000).

[46] B. A. Collins et al., Nat. Mater. **11**, 536 (2012).

[47] R. J. Kline, M. D. Mcgehee, and M. F. Toney, Nat. Mater. **5**, 222 (2006).

[48] P. J. Brown et al., Phys. Rev. B **67**, 064203 (2003).

[49] M. Schott, J. Phys. Chem. B **110**, 15864 (2006).

[50] K. Becker et al., J. Phys. Chem. B **112**, 4859 (2008).

[51] J. G. Müller, M. Anni, U. Scherf, J. M. Lupton, and J. Feldmann, Phys. Rev. B **70**, 035205 (2004).

[52] S. Liu et al., J. Phys. Chem. B **117**, 4197 (2013).

[53] C. W. Hollars, S. M. Lane, and T. Huser, Chem. Phys. Lett. **370**, 393 (2003).

[54] T. H. Lee et al., Appl. Phys. Lett. **85**, 100 (2004).

[55] F. C. De Schryver et al., Acc. Chem. Res. **38**, 514 (2005).

[56] J. Hofkens et al., PNAS **100**, 13146 (2003).

[57] W. J. D. Beenken and T. Pullerits, J. Phys. Chem. B **108**, 6164 (2004).

[58] N. Banerji, S. Cowan, E. Vauthey, and A. J. Heeger, J. Phys. Chem. C **115**, 9726 (2011).

[59] N. P. Wells and D. A. Blank, Phys. Rev. Lett. **100**, 086403 (2008).

[60] M. J. Walter and J. M. Lupton, Phys. Rev. Lett. **103**, 167401 (2009).

[61] F. Schindler, J. M. Lupton, J. Muller, J. Feldmann, and U. Scherf, Nat. Mater. **5**, 141 (2006).

[62] J. Müller et al., Phys. Rev. B **72**, 205339 (2005).

[63] J. C. Bolinger et al., Acc. Chem. Res. **45**, 1992 (2012).

[64] B. J. Schwartz, Annu. Rev. Phys. Chem. **54**, 141 (2003).

[65] T. Stangl et al., J. Am. Chem. Soc. **135**, 78 (2013).

[66] F. Schindler, J. M. Lupton, J. Feldmann, and U. Scherf, PNAS **101**, 14695 (2004).

[67] E. Da Como, K. Becker, J. Feldmann, and J. M. Lupton, Nano Lett. **7**, 2993 (2007).

[68] J. C. Bolinger et al., Acc. Chem. Res. **45**, 1992 (2012).

[69] J. M. Lupton, Adv. Mater. **22**, 1689 (2010).

[70] J. M. Lupton, ChemPhysChem **13**, 901 (2012).

[71] K. Becker et al., J. Phys. Chem. B **112**, 4859 (2008).

[72] E. Mena-Osteritz et al., Angew. Chem. Int. Ed. **39**, 2680 (2000).

[73] J. G. Müller, M. Anni, U. Scherf, J. M. Lupton, and J. Feldmann, Phys. Rev. B **70**, 035205 (2004).

[74] C. Hettich et al., Science **298**, 385 (2002).

[75] J. G. Müller et al., Phys. Rev. Lett. **91**, 267403 (2003).

[76] F. A. Feist, G. Tommaseo, and T. Basché, Phys. Rev. Lett. **98**, 208301 (2007).

CHAPTER 6

CONCLUDING REMARKS

6.1 Summary

Organic semiconducting materials for optoelectronic applications have been discussed as low-cost alternatives to inorganic materials for many years. While products containing organic light-emitting diodes entered the consumer market about a decade ago, organic-based photovoltaic cells can still be regarded as being in the stages of research and development. The scientific contribution of this work provides several crucial aspects to understanding the complexity of the basic photoprocesses in π-conjugated materials. This summary contextualizes the results of this work in terms of the larger field of organic optoelectronics.

6.1.1 Exciton Dynamics

Exciton localization in the π-conjugated model molecule was found to be random and not correlated with the orientation of the polarization of the excitation light. The result was largely anticipated but the experimental proof has important consequences: it puts a critical perspective on the paradigm built around the concept of a chromophore. In several studies of photophysical phenomena, notably of excitation energy transfer, chromophores of π-conjugated polymers are assumed to be static and often times linear [1, 2]. Considering the amorphous nature of organic materials, this assumption seems out of place. Yet the established paradigm is remarkably persistent [3–5] for a profound reason: incorporating static chromophores in models and computational methods is simple. There are, however, studies that show that chromophore bending does not necessarily break conjugation [6] and studies that consider exciton dynamics in the nonadiabatic regime to model energy transport [7, 8]. The results presented in this work might further stimulate such studies and "would hopefully allow more details to be revealed of this fascinating general picture of conjugated molecules" [9].

On a side note: dynamic localization has only recently been reported in photosynthetic complexes [10], which constitute a circular, strongly coupled multichromophoric system that is rather similar to the model molecule employed in this work, with the crucial difference of not being conjugated but rather constituting a supramolecular aggregate.

6.1.2 Single Molecule Morphology in P3HT

Thermally annealed or self-assembled films of poly-(3-hexylthiophene) (P3HT) have a strong tendency to crystallize [11, 12]. Concomitantly, the optical spectra are extended to lower energies and exhibit a modified vibronic structure which is explained in terms of an H-aggregate model [13, 14], with a vibronic peak ratio of $I_{0-1}/I_{0-0} > 1$. In this work, single transition lines from individual P3HT molecules were observed to scatter over a large energy range of over 0.8 eV. Importantly, 0-0 transitions of single molecules were identified at the same energies of the spectrum which has previously been attributed to aggregate emission in the bulk [13, 14]. However, a change in the vibronic peak ratio was not observed on the single molecule level, implying that the emission arose from nonaggregated species. This finding reopens the question of the origins of the spectral red-shift of electronic transitions in bulk films. As discussed above, certain chromophore geometries (bending) may be responsible for the observed low energy transitions [6, 15], but this hypothesis requires experimental proof.

6.2 Future Prospects

The nature of curiosity is not to answer questions but to ask them. Naturally, during the course of this work more new questions arose than were answered – some of them are discussed here.

- *Electromagnetic coupling in the macrocycle molecule.* Photon statistics measurements of the macrocycle model molecule show characteristic behavior of a single photon source (Chapter 3), implying that the large molecule behaves as one quantum emitter. In addition, the transient fluorescence polarization anisotropy measurements in solution (Chapter 4) exhibit a very fast (< 2 ps) depolarization. While it can be tempting to interpret both results as evidence for fully delocalized excitations around the perimeter, these results must be treated with caution.

Photon statistics measurements would lead to the same result in the case of very efficient singlet-singlet annihilation in the presence of several excited states located on the ring. Furthermore, efficient energy transfer between different chromophores on the ring would give the same anisotropy depolarization as observed in Chapter 4. However, time-resolved two-photon excitation techniques [16] and more advanced ultrafast coherent pump-probe techniques [2] may be able to differentiate between strong and weak excitonic coupling in the ring. A signature of strong coupling could be polarization beating in transient spectroscopy.

- *Mechanism of torsional relaxation.* The rate of torsional relaxation is known to be modified by temperature and solvents with different viscosity [17]. In particular, studying torsional relaxation in solution at different temperatures can help to determine the activation barrier energy of this process. This, in turn, may provide more insight into the exact mechanism of torsional relaxation and help to elucidate the difference in transient fluorescence spectral dynamics between the dimer and the hexamer (Chapter 4).

- *Extent of torsional relaxation.* The observed spectral relaxation in the dimer, which was attributed to torsional relaxation, is not reflected in a change of anisotropy on the same timescale of order 100 ps. This result was interpreted in terms of an insignificant change of the emission transition dipole during torsional relaxation. While this interpretation is reasonable, simultaneous measurements of emission and absorption polarization [18] of single dimer molecules can provide additional verification of the observation, and may offer additional insight into the relaxation process.

- *Chromophore geometry.* Polarization spectroscopy experiments in poly(*para*-phenylene vinylene) have shown a correlation between chain conformation and peak position of single polymer chains [15]. Similar measurements on the single molecule level of well defined P3HT oligomers may be able to correlate the amount of bending in individual chains to the energy of their optical transition. Moreover, modification of chain morphology can be aided *in situ*, for example by solvent-vapor annealing techniques [19].

6.3 References

[1] S. C. J. Meskers, J. Hübner, M. Oestreich, and H. Bässler, Chem. Phys. Lett. **339**, 223 (2001).

[2] E. Collini and G. D. Scholes, Science **323**, 369 (2009).

[3] W. J. D. Beenken, Phys. Status Solidi A **206**, 2750 (2009).

[4] J. M. Lupton, ChemPhysChem **13**, 901 (2012).

[5] W. Barford, E. R. Bittner, and A. Ward, J. Phys. Chem. A **116**, 10319 (2012).

[6] W. J. D. Beenken and T. Pullerits, J. Phys. Chem. B **108**, 6164 (2004).

[7] T. R. Nelson, *Nonadiabatic Excited State Molecular Dynamics: Perspectives for a Robust Future*, PhD thesis, University of Rochester, 2013.

[8] T. Nelson, S. Fernandez-Alberti, A. E. Roitberg, and S. Tretiak, Acc. Chem. Res. **47**, 1155 (2014).

[9] I. G. Scheblykin, Nat. Chem. **5**, 903 (2013).

[10] A. F. Fidler, V. P. Singh, P. D. Long, P. D. Dahlberg, and G. S. Engel, Nat. Commun. **5**, (2014).

[11] R. D. McCullough, S. Tristram-Nagle, S. P. Williams, R. D. Lowe, and M. Jayaraman, J. Am. Chem. Soc. **115**, 4910 (1993).

[12] H. Sirringhaus et al., Nature **401**, 685 (1999).

[13] J. Clark, C. Silva, R. H. Friend, and F. C. Spano, Phys. Rev. Lett. **98**, 206406 (2007).

[14] F. C. Spano, J. Chem. Phys. **122**, 234701 (2005).

[15] K. Becker et al., J. Phys. Chem. B **112**, 4859 (2008).

[16] O. Varnavski, P. Bäuerle, and T. Goodson III, Opt. Lett. **32**, 3083 (2007).

[17] R. E. Di Paolo et al., ChemPhysChem **8**, 2657 (2007).

[18] O. Mirzov et al., Small **5**, 1877 (2009).

[19] J. Vogelsang, T. Adachi, J. Brazard, D. A. Vanden Bout, and P. F. Barbara, Nat. Mater. **10**, 942 (2011).

APPENDIX

SUPPORTING INFORMATION FOR CHAPTER 3: FLUCTUATING EXCITON LOCALIZATION IN GIANT π-CONJUGATED SPOKED-WHEEL MACROCYCLES

This chapter is a reprint of the supporting information of the article "Fluctuating exciton localization in giant π-conjugated spoked-wheel macrocycles" published in September 2013 in the journal *Nature Chemistry* in volume 5 on pages 964-970.

Fluctuating exciton localisation in giant π-conjugated spoked-wheel macrocycles

Vikas Aggarwal[1], Alexander Thiessen[2], Alissa Idelson[1], Daniel Kalle[1], Dominik Würsch[3], Thomas Stangl[3], Florian Steiner[3], Stefan-S. Jester[1], Jan Vogelsang[3], Sigurd Höger[1], John M. Lupton[2,3]

[1]Kekulé-Institut für Organische Chemie und Biochemie der Universität Bonn, Gerhard-Domagk-Str. 1, 53121 Bonn, Germany

[2]Department of Physics and Astronomy, University of Utah, Salt Lake City, UT 84112, USA

[3]Institut für Experimentelle und Angewandte Physik, Universität Regensburg, D-93040 Regensburg, Germany

Corresponding authors.
E-mail: hoeger@uni-bonn.de; john.lupton@ur.de

Table of contents

1. General methods

1.1. Materials and general procedures and equipment

Reagents were purchased at reagent grade from commercial sources and used without further purification. All water and/or air-sensitive reactions were carried out in preheated glassware using standard *Schlenk* techniques under argon. Unless stated otherwise, all glassware in which the reactions were carried out was evacuated, heated over 100 °C, and flushed with argon prior to loading with the reagents. Solvents were either purchased in anhydrous quality or were dried and distilled according to standard methods (THF (dried over Na), piperidine (dried over CaH_2)). Solvents used for workup were purified by distillation. ^1H and ^{13}C NMR spectra were recorded on a Bruker DPX 300 (^1H: 300 MHz, ^{13}C: 75 MHz), DPX 400 (^1H: 400 MHz, ^{13}C: 100.6 MHz) or DPX 500 (^1H: 500 MHz, ^{13}C: 125.8 MHz) spectrometer. Chemical shifts are given in parts per million (ppm) referenced to residual ^1H or ^{13}C signals in deuterated solvents. Mass spectra were measured on a Bruker Daltronics autoflex II TOF/TOF (MALDI-MS; matrix material: DCTB or dithranol), on a Finnigan ThermoQuest MAT 95 XL (EI-MS) or on an AEI MS-5 (EI-HRMS). *m/z* peaks smaller than 10 % (compared to the basis peak) are not reported. UV-VIS absorption spectra were recorded on a Perkin-Elmer Lambda 18 spectrophotometer using 0.1 mm, 0.2 mm, 1.0 mm, 10 mm and 100 mm quartz cuvettes manufactured by Hellma. Solution fluorescence experiments were run on a Perkin-Elmer LS 50 B spectrofluorometer in all-transparent 10 mm quartz cuvettes by monochromatic excitation at the indicated wavelength. Melting points were determined using a Leica DMLB microscope with resistive heating socket controlled by a Leica LMW transformer and a Testo 925 digital thermometer. Thin layer chromatography was conducted on silica gel coated aluminium plates (Macherey-Nagel, Alugramm SIL G/UV_{254}, 0.25 mm coating with fluorescence indicator). For purification by column chromatography, Silica gel 60 M (Macherey-Nagel, 0.04-0.063 mm, 230-400 mesh) was used as the stationary phase that was suspended in the indicated solvent. The liquid phase was chosen in such a way that the R_f-values of the desired compounds were between 0.20 and 0.30. Gel permeation chromatography (GPC, also size exclusion chromatography (SEC)) was performed using THF (HPLC grade, stabilized with 2.5 ppm BHT) at r.t. GPC analyses were run on an Agilent Technologies system at a flow rate of 1 mL/min using an IsoPump G1310 A, a G1314B VWD detector and PSS columns (Polymer Standards Service (PSS), Mainz, Germany; 10^2, 10^3, 10^5, and 10^6 Å, 5µ, 8 x 300 mm). All molecular weights were determined after polystyrene (PS) calibration (using PS standard substances obtained from PSS). For the preparative separation of product mixtures *via* GPC a Shimadzu recycling GPC system was employed, equipped with an LC-20 AD pump, an SPD-20 A UV detector and a set of three preparative columns from PSS (either 10^3 Å, 5µ, 20 x 300 mm or linear S, 5µ, 20 × 300 mm), operated at a flow rate of 5 mL/min. Microwave assisted reactions were performed with a Discover LabMate system manufactured by CEM.

1.2. Optical spectroscopy, single-molecule spectroscopy

Single-molecule emission was studied either at room temperature, in air, or under cryogenic conditions under vacuum.

Single-molecule experiments at cryogenic temperatures

The ring molecules were dispersed in an optically inert polymer matrix (Zeonex 480, Zeon Corporation) at concentrations of 10^{-6} g/L and spin-coated on quartz substrates in a glove box under nitrogen atmosphere yielding film thicknesses of 20 nm. The samples were mounted on the cold finger of a He cryostat (ST-500, Janis Research Company Inc.) and kept under a vacuum of 10^{-7} mbar during the measurement at 4 K.

Photoluminescence emission was detected with a long working-distance microscope objective (7.7 mm, NA 0.55, Olympus America Inc.) that projects the emission onto the entrance slit of a 50 cm spectrograph (ARC-1-015-500, Princeton Instruments) with a CCD camera (CoolSnap:HQ2, Princeton Instruments).

Sample preparation for room-temperature single-molecule spectroscopy

The analyte molecules were embedded in a poly(methyl methacrylate) (PMMA, M_n = 46 kDa from Sigma Aldrich Co.) host matrix. The following steps were conducted:

(i) Borosilicate glass cover slips were cleaned in a 2% Hellmanex III (Hellma Analytics) solution, followed by rinsing with MilliQ water.

(ii) The glass cover slips were transferred into a UV-ozone cleaner (Novascan, PSD Pro Series UV) to bleach the glass cover slips from residual contaminant fluorescent molecules.

(iii) The analyte was diluted in toluene to single-molecule concentration (~ 10^{-12} M) and mixed with a 1 w/w % PMMA/toluene solution.

(iv) The analyte/PMMA/toluene solution was dynamically spin-coated at 2000 rpm onto the glass cover slips, which leads to a film thickness of about 50 nm with an average analyte density of 40 individual molecules in a range of 50 × 50 μm^2.

(v) Single-molecule emission was studied under ambient conditions. It was found that under exposure to dry nitrogen, the single-molecule emission was substantially reduced, which is most likely due to the build-up of triplet excitons which can be quenched by molecular oxygen.

It was found that under the latter conditions, and under exposure to dry nitrogen at room temperature, the single-molecule emission was substantially reduced, which is most likely due to the build-up of triplet excitons which can be quenched by molecular oxygen.

Fluorescence quantum yields

The fluorescence quantum yields of the oligomer, ring and precursor were measured by ensemble absorption and fluorescence spectroscopy. The absorption spectra were recorded for various concentrations with a Perkin Elmer spectrometer (Lambda 650). The concentrations were chosen so that self-quenching and reabsorption can be neglected. Toluene was used as a solvent for both samples, which was measured against a standard fluorophore with known fluorescence quantum yield (ATTO-TEC GmbH, ATTO 390). The fluorescence spectra were measured with a Horiba Jobin-Yvon Fluoromax 4 fluorescence spectrometer and compared with the standard fluorophore. The fluorescence quantum yields for the monomer **9**, dimer **10**, hexamer **11**, and the ring **1** are reported in Table 1 in the main text.

Linear dichroism, emission polarisation cross-correlation and photon statistics

Fluorescence transients including the linear dichroism in excitation and emission of single ring molecules were recorded via a confocal fluorescence microscope. An inverted microscope (Olympus, IX71) with a high numerical objective (Olympus, APON 60XOTIRF, NA=1.49) was used. The excitation source was provided by a fibre-coupled diode laser (PicoQuant, LDH-C-405) with a wavelength of 405 nm in quasi-continuous wave mode (pulsed excitation, 20 MHz repetition rate). The excitation light was passed through a clean-up filter (AHF Analysentechnik, HC Laser Clean-up MaxDiode 405/10) and a Glan-Thompson polariser to provide linearly polarised excitation light. The polarisation of the excitation light was switched by an electro-optical modulator (FastPulse Technology Inc., 3079-4PW) and an additional $\lambda/4$ waveplate between horizontal and vertical polarisation every 500 µs, as described elsewhere.[2] The laser beam was expanded and collimated via a lens system and coupled into the oil immersion objective through the back port of the microscope and a dichroic mirror (AHF Analysentechnik RDC 405 nt). A diffraction limited spot was generated with an excitation power of 50 nW to ensure that all measurements are performed in the linear excitation regime, far below single-molecule saturation intensity. The fluorescence signal was either split by a polarising beam splitter (Thorlabs, CM1-PBS251) into two orthogonal polarising detection channels or by a 50/50 beam splitter into two equivalent detection channels. Avalanche photodiodes from Picoquant (τ-SPAD-20) were used as detectors and the signal was recorded via a time-correlated single photon counting (TCSPC) module from Picoquant (HydraHarp 400). The polarising beam splitter was used to calculate and follow the linear dichroism, D, of a single analyte molecule in time, and the 50/50 beam splitter was applied for photon anti-bunching measurements. For the acquisition of the linear dichroism in excitation and emission the detected fluorescence photons were flagged by the TCSPC module according to the excitation polarisation used. Therefore, four photon streams were generated: $I_{\mathrm{H}}^{\mathrm{H}}$, $I_{\mathrm{H}}^{\mathrm{V}}$, $I_{\mathrm{V}}^{\mathrm{H}}$ and $I_{\mathrm{V}}^{\mathrm{V}}$, where the lower index represents the excitation polarisation and the upper index indicates the emission polarisation, respectively. From these four photon streams the linear dichroism in excitation, $D_{excitation}$, and emission, $D_{emission}$, can be calculated according to:

$$D_{excitation} = \frac{\left(I_{\mathrm{H}}^{\mathrm{H}} + I_{\mathrm{H}}^{\mathrm{V}}\right) - \left(I_{\mathrm{V}}^{\mathrm{H}} + I_{\mathrm{V}}^{\mathrm{V}}\right)}{\left(I_{\mathrm{H}}^{\mathrm{H}} + I_{\mathrm{H}}^{\mathrm{V}}\right) + \left(I_{\mathrm{V}}^{\mathrm{H}} + I_{\mathrm{V}}^{\mathrm{V}}\right)} \quad \text{and} \quad D_{emission} = \frac{\left(I_{\mathrm{H}}^{\mathrm{H}} + I_{\mathrm{V}}^{\mathrm{H}}\right) - \left(I_{\mathrm{H}}^{\mathrm{V}} + I_{\mathrm{V}}^{\mathrm{V}}\right)}{\left(I_{\mathrm{H}}^{\mathrm{H}} + I_{\mathrm{V}}^{\mathrm{H}}\right) + \left(I_{\mathrm{H}}^{\mathrm{V}} + I_{\mathrm{V}}^{\mathrm{V}}\right)}$$

A fluorescence image (size of 20 × 20 µm², integration time 2 ms/pixel with a resolution of 50 nm/pixel) was recorded by stage scanning (Physik Instrumente, model P-527.3CL), exciting at 405 nm, in order to find the analyte molecules and extract $D_{excitation}$ and $D_{emission}$ for each recorded molecule. Appropriate spots with homogeneous fluorescence intensity were selected and subsequently placed in the laser focus to record single-molecule transients of the analyte molecules. The control of the experiments and the subsequent data analysis including the cross-correlation was achieved by using a home-written LabView program.

For the fluorescence photon polarisation cross-correlation experiments the EOM was shut off and circularly polarised excitation light was used instead. For each molecule the first 100 ms of each fluorescent transient was cross-correlated between the two orthogonal polarisation detection channels according to the following equation:

$$g_{\mathrm{cross}}^{2}(\tau) = \frac{\left\langle I^{\mathrm{H}}(t) I^{\mathrm{V}}(t+\tau) \right\rangle}{\left\langle I^{\mathrm{H}}(t) I^{\mathrm{V}}(t) \right\rangle} - 1$$

The setup was used in a Hanbury-Brown-Twiss geometry to measure the probability of a molecule emitting more than one photon at a time. The measurement starts when a photon is recorded by one detector and stops when the other detector registers the next photon. Pulsed excitation was applied with a repetition rate of 20 MHz and pulses to increase the signal-to-background ratio. The pulse width was <88 ps. The plot in Figure 2c (main text) shows histograms of the photon arrival time differences at intervals of 0.5 ns of an ensemble of 100 ring molecules. A clear minimum is seen in the histograms at $\Delta t = 0$. The probability that two photons are detected within one laser pulse is 11 % of the probability to detect two photons in two different laser pulses. An average signal-to-background ratio of ~30 was measured, which leads to an expected probability of ~12 % to measure two photons at the same time for a single emitter.[4] This threshold is indicated by the dashed line in Fig. 2c. Therefore it can be concluded that the ring molecules behave as one single emitter.

Instrument response of single-molecule polarisation anisotropy measurement using fluorescent beads

For the measurement of the internal instrument response function (IRF), regarding the $D_{excitation}$ and $D_{emission}$ histograms in Figure 2b, the setup was calibrated using fluorescent beads (Spherotech Inc., Fluorescent Particles Light Yellow, FP-0245-2). The excitation intensity was chosen so that the emission intensity was comparable to the emission intensity from the analyte molecules. The spectral characteristics of the beads are similar to those of the rings. The same measurement procedure as described above was applied to the fluorescent bead sample.

1.3. Scanning tunnelling microscopy (STM)

Scanning tunnelling microscopy (STM) was performed under ambient conditions at the solution/solid interface of 1,2,4-trichlorobenzene (TCB), phenyl octane (PHO), or 1-octanoic acid (OA) (in order of preference) and highly oriented pyrolytic graphite (HOPG). Typically, 1 µL of a 10^{-4}–10^{-7} M solution of the compound of interest in TCB, PHO, or OA was dropped onto a piece of freshly cleaved HOPG at r.t. Subsequently the STM measurements were performed *in situ* (with the tip immersed in the solution) and typically completed within 30 min after sample preparation. In the cases indicated, the drops were deposited onto warm substrates at temperatures of 60–80 °C, whereupon the sample was kept at the temperature for approx. 20 s, then was allowed to cool to r.t., and was subsequently examined by STM. Bias voltages between -1.0 V and -1.6 V and tunnelling current set points between 2 pA to 17 pA were applied to image the supramolecular adlayers.

The experimental setup consists of an Agilent 5500 scanning probe microscope that is placed on a Halcyonics actively damping microscopy workstation and is acoustically isolated with a home-built noise damping box. STM tips were cut from Pt/Ir (80/20) wire using scissors and modified – after approaching to the interface – by short voltage pulses. HOPG was obtained from Mikromasch in ZYB quality. All STM images (unless otherwise noted) were calibrated by subsequent immediate acquisition of an additional image at reduced bias voltage, therefore the atomic lattice of the HOPG surface is observed which is used as a calibration grid. Data processing, also for image calibration, was performed using the SPIP 5 (Image Metrology) software package. Molecular models corresponding to the STM data were built using Spartan'08.

2. Synthesis of the ring 1

1 was synthesized according to the previously reported modular approach.[5,6] The three building blocks, the hub unit, the spoke unit, and the rim unit, were prepared independently according to Figure S1 and Figure S2, and assembled as outlined in the main text of the manuscript. While the compounds **6**,[5, 7] **S11**,[8] and **S12**[8] were synthesized according to literature procedures, known procedures were adapted for the preparation of the compounds **S2-S5**.[9, 10, 11] Therefore, the latter are described below along with the synthesis of all new compounds. The identities and purities of all new compounds are proven by the inclusion of MS (EI-MS or MALDI-TOF MS) and ^{1}H and ^{13}C NMR spectra (Except for **9**, **10**, and **11,** for which ^{13}C NMR spectra could not be recorded. Instead, GPC traces are presented for these compounds.).

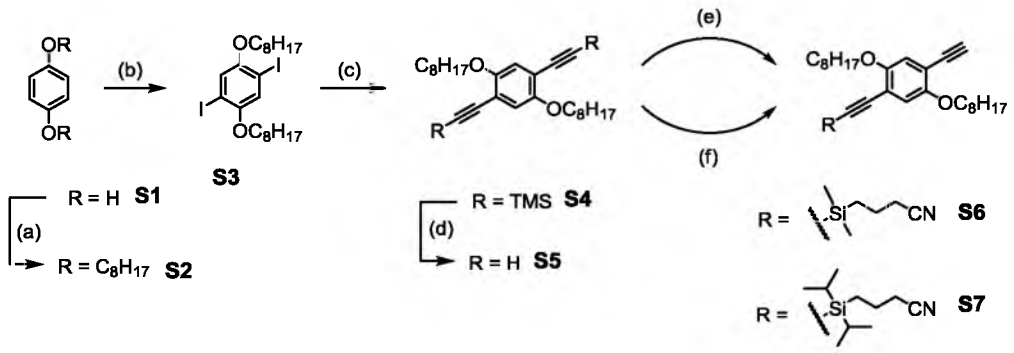

Figure S1: Synthesis of the building blocks **S6** and **S7** that were required for the construction of the spoke and the rim units, respectively.[9, 10] (a) 1-Iodooctane, K_2CO_3, KI, DMF, r.t. - 80 °C, 265 h, 75 %; (b) ICl, MeOH, $CHCl_3$, 15 °C - 80 °C, 24 h, 89 %; (c) $[PdCl_2(PPh_3)_2]$, CuI, PPh_3, TMSA, THF, piperidine, r.t., 17 h, 83 %; (d) K_2CO_3, THF, methanol, r.t., 2 h, 91 %; (e) 1) EtMgBr, THF, r.t., 45 min, 2) 3-cyanopropyldimethylsilyl chloride, THF, r.t., 17 h, 60 %; (f) 1) EtMgBr, THF, r.t., 45 min, 2) 3-cyanopropyldiisopropylsilyl chloride, THF, r.t., 17 h, 46 %.

Synthesis of the spoke module

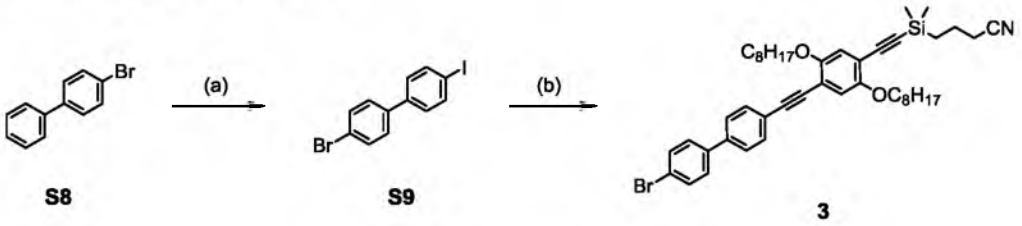

S8 **S9** **3**

Synthesis of the rim module

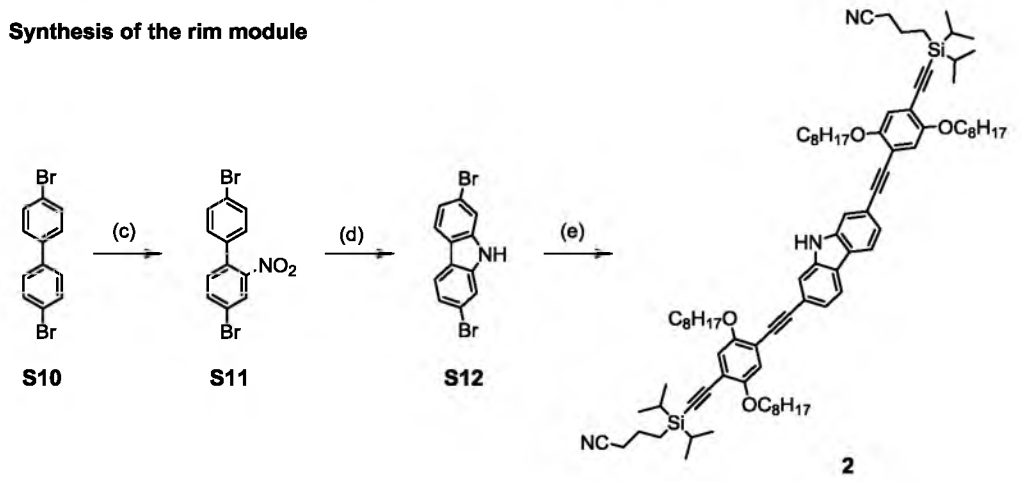

S10 **S11** **S12** **2**

Synthesis of the hub module

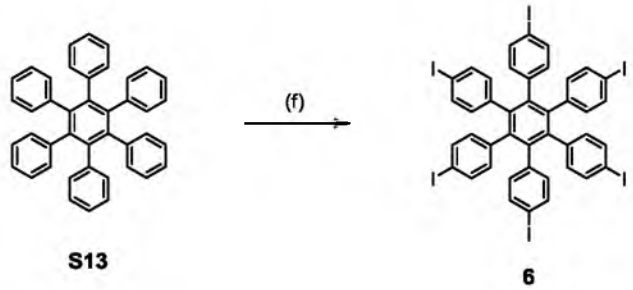

S13 **6**

Figure S2: Synthesis of the three modules. (a) I_2, HIO_3, CCl_4, HOAc, H_2SO_4, H_2O, 110 °C, 21 h, 86 %; (b) **S6**, $Pd(PPh_3)_2Cl_2$, PPh_3, CuI, piperidine, 50 °C, 17 h, 54 %; (c) HNO_3, HOAc, H_2O, 100 °C, 60 %;[8] (d) PEt_3, 156 °C, 47 %;[8] (e) 1. *n*-BuLi, THF, 0 °C, 30 min, 2. trimethylsilyl chloride, THF, 0 °C - r.t., 30 min,[12] 3. **S7**, $Pd(PPh_3)_2Cl_2$, PPh_3, CuI, piperidine, 80 °C, 40 h, 80 %; (f) PIFA, I_2, CH_2Cl_2, r.t., 72 h, 60 %.

S2

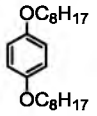

Hydroquinone (**S1**) (12.00 g, 0.109 mol), 1-bromooctane (96.75 g, 0.501 mmol), K_2CO_3 (75.00 g, 0.543 mol), and KI (9.13 g, 0.055 mol) were suspended in DMF (p. A.) (250 mL) and stirred at 80 °C overnight. After cooling to r.t., the reaction mixture was extracted with diethyl ether, washed with aq. H_2SO_4 (10 %) (until acidic), and brine, followed by drying over $MgSO_4$ and filtration. The filtrate was concentrated *in vacuo*, and **S2**[9, 10] (27.6 g, 0.082 mol, 75 %) was isolated as an off-white solid by precipitation with methanol and filtration.

^{1}H NMR (300 MHz, $CDCl_3$, 298 K) δ [ppm] = 6.82 (s, 4 H), 3.90 (t, $^3J_{H,H}$ = 6.6 Hz, 4 H), 1.85 – 1.67 (m, 4 H), 1.52 – 1.19 (m, 20 H), 0.97 – 0.81 (m, 6 H). ^{13}C NMR (75 MHz, $CDCl_3$, 298 K) δ [ppm] = 153.35, 115.54, 68.82, 31.98, 29.57, 29.54, 29.41, 26.23, 22.82, 14.25.MS (EI, 70 eV) (calcd. for $C_{22}H_{38}O_2$: 334.29): m/z (%) 334.3 (100) $[M]^+$, 222.1 (15) $[M\text{-}C_8H_{16}]^+$, 110.0 (90) $[M\text{-}C_{16}H_{32}]^+$.

S3

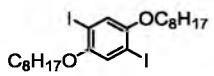

Iodine monochloride (56.71 g, 349.3 mmol) was dissolved in MeOH (150 mL) under cooling with an ice/water-bath (T < 15 °C). Then, **S2** (27.17 g, 81.2 mmol) was added, and the mixture was stirred for 4 h at 80 °C. As the reaction was not complete, solid iodine monochloride (4.00 g, 24.6 mmol) was added and stirring was continued for 3 h at 80 °C and overnight at 40 °C. Upon cooling to r.t., a precipitate formed that was isolated by filtration and washed with methanol and aq. $NaHSO_3$ (10 %). The solid was dissolved in diethyl ether and brine. The organic phase was dried over $MgSO_4$, and the solvent was removed to yield **S3**[9, 10] (42.16 g, 71.9 mmol, 89 %) as an off-white solid.

^{1}H NMR (300 MHz, $CDCl_3$, 298 K) δ [ppm] = 7.17 (s, 2 H), 3.92 (t, $^3J_{H,H}$ = 6.4 Hz, 4 H), 1.87 – 1.73 (m, 4 H), 1.56 – 1.42 (m, 4 H), 1.42 – 1.20 (m, 16 H), 0.96 – 0.83 (m, 6 H); ^{13}C NMR (75 MHz, $CDCl_3$, 298 K) δ [ppm] = 153.02, 122.96, 86.46, 77.58, 77.16, 76.74, 70.53, 31.96, 29.40, 29.38, 29.31, 26.19, 22.82, 14.27; MS (EI, 70 eV) (calcd. for $C_{22}H_{36}I_2O_2$: 586.08): m/z (%) 586.2 (59) $[M]^+$, 474.0 (12) $[M\text{-}C_8H_{16}]^+$, 460 (18) $[M\text{-}I]^+$, 361.9 (100) $[M\text{-}C_{16}H_{32}]^+$, 361 (28) $[M\text{-}C_{16}H_{32}\text{-}I]^+$.

S4

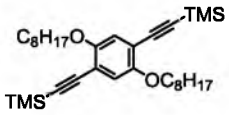

S3 (42.16 g, 71.9 mmol), $Pd(PPh_3)_2Cl_2$ (0.50 g, 0.7 mmol), CuI (0.27 g, 1.4 mmol), and PPh_3 (0.57 g, 2.2 mmol) were dissolved in THF (75 mL) and piperidine (150 mL). Trimethysilylacetylene (19.05 g, 27.2 mL, 194.0 mmol) was added dropwise at 0 °C, and this mixture was stirred overnight at r.t. The reaction was terminated by the addition of water and diethyl ether. The combined organic phases were then washed subsequently with aq. H_2SO_4 (10 %, until acidic), water, and brine. After drying over $MgSO_4$ and concentration *in vacuo*, the residue was filtered over silica (CH:DCM = 2:1). Slightly orange crystals of **S4**[10] (31.30 g, 59.4 mmol, 83 %) were obtained by recrystallisation from *i*-PrOH.

^{1}H NMR (300 MHz, $CDCl_3$, 298 K) δ [ppm] = 6.89 (s, 2 H), 3.94 (t, $^3J_{H,H}$ = 6.3 Hz, 4 H), 1.89 – 1.70 (m, 4 H), 1.62 – 1.42 (m, 4 H), 1.42 – 1.19 (m, 16 H), 0.98 – 0.80 (m, 6 H), 0.25 (s, $^3J_{H,H}$ = 3.4 Hz, 18 H); ^{13}C NMR (75 MHz, $CDCl_3$, 298 K) δ [ppm] = 154.16, 117.35, 114.10, 101.22, 100.21, 69.60, 32.00, 29.55, 29.51, 29.45, 26.18, 22.82, 14.24, 0.11; MS (EI, 70 eV) (calcd. for $C_{32}H_{45}O_2Si_2$: 526.73): m/z (%) 526.4 (100) $[M]^+$, 287.1 (20) $[M\text{-}C_{17}H_{35}]^+$.

S5

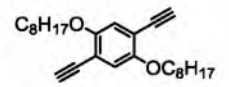

S4 (30.00 g, 57.0 mmol) and K_2CO_3 (62.97 g, 455.6 mmol) were suspended in methanol (200 mL) and distilled THF (500 mL), and stirred at r.t. overnight. The reaction mixture was taken up in water and diethyl ether. Following phase separation, the aqueous phase was extracted twice with diethyl ether. The combined organic phases were washed with aq. H_2SO_4 (10 %) and brine, and dried over $MgSO_4$. The solvent was removed and the residue was precipitated from dichloromethane/methanol. Filtration yielded **S5**[10] (19.78 g, 51.7 mmol, 91 %) as a slightly orange solid.

^{1}H NMR (300 MHz, $CDCl_3$, 298 K) δ [ppm] = 6.95 (s, 2 H), 3.97 (t, $^3J_{H,H}$ = 6.6 Hz, 4 H), 3.32 (s, 2 H), 1.90 – 1.71 (m, 4 H), 1.53 – 1.18 (m, 20 H), 0.98 – 0.79 (m, 6 H); ^{13}C NMR (75 MHz, $CDCl_3$, 298 K) δ [ppm] = 154.11, 117.88, 113.39, 82.53, 79.92, 69.80, 31.94, 29.43, 29.37, 29.27, 26.04, 22.80, 14.25; MS (EI, 70 eV) (calcd. for $C_{26}H_{38}O_2$: 382.29): m/z (%) 382.2 $[M]^+$, 270.1 (10) $[M\text{-}C_8H_{17}]^+$, 158.0 (100) $[M\text{-}C_{16}H_{32}]^+$.

S6

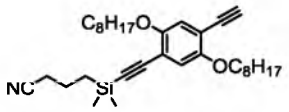

S5 (7.00 g, 18.3 mmol) was suspended in THF (120 mL) and ethylmagnesium bromide (1.0 M solution in THF) (19.2 mmol, 19.2 mL) was added slowly at r.t. The resulting solution was stirred for 60 min prior to the addition of 3-cyanopropyldimethylsilyl chloride (94 %; CPDMS-Cl)[13] (3.78 g, 22.0 mmol, 3.8 mL). After stirring overnight, the reaction was diluted with dichloromethane and aq. H_2SO_4 (10 %). The organic phase was washed successively with aq. H_2SO_4 (10 %), water, and brine and dried over $MgSO_4$. Removal of the solvent and purification by column chromatography (first column: CH:EA = 7:1; second column: CH:DCM = 3:1) yielded pure **S6** (5.54 g, 10.9 mmol, 60 %) as a white solid.

^{1}H NMR (300 MHz, $CDCl_3$, 298 K) δ [ppm] = 6.92 (s, 1 H), 6.91 (s, 1 H), 4.04 – 3.88 (m, 4 H), 3.33 (s, 1 H), 2.43 (t, $^3J_{H,H}$ = 7.0 Hz, 2 H), 1.93 – 1.71 (m, 6 H), 1.55 – 1.41 (m, 4 H), 1.41 – 1.19 (m, 16 H), 0.98 – 0.77 (m, 8 H), 0.33 – 0.20 (m, 6 H); ^{13}C NMR (75 MHz, $CDCl_3$, 298 K) δ [ppm] = 154.13, 154.10, 119.83, 117.60, 117.38, 113.93, 113.31, 102.46, 98.06, 82.61, 80.00, 77.58, 77.16, 76.74, 69.81, 69.46, 31.98, 31.94, 29.50, 29.46, 29.44, 29.36, 29.29, 26.12, 26.05, 22.80, 20.79, 20.59, 15.86, 14.25, 14.23, -1.67; MS (EI, 70 eV) (calcd. for $C_{32}H_{49}NO_2Si$: 507.35): m/z (%) 507.4 (100) $[M]^+$, 395.3 (18) $[M\text{-}C_8H_{16}]^+$, 283.2 (20)$[M\text{-}C_{16}H_{32}]^+$, 126.1 (22) $[C_6H_{12}NSi]^+$.

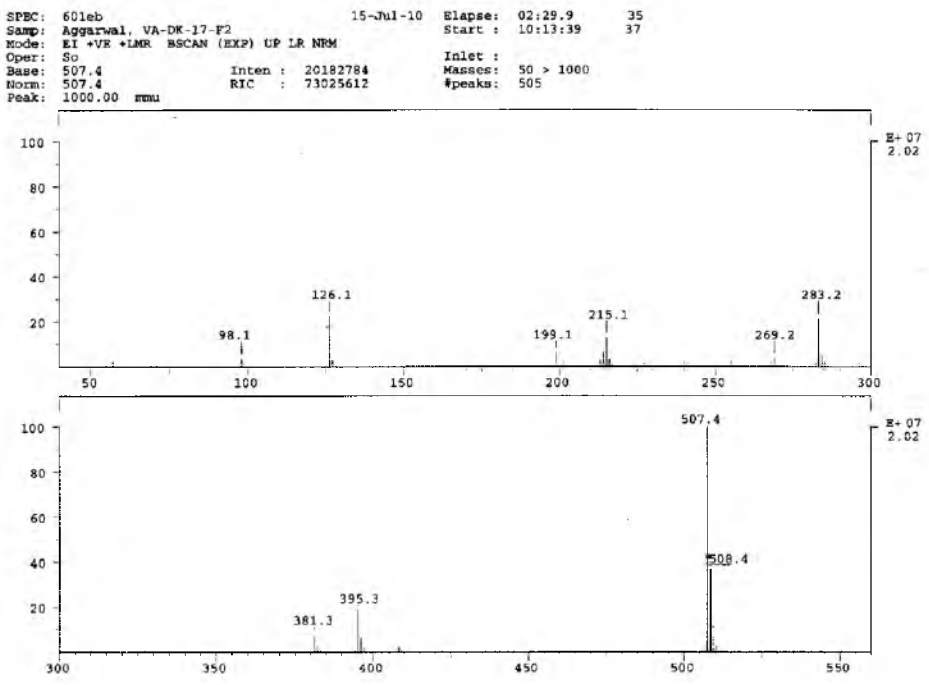
SPEC: 601eb 15-Jul-10 Elapse: 02:29.9 35
Samp: Aggarwal, VA-DK-17-F2 Start : 10:13:39 37
Mode: EI +VE +LMR BSCAN (EXP) UP LR NRM
Oper: So Inlet :
Base: 507.4 Inten : 20182784 Masses: 50 > 1000
Norm: 507.4 RIC : 73025612 #peaks: 505
Peak: 1000.00 mmu
E+ 07
2.02
98.1
126.1
199.1
215.1
269.2
283.2
507.4
508.4
381.3
395.3

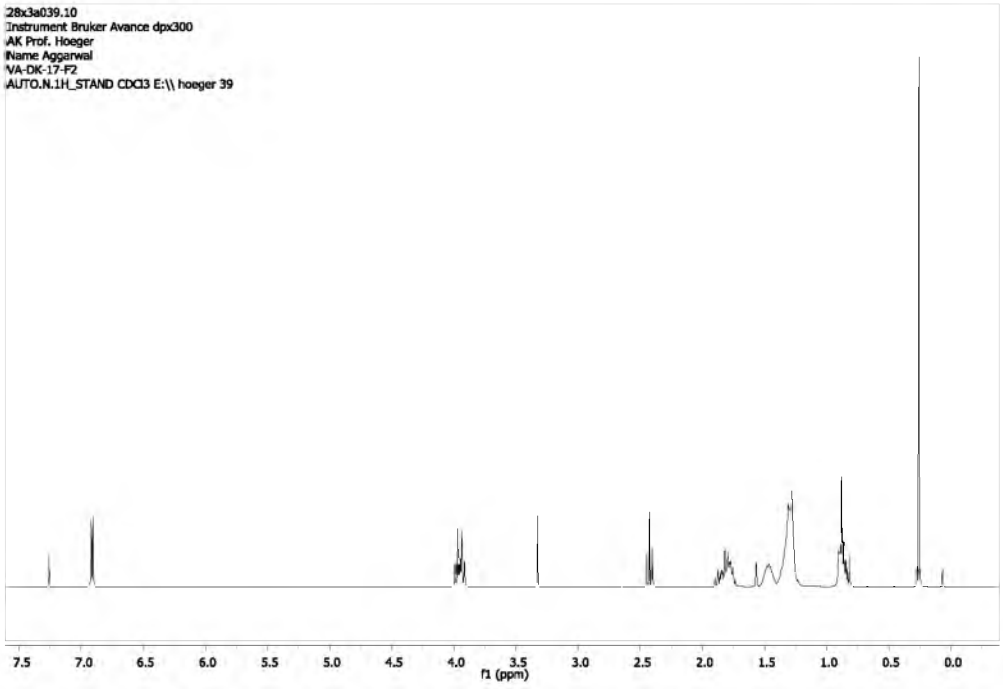
28x3a039.10
Instrument Bruker Avance dpx300
AK Prof. Hoeger
Name Aggarwal
VA-DK-17-F2
AUTO.N.1H_STAND CDCl3 E:\\ hoeger 39
f1 (ppm)

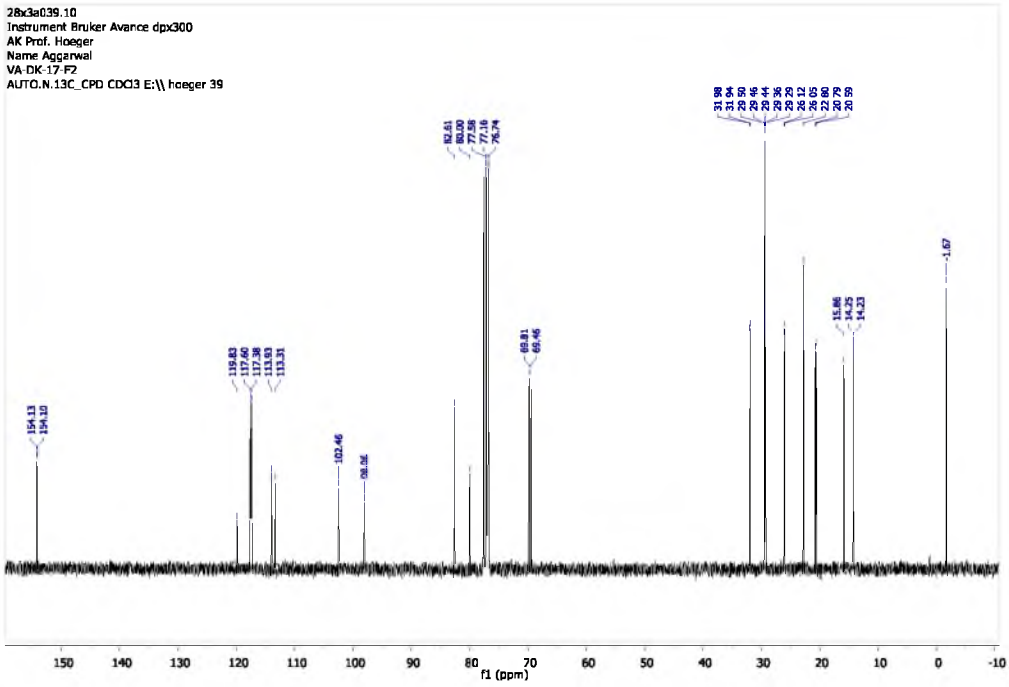
28x3a039.10
Instrument Bruker Avance dpx300
AK Prof. Hoeger
Name Aggarwal
VA-DK-17-F2
AUTO.N.13C_CPD CDCl3 E:\\ hoeger 39
154.13
154.10
119.83
117.60
117.38
113.93
113.31
102.46
98.86
82.61
80.00
77.58
77.16
76.74
69.81
69.46
31.98
31.54
29.90
29.46
29.44
29.36
29.29
26.12
25.65
25.60
22.79
20.59
15.86
14.25
14.23
-1.67
150
140
130
120
110
100
90
80
70
60
50
40
30
20
10
0
-10
f1 (ppm)

S7

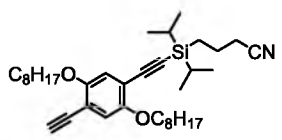

S5 (9.60 g, 25.1 mmol) was suspended in THF (160 mL) and ethylmagnesium bromide (1.0 M solution in THF) (26.4 mmol, 26.4 mL) was added slowly at r.t. The resulting solution was stirred for 60 min prior to the addition of 3-cyanopropyldimethylsilyl chloride (97 %) (7.89 g, 35.1 mmol, 8.1 mL). After 18 h the conversion of **S5** was not sufficient yet. Therefore, ethylmagnesium bromide (1.0 M solution in THF) (7.5 mmol, 7.5 mL) and 30 min later 3-cyanopropyldimethylsilyl chloride (97 %, CPDIPS-Cl)[14] (1.13 g, 5.0 mmol, 1.2 mL) were added. After stirring overnight, the reaction was diluted with dichloromethane and aq. H_2SO_4 (10 %). The organic phase was washed with water and brine, and dried over $MgSO_4$. Removal of the solvent and purification by column chromatography (CH:DCM = 3:1), yielded **S7** (6.50 g, 11.5 mmol, 46 %) as a yellowish solid.

^{1}H NMR (400 MHz, $CDCl_3$, 298 K) δ [ppm] = 6.91 (s, 1 H), 6.90 (s, 1 H), 3.98 (t, $^3J_{H,H}$ = 6.6 Hz, 2 H), 3.93 (t, $^3J_{H,H}$ = 6.4 Hz, 2 H), 3.33 (s, 1 H), 2.42 (t, $^3J_{H,H}$ = 7.0 Hz, 2 H), 2.00 – 1.66 (m, 6 H), 1.54 – 1.40 (m, 4 H), 1.40 – 1.21 (m, 16 H), 1.16 – 1.01 (m, 14 H), 0.94 – 0.78 (m, 8 H); ^{13}C NMR (101 MHz, $CDCl_3$, 298 K) δ [ppm] = 154.27, 154.03, 119.89, 117.66, 117.21, 114.05, 113.19, 103.76, 95.40, 82.50, 80.08, 69.90, 69.32, 32.00, 31.93, 29.54, 29.51, 29.44, 29.36, 29.33, 26.23, 26.05, 22.81, 22.80, 21.42, 20.89, 18.37, 18.12, 14.25, 14.23, 11.92, 9.75; MS (EI, 70 eV) (calcd. for $C_{36}H_{57}NO_2Si$: 563.42): m/z (%) 563.4 (100) $[M]^+$, 520.3 (75) $[M\text{-}C_3H_7]^+$, 408.2 (11) $[M\text{-}C_{11}H_{23}]^+$.

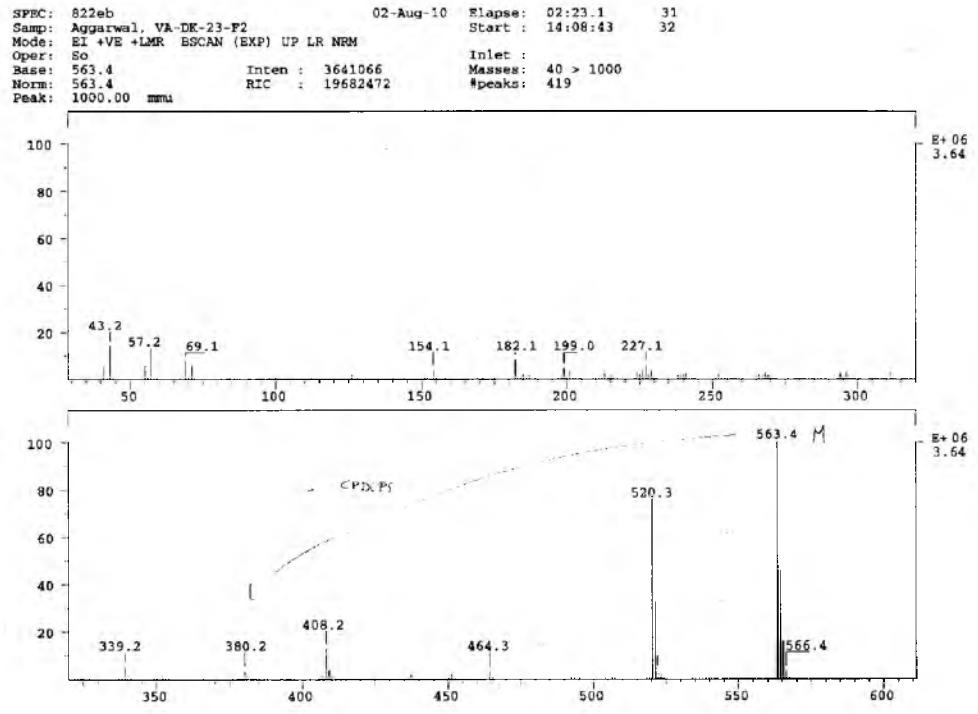
SPEC: 822eb 02-Aug-10 Elapse: 02:23.1 31
Samp: Aggarwal, VA-DK-23-F2 Start : 14:08:43 32
Mode: EI +VE +LMR BSCAN (EXP) UP LR NRM
Oper: So Inlet :
Base: 563.4 Inten : 3641066 Masses: 40 > 1000
Norm: 563.4 RIC : 19682472 #peaks: 419
Peak: 1000.00 mmu
E+06
3.64
43.2
57.2
69.1
154.1
182.1
199.0
227.1
563.4 M
520.3
408.2
339.2
380.2
464.3
566.4

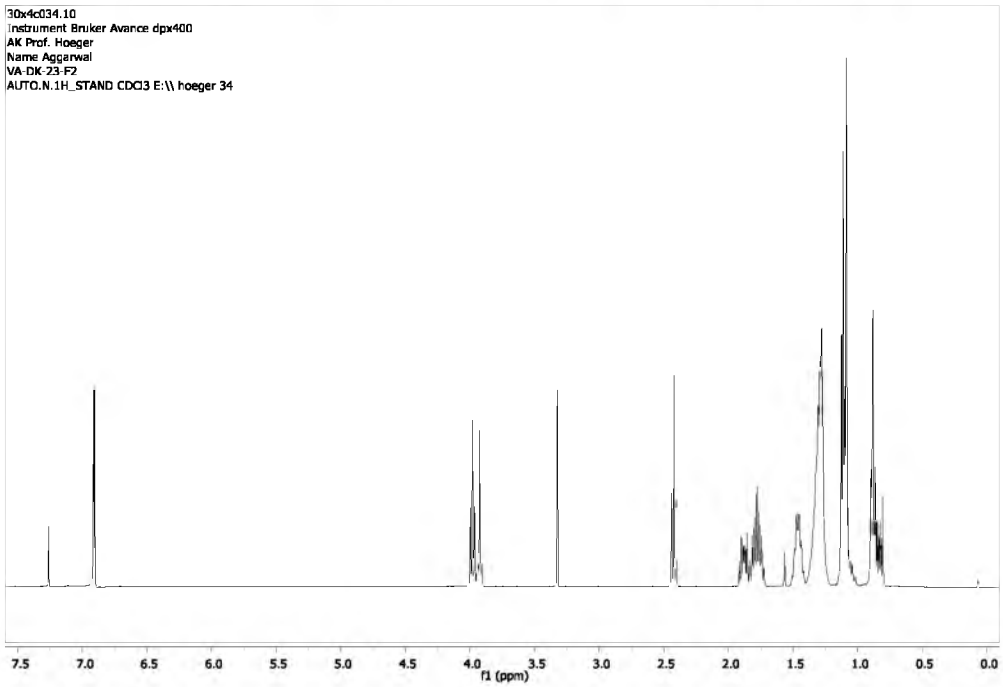
30x4c034.10
Instrument Bruker Avance dpx400
AK Prof. Hoeger
Name Aggarwal
VA-DK-23-F2
AUTO.N.1H_STAND CDCl3 E:\\ hoeger 34
f1 (ppm)

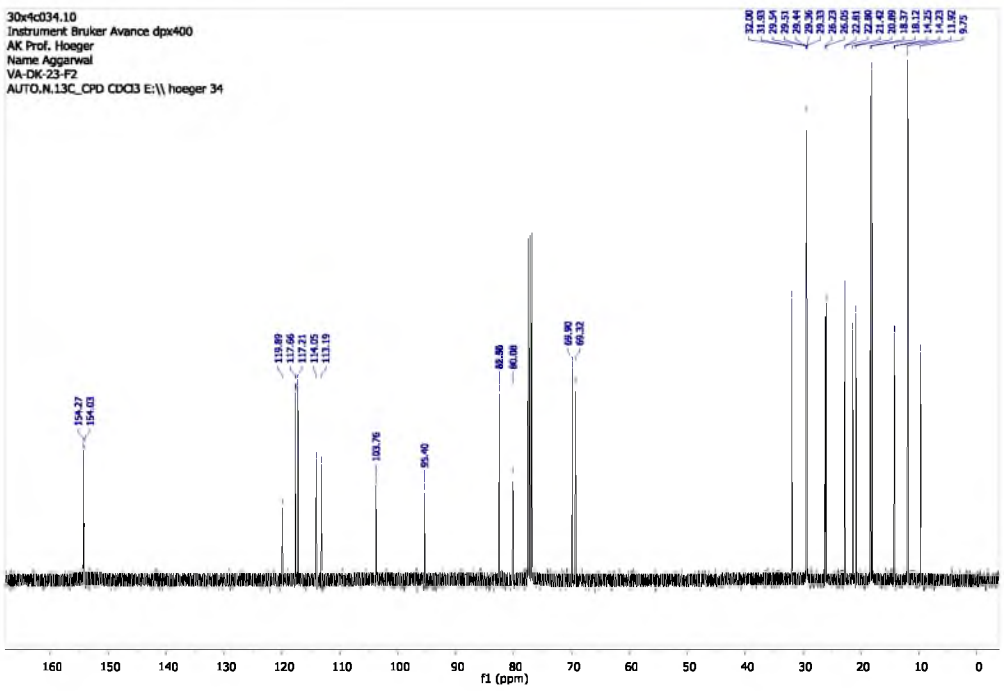

S9

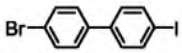

4-bromobiphenyl (**S8**) (3.00 g, 12.87 mmol), iodine (1.80 g, 7.1 mmol), iodic acid (0.60 g, 3.22 mmol), carbon tetrachloride (5.0 mL), water (0.3 mL), glacial acetic acid (22.0 mL), and conc. H_2SO_4 (1.8 mL) were mixed and refluxed at 110 °C overnight. Then, a second portion of iodic acid (0.06 g, 0.4 mmol) and iodine (0.18 g, 0.7 mmol) were added and refluxing was continued for 4 h. After cooling to r.t., the reaction was diluted with dichloromethane and aq. $NaHSO_3$ (10 %). The organic phase was washed with aq. $NaHSO_3$ (10 %), water, and brine, and dried over $MgSO_4$. Removal of the solvent and recrystallisation from methanol yielded **S9**[15] (3.97 g, 11.1 mmol, 86 %) as a white solid.

^{1}H NMR (300 MHz, $CDCl_3$, 298 K) δ [ppm] = 7.82 – 7.73 (m, 2 H), 7.61 – 7.53 (m, 2 H), 7.46 – 7.38 (m, 2 H), 7.33 – 7.27 (m, 2 H); ^{13}C NMR (75 MHz, $CDCl_3$, 298 K) δ [ppm] = 139.62, 139.09, 138.13, 132.16, 128.87, 128.59, 122.14, 93.60; MS (EI, 70 eV) (calcd. for $C_{12}H_8BrI$: 357.89): m/z (%) 357.9 (100) $[M]^+$, 152.0 $[M\text{-}BrI]^+$. EI-MS reveals the presence of traces of 4,4'-diiodobiphenyl (m/z = 405.9).

3

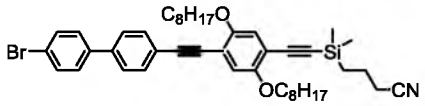

S9 (2.65 g, 7.38 mmol), $Pd(PPh_3)_2Cl_2$ (0.10 g, 0.15 mmol), CuI (0.04 g, 0.22 mmol), and PPh_3 (0.12 g, 0.44 mmol) were dissolved in THF (12 mL) and piperidine (60 mL). **S6** (4.99 g, 9.82 mmol) was added at r.t. and the reaction was stirred overnight at 50 °C. After cooling to r.t., the reaction was terminated by the addition of aq. H_2SO_4 (10 %) and dichloromethane. Following extraction of the aqueous phase with dichloromethane, the combined organic phases were washed subsequently with aq. H_2SO_4 (10 %, until acidic), water, and brine. Drying over $MgSO_4$ and concentration *in vacuo* gave the crude product that was purified by column chromatography (first column: CH:DCM = 2:1 – 3:4; second column: CH:DCM = 3:2). **3**(2.93 g, 3.96 mmol, 54 %) was obtained as slightly yellow solid. In addition, the twofold coupling product was isolated, too (1.92 g, 1.65 mmol, 22 %).

^{1}H NMR (300 MHz, $CDCl_3$, 298 K) δ [ppm] = 7.66 – 7.50 (m, 6 H), 7.50 – 7.42 (m, 2 H), 6.98 (s, 1 H), 6.95 (s, 1 H), 4.07 – 3.94 (m, 4 H), 2.44 (t, $^3J_{H,H}$ = 7.0 Hz, 2 H), 1.96 – 1.73 (m, 6 H), 1.64 – 1.45 (m, 4 H), 1.45 – 1.19 (m, 16 H), 0.96 – 0.79 (m, 8 H), 0.34 – 0.22 (m, 6 H); ^{13}C NMR (75 MHz, $CDCl_3$, 298 K) δ [ppm] = 154.35, 153.61, 139.84, 139.38, 132.23, 132.11, 128.68, 126.90, 122.88, 122.08, 119.84, 117.46, 116.71, 114.64, 113.37, 102.72, 98.00, 94.90, 86.99, 69.80, 69.47, 31.99, 31.96, 29.53, 29.52, 29.50, 29.48, 29.46, 27.05, 26.23, 26.15, 22.82, 20.81, 20.60, 15.90, 14.24, -1.64; MS (EI, 70 eV) (calcd. for $C_{44}H_{56}BrNO_2Si$: 737.33): m/z (%) 737.3/739.3 (87/100) $[M]^+$, 126.1 (22) $[C_6H_{12}NSi]^+$.

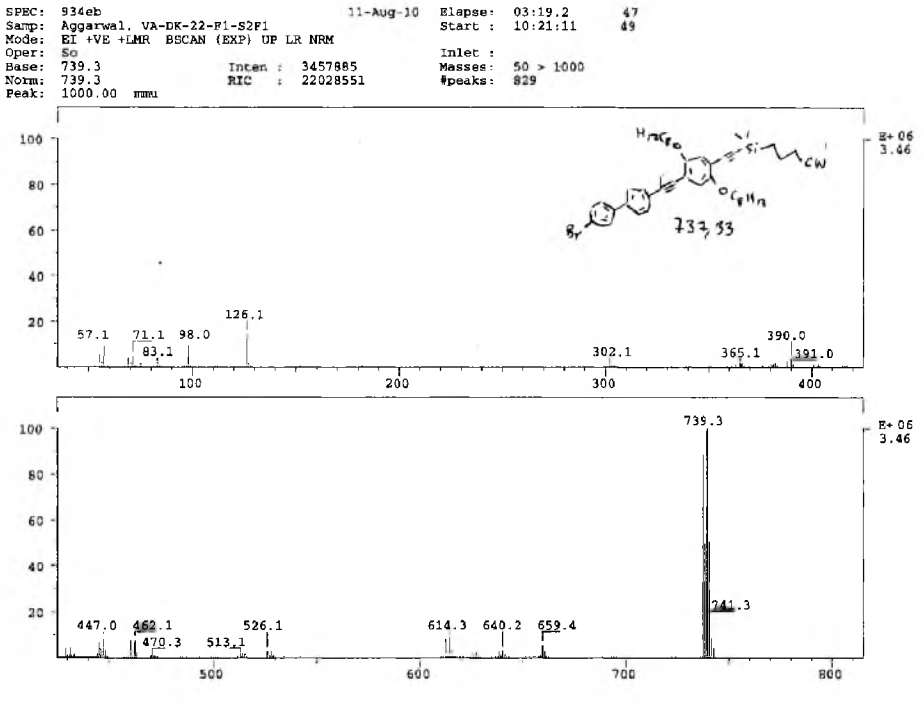
SPEC: 934eb 11-Aug-10 Elapse: 03:19.2 47
Samp: Aggarwal, VA-DK-22-F1-S2F1 Start : 10:21:11 49
Mode: EI +VE +LMR BSCAN (EXP) UP LR NRM
Oper: So Inlet :
Base: 739.3 Inten : 3457885 Masses: 50 > 1000
Norm: 739.3 RIC : 22028551 #peaks: 829
Peak: 1000.00 mmu
E+06
3.46
126.1
57.1
71.1
98.0
83.1
302.1
365.1
390.0
391.0
739.3
241.3
447.0
462.1
470.3
513.1
526.1
614.3
640.2
659.4

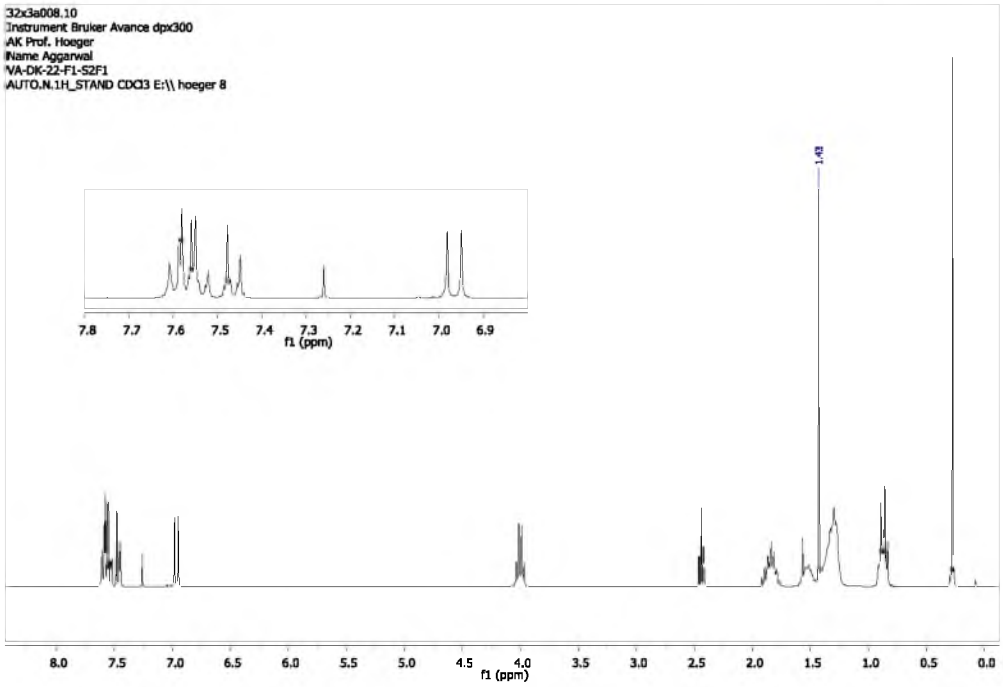
32x3a008.10
Instrument Bruker Avance dpx300
AK Prof. Hoeger
Name Aggarwal
VA-DK-22-F1-S2F1
AUTO.N.1H_STAND CDCl3 E:\\ hoeger 8
f1 (ppm)

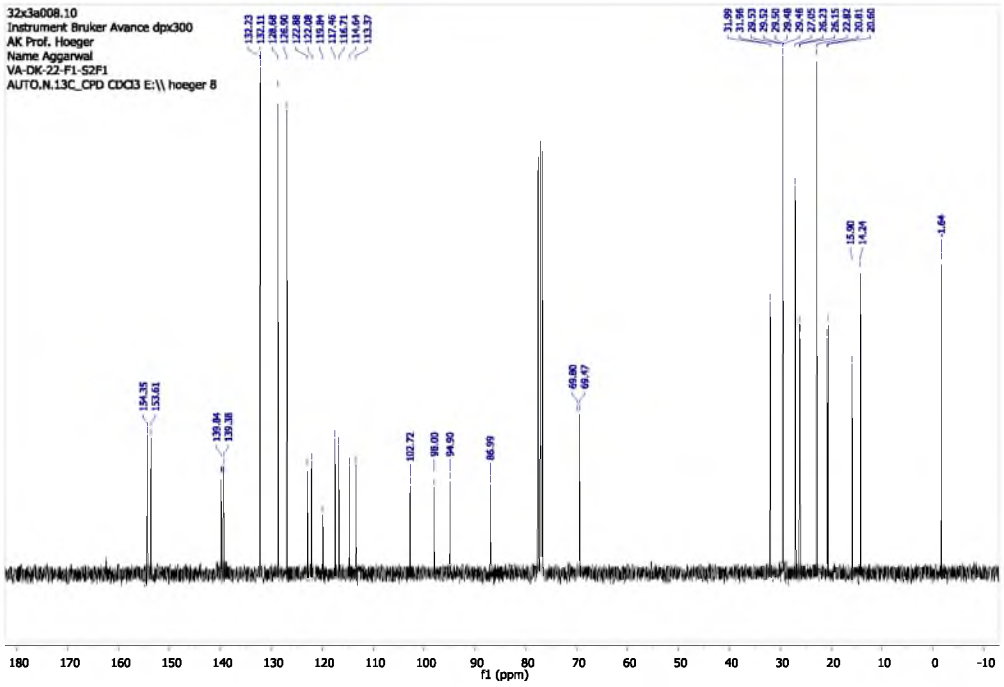

2

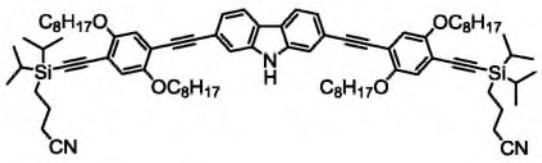

S12 (100 mg, 308 µmol) was dissolved in THF (3 mL) and *n*-BuLi (1.6M in hexane) (0.2 mmol, 0.2 mL) was added at 0 °C. Stirring was continued for 30 min, before trimethylsilyl chloride (97 %) (36.2 mg, 323 µmol, 43µL) was added at r.t. After additional 30 min of stirring, $Pd(PPh_3)_2Cl_2$ (4.3 mg, 6 µmol), CuI (1.8 mg, 9 µmol), PPh_3 (4.8 mg, 18 µmol), and piperidine (6 mL) were added and stirred for 5 min. Then **S7** (381.7 mg, 677 µmol) was added and the reaction was heated to 80 °C. Since the conversion was not complete after one night, additional $Pd(PPh_3)_2Cl_2$ (6.3 mg, 9 µmol), CuI (3.0 mg, 16 µmol), PPh_3 (6.4 mg, 24 µmol), and **S7** (92.1 mg, 163 µmol) were added and the reaction was stirred another 20 h at 80 °C. Then, the reaction was cooled to r.t. and diluted with aq. H_2SO_4 (10 %) and dichloromethane. After phase separation and extraction of the aqueous layer with dichloromethane, the combined organic phases were washed subsequently with aq. H_2SO_4 (10 %, until acidic), water, and brine. Drying over $MgSO_4$ and concentration *in vacuo* gave the crude product that was purified by column chromatography (first column: CH:DCM = 1:3; second column: CH:DCM = 1:2). **2** (318.1 mg, 246 µmol, 80 %) was obtained as a yellow solid.

^{1}H NMR (400 MHz, $CDCl_3$, 298 K) δ [ppm] = 8.28 (s, 1 H), 8.00 (d, $^{3}J_{H,H}$ = 8.1 Hz, 2 H), 7.61 (s, 2 H), 7.43 (d, $^{3}J_{H,H}$ = 8.1 Hz, 2 H), 7.01 (s, 2 H), 6.97 (s, 2 H), 4.05 (t, $^{3}J_{H,H}$ = 6.4 Hz, 4 H), 3.99 (t, $^{3}J_{H,H}$ = 6.4 Hz, 4 H), 2.44 (t, $^{3}J_{H,H}$ = 7.0 Hz, 4 H), 1.99 – 1.73 (m, 12 H), 1.64 – 1.44 (m, 8 H), 1.44 – 1.21 (m, 32 H), 1.21 – 1.02 (m, 28 H), 0.97 – 0.79 (m, 16 H); ^{13}C NMR (126 MHz, $CDCl_3$, 298 K) δ [ppm] = 154.51, 153.50, 139.85, 123.83, 123.25, 121.03, 120.50, 119.95, 117.75, 116.31, 114.78, 113.84, 113.27, 104.06, 96.23, 95.24, 86.16, 69.92, 69.31, 32.01, 31.98, 29.58, 29.56, 29.49, 29.46, 27.04, 26.27, 26.24, 22.83, 22.79, 21.44, 20.91, 18.39, 18.15, 14.25, 14.23, 11.94, 9.77; MS (MALDI-TOF, DCTB) (calcd. for $C_{84}H_{119}N_3O_4Si_2$ monoisotopic: 1289.87, distr. max.: 1291.03): *m/z* 1289.9 $[M]^+$; GPC (in THF vs. PS): M_p = 1840 g mol^{-1}.

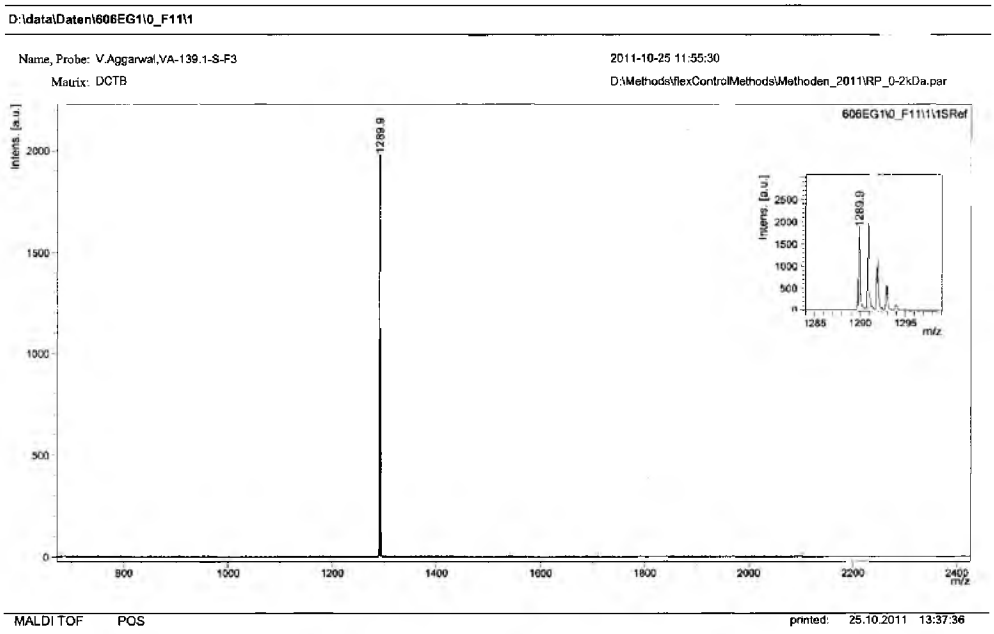

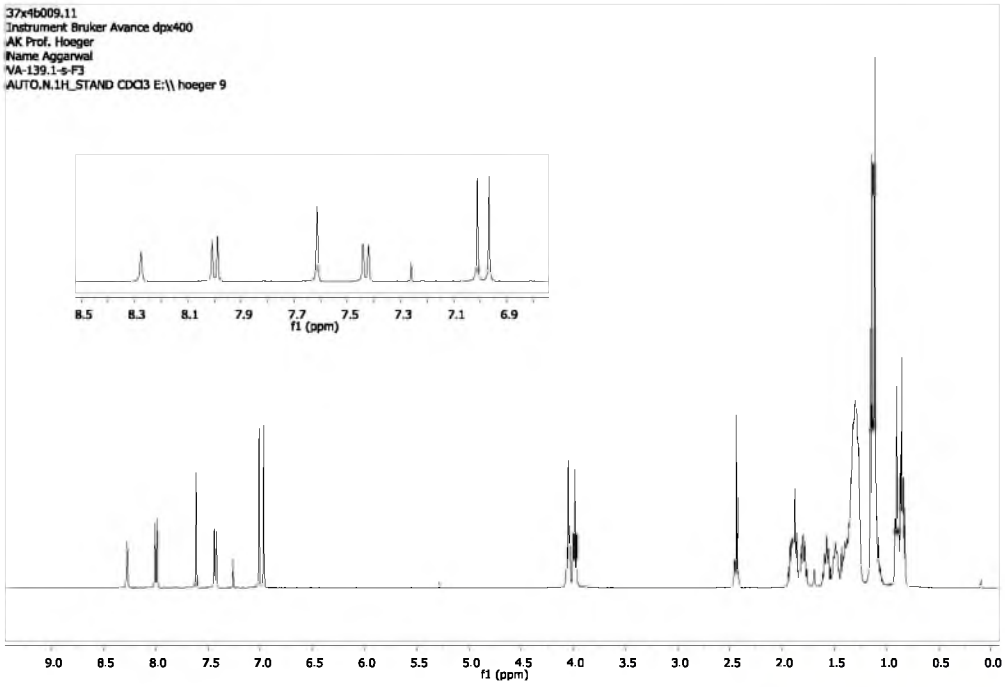
37x4b009.11
Instrument Bruker Avance dpx400
AK Prof. Hoeger
Name Aggarwal
VA-139.1-s-F3
AUTO.N.1H_STAND CDCl3 E:\\ hoeger 9
f1 (ppm)

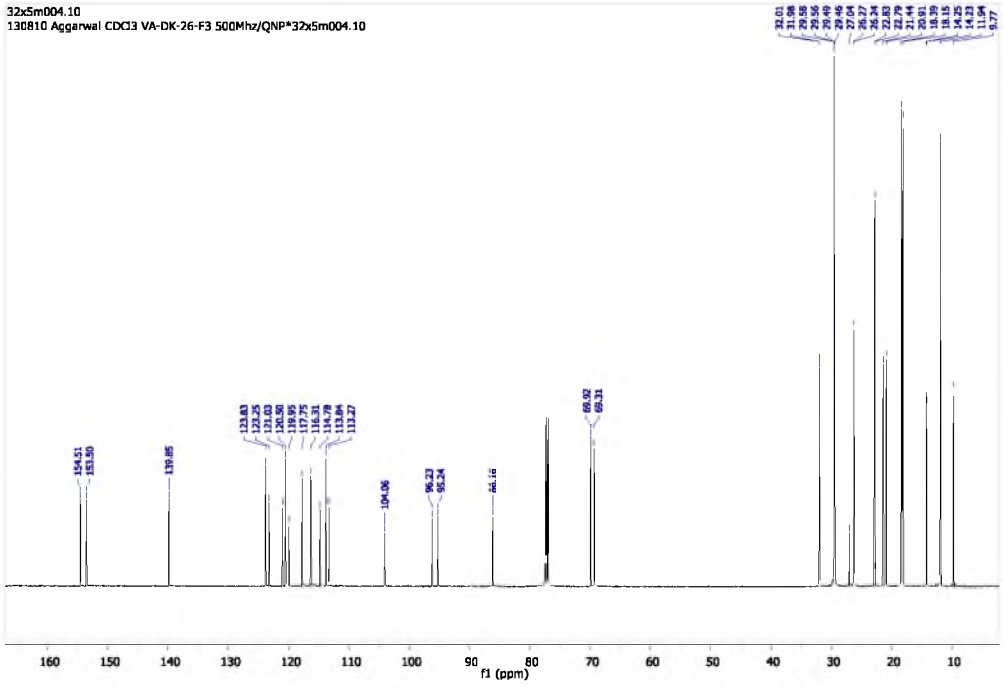
32x5m004.10
130810 Aggarwal CDCl3 VA-DK-26-F3 500Mhz/QNP*32x5m004.10
f1 (ppm)

4

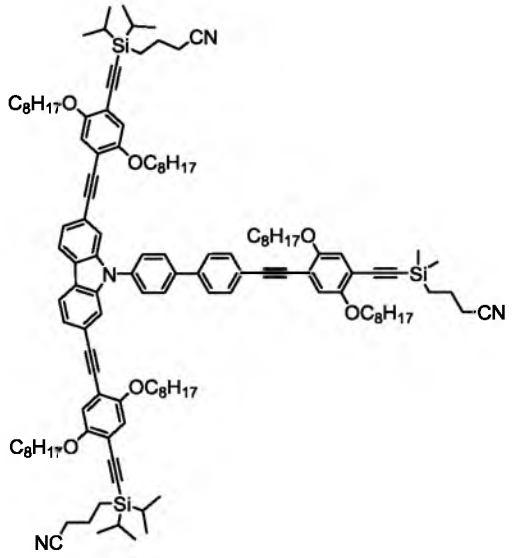

2 (608 mg, 471 µmol), **3** (487 mg, 659 µmol) and 2-di-*t*-butylphosphino-2′,4′,6′-triisopropylbiphenyl (*t*Bu-XPhos) (120 mg, 283 µmol) were dissolved in toluene (20 mL) and heated to 80 °C. After 5 min, a mixture of Pd_2dba_3 (86 mg, 94 µmol) and NaO*t*Bu (82 mg, 848 µmol) was added at 80 °C under argon flow. After 1 h, the reaction was cooled to r.t., diluted with MTBE, and washed with aq. H_2SO_4 (10 %), water, and brine. Drying over $MgSO_4$ and concentration *in vacuo* gave the crude product that was purified by column chromatography (CH:DCM = 4:3) and recGPC. **4** (603 mg, 309 µmol, 66 %) was obtained as a yellow oil.

^{1}H NMR (400 MHz, $CDCl_3$, 298 K) δ [ppm] = 8.09 (d, $^3J_{H,H}$ = 8.1 Hz, 2 H), 7.93 – 7.83 (m, 2 H), 7.75 – 7.60 (m, 8 H), 7.55 – 7.46 (m, 2 H), 7.01 (s, 1 H), 6.99 – 6.95 (m, 3 H), 6.94 (s, 2 H), 4.09 – 3.99 (m, 8 H), 3.96 (t, $^3J_{H,H}$ = 6.4 Hz, 4 H), 2.51 – 2.39 (m, 6 H), 1.98 – 1.73 (m, 18 H), 1.68 – 1.44 (m, 12 H), 1.44 – 1.17 (m, 48 H), 1.17 – 1.02 (m, 28 H), 0.98 – 0.78 (m, 24 H), 0.33 – 0.26 (m, 6 H); ^{13}C NMR (101 MHz, $CDCl_3$, 298 K) δ [ppm] = 154.36, 154.20, 153.48, 153.37, 141.17, 139.92, 139.76, 136.38, 132.21, 128.50, 127.56, 126.93, 124.11, 123.12, 122.91, 121.11, 120.42, 119.75, 119.70, 117.64, 117.31, 116.61, 116.11, 114.55, 114.49, 113.26, 113.18, 113.04, 103.89, 102.57, 97.88, 96.07, 95.12, 94.73, 86.98, 86.18, 69.74, 69.64, 69.33, 69.14, 31.84, 31.80, 31.74, 29.39, 29.37, 29.33, 29.30, 29.27, 29.26, 29.23, 26.08, 26.07, 25.99, 25.96, 22.67, 22.66, 22.65, 22.63, 22.60, 21.27, 20.73, 20.69, 20.65, 20.44, 18.22, 17.98, 15.73, 14.10, 14.07, 14.05, 11.78, 9.61, -1.80; MS (MALDI-TOF, DCTB) (calcd. for $C_{128}H_{174}N_4O_6Si_3$ monoisotopic: 1947.27, distr. max.: 1949.03): *m/z* 2197.3 $[M+DCTB]^+$, 1947.2 $[M]^+$; GPC (in THF vs. PS): M_p = 2840 g mol^{-1}.

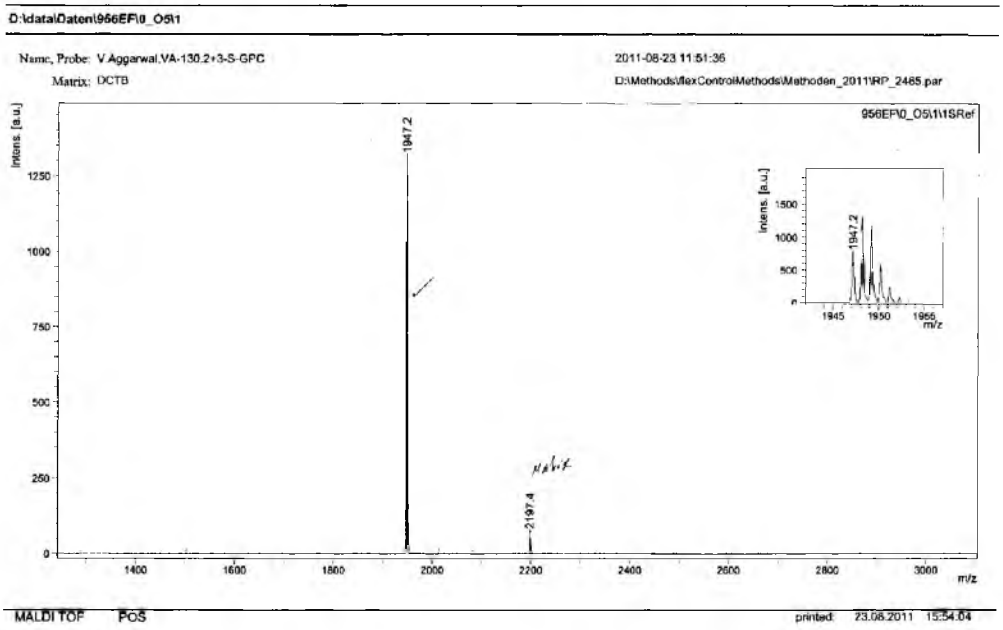
D:\data\Daten\956EF\0_O5\1
Name, Probe: V.Aggarwal,VA-130.2+3-S-GPC
Matrix: DCTB
2011-08-23 11:51:36
D:\Methods\flexControlMethods\Methoden_2011\RP_2465.par
956EF\0_O5\1\1SRef
Intens. [a.u.]
1947.2
2197.4
m/z
MALDI TOF
POS
printed: 23.08.2011 15:54:04

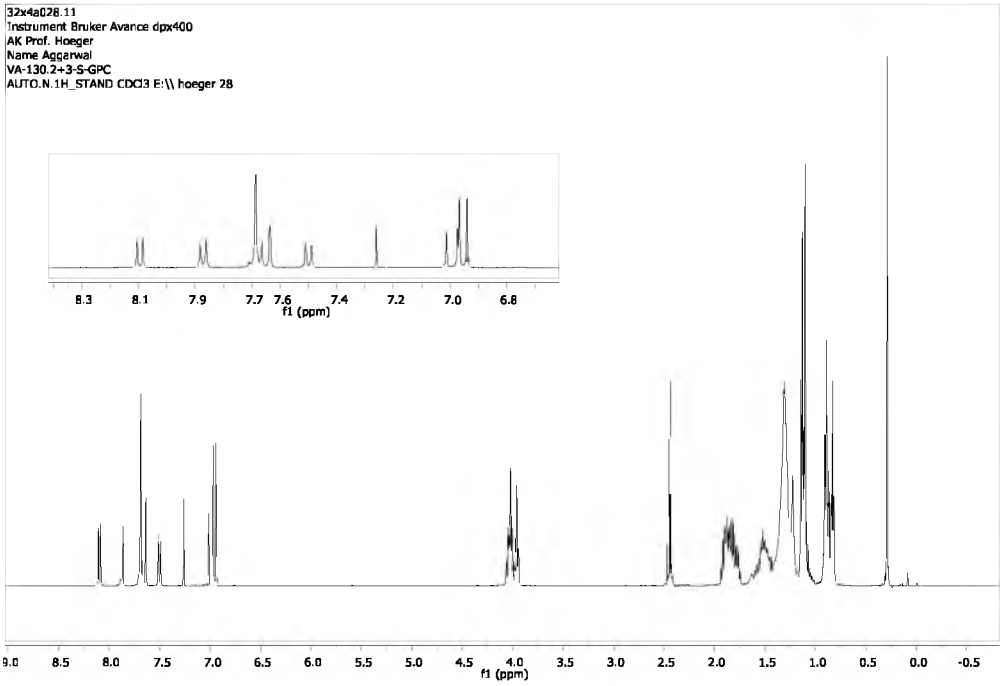
32x4a028.11
Instrument Bruker Avance dpx400
AK Prof. Hoeger
Name Aggarwal
VA-130.2+3-S-GPC
AUTO.N.1H_STAND CDCl3 E:\\ hoeger 28
f1 (ppm)

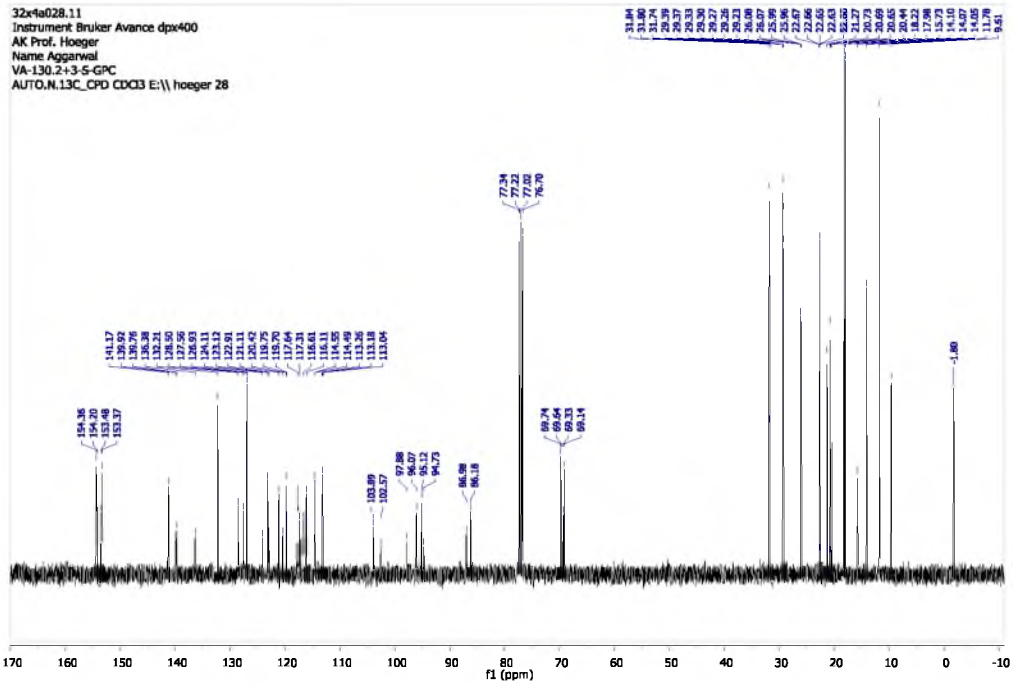
32x4a028.11
Instrument Bruker Avance dpx400
AK Prof. Hoeger
Name Aggarwal
VA-130.2+3-S-GPC
AUTO.N.13C_CPD CDCl3 E:\\ hoeger 28
f1 (ppm)

5

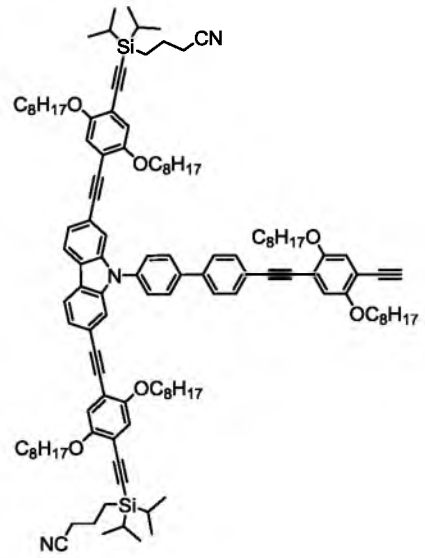

4 (1.068 g, 548 µmol) and K_2CO_3 (379 mg, 2.740 mmol) were suspended in THF (50 mL) and methanol (20 mL) and stirred for 1 h at r.t. before the reaction was diluted with MTBE. The organic phase was washed with aq. H_2SO_4 (10 %, until acidic), water, and brine. After drying over anhydrous $MgSO_4$ and removal of the solvent under reduced pressure, the residue was purified by column chromatography (CH:DCM = 2:1 – 11:9). **5** (945 mg, 518 µmol, 95 %) was obtained a yellow oil that solidified upon standing.

^{1}H NMR (400 MHz, $CDCl_3$, 298 K) δ [ppm] = 8.10 (d, $^3J_{H,H}$ = 8.1 Hz, 2 H), 7.87 (d, $^3J_{H,H}$ = 8.5 Hz, 2 H), 7.76 – 7.61 (m, 8 H), 7.55 – 7.46 (m, 2 H), 7.04 (s, 1 H), 7.01 (s, 1 H), 6.97 (s, 2 H), 6.94 (s, 2 H), 4.11 – 3.99 (m, 8 H), 3.96 (t, $^3J_{H,H}$ = 6.4 Hz, 4 H), 3.37 (s, 1 H), 2.43 (t, $^3J_{H,H}$ = 7.0 Hz, 4 H), 1.97 – 1.72 (m, 16 H), 1.66 – 1.44 (m, 12 H), 1.44 – 1.17 (m, 48 H), 1.17 – 1.00 (m, 28 H), 0.97 – 0.78 (m, 22 H); ^{13}C NMR (101 MHz, $CDCl_3$, 298 K) δ [ppm] = 154.50, 154.31, 153.64, 153.51, 141.31, 140.07, 139.91, 136.53, 132.36, 128.64, 127.70, 127.07, 124.26, 123.27, 123.06, 121.26, 120.56, 119.89, 117.94, 117.79, 117.03, 116.25, 114.70, 113.32, 113.19, 112.86, 104.04, 96.21, 95.26, 94.75, 87.01, 86.33, 82.51, 80.14, 69.89, 69.80, 69.78, 69.28, 31.98, 31.95, 31.94, 31.89, 29.53, 29.51, 29.47, 29.44, 29.42, 29.41, 29.38, 29.37, 29.30, 26.23, 26.21, 26.11, 26.06, 22.82, 22.79, 22.78, 21.42, 20.88, 18.36, 18.12, 14.24, 14.22, 14.20, 11.93, 9.75; MS (MALDI-TOF, DCTB) (calcd. for $C_{122}H_{163}N_3O_6Si_2$ monoisotopic: 1822.21, distr. max.: 1823.79): *m/z* 2072.2 $[M+DCTB]^+$, 1822.0 $[M]^+$; GPC (in THF vs. PS): M_p = 2540 g mol^{-1}.

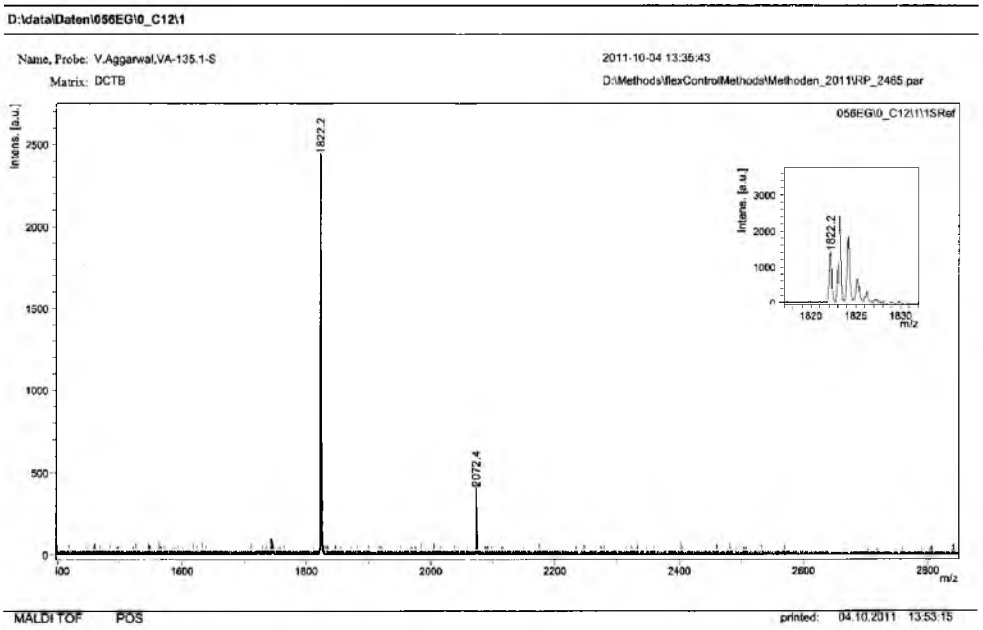
D:\data\Daten\056EG\0_C12\1
Name, Probe: V.Aggarwal,VA-135.1-S
Matrix: DCTB
2011-10-04 13:35:43
D:\Methods\flexControl\Methods\Methoden_2011\RP_2465.par
056EG\0_C12\1\1SRef
Intens. [a.u.]
1822.2
2072.4
m/z
MALDI TOF
POS
printed: 04.10.2011 13:53:15

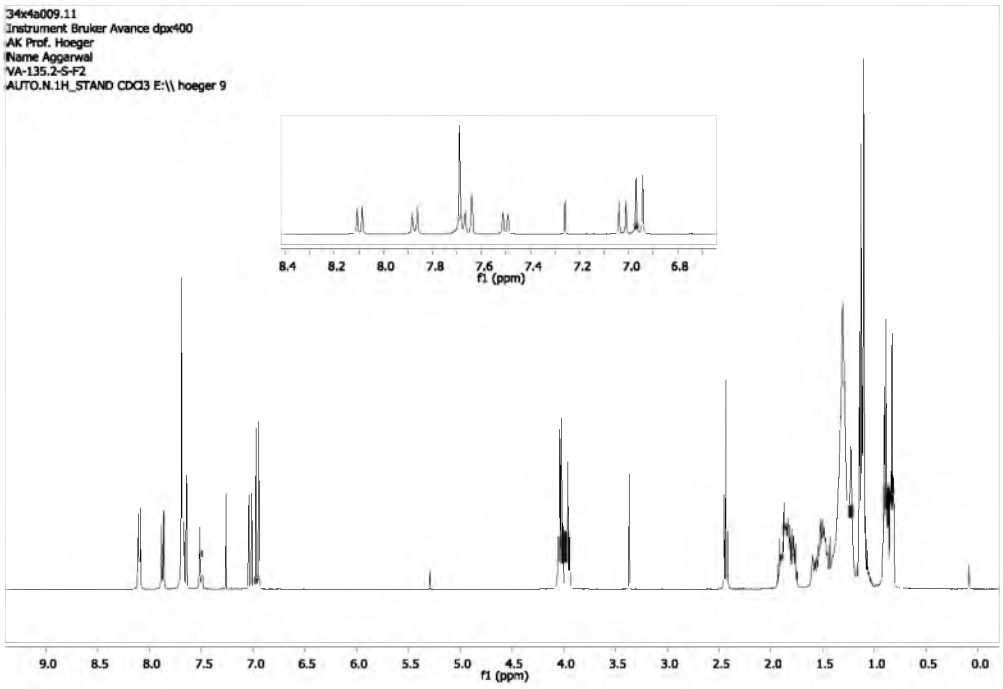
34x4a009.11
Instrument Bruker Avance dpx400
AK Prof. Hoeger
Name Aggarwal
VA-135.2-S-F2
AUTO.N.1H_STAND CDCl3 E:\\ hoeger 9
f1 (ppm)

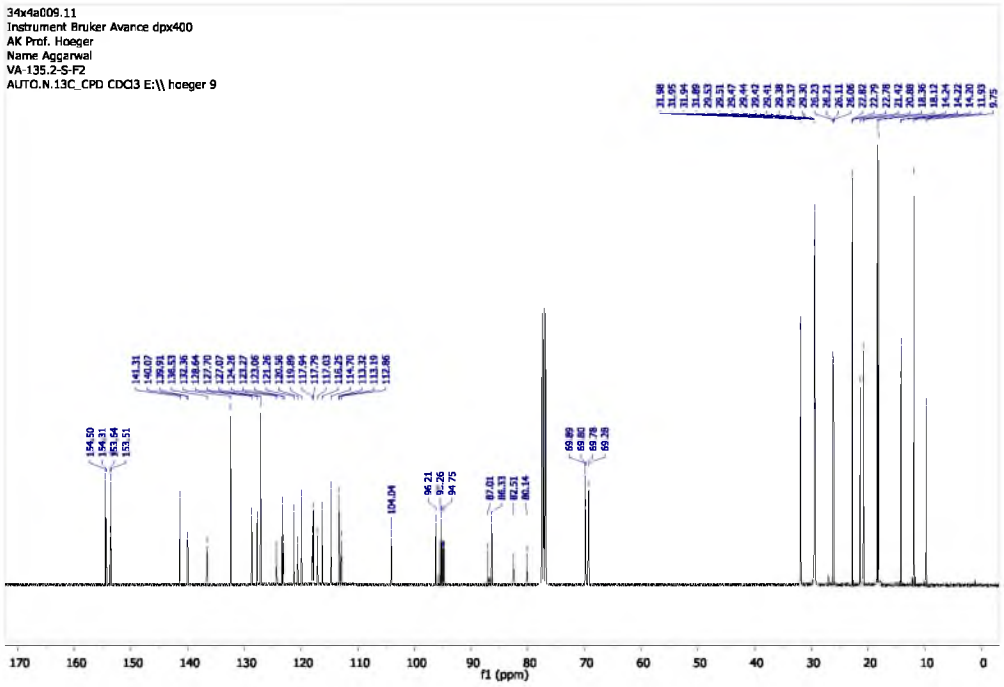
34x4a009.11
Instrument Bruker Avance dpx400
AK Prof. Hoeger
Name Aggarwal
VA-135.2-S-F2
AUTO.N.13C_CPD CDCl3 E:\\ hoeger 9
f1 (ppm)

7

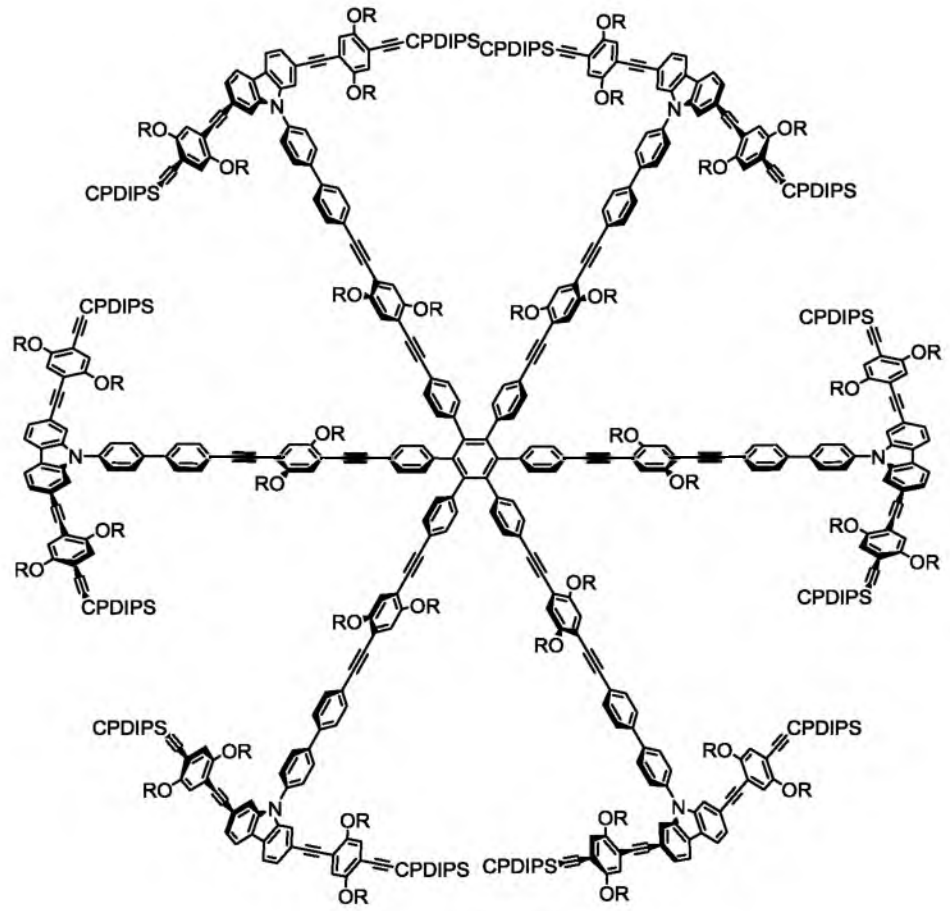

6 (19.0 mg, 14.7 µmol), CuI (3.4 mg, 17.7 µmol), Pd_2dba_3 (4.0 mg, 4.4 µmol), and tri(*t*-butyl)phosphane (6.0 mg, 29.5 µmol) were mixed in a microwave tube and sealed with a septum. In parallel, a solution of **5** (241.7 mg, 132.6 µmol) in piperidine (2 mL) was purged with argon for 1 h. Then the latter was transferred to the microwave tube and the mixture was heated at 120 °C for 16 min in a microwave instrument (max. power: 300 W). After cooling to r.t., the tube was opened and the reaction mixture was diluted with MTBE. The organic phase was washed with aq. H_2SO_4 (10 %) and brine. It was dried over $MgSO_4$ and the solvent was removed under reduced pressure. The residue was purified by column chromatography (CH:DCM = 65:35 - 68:32), and **7** (126 mg, 10.9 µmol, 74 %) was obtained as a yellow solid.

^{1}H NMR (500 MHz, $CDCl_3$, 298 K) δ [ppm] = 8.09 (d, $^{3}J_{H,H}$ = 8.2 Hz, 12 H), 7.87 (d, $^{3}J_{H,H}$ = 8.5 Hz, 12 H), 7.76 – 7.60 (m, 48 H), 7.55 – 7.46 (m, 12 H), 7.16 (d, $^{3}J_{H,H}$ = 8.0 Hz, 12 H), 7.03 (s, 6 H), 7.02 (s, 6 H), 6.96 (s, 12 H), 6.93 (s, 12 H), 6.86 (d, $^{3}J_{H,H}$ = 8.1 Hz, 12 H), 4.10 – 3.99 (m, 48 H), 3.99 – 3.90 (m, 24 H), 2.42 (t, $^{3}J_{H,H}$ = 7.0 Hz, 24 H), 1.95 – 1.72 (m, 96 H), 1.62 – 1.16 (m, 360 H), 1.15 – 0.97 (m, 168 H), 0.97 – 0.76 (m, 132 H); ^{1}H NMR (500 MHz, CD_2Cl_2, 298 K) δ [ppm] = 8.14 (d, $^{3}J_{H,H}$ = 8.1 Hz, 12 H), 7.92 (d, $^{3}J_{H,H}$ = 8.5 Hz, 12 H), 7.79 – 7.66 (m, 36 H), 7.64 (s, 12 H), 7.54 – 7.44 (m, 12 H), 7.20 (d, $^{3}J_{H,H}$ = 8.2 Hz, 12 H), 7.05 (s, 6 H), 7.02 (s, 6 H), 6.99 (s, 12 H), 6.97 – 6.93 (m, 24 H), 4.08 – 3.98 (m, 48 H), 3.98 – 3.92 (m, 24 H), 2.41 (t, $^{3}J_{H,H}$ = 7.0 Hz, 24 H), 1.96 – 1.71 (m, 96 H), 1.65 – 1.17 (m, 360 H), 1.17 – 0.99 (m, 168 H), 0.99 – 0.76 (m, 132 H); ^{13}C NMR (126 MHz, $CDCl_3$, 298 K) δ [ppm] = 154.78, 154.06, 153.94, 153.79, 141.60, 140.49, 140.41, 140.10, 136.79, 132.63, 131.73, 130.90, 128.94, 127.99, 127.36, 124.58, 123.55, 123.50, 121.54, 121.26, 120.86, 120.21, 118.04, 117.40, 117.28, 116.51, 114.96, 114.65, 114.07, 113.58, 113.47, 104.31, 96.51, 95.56, 94.91, 87.61, 86.62, 70.16, 70.04, 70.00, 69.56, 32.27, 32.25, 32.24, 32.18, 29.82, 29.79, 29.75, 29.73, 29.71, 29.68, 26.52, 26.42, 26.40, 23.14, 23.13, 23.09, 23.08, 21.70, 21.17, 18.65, 18.41, 14.63, 14.57, 14.52, 14.50, 12.20, 10.04; ^{13}C NMR (126 MHz, CD_2Cl_2, 298 K) δ [ppm] = 154.88, 154.20, 154.11, 153.93, 141.87, 140.89, 140.63, 140.50, 140.40, 136.88, 132.68, 132.04, 130.83, 129.11, 128.15, 127.61, 124.49, 123.69, 123.50, 121.66, 121.44, 121.10, 120.32, 117.99, 117.47, 117.28, 116.70, 114.90, 114.62, 114.20, 113.84, 113.62, 104.31, 96.45, 95.91, 95.35, 94.94, 87.71, 86.85, 86.80, 70.22, 70.14, 69.82, 32.44, 32.35, 29.97, 29.93, 29.90, 29.88, 29.83, 29.83, 26.69, 26.67, 26.58, 26.54, 23.31, 23.29, 23.25, 23.24, 21.89, 21.22, 18.56, 18.32, 14.57, 14.50, 14.45, 14.43, 12.35, 10.14;MS (MALDI-TOF, DCTB) (calcd. for $C_{774}H_{996}N_{18}O_{36}Si_{12}$ monoisotopic: 11455.39, distr. max.: 11465.32): *m/z*11965.9 $[M+2*DCTB]^{+}$, 11716.6 $[M+DCTB]^{+}$, 11465.3 $[M]^{+}$, 5856.8 $[M+DCTB]^{2+}$, 5733.5 $[M]^{2+}$; GPC (in THF vs. PS): M_p = 11580 g mol^{-1}.

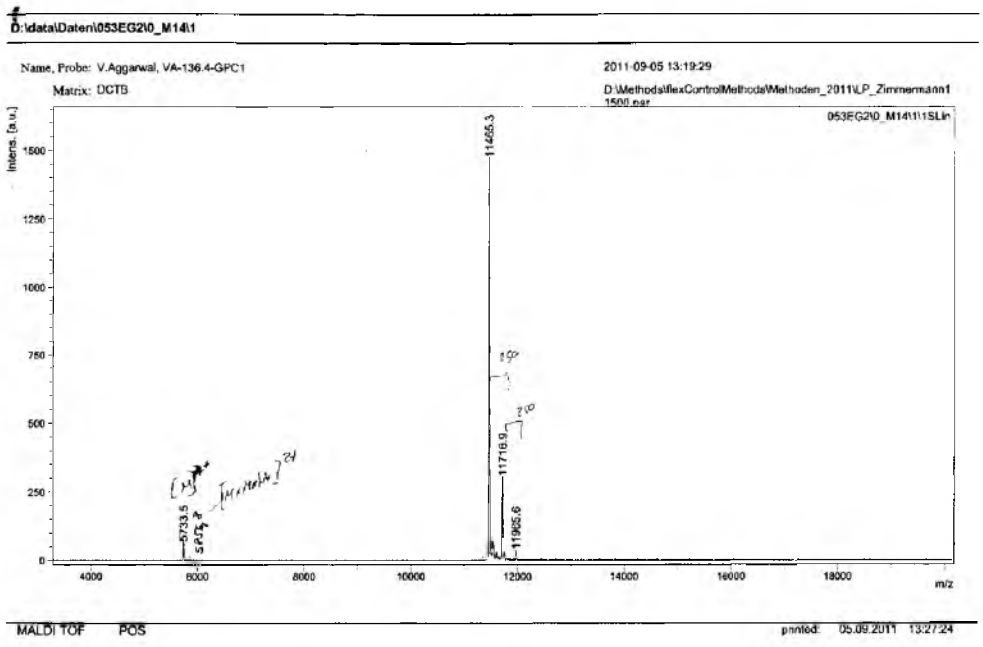
D:\data\Daten\053EG2\0_M14\1
Name, Probe: V.Aggarwal, VA-136.4-GPC1
Matrix: DCTB
2011-09-05 13:19:29
D:\Methods\flexControl\Methoden_2011\LP_Zimmermann1
053EG2\0_M141\1SLin
Intens. [a.u.]
11465.3
11716.9
11965.6
5733.5
[M]+
[M+NaH]+
2H
m/z
MALDI TOF
POS
printed: 05.09.2011 13:27:24

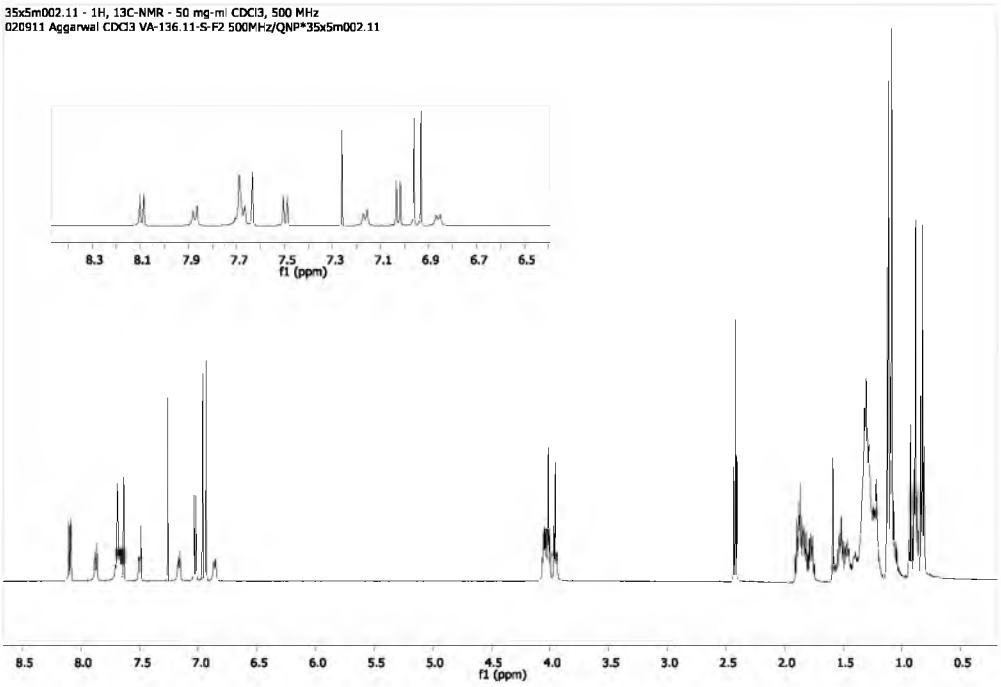
35x5m002.11 - 1H, 13C-NMR - 50 mg-ml CDCl3, 500 MHz
020911 Aggarwal CDCl3 VA-136.11-S-F2 500MHz/QNP*35x5m002.11
f1 (ppm)

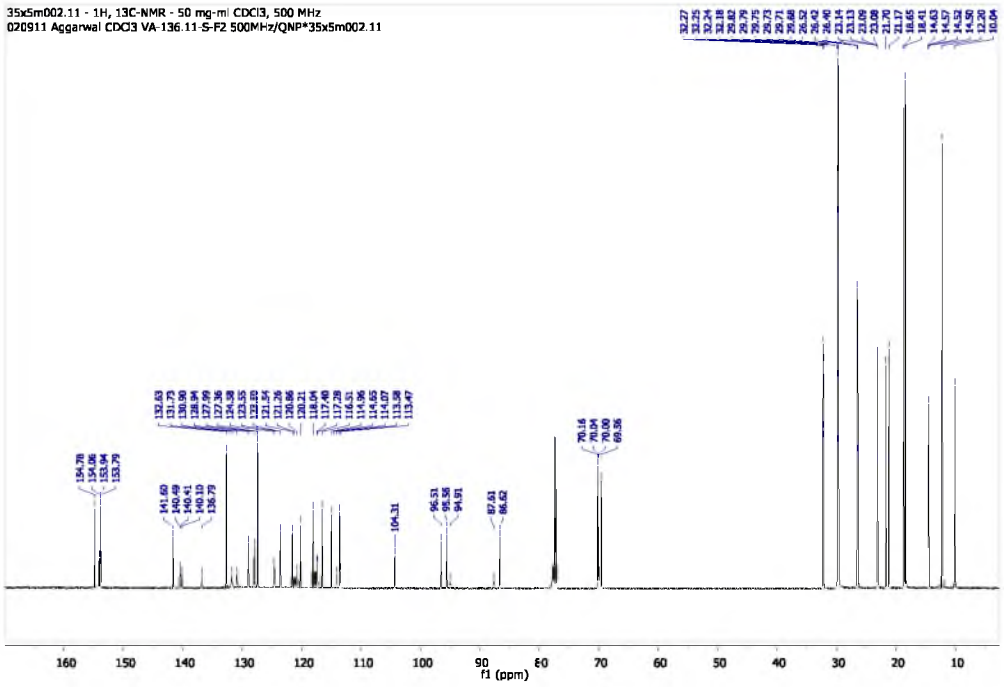
35x5m002.11 - 1H, 13C-NMR - 50 mg-ml CDCl3, 500 MHz
020911 Aggarwal CDCl3 VA-136.11-S-F2 500MHz/QNP*35x5m002.11
f1 (ppm)

8

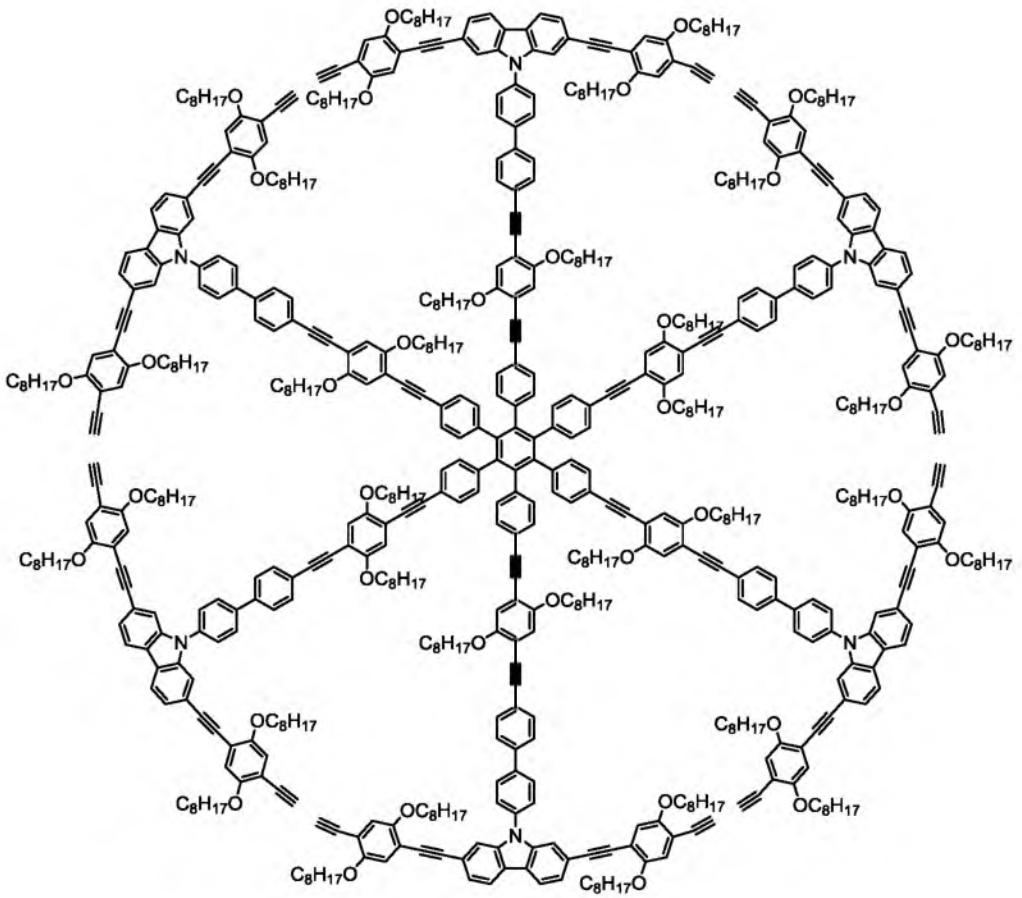

To a solution of **7** (270 mg, 23.5 µmol) in THF (23 mL) a solution of TBAF in THF (1 M) (0.707 mmol, 0.71 mL) was added at 0 °C. The reaction was stirred 20 min at 0 °C and 3 h at r.t. Then, extraction with MTBE and dichloromethane was followed by washing with water and brine. After drying over $MgSO_4$ and removal of the solvent, the crude product was obtained and purified by column chromatography (CH:DCM = 60:40 – 52:48) and recGPC. **8** (166 mg, 17.9 µmol, 74 %) was isolated as a yellow solid.

^{1}H NMR (500 MHz, $CDCl_3$, 298 K) δ [ppm] = 8.09 (d, $^3J_{H,H}$ = 8.1 Hz, 12 H), 7.87 (d, $^3J_{H,H}$ = 8.3 Hz, 12 H), 7.76 – 7.59 (m, 48 H), 7.49 (d, $^3J_{H,H}$ = 8.4 Hz, 12 H), 7.16 (d, $^3J_{H,H}$ = 7.9 Hz, 12 H), 7.03 (s, 6 H), 7.02 (s, 6 H), 6.99 (s, 12 H), 6.97 (s, 12 H), 6.86 (d, $^3J_{H,H}$ = 8.0 Hz, 12 H), 4.14 – 3.93 (m, 72 H), 3.33 (s, 12 H), 1.99 – 1.73 (m, 72 H), 1.65 – 1.14 (m, 360 H), 1.03 – 0.75 (m, 108 H); ^{13}C NMR (126 MHz, $CDCl_3$, 298 K) δ [ppm] = 154.30, 153.77, 153.65, 153.57, 141.30, 140.19, 140.16, 140.12, 139.81, 136.49, 132.34, 131.44, 130.60, 128.65, 127.69, 127.07, 124.27, 123.28, 123.20, 121.22, 120.97, 120.57, 117.95, 117.11, 116.99, 116.84, 114.82, 114.35, 113.78, 113.22, 112.61, 96.19, 95.25,

94.62, 87.32, 86.37, 86.10, 82.46, 80.14, 69.76, 69.72, 31.96, 31.95, 31.92, 31.89, 29.53, 29.50, 29.46, 29.44, 29.42, 29.39, 29.38, 29.34, 29.27, 26.24, 26.13, 26.09, 26.03, 22.85, 22.84, 22.78, 14.34, 14.27, 14.24, 14.20. MS (MALDI-TOF, DCTB) (calcd. for $C_{654}H_{768}N_6O_{36}$ monoisotopic: 9281.84, distr. max.: 9289.11): *m/z* 9788.3 $[M+2*DCTB]^+$, 9539.0 $[M+DCTB]^+$, 9289.1 $[M]^+$, 9170.0 $[M-C_8H_{17}]^+$; GPC (in THF vs. PS): M_p = 11360 g mol^{-1}.

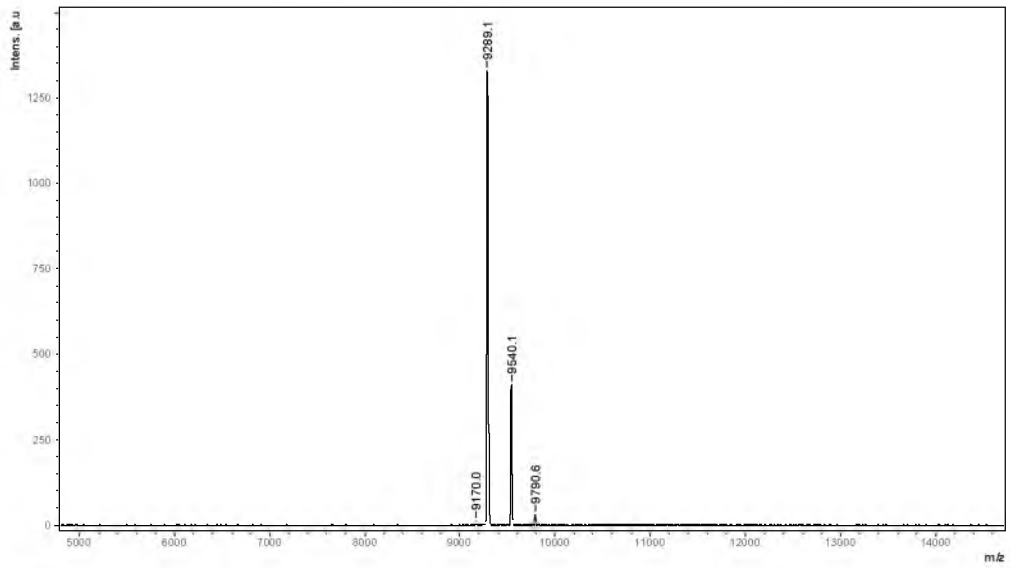

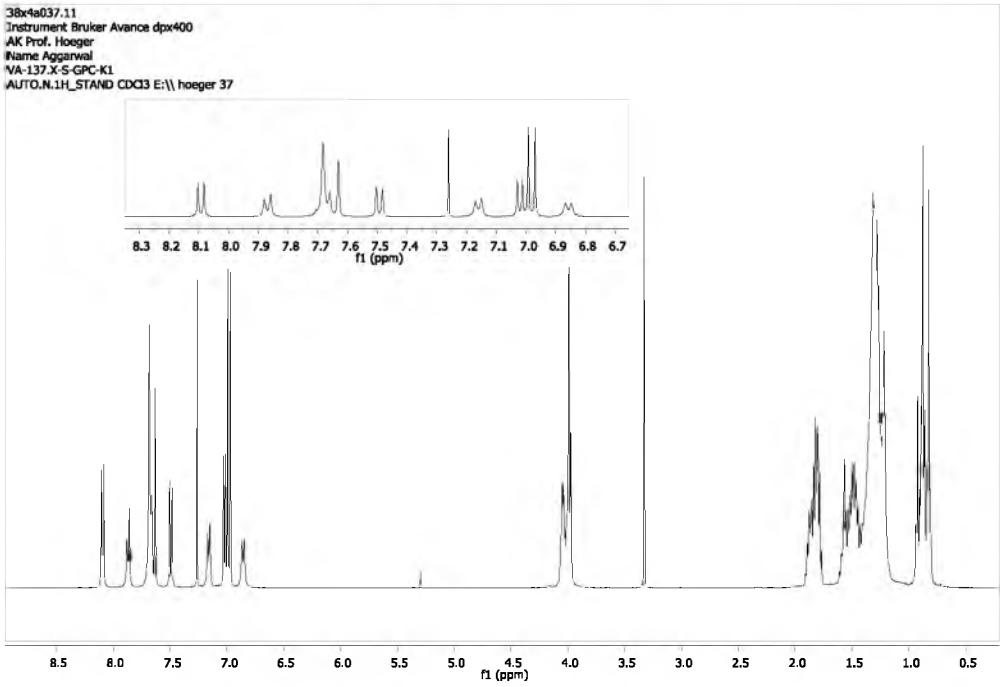

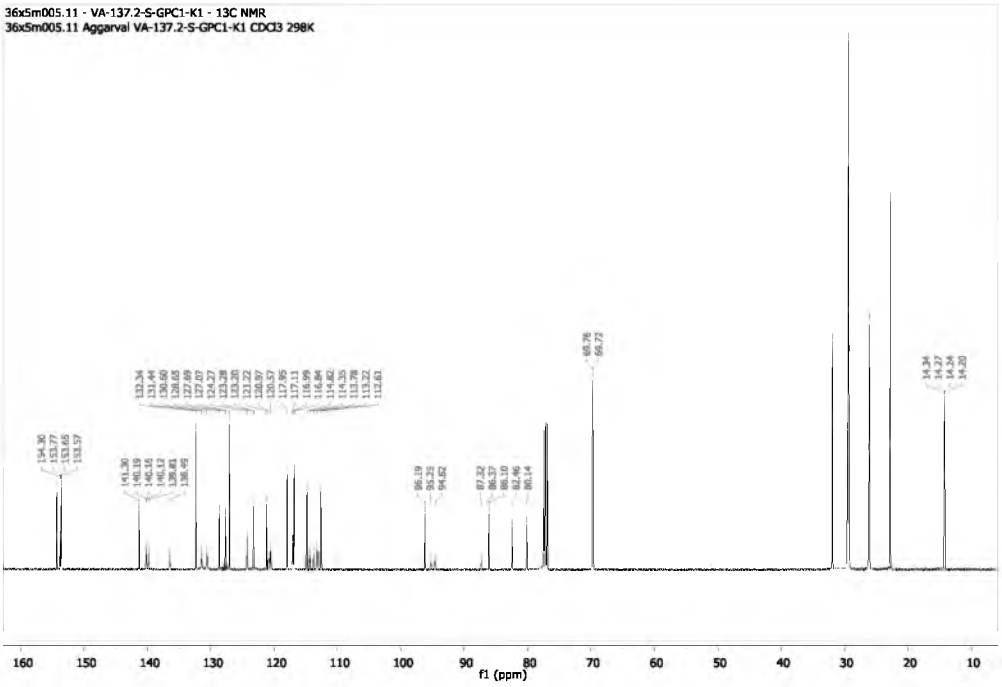
36xSm005.11 - VA-137.2-S-GPC1-K1 - 13C NMR
36xSm005.11 Aggarwal VA-137.2-S-GPC1-K1 CDCl3 298K
f1 (ppm)

1

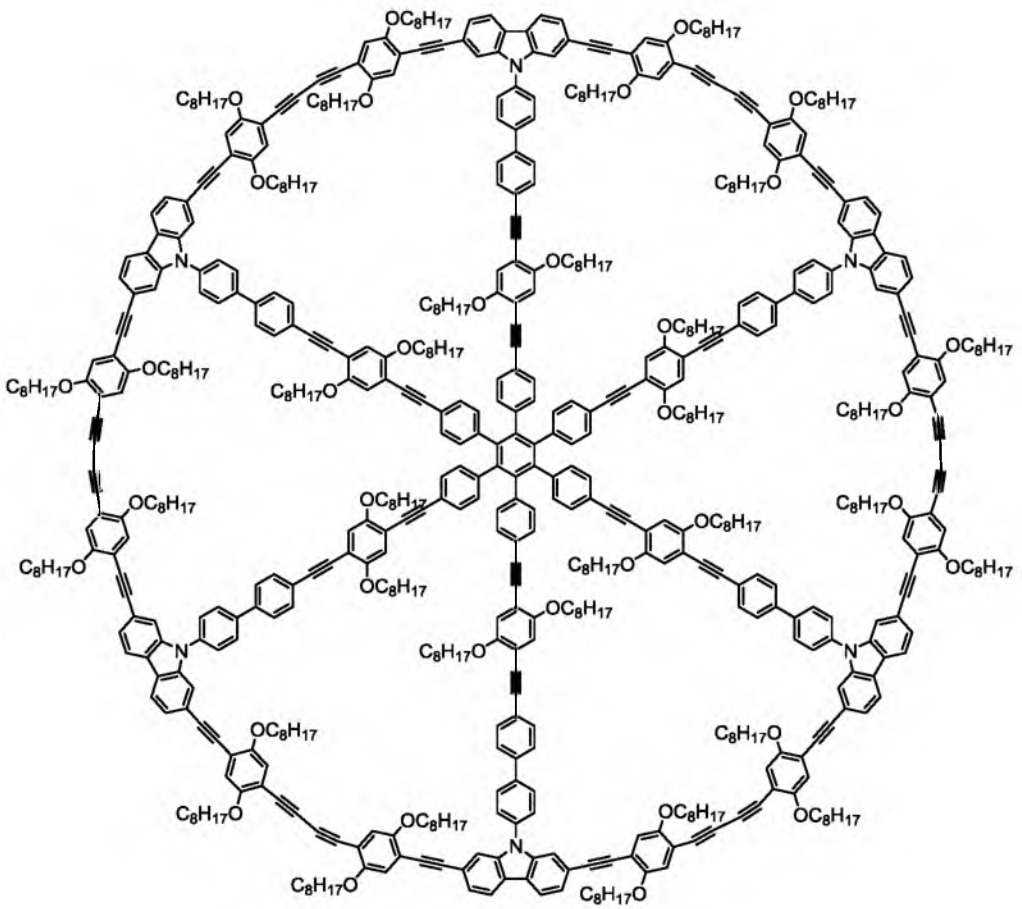

A solution of THF (45 mL) and diisopropyl amine (50 mL) was purged with air for 60 min prior to the addition of CuI (8.6 mg, 45.2 µmol), I_2 (17.2 mg, 67.8 µmol), and $Pd(PPh_3)_2Cl_2$ (21.2 mg, 30.1 µmol). The catalyst solution was heated to 50 °C and a solution of **8** (35.0 mg, 3.77 µmol) in THF (30 mL) was added with a constant rate over 60 h under vigorous stirring. After cooling to r.t., the reaction was diluted with toluene and concentrated *in vacuo*. Then the residue was redissolved in dichloromethane and washed with aq. H_2SO_4 (10 %), water, and brine. After drying over $MgSO_4$ and removal of the solvent, the crude product was purified by flash chromatography (CH:DCM = 1:2) and recGPC. **1** (19.0 mg, 2.0 µmol, 54 %) was obtained as a yellow solid.

^{1}H NMR (500 MHz, $CDCl_3$, 298 K) δ [ppm] = 8.10 (d, $^3J_{H,H}$ = 8.0 Hz, 12 H), 7.87 (d, $^3J_{H,H}$ = 8.4 Hz, 12 H), 7.76 – 7.60 (m, 48 H), 7.52 – 7.41 (m, 12 H), 7.15 (d, $^3J_{H,H}$ = 8.1 Hz, 12 H), 7.02 (s, 6 H), 7.01 – 6.98 (m, 18 H), 6.97 (s, 12 H), 6.84 (d, $^3J_{H,H}$ = 8.1 Hz, 12 H), 4.11 – 3.88 (m, 72 H), 1.97 – 1.71 (m, 72 H), 1.69 – 1.08 (m, 360 H), 0.98 – 0.74 (m, 108 H); ^{13}C NMR (126 MHz, $CDCl_3$, 298 K) δ [ppm] = 155.24, 153.73, 153.65, 153.59, 141.41, 140.16, 139.76, 136.42, 132.35, 131.46, 130.60, 128.64,

127.80, 127.03, 123.37, 123.24, 121.28, 120.90, 120.80, 117.84, 117.09, 117.00, 116.93, 115.35, 114.32, 114.25, 113.70, 112.70, 96.88, 95.29, 94.67, 87.39, 86.42, 86.19, 79.76, 79.60, 79.56, 69.91, 69.78, 69.70, 69.67, 31.97, 31.94, 31.88, 29.53, 29.51, 29.46, 29.43, 29.39, 29.37, 29.30, 29.28, 29.27, 26.24, 26.14, 26.07, 26.01, 22.86, 22.84, 22.81, 22.78, 14.35, 14.28, 14.26, 14.22; MS (MALDI-TOF, DCTB) (calcd. for $C_{654}H_{756}N_6O_{36}$ monoisotopic: 9269.75, distr. max.: 9277.02): *m/z* 10017.8 $[M+3*DCTB]^+$, 9777.8 $[M+2*DCTB]^+$, 9527.5 $[M+DCTB]^+$, 9777.8 $[M]^+$; GPC (in THF vs. PS): M_p = 9940 g mol^{-1}.

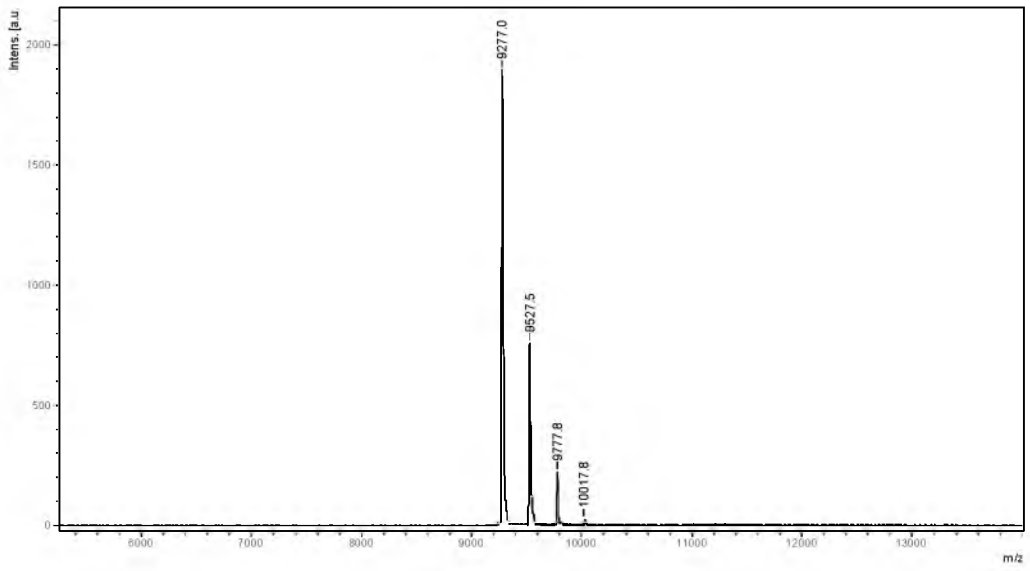

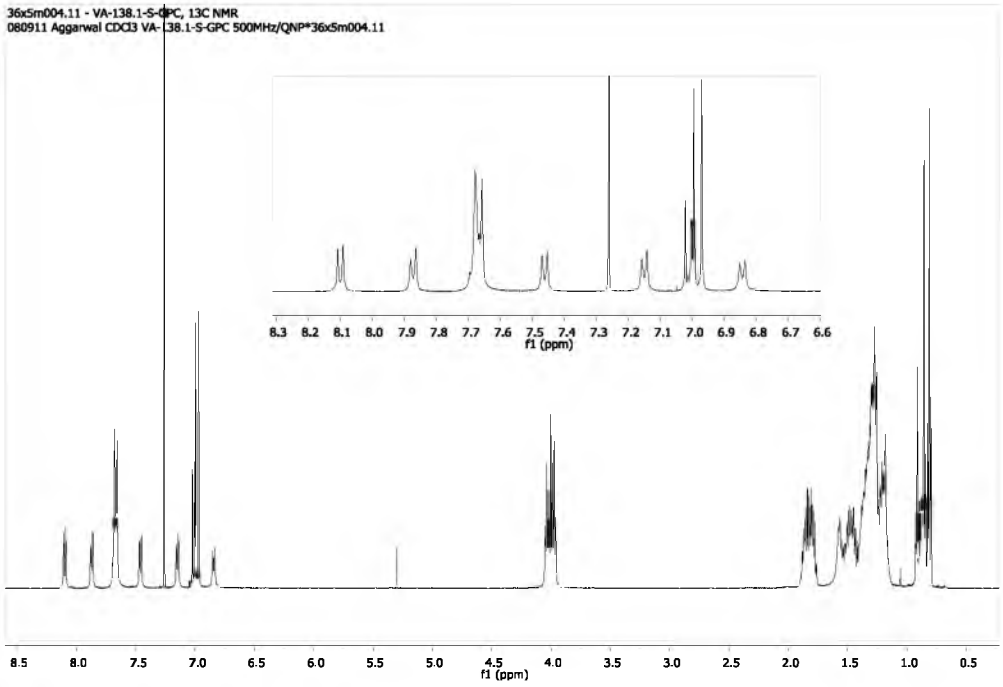
36x5m004.11 - VA-138.1-S-GPC, 13C NMR
080911 Aggarwal CDCl3 VA-138.1-S-GPC 500MHz/QNP*36x5m004.11
f1 (ppm)

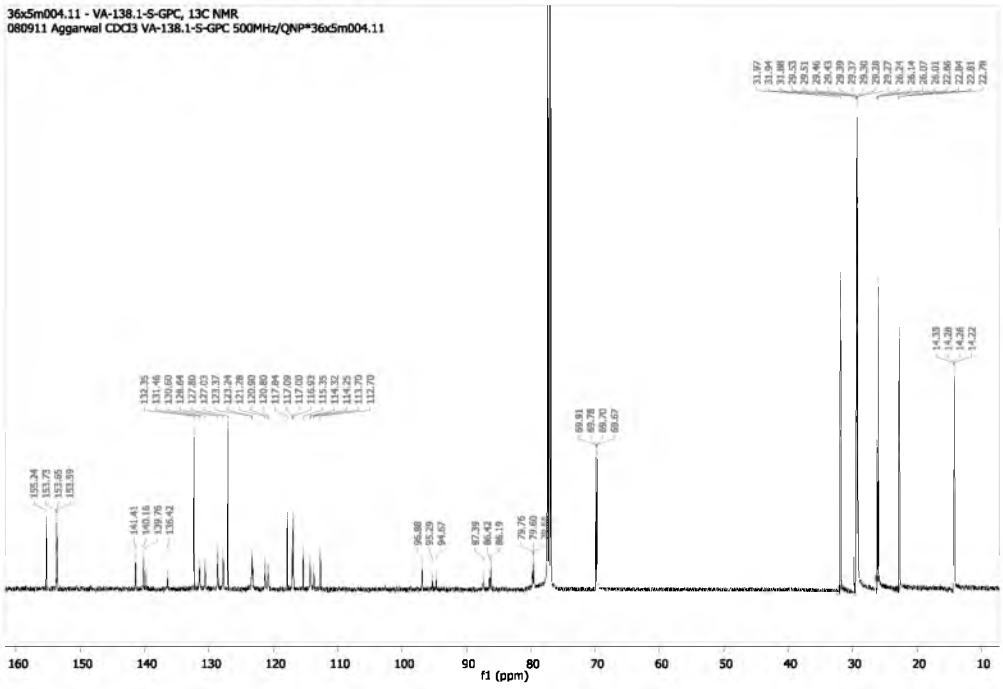
36x5m004.11 - VA-138.1-S-GPC, 13C NMR
080911 Aggarwal CDCl3 VA-138.1-S-GPC 500MHz/QNP*36x5m004.11
f1 (ppm)

GPC

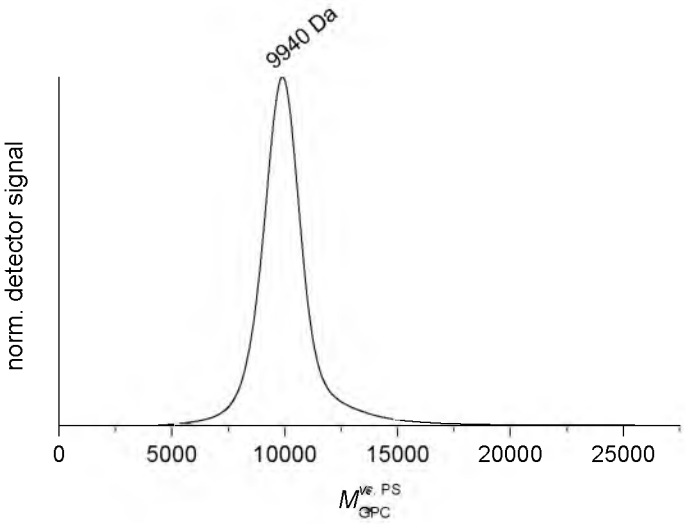
9940 Da
norm. detector signal
0
5000
10000
15000
20000
25000
$M_{GPC}^{vs.\ PS}$

3. Synthesis of the linear oligomers

The linear oligomers were synthesized according to

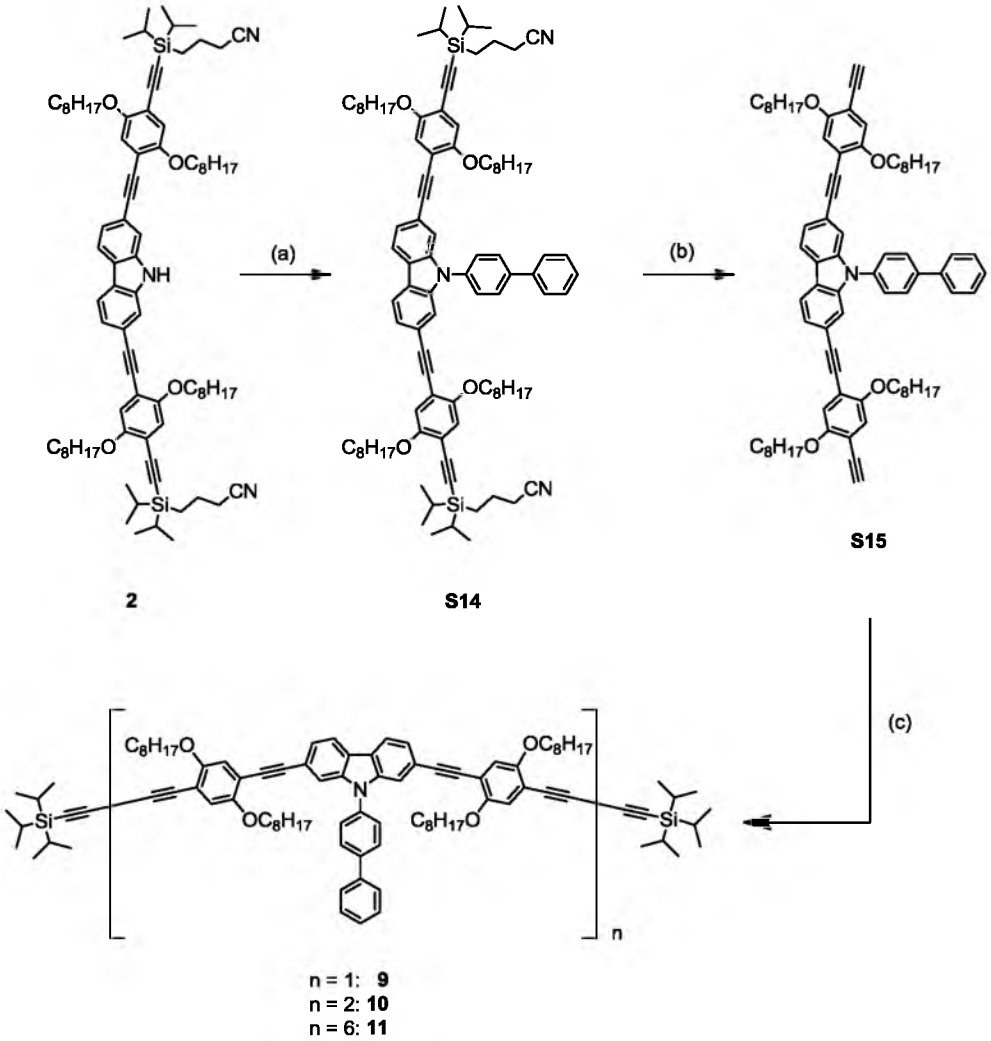

Figure **S3**.

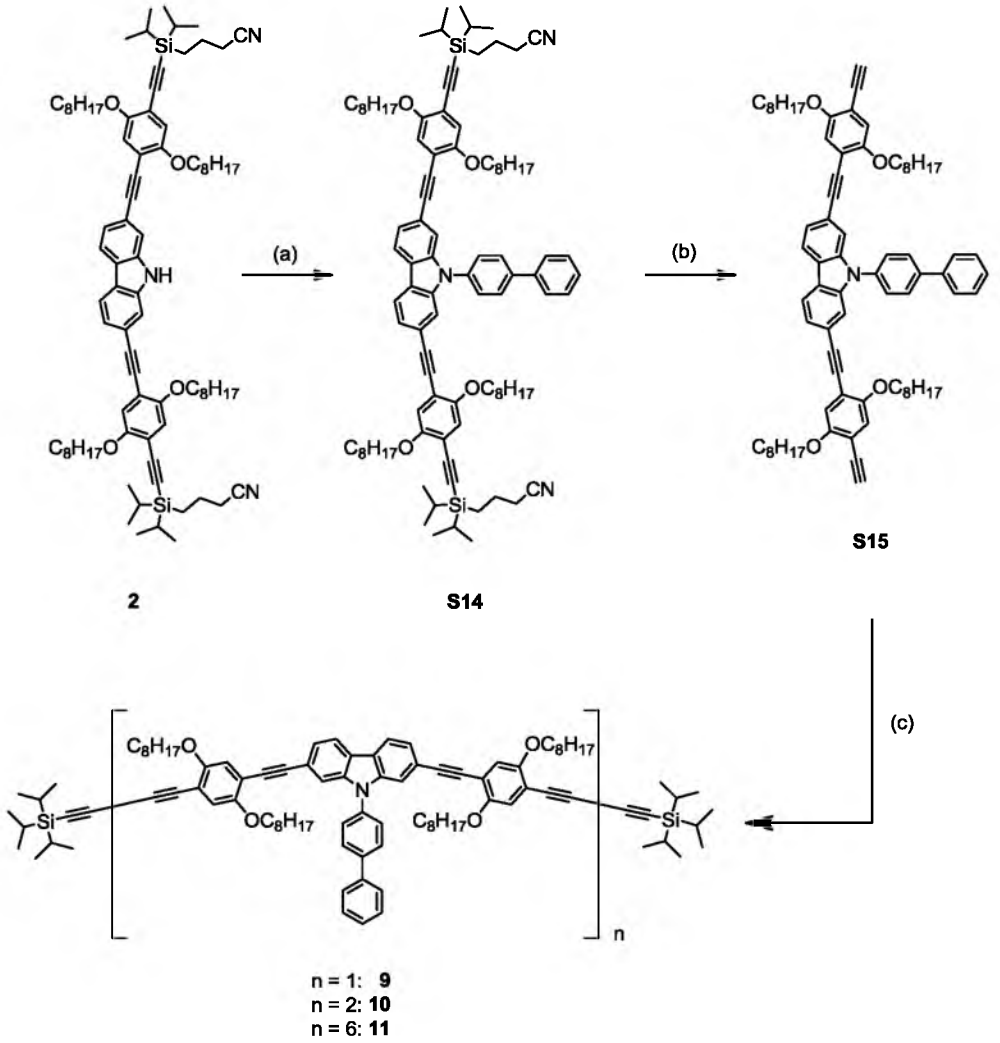

Figure S3: Synthesis of the linear reference compounds **9**, **10**, **11**. (a) 4-Bromobiphenyl, *t*Bu-XPhos, Pd_2dba_3, NaO*t*Bu, o-Xylene, 85 °C, 2 h, 61 %; (b) TBAF, THF, 0 °C-r.t., 105 min; (c) 1. TIPSA, $Pd(PPh_3)_2Cl_2$, CuI, I_2, air, 50 °C, 150 min; 2. TIPSA, 50 °C, 10 min.

S14

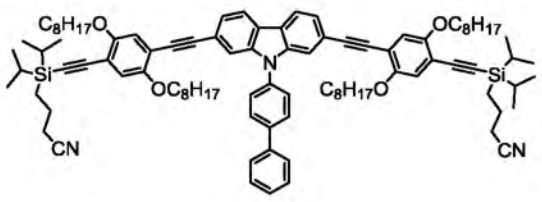

A solution of **2** (122.0 mg, 94.5 µmol) and 4-bromobiphenyl (110.1 mg, 472.3 µmol) in o-xylene was purged with argon for 1 h prior to heating to 85 °C and subsequent addition of a mixture of Pd_2dba_3 (8.7 mg, 9.5 µmol), NaO*t*Bu (13.6 mg, 141.5 µmol), and *t*Bu-Xphos (16.1 mg, 37.9 µmol). After 2 h the reaction was allowed to cool to r.t. and diluted with MTBE and dichloromethane. The organic phase was washed with aq. H_2SO_4 (10 %), water, and brine and dried over $MgSO_4$ before the solvent was removed *in vacuo*. The residue was purified by column chromatography (CH:DCM = 45:55) to yield **S14** (83.0 mg, 57.5 µmol, 61 %) as a yellow oil.

^{1}H NMR (400 MHz, $CDCl_3$, 298 K) δ [ppm] = 8.10 (s, $^3J_{H,H}$ = 8.1 Hz, 2 H), 7.85 (d, $^3J_{H,H}$ = 8.4, 2.9 Hz, 2 H), 7.76 – 7.68 (m, 2 H), 7.68 – 7.61 (m, 4 H), 7.58 – 7.47 (m, 4 H), 7.47 – 7.39 (m, 1 H), 6.98 (s, 2 H), 6.95 (s, 2 H), 4.02 (t, $^3J_{H,H}$ = 6.4 Hz, 4 H), 3.96 (t, $^3J_{H,H}$ = 6.4 Hz, 4 H), 2.44 (t, $^3J_{H,H}$ = 7.0 Hz, 4 H), 2.01 – 1.71 (m, 12 H), 1.58 – 1.41 (m, 8 H), 1.41 – 1.19 (m, 32 H), 1.19 – 1.02 (m, 28 H), 0.94 – 0.77 (m, 16 H); ^{13}C NMR (101 MHz, $CDCl_3$, 298 K) δ [ppm] = 154.50, 153.51, 141.37, 141.02, 140.23, 136.15, 129.12, 128.78, 127.90, 127.61, 127.24, 124.17, 123.22, 121.21, 120.53, 119.90, 117.78, 116.24, 114.73, 113.28, 113.23, 104.06, 96.27, 95.23, 86.29, 69.89, 69.27, 31.98, 31.88, 29.53, 29.44, 29.42, 29.40, 29.37, 26.23, 26.10, 22.80, 22.77, 21.42, 20.88, 18.37, 18.12, 14.22, 14.19, 11.93, 9.76; MS (MALDI-TOF, DCTB) (calcd. for $C_{96}H_{127}N_3O_4Si_2$ monoisotopic: 1441.94, distr. max.: 1443.22): *m/z* 1691.9 $[M+DCTB]^+$, 1441.9 $[M]^+$; GPC (in THF vs. PS): M_p = 1890 g mol^{-1}.

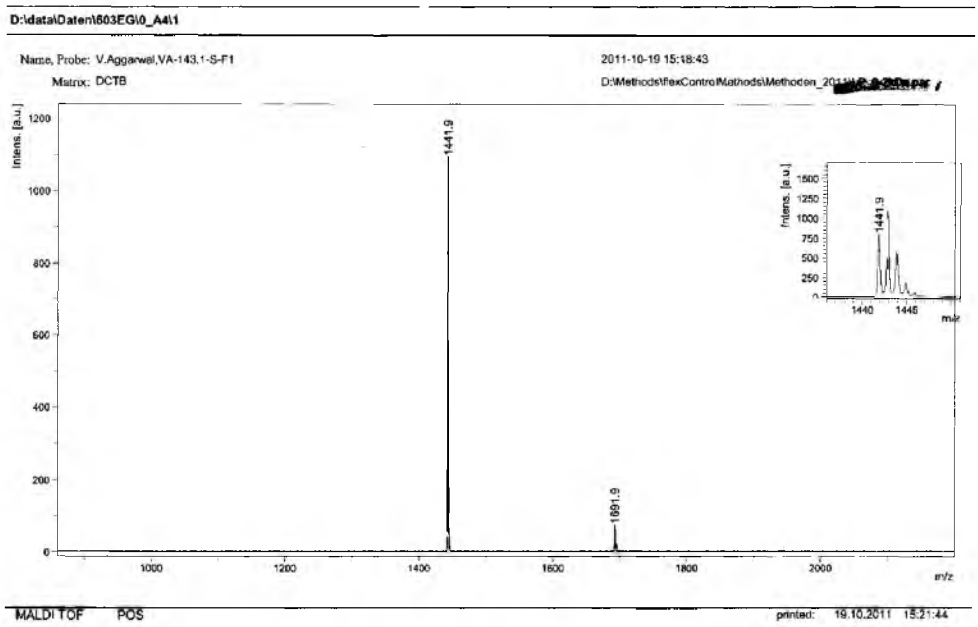
D:\data\Daten\603EG\0_A4\1
Name, Probe: V.Aggarwal,VA-143.1-S-F1
Matrix: DCTB
2011-10-19 15:18:43
Intens. [a.u.]
1441.9
1691.9
m/z
MALDI TOF POS
printed: 19.10.2011 15:21:44

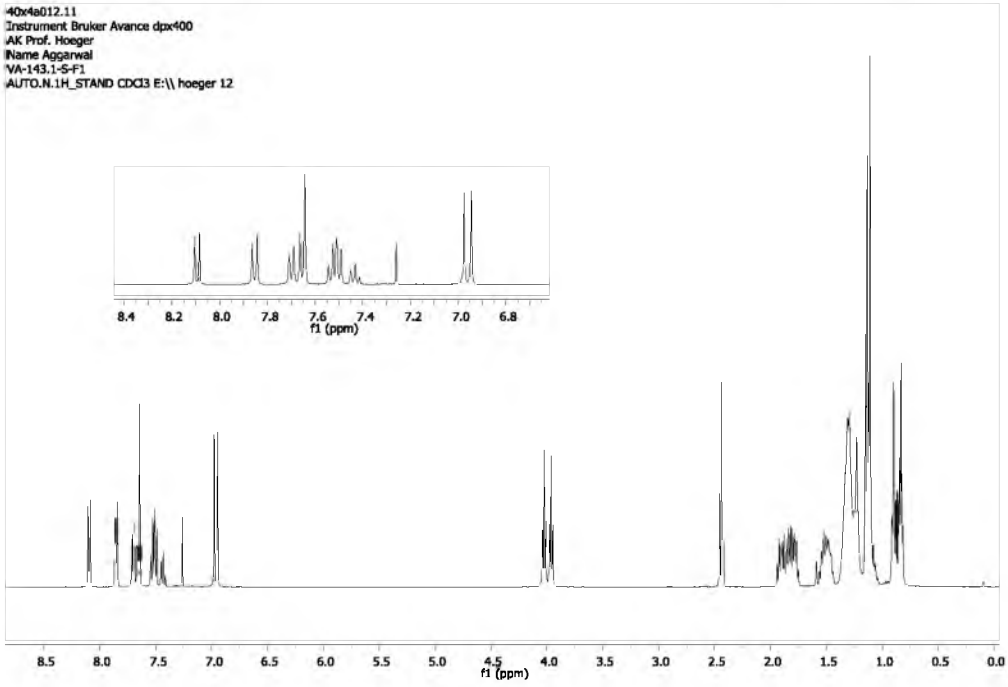
40x4a012.11
Instrument Bruker Avance dpx400
AK Prof. Hoeger
Name Aggarwal
VA-143.1-S-F1
AUTO.N.1H_STAND CDCl3 E:\\ hoeger 12
f1 (ppm)

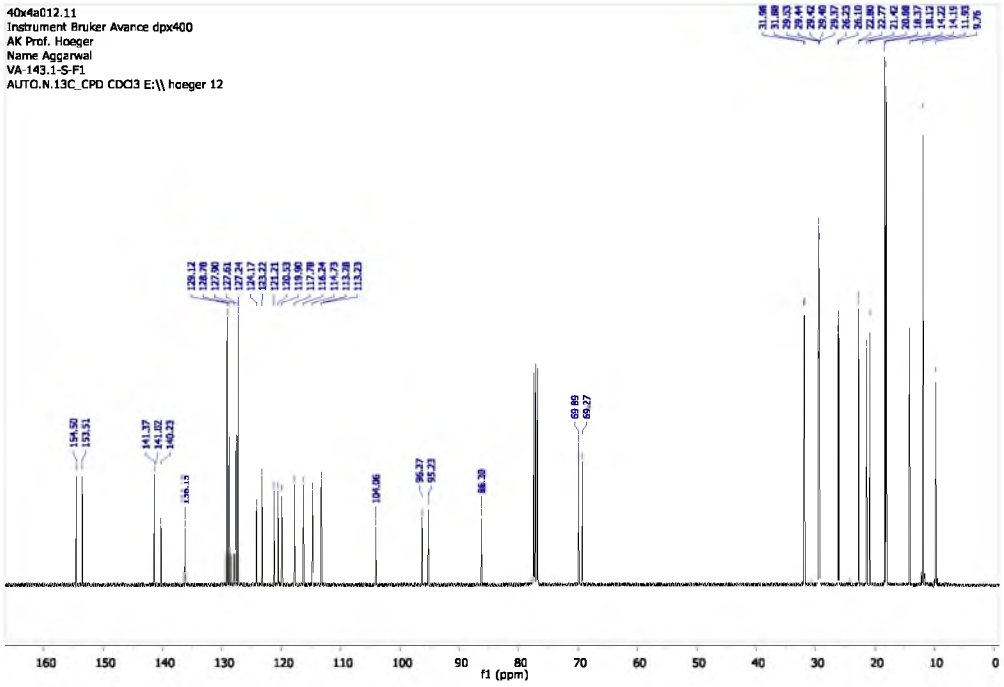
40x4a012.11
Instrument Bruker Avance dpx400
AK Prof. Hoeger
Name Aggarwal
VA-143.1-S-F1
AUTO.N.13C_CPD CDCl3 E:\\ hoeger 12
f1 (ppm)

S15

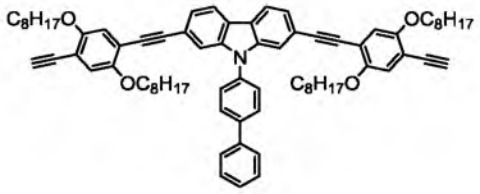

To solution of **S14** (82.0 mg, 56.8 µmol) in THF (25 mL), a solution of TBAF in THF (1 M) (170.0 mmol, 0.17 mL) was added at 0 °C. The reaction was stirred for 15 min at 0 °C and for 90 min at r.t. It was then diluted with MTBE and dichloromethane and washed with water and brine. After drying over $MgSO_4$ and removal of the solvent, the crude product was purified by column chromatography (CH:DCM = 70:30 – 65:35) and recGPC. **S15** (50.0 mg, 46.3 µmol, 81 %) was isolated as a yellow solid.

^{1}H NMR (400 MHz, $CDCl_3$, 298 K) δ [ppm] = 8.10 (d, $^3J_{H,H}$ = 8.1 Hz, 2 H), 7.90 – 7.80 (m, 2 H), 7.75 – 7.62 (m, 6 H), 7.58 – 7.47 (m, 4 H), 7.47 – 7.40 (m, 1 H), 7.01 (s, 2 H), 6.98 (s, 2 H), 4.00 (t, $^3J_{H,H}$ = 6.3 Hz, 8 H), 3.35 (s, 2 H), 1.93 – 1.73 (m, 8 H), 1.60 – 1.42 (m, 8 H), 1.42 – 1.16 (m, 32 H), 0.99 – 0.77 (m, 12 H); ^{13}C NMR (101 MHz, $CDCl_3$, 298 K) δ [ppm] = 154.31, 153.57, 141.36, 141.02, 140.22, 136.14, 129.11, 128.78, 127.90, 127.60, 127.24, 124.17, 123.23, 121.19, 120.53, 117.95, 116.85, 114.88, 113.24, 112.59, 96.24, 86.08, 82.42, 80.16, 69.76, 69.72, 31.91, 31.90, 31.88, 29.42, 29.38, 29.37, 29.34, 29.27, 26.08, 26.03, 22.77, 22.77, 14.22, 14.18; MS (MALDI-TOF, DCTB) (calcd. for $C_{76}H_{89}NO_4$ monoisotopic: 1079.68, distr. max.: 1080.52): *m/z* 1329.9 $[M+DCTB]^+$, 1079.7 $[M]^+$; GPC (in THF vs. PS): M_p = 1520 g mol^{-1}.

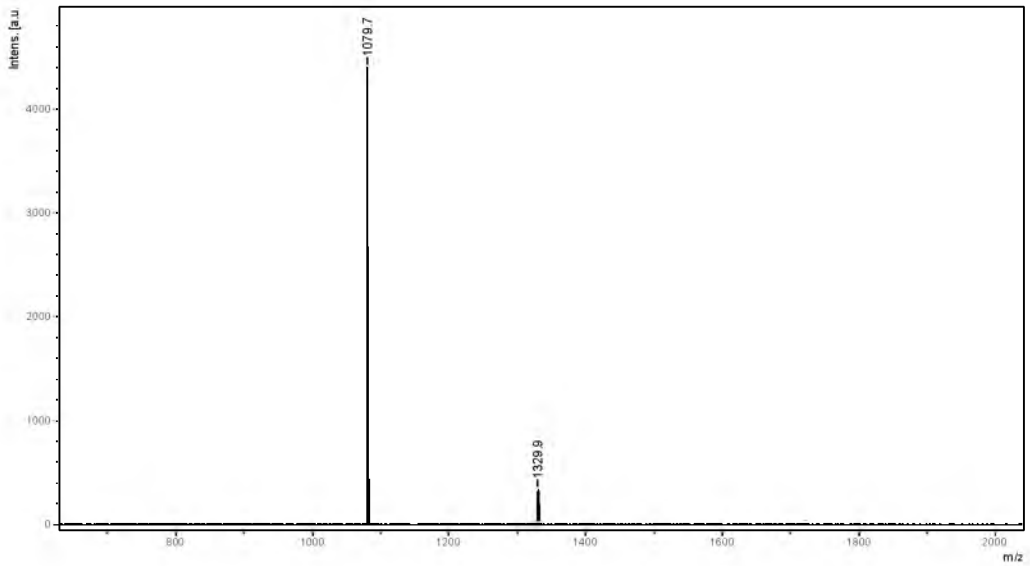

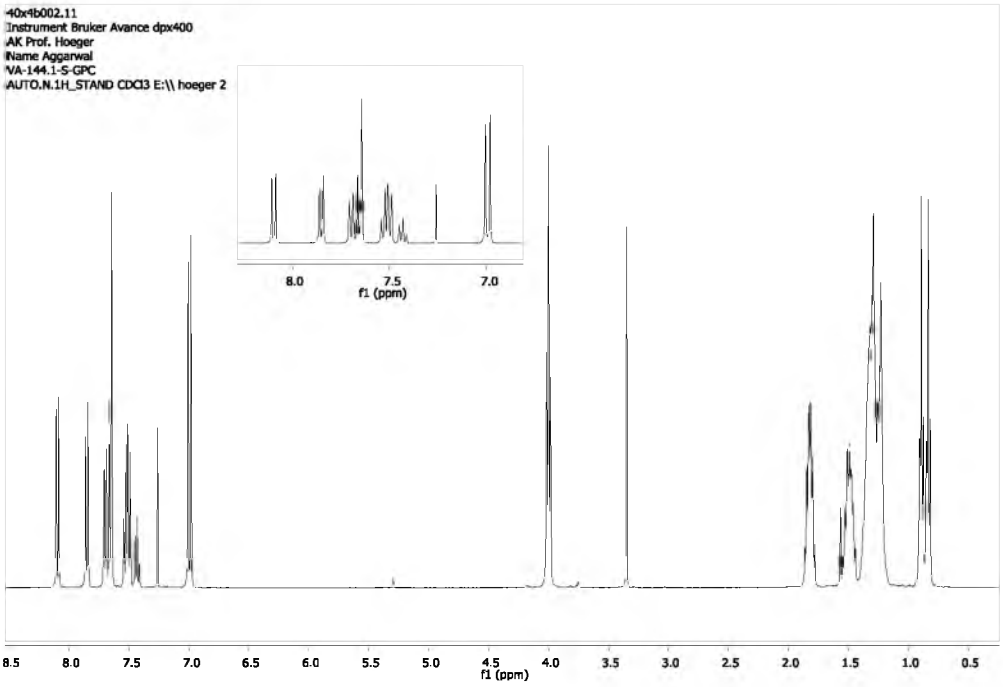
40x4b002.11
Instrument Bruker Avance dpx400
AK Prof. Hoeger
Name Aggarwal
VA-144.1-S-GPC
AUTO.N.1H_STAND CDCl3 E:\\ hoeger 2
8.0
7.5
7.0
f1 (ppm)
8.5 8.0 7.5 7.0 6.5 6.0 5.5 5.0 4.5 4.0 3.5 3.0 2.5 2.0 1.5 1.0 0.5
f1 (ppm)

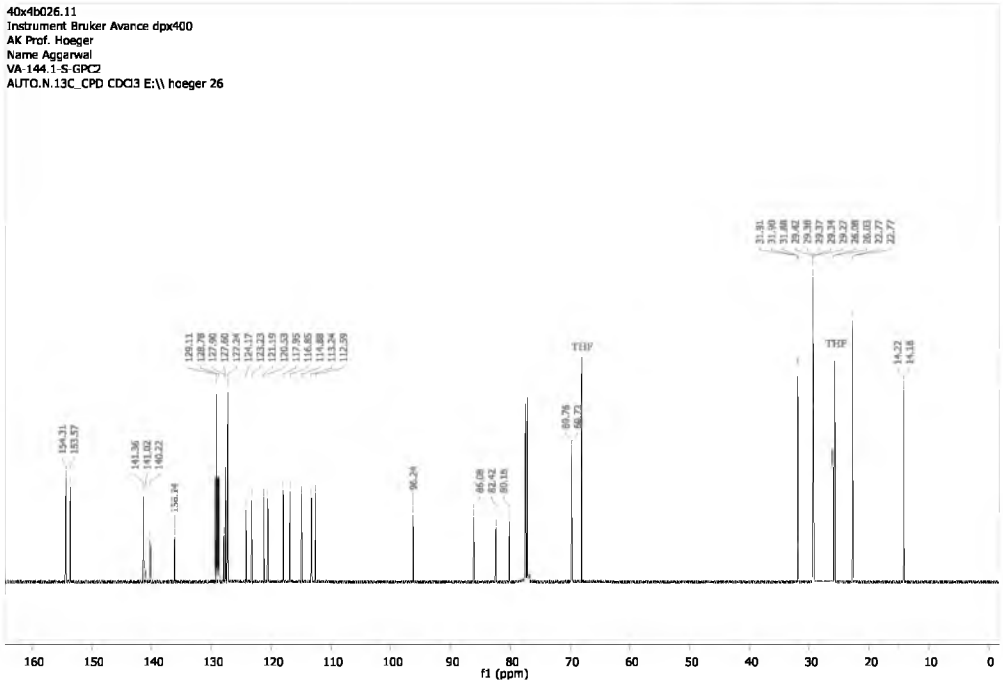
40x4b026.11
Instrument Bruker Avance dpx400
AK Prof. Hoeger
Name Aggarwal
VA-144.1-S-GPC2
AUTO.N.13C_CPD CDCl3 E:\\ hoeger 26
THF
THF
160 150 140 130 120 110 100 90 80 70 60 50 40 30 20 10 0
f1 (ppm)

9, 10, 11

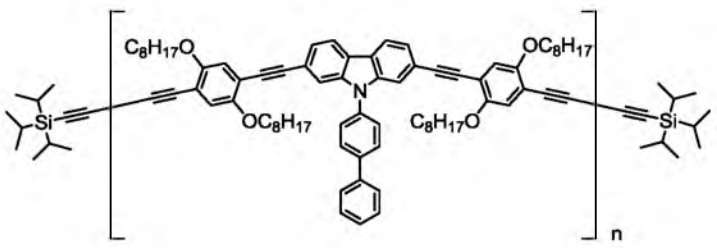

A solution of CuI (19.0 mg, 100.0 µmol), I_2 (42.2 mg, 166.6 µmol), $Pd(PPh_3)_2Cl_2$ (35.2 mg, 50.0 µmol), THF (15 mL), and diisopropyl amine (10 mL) was purged with air for 60 min. Then the solution was heated to 50 °C and a solution of **S15** (45.0 mg, 41.7 µmol) and triisopropylsilyl acetylene (3.0 mg, 16.7 µmol) in THF (5 mL) was added under vigorous stirring. After 150 min, triisopropylsilyl acetylene (570.0 mg, 3123.5 µmol, 0.7 mL) was added and stirring was continued for 10 min at 50 °C. The reaction was allowed to cool to r.t., diluted with chloroform and washed with aq. H_2SO_4 (10 %), water, and brine. After drying over $MgSO_4$ and removal of the solvent, the crude product was fractioned by *Soxhlet* extraction (methanol, acetone, diethyl ether, dichloromethane, and chloroform). The catalyst and 1,4-bis(triisopropylsilyl)buta-1,3-diyne were washed out with methanol. The monomer (**9**), along with some of the dimer (**10**) and the trimer, was found in the acetone fraction, while all higher oligomers (including **11**) had been eluted with dichloromethane. The chloroform fraction contained some polymeric material. The acetone (12 mg), the dichloromethane (39 mg) and the chloroform (10 mg) fractions were further separated by recGPC. The carbazole-based oligomers **9**, **10**, and **11** were obtained as yellow solids.

9 (linear monomer) (2.8 mg, 1.943 µmol)

^{1}H NMR (400 MHz, $CDCl_3$, 298 K) δ [ppm] = 8.13 – 8.05 (m, 2 H), 7.89 – 7.81 (m, 2 H), 7.73 – 7.60 (m, 6 H), 7.56 – 7.39 (m, 5 H), 7.00 – 6.93 (m, 4 H), 4.06 – 3.91 (m, 8 H), 1.90 – 1.74 (m, 8 H), 1.53 – 1.40 (m, 8 H), 1.40 – 1.16 (m, 32 H), 1.11 (s, 42 H), 0.97 – 0.77 (m, 12 H).MS (MALDI-TOF, DCTB) (calcd. for $C_{98}H_{129}NO_4Si_2$ monoisotopic: 1439.95, distr. max.: 1441.25): *m/z* 1439.9 $[M]^+$; GPC (in THF vs. PS): M_p = 2060 g mol^{-1}.

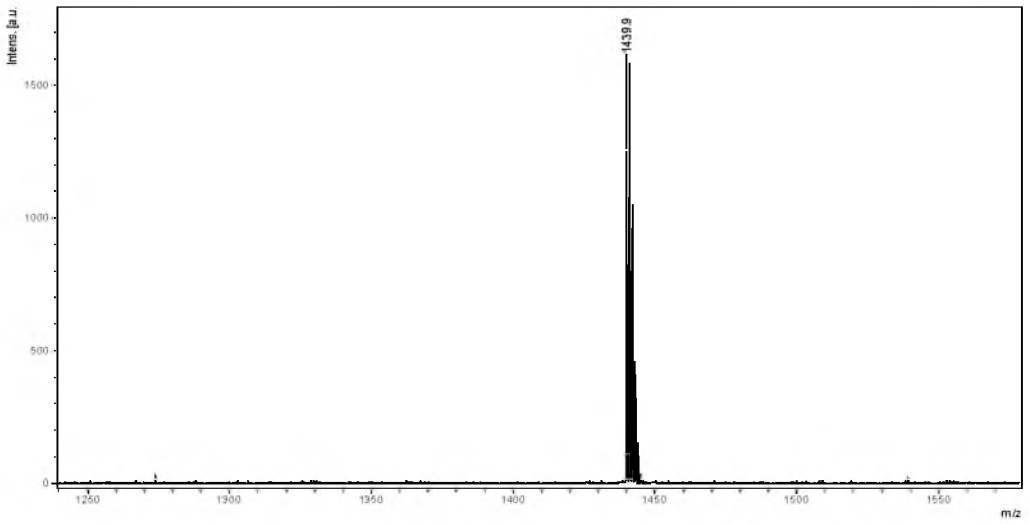

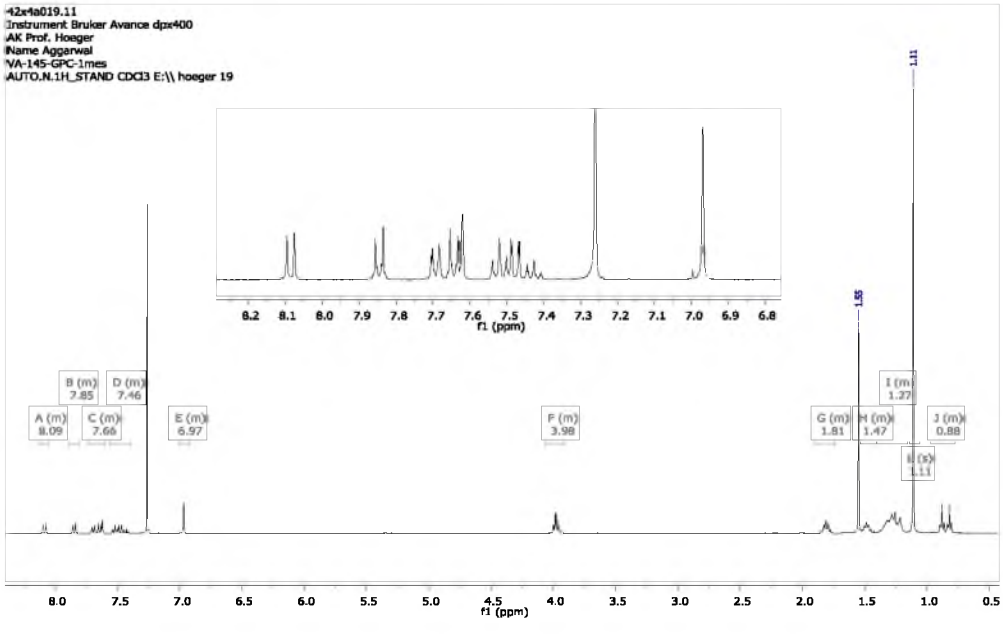

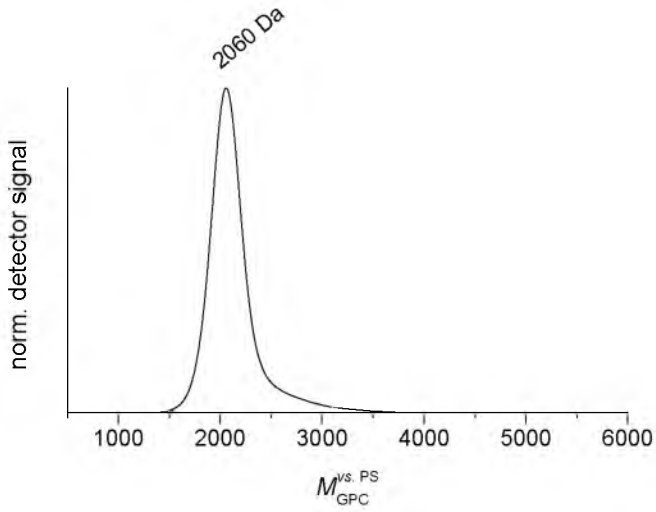

10 (linear dimer) (1.9 mg, 0.754 µmol, 4 %)

^{1}H NMR (400 MHz, $CDCl_3$, 298 K) δ [ppm] = 8.09 (d, $^3J_{H,H}$ = 8.1 Hz, 4 H), 7.91 – 7.80 (m, 4 H), 7.75 – 7.59 (m, 12 H), 7.58 – 7.38 (m, 10 H), 7.02 – 6.94 (m, 8 H), 4.11 – 3.89 (m, 16 H), 1.92 – 1.74 (m, 16 H), 1.55 – 1.41 (m, 16 H), 1.40 – 1.16 (m, 64 H), 1.11 (s, 42 H), 0.95 – 0.71 (m, 24 H); MS (MALDI-TOF, DCTB) (calcd. for $C_{174}H_{216}N_2O_8Si_2$ monoisotopic: 2517.61, distr. max.: 2519.76): *m/z* 2517.6 $[M]^+$; GPC (in THF vs. PS): M_p = 4220 g mol^{-1}.

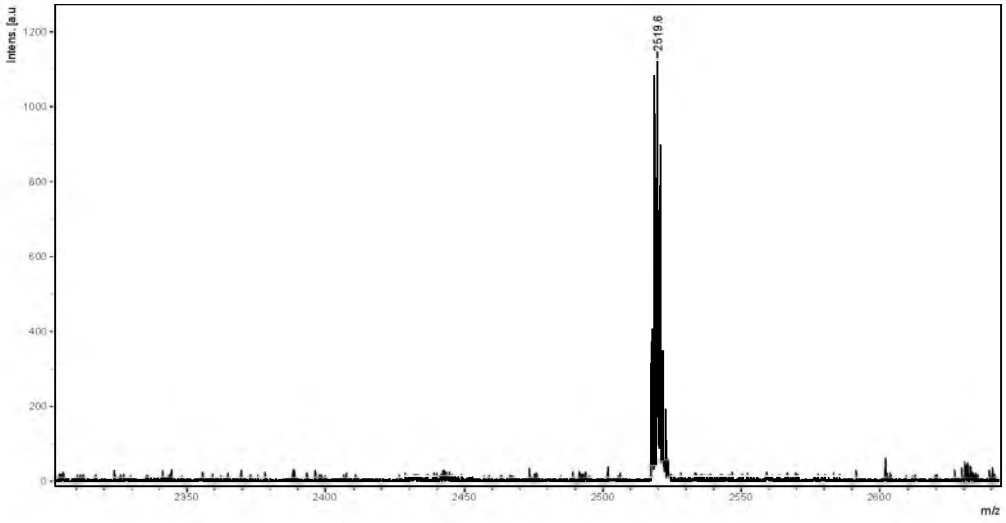

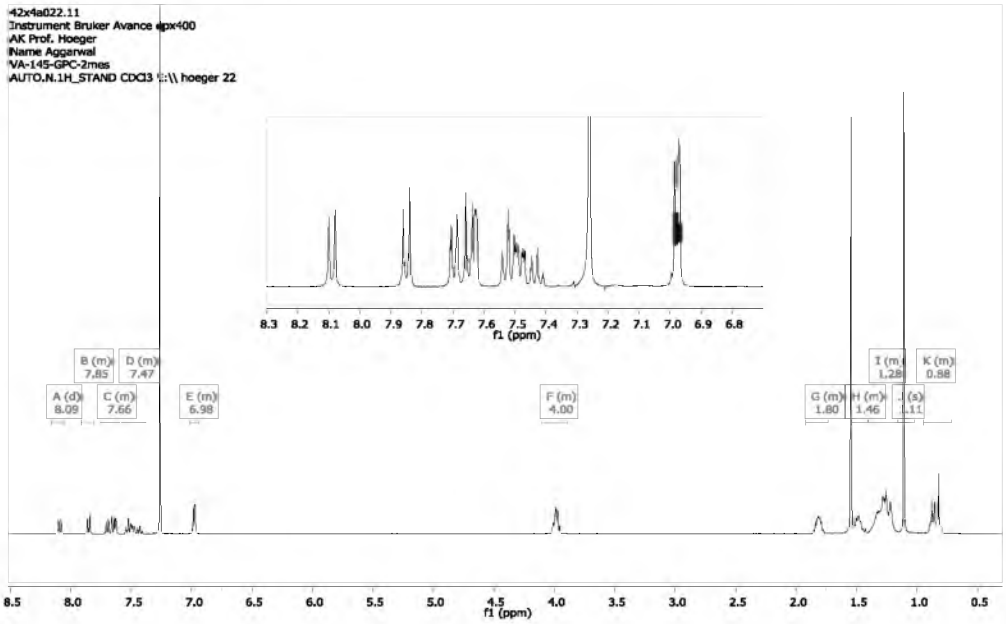
42x4a022.11
Instrument Bruker Avance dpx400
AK Prof. Hoeger
Name Aggarwal
VA-145-GPC-2mes
AUTO.N.1H_STAND CDCl3
hoeger 22
A (d) 8.09
B (m) 7.85
C (m) 7.66
D (m) 7.47
E (m) 6.98
F (m) 4.00
G (m) 1.80
H (m) 1.46
I (m) 1.28
J (s) 1.11
K (m) 0.88
f1 (ppm)

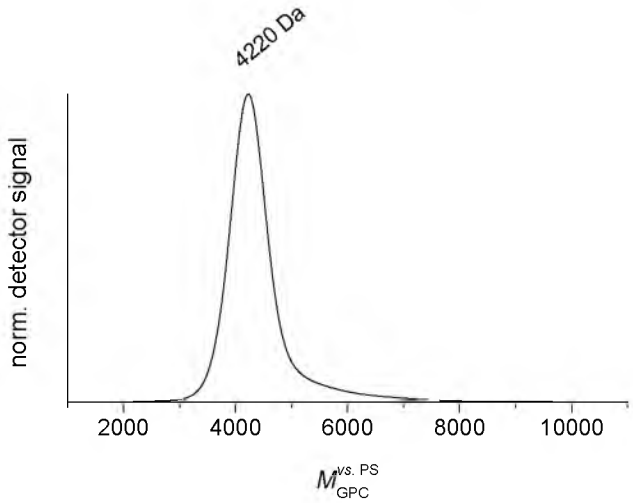
4220 Da
norm. detector signal
2000
4000
6000
8000
10000
M vs. PS GPC

11 (linear hexamer) (3.3 mg, 0.483 µmol, 7 %)

^{1}H NMR (400 MHz, $CDCl_3$, 298 K) δ [ppm] = 8.18 – 8.01 (m, 12 H), 7.92 – 7.80 (m, 12 H), 7.78 – 7.60 (m, 36 H), 7.58 – 7.39 (m, 30 H), 7.06 – 6.93 (m, 24 H), 4.06 – 3.94 (m, 48 H), 1.90 – 1.75 (m, 48 H), 1.53 – 1.43 (m, 48 H), 1.42 – 1.15 (m, 192 H), 1.15 – 1.03 (m, 42 H), 0.95 – 0.77 (m, 72 H); MS (MALDI-TOF, dithranol) (calcd. for $C_{478}H_{564}N_6O_{24}Si_2$ monoisotopic: 6828.26, distr. max.: 6833.79): *m/z* 7082.6 $[M+249]^+$, 7058.2 $[M+dithranol]^+$, 6945.9$[M+112]^+$, 6833.7 $[M]^+$, 6718.4 $[M-C_8H_{16}]^+$; GPC (in THF vs. PS): M_p = 15700 g mol^{-1}.

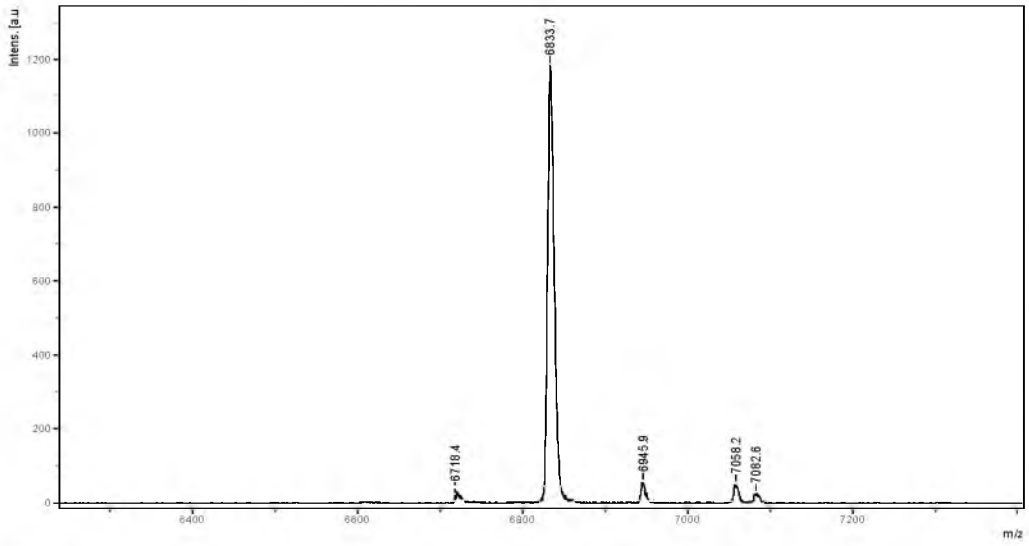

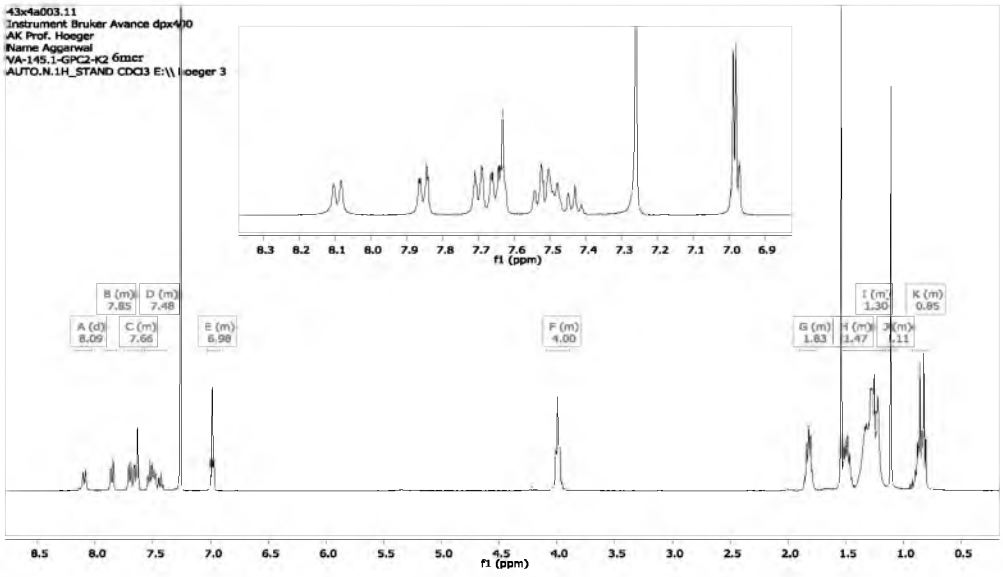

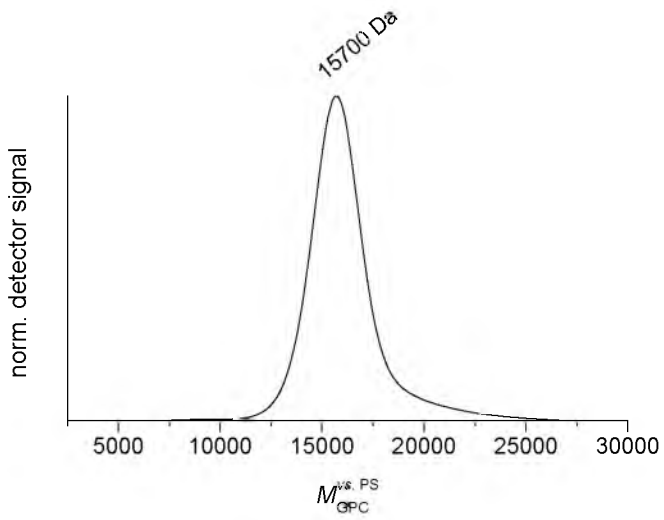
15700 Da
norm. detector signal
5000
10000
15000
20000
25000
30000
$M_{GPC}^{vs.\ PS}$

4. Scanning tunnelling microscopy (STM)

STM images of the precursor **8** and the ring **1** from Figure 2b in the main text are shown in larger size in Figure S4a and b, and molecular models are superimposed. In all images, regions covered with conjugated backbones and alkoxy side chains are observed with high and low tunnelling current, which are – convolved with the height information – encoded in bright and dark color, respectively. Both compounds self-assemble to form monolayers at the OA/HOPG interface. The rigid backbones of the precursor molecules **8** (Figure S4a) align in parallel to the HOPG substrate and interact intermolecularly via interdigitating side chains. Hexagon-shaped objects with an internal hub/spoke system are observed that match well with the expected size and geometry of the molecules. The resulting hexagonal crystalline patterns exhibit domain sizes of several 10×10 nm^2. A unit cell of $a = b = (6.7 \pm 0.2)$ nm, $\gamma(a,b) = (60 \pm 2)°$ is indexed. In the STM image of the ring **1** (Figure S4b), the conjugated rims, the spokes, and the central hub are even more clearly resolved. Again, the backbones are intermolecularly separated by regions covered by adsorbed octyloxy side chains. Contrary to the precursor molecules, the rings do not form a highly-ordered crystalline hexagonal pattern, but slight deviations of the intermolecular distances and relative orientations occur. This is attributed to the variety of possible interdigitation schemes as a result of different octyloxy side chain configurations. The STM images show conclusively that the molecular spoked wheels exhibit a well-defined shape-persistent architecture.

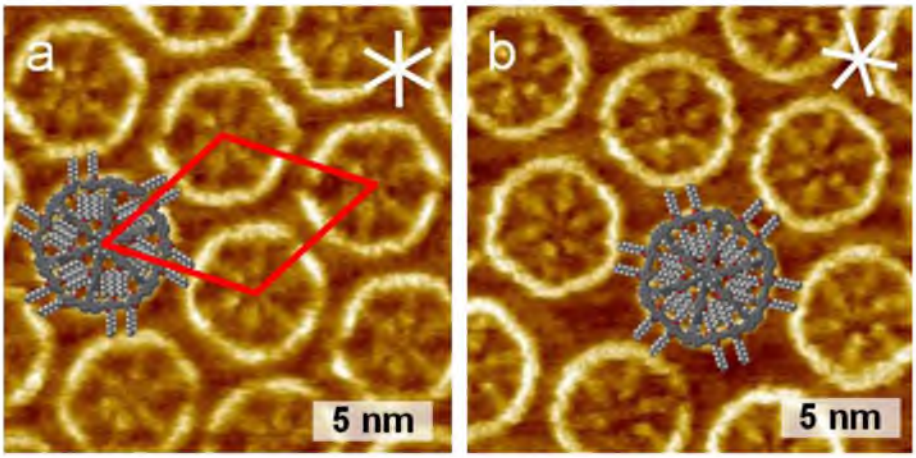

Figure S4. STM images of monolayers of a) precursor **8** and b) ring **1** at the OA/HOPG interface, and superimposed molecular models of the respective compounds. Image parameters: a) 19.0×19.0 nm^2, $V_S = -1.6$ V, $I_t = 5$ pA, $c = 2\times10^{-6}$ M, 30 s annealed at 70 °C; b) 19.0×19.0 nm^2, $V_S = -1.4$ V, $I_t = 2$ pA, $c = 10^{-5}$ M, 20 s annealed at 80 °C. Unit cell for a: $a = b = (6.7 \pm 0.2)$ nm, $\gamma(a,b) = (60 \pm 2)°$. The red and white lines indicate unit cell and HOPG main axis directions, respectively.

Enlarged versions of the STM images of the dimer and the hexamer from Figure 2b in the main text, along with the monomer are shown in Figure S5, together with superimposed molecular models. The monomers (Figure S5a) form crystalline monolayer patterns at the PHO/HOPG interface in which the backbones of the molecules are separated by interdigitating octyloxy side chains. The bent geometry of the backbones is clearly visible. An oblique unit cell with a = (6.7 ± 0.2) nm, b = (1.7 ± 0.1) nm, γ (a,b) = (86 ± 2)° is indexed, containing two molecules of opposite orientation with respect to the curvature of the backbones. The dimers (Figure S5b) adsorb at the TCB/HOPG interface into a similar pattern in which bent units are found to form sinuously shaped lines that are separated from each other by regions covered by the octyloxy side chains. An oblique unit cell of a = (7.3 ± 0.2) nm, b = (1.6 ± 0.1) nm, γ (a,b) = (78 ± 2)° is indexed. The triisopropylsilyl groups are clearly visible as bright dots. The hexamer (Figure S5c) does not crystallize into a two-dimensional pattern at the TCB/HOPG interface, but – aside from regions with backbones aligned in parallel (with a distance of (1.7 ± 0.2) nm) – regions are found where randomly bent caterpillar-shaped backbones are adsorbed on the substrate, as represented by the example molecular model that is fitted to one hexamer chain.

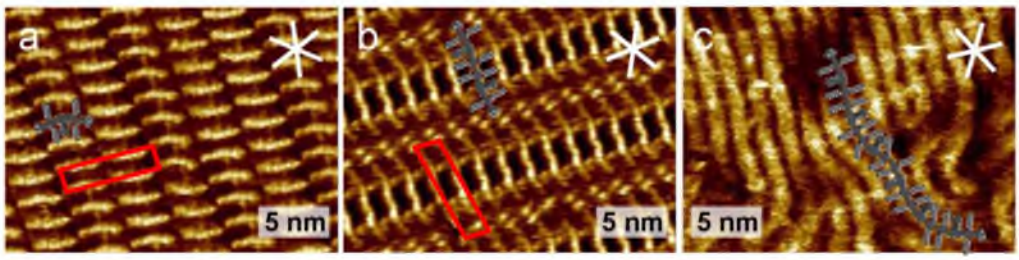

Figure S5. a)-c) STM images of monolayers of a) monomer, b) dimer, and c) hexamer at the solution/HOPG interface, and superimposed molecular models of the respective compounds. Image parameters: a) 22.8×16.6 nm^2, V_S = –1.06 V, I_t = 16 pA, c = 10^{-4} M in PHO, 20 s annealed at 80 °C; b) 22.8×16.6 nm^2, V_S = –1.0 V, I_t = 17 pA, c = 10^{-5} M in TCB, 20 s annealed at 80 °C; c) 22.8×16.6 nm^2, V_S = –1.5 V in TCB, I_t = 9 pA, c = 10^{-5} M, 30 s annealed at 80 °C. Unit cells for a: a = (6.7 ± 0.2) nm, b = (1.7 ± 0.1) nm, γ(a,b) = (86 ± 2)°; for b: a = (7.3 ± 0.2) nm, b = (1.6 ± 0.1) nm, γ(a,b) = (78 ± 2)°. The red and white lines indicate unit cell and HOPG main axis directions, respectively.

5. Optical ensemble spectra of the compounds

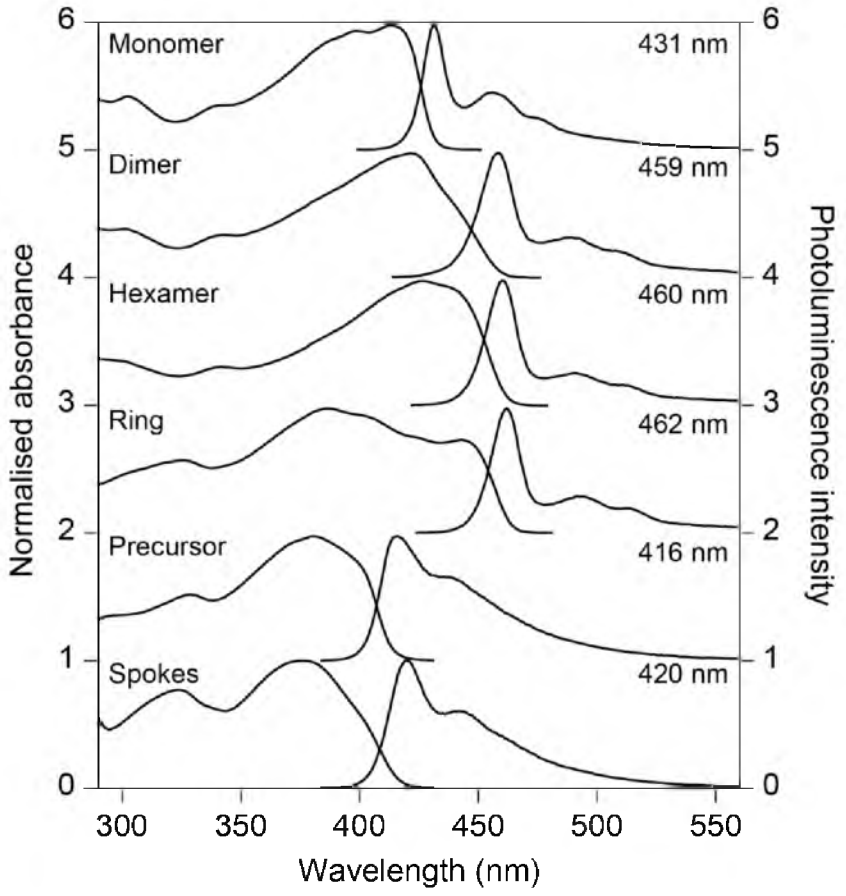

Figure S6. Absorption and photoluminescence (PL) spectra of the monomer **9**, dimer **10**, hexamer **11**, closed ring **1** (with the contour length of the hexamer), open ring precursor **8** and spokes of the ring (see Scheme 1 in main text for chemical structures) measured in toluene solution at room temperature (the complete spoke molecular structure consists of the red and blue units marked in Scheme 1, terminated by a sole carbazol unit at the end of each spoke without any ethynylene units attached to the carbazole). The peak wavelength of the corresponding PL spectrum is given to the right. The effective size of the emissive (relaxed, self-trapped) exciton, the coherence length, in the hexamer and the rings is given by the dimer unit, since an increase in molecule length does not change the PL spectrum substantially. The precursor molecule is slightly blue-shifted with respect to the monomer due to the absence of the terminal ethynylene units.

6. Additional examples of single-molecule linear dichroism fluctuation

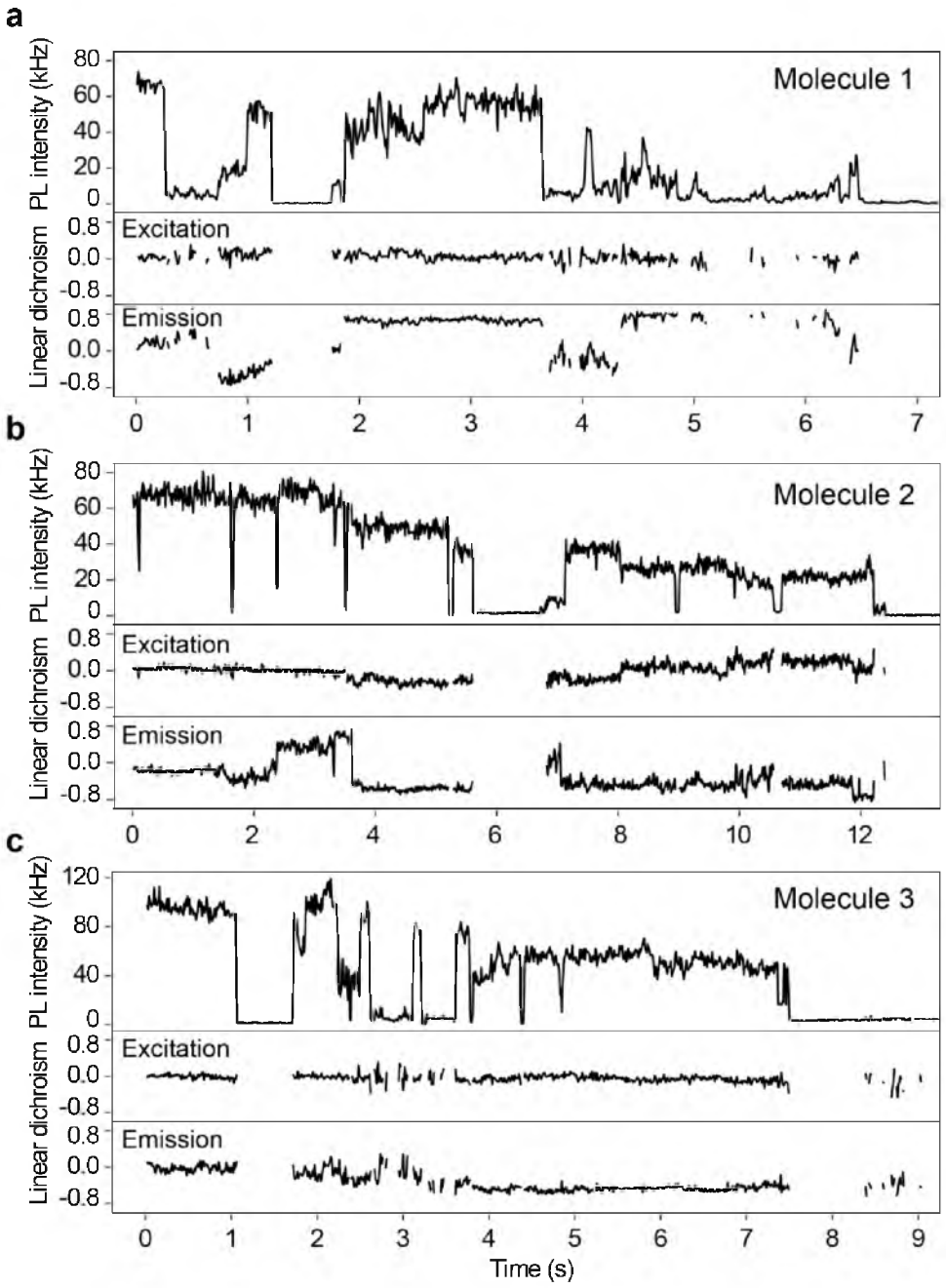

Figure S7. Fluctuations of the linear dichroism of three different single ring molecules. In general, strong fluctuations of the linear dichroism in emission are observed, whereas the linear dichroism in excitation fluctuates very little.

7. Photoinduced evolution of the linear dichroism

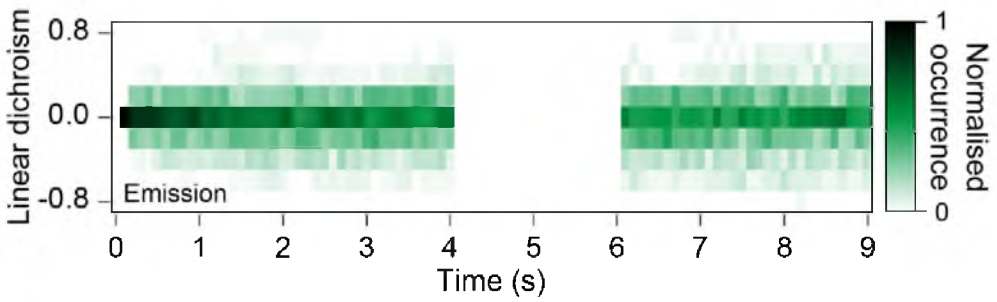

Figure S8. Ensemble evolution of the linear dichroism of 92 ring molecules. Only molecules which exhibit an initial linear dichroism between -0.1 and 0.1 were considered. The excitation of the molecules was switched off between 4 and 6 seconds. No reversibility in the broadening of the linear dichroism histogram due to photoinduced symmetry breaking can be observed after continuing the excitation at time 6 s, implying that the emission of the ring does not revert to the initial unpolarised appearance after terminating illumination.

8. Comparison of room-temperature and low-temperature linear dichroism

Measurements of linear dichroism at room and at low temperature differ fundamentally. At room temperature, the sample is scanned and imaged confocally. A molecular fingerprint is gained by the time tagging of the detected photons, yielding the fluorescence lifetime. Since imaging occurs confocally, a single molecule is only excited when its fluorescence is also detected. In out low-temperature microscope, single molecules are excited and detected in the wide field. This approach is potentially more susceptible to contaminations on the sample surface. The only way to ensure that fluorescence from a single ring molecule is detected is to inspect its spectrum. This requires that the fluorescence light is dispersed through a grating, which removes the horizontal spatial information in the single-molecule image. Since excitation occurs in the wide field, a single molecule can also be excited without being imaged. To find single molecules, individual spots are identified in the wide-field fluorescence image. The spectrometer is then centred on a single spot, the slit closed, and the emission spectrum recorded through a grating. This process implies that the single molecule has to be illuminated before the spectrum can be recorded. On average, excitation densities at low temperatures are 10 times higher than at room temperature (100 Wcm^{-2} vs. 10 Wcm^{-2}). There are two reasons for this higher excitation density. The numerical aperture is much lower in our low temperature microscope (0.55 vs. 1.49 at room temperature), and triplet build-up is a greater problem. Carbazole units are known to give rise to appreciable spin-orbit coupling, promoting triplet formation. This effect

only becomes apparent at high excitation densities and under vacuum, since oxygen is an effective triplet scavenger. Room temperature measurements were therefore performed under air, and hence no saturation effect is observed. We quench triplets at low temperatures, so the molecules invariably appear much dimmer: the triplets live longer (preliminary ensemble phosphorescence decays suggest lifetimes of order 10 ms at 20 K).

Out of 89 single ring molecules identified spectrally (*after* initial illumination to find a suitable spot as described above) at 4 K, no event of unpolarised emission was found. The example of seemingly unpolarised emission shown in Fig. 4b of the main text clearly results from a dipole oriented at 45° with respect to the detectors, since it changes its orientation with time.

In contrast, the rings generally appear unpolarised during *initial* illumination at 4 K, just like at room temperature (spontaneous symmetry breaking should not be a thermally-activated process). Figure S9 shows a preliminary linear dichroism histogram for 61 molecules recorded within 100 ms of initial illumination. The shape of the histogram is quite similar to the room temperature histogram (Fig. 2b in the main text) and indicates that the fluorescence originates from unpolarised emitters rather than from a random distribution of linear dipoles which, in contrast, would lead to maxima in the histogram at $D = \pm 1$ (cf. the case of the dimers in Fig. 2b). 20 % of the molecules are found to fall in the range of $D = \pm 0.1$, this result is comparable to the room temperature measurement. We stress that the data in Figure S9 were taken from wide-field fluorescence images and therefore cannot fully exclude signals coming from possible contaminations on the surface, since the molecules are not identified spectrally or through their fluorescence lifetime, as explained above. In control measurements using identical substrates without the rings dispersed no unpolarised emission was observed, implying that distortion of the histogram by contaminant emission is rather unlikely. We are therefore confident that room-temperature and low-temperature unpolarised emission are fundamentally comparable.

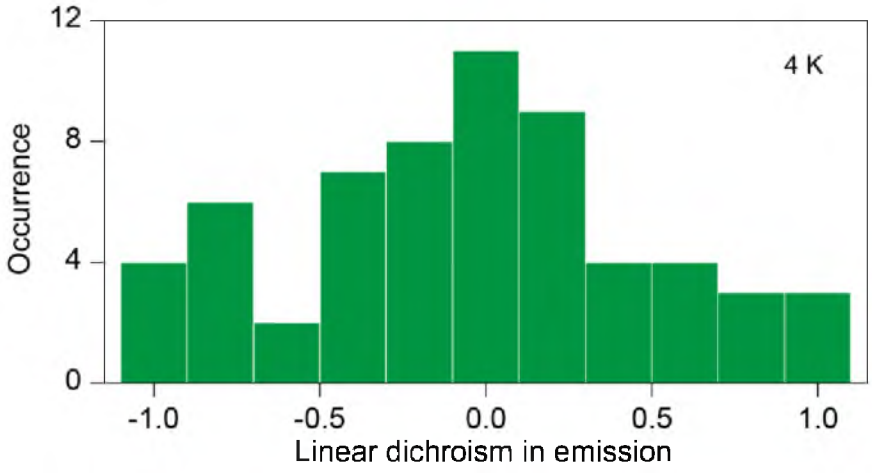

Figure S9. Linear dichroism at 4 K under initial illumination. The 61 molecules were measured in wide-field imaging mode within 100 ms of illumination. The shape of the distribution resembles the histogram measured under room temperature (Fig. 2b, main text), indicating unpolarised emitters rather than a random distribution of linear dipoles.

9. Wide-field polarised excitation fluorescence microscopy

Additionally to the linear dichroism in excitation, $D_{excitation}$, measured confocally, we address the nature of the absorbing transition dipole by determining the distribution of excitation polarisation anisotropy values from molecule to molecule via wide-field polarised excitation fluorescence microscopy.

An inverted microscope (Olympus IX71) was used for wide-field illumination and detection. The excitation source was provided by a fibre-coupled diode laser (PicoQuant, LDH-C-405) with a wavelength of 405 nm in continuous wave mode. The excitation light was passed through a clean-up filter (AHF Analysentechnik, HC Laser Clean-up MaxDiode 405/10) and a Glan-Thompson polariser to provide linearly polarised excitation light. The polarisation of the excitation light was rotated by an electro-optical modulator (FastPulse Technology Inc., 3079-4PW) and an additional $\lambda/4$ waveplate, as described elsewhere.[2] The laser beam was expanded and focused via a lens system onto the back-focal plane of the 1.35 NA oil immersion objective (Olympus, UPLSAPO 60XO) through the back port and a dichroic mirror (AHF Analysentechnik RDC 405 nt) in the microscope. An excitation area of ~80 × 80 µm² was generated in the focal plane and the fluorescence of the sample was collected by the same objective and passed through the dichroic mirror. The fluorescence signal was imaged on an EMCCD camera (Andor, iXon3 897) after an additional magnification of 1.6× and after passing a fluorescence filter (AHF Analysentechnik Edge Basic LP 405 long pass filter). The excitation intensity was set to 100 mW/cm². The overall magnification of 96× results in a resolution of 160 nm² per pixel leading to diffraction limited spots of ~ 2×2 pixels for a single molecule.

The polarisation of the excitation light was rotated in the x-y-plane by 180° over periods of 20 s and the fluorescence intensity of each individual fluorescence spot was recorded as a function of the polarisation angle. A point size of 5 × 5 pixels was assumed for the calculation of the overall intensity and the local background of the surrounding area (13 × 13 pixels) was subtracted for each molecule. The data analysis was conducted with a home-written software provided by the Barbara lab using MATLAB.[3] A molecule with a single linear transition dipole moment will modulate its fluorescence with excitation polarisation following a cosine-squared law. Deviations from a linear dipole result in a modification of fluorescence modulation following $I(\theta) \propto 1 + M\cos(2\theta)$, where θ is the angle of excitation polarisation and M the modulation depth, a value of 1 signifying a linear dipole and 0 an unpolarised absorber.

Fig. S10a,b) shows histograms of M values for the dimer and ring. As expected, the dimer displays an almost linearly-polarised absorption ($M \rightarrow 1$). For the ring, the anisotropy approaches zero. To quantify the accuracy of the measurement, we superimpose anisotropy measurements of fluorescent polystyrene beads of comparable spectral properties and photon count rates (black bars), the histogram of which shows a narrow peak around M=0.1. We note that if the rings did adopt random orientations within the thin matrix film, a large population of molecules with high anisotropy values would be expected from orientations perpendicular to the sample plane.[16] Since this is not observed, we conclude that most of the rings lie in the plane of the film, possibly as a consequence of sheer forces arising during spin coating. As a consequence, polarisation artefacts regarding the linear dichroism in excitation, $D_{excitation}$, which could potentially arise due to the use of a high numerical aperture objective

(NA=1.49) can be neglected,[17] because the ring molecules clearly lie within the xy-plane in the laboratory frame.

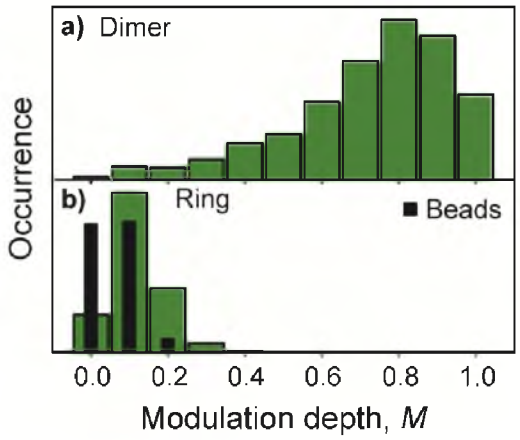

Figure S10. The modulation depth, M, of the emission intensity is recorded as the polarisation of the laser is rotated in the sample plane. Modulation depth histograms show a change from close to linearly-polarised absorption in the dimer (a, 488 molecules) to virtually unpolarised absorption in the rings (b, 238 molecules). The black bars indicate the instrument response for excitation of an isotropic fluorescent bead yielding the same photon count rate as the ring.

References

[1] Lakowicz, J. R., *Principles of Fluorescence Spectroscopy*, 2nd ed., (Kluwer Academic/Plenum, New York, 1999).

[2] Higgins, D. A., VandenBout, D. A., Kerimo, J. & Barbara, J. Polarization-Modulation Near-Field Scanning Optical Microscopy of Mesostructured Materials. *J. Phys. Chem.* **100**, 13794-13803 (1996).

[3] Adachi, T. *et al.* Highly Ordered Single Conjugated Polymer Chain Rod Morphologies. *Phys. Chem. C* **114**, 20896-20902 (2010).

[4] Sauer, M. *et al.* Measuring the Number of Independent Emitters in Single-Molecule Fluorescence Images and Trajectories Using Coincident Photons. *Anal. Chem.***74**, 5342-5349 (2002).

[5] Mössinger, D. *et al.* Large All-Hydrocarbon Spoked Wheels of High Symmetry: Modular Synthesis, Photophysical Properties, and Surface Assembly. *J. Am. Chem. Soc.* **132**, 1410-1423 (2010).

[6] Lei S. *et al.* Two-Dimensional Oligo(phenylene-ethynelene-butadiynylene)s: All-Covalent Nanoscale Spoked Wheels. *Chem. Eur. J.* **15**, 2518-2535 (2009).

[7] Kobayashi, K. *et al.* Syntheses of Hexacis(4-functionalized-phenyl)nebzenes and Hexakis[4-(4′-functionalized-phenylethynyl)phenyl]benzenes Directed to Host Molecules for Guest-Insclusion Networks. *J. Org. Chem.***70**, 749-752 (2005).

[8] Dierschke, F., Grimsdale, A. C. & Müllen, K. Efficient Synthesis of 2,7-Dibromcarbazoles as Components for Electroactive Materials. *Synthesis* **16**, 2470-2472 (2003).

[9] Nierengarten, J.-F., Gu, T., Hadziioannou, G., Tsamouras, D. & Krasnikov, V. A New Iterative Approach for the Synthesis of Oligo(phenyleneethynediyl) Derivates and Ist Application for the preparation of Fullerene Oligo(phenyleneethynediyl) Conjugates as Active Photovoltaic Materials. *Helv. Chim. Acta* **87**, 2948-2966 (2004).

[10] Susumu, K. *et al.* Two-Photon Absorption Properties of Proquinoidal D-A-D and A-D-A Quadrupolar Chromophores. *J. Phys. Chem. A* **115**, 5525-5539 (2011).

[11] Wariishi, K., Morishima, S. & Inagaki, Y. A Facile Synthesis of 1,4-Dialkoxy-2,5-diiodobenzenes: Reaction of Dialkoxybenzenes with Iodine Monochloride in Alcoholic Solvents. *Org. Process Res. Dev.* **7**, 98-100 (2003).

[12] Gibson, V. C., Spitzmesser, S. K., White, A. J. P. & Williams, D. J. Synthesis and reactivity of 1,8-bis(imino)carbazaloide complexes of iron, cobalt and manganese. *Dalton Trans.*, 2718-2727 (2003).

[13] Höger, S. & Bonrad, K. [(3-Cyanopropyl)dimethylsilyl]acetylene, a Polar Analogue of (Trimethylsilyl)acetylene: Synthesis and Approach in the Preparation of Monoprotected Bisacetylenes. *J. Org. Chem.* **65**, 2243-2245 (2000).

[14] Gaefke, G. & Höger, S. [(3-Cyanopropyl)diisopropylsilyl]acetylene, a More Stable Analogue of [(3-Cyanopropyl)dimethylsilyl]acetylene. *Synthesis* **14**, 2155-2157 (2008).

[15] Moroda, A. & Togo, H. Biphenyl- and terphenyl-based recyclable organic trivalent iodine reagents. *Tetrahedron* **62**, 12408-12414 (2006).

[16] Tubasum, S., Cogdell, R. J., Scheblykin, I. G. & Pullerits, T. Excitation-Emission Polarization Spectroscopy of Single Light Harvesting Complexes. *J. Phys. Chem. B* **115**, 4963-4970 (2011).

[17] Thomsson, G., Sforazzini, G., Anderson, H. L. & Scheblykin, I. G. Excitation polarization provides structural resolution of individual non-blinking nano-objects. *Nanoscale* **5**, 3070 (2013).